ABSTRACT

Title of Dissertation: A GENERALIZED METHODOLOGY TO CHARACTERIZE COMPOSITE MATERIALS FOR PYROLYSIS MODELS

Mark B. McKinnon, Doctor of Philosophy, 2016

Dissertation directed by: Associate Professor Stanislav I. Stoliarov, Fire Protection Engineering

The predictive capabilities of computational fire models have improved in recent years such that models have become an integral part of many research efforts. Models improve the understanding of the fire risk of materials and may decrease the number of expensive experiments required to assess the fire hazard of a specific material or designed space. A critical component of a predictive fire model is the pyrolysis sub-model that provides a mathematical representation of the rate of gaseous fuel production from condensed phase fuels given a heat flux incident to the material surface.

The modern, comprehensive pyrolysis sub-models that are common today require the definition of many model parameters to accurately represent the physical description of materials that are ubiquitous in the built environment. Coupled with the increase in the number of parameters required to accurately represent the pyrolysis of materials is the increasing prevalence in the built environment of engineered composite materials that have never been measured or modeled. The motivation behind this project is to develop a systematic,

generalized methodology to determine the requisite parameters to generate pyrolysis models with predictive capabilities for layered composite materials that are common in industrial and commercial applications. This methodology has been applied to four common composites in this work that exhibit a range of material structures and component materials.

The methodology utilizes a multi-scale experimental approach in which each test is designed to isolate and determine a specific subset of the parameters required to define a material in the model. Data collected in simultaneous thermogravimetry and differential scanning calorimetry experiments were analyzed to determine the reaction kinetics, thermodynamic properties, and energetics of decomposition for each component of the composite. Data collected in microscale combustion calorimetry experiments were analyzed to determine the heats of complete combustion of the volatiles produced in each reaction. Inverse analyses were conducted on sample temperature data collected in bench-scale tests to determine the thermal transport parameters of each component through degradation. Simulations of quasi-one-dimensional bench-scale gasification tests generated from the resultant models using the ThermaKin modeling environment were compared to experimental data to independently validate the models.

A GENERALIZED METHODOLOGY TO CHARACTERIZE COMPOSITE MATERIALS FOR PYROLYSIS MODELS

by

Mark B. McKinnon

Dissertation submitted to the Faculty of the Graduate School of the
University of Maryland, College Park, in partial fulfillment
of the requirements for the degree of
Doctor of Philosophy
2016

Advisory Committee:
Professor Stanislav I. Stoliarov, Chair
Dr. Morgan Bruns
Professor Michael Gollner
Professor Kenneth Kiger
Professor Peter Sunderland
Professor Norman Wereley

Acknowledgements

First, I would like to thank my parents, Michael and Margaret McKinnon, who have acted as my closest advisors and largest supporters my entire life. Beginning with youth sports programs and continuing all the way to helping me move furniture up a four floor walk-up in the East Village from a minivan double parked in the bus lane outside, they have always been willing to help me in any way that I needed it and have served as a constant reminder of the rewards that result from hard work. My brother and sisters have also helped me with advice and, whether or not they were aware, motivated me with unspoken sibling rivalries over the years. I would also like to thank all my friends for always helping me to unwind when they knew I needed to and for always forgiving me for losing contact for months at a time when I got caught up in my research.

Many of my lab-mates have come to be very close friends and were always willing to discuss ideas on this research as well as just about any topic. I am certainly indebted to each of them for the valuable insight they provided that, in many cases, found its way into this manuscript in some form. Thanks in particular to Isaac Leventon, Cameron Novak, Tom Feng, Colleen Frances, Kevin Korver, Xuan Liu, and Cara Hamel. Several of my lab-mates also collaborated on several projects that have served as the foundation of this research and they will continue to develop the work presented here to make the results more universally applicable. These colleagues who deserve acknowledgement are Jing Li, Artur Witkowski, Mollie Semmes, Geraldine Martin, Nathan Kahla, Yan Ding, and Josh Swann. Remember the names of all of my

lab-mates because I am confident that all of them will do incredible things in the coming years.

Several agencies are responsible for providing funding, motivation, and support for the work presented in this dissertation. The experiments and analysis conducted on corrugated cardboard were funded by FM Global and monitored by Sergey Dorofeev. The work presented on low-pile carpet was supported by NIST Grant # 60NANB10D0226 and monitored by Kevin McGrattan. FAA Grant # 12-G-011, monitored by Rich Lyon, funded the investigation on the carbon fiber laminate composite.

My dissertation committee deserves acknowledgement for providing valuable comments and questions that have certainly improved the robustness and clarity of the information presented in this dissertation. At various stages in this dissertation, the committee consisted of the following people: Morgan Bruns, Michael Gollner, Kenneth Kiger, Randy McDermott, Peter Sunderland, Arnaud Trouvé, and Norman Wereley. My advisor, Stanislav Stoliarov, deserves the most significant acknowledgement. Stas has the most impressive work ethic I have ever encountered. His drive to change the understanding of material flammability and the status quo in pyrolysis research is unparalleled. He provided all of the motivation for this research and worked hard to make sure I never had to worry about where my funding would come from the next semester. More impressive has been his ability to do the same for countless other individuals. Words cannot express how thankful I am to him.

Table of Contents

List of Tables

List of Figures

Nomenclature

Symbols	Description
b	coefficient in transient heating rate expression (Eq. 4.7)
c	heat capacity [J $kg^{-1}K^{-1}$]
g	Arbitrary function of a reaction model in differential form
h	heat evolved in reaction [J kg^{-1}]
k	thermal conductivity [W $m^{-1}K^{-1}$]
m	mass [kg]
p	Arbitrary property
q	heat flux due to thermal conduction [W m^{-2}]
$\dot{q}$	heat flow rate to a sample material [W kg^{-1}]
r	reaction rate [kg $m^{-3}s^{-1}$]
t	time [s]
x	Cartesian coordinate for depth into sample [m]
y	Cartesian coordinate for length of sample [m]
z	conserved quantity (mass or temperature)
A	Arrhenius pre-exponential factor [$\left(m^3\ kg^{-1}\right)^{n-1}\ s^{-1}$] (for reaction of order n)
E	activation energy [J mol^{-1}]
F	Rate of change of thermo-physical property in terms of conserved quantity
I	radiant flux [W m^{-2}]
J	mass flux [kg $m^{-2}s^{-1}$]
N	number over which a summation is performed
R	universal gas constant [J $mol^{-1}K^{-1}$]
T	temperature [K]
V	volume fraction
Subscripts	
g	gas g
i	reaction i
j	component j
k	component k
n	coefficient for last term in Eq. 2.1
ex	radiation from external sources
rr	re-radiation from sample material
int	intermediate component
$back$	back surface
$peak$	maximum mass loss rate or temperature at which the maximum occurs

Superscripts

0	Net radiation
x	in the direction of the depth of the material
y	in the direction parallel to the surface of the material
n	exponent for last term in Eq. 2.1
α	conversion
β	coefficient of cubic term in effective thermal conductivity [W $m^{-1}K^{-4}$]
γ	reflection loss coefficient
δ	thickness of sample [m]
ϵ	emissivity
η	Coefficient of T^3 term in Eq. 4.16
θ	Fraction of a mixture that is modeled as layers oriented parallel to flow Eq. (8.1)
κ	absorption coefficient [m^2 kg^{-1}]
λ	Mass transport coefficient [m^2 kg^{-1}]
ν	stoichiometric coefficient
ξ	mass concentration [kg m^{-3}]
ρ	density [kg m^{-3}]
σ	Stefan-Boltzmann constant [W $m^{-2}K^{-4}$]
τ	fraction of radiation transmitted through sample material
φ	heating rate [K s^{-1}]

Acronyms

BFL	Cardboard B-flute layer
BMS	Boeing Material Specification
CAPA	Controlled Atmosphere Pyrolysis Apparatus
CB	cardboard
CFL	Cardboard C-flute layer
DSC	Differential Scanning Calorimetry
FAA	US Federal Aviation Administration
FPA	Fire Propagation Apparatus
FRP	Fiber-reinforced Polymer
HRR	heat release rate
LB	Cardboard linerboard
LDPE	Low-density polyethylene
MLR	mass loss rate
MCC	Microscale Combustion Calorimetry
NIST	US National Institute of Standards and Technology
PA6	Polyamide-6
PET	Polyethylene Terephthalate

SLPM	Standard liters per minute (at 1 atm and 298 K)
STA	Simultaneous Thermal Analysis
TGA	Thermogravimetric Analysis
TRP	Thermal Response Parameter
UP	Unsaturated Polyester
VAE	Vinyl-acetate ethylene

Chapter 1: Introduction

Computational fire models have significantly improved in recent years as computing power has advanced and research has been conducted to better understand how to most accurately depict fire events with computer codes. Fire models have begun to and are predicted to continue to change the methods by which fire research is conducted. Although modeling cannot completely replace full-scale testing, it can provide insight about full-scale tests and can be used to extrapolate results to reduce the number of full-scale tests required in an investigation. Improved understanding of the fire risk of materials in the built environment through a range of orientations and scales provides practitioners of fire models a basis from which to provide better-informed advice and designs.

Historically, fire models have been limited in use to only determine the projected consequences of a prescribed fire event. The prescribed fire for these models is based on a burning rate profile that is formulated from observations and analysis of actual fire events and relies on assumptions about the fuel type and load present in an enclosure as well as the ventilation and environmental heating conditions in the enclosure. In reality, there are many factors that can affect the burning rate of a material, and the prescribed burning rate curve is an idealization that can predict misleading consequences. Recent advances in fire models have led to several models that represent condensed-phase materials that can physically interact with the simulated environment to produce realistic predictions about ignition, the evolution of the burning rate, and spread of a fire.

A critical component of predictive fire models is the pyrolysis sub-model that represents gaseous fuel production from the condensed phase given a radiant and/or

convective heat flux incident to the material surface. Some pyrolysis sub-models have been developed to calculate heat transfer, thermal degradation, heterogeneous reactions, and mass transport, and have been coupled to gas-phase solvers in fire models. The majority of fire research and the largest emphasis in the development of fire models have been dedicated to gas phase phenomena due to the complexity of the fundamental physical and chemical processes that characterize pyrolysis. This has resulted in a lack of understanding about pyrolysis and the inability to accurately describe the pyrolysis of solid phase materials. As computational fire models have become more frequently relied upon and increasingly complicated, it has become evident that more sophisticated pyrolysis sub-models are required to match the sophistication of gas-phase solvers and accurately predict fire behavior.

One of the distinguishing factors between pyrolysis models is the set of assumptions made to simplify the physical description of the material and the process through which it transmits heat and degrades. The simplifying approximations that define the complexity of the pyrolysis model also dictate the parameters required to fully define the material in the model as well as the initial and boundary conditions related to the specific orientation and scale to be modeled. Essential to accurate predictions with pyrolysis models are a set of parameters that correspond to material properties and reaction kinetics for the material of interest.

The complete set of parameters required for accurate pyrolysis model predictions have been determined and are publicly available for few common engineered materials. Few materials have been characterized in this way because the breadth of thermo-physical properties and reaction parameters required to completely define a material and validate

the resulting model requires an extensive experimental and analytical effort and, due to the fact that many of these properties are temperature-dependent and the materials are known to decompose at high temperatures, methods do not currently exist to efficiently measure all of the requisite properties. Several researchers have attempted to simplify the process of determining these required parameters through engineering approximations [1,2], novel experimental apparatuses [3–5], and numerical optimization schemes used in analysis [6,7].

Further complicating the lack of a generalized, comprehensive method to characterize materials commonly encountered in the built environment is the rapid development and utilization of engineered polymers and advanced composites. As manufacturing technology has improved and structural material requirements in the built environment have become more demanding, there has been a marked increase in the prevalence of composite materials to replace conventional materials. These materials provide improvements to the built environment in terms of structural stability and costs, but inherently lack the fire-resistive qualities of the materials that they generally replace. The thermo-physical properties and pyrolysis behavior of advanced composite materials are currently not well documented nor well understood, which complicates justification of adoption of these materials for situations that have a low tolerance to fire damage. The development of pyrolysis models for composites and engineered materials can improve the understanding of the flammability characteristics of engineered materials and inform the design of the built environment to mitigate the effects of fires.

The fire protection industry lacks a publicly accessible database with thermo-physical properties corresponding to materials commonly encountered in the built

environment. The developers of the NIST Fire Dynamics Simulator (FDS) have begun to build repositories of material property sets used for validation of FDS although the list of materials is sparse as of yet [8]. With the significant push in the industry toward performance-based design and the increasing reliance on computational modeling, a database that may be used to define commonly encountered materials has become a necessity. To populate such a database would require a methodology that could be followed to efficiently determine the properties of previously uncharacterized materials. Maintaining the database such that it is current with a new generation of composites and engineered polymers will pose a significant challenge, but this process can be facilitated by intelligent design of a generalized methodology to characterize these materials.

The motivation behind this project is to develop a systematic methodology to measure the thermo-physical properties and determine the thermal degradation reaction parameters for layered and laminate composite materials that are common in industrial and commercial applications to parameterize fire models to improve predictive capabilities. The generalized methodology presented in this document allows experimental conditions to be replicated and estimated parameters to be independently validated.

This document is structured to present all pertinent background information that forms the foundation of the methodology and facilitates understanding of the analysis prior to the description of the experimental methods and analyses. This background information about pyrolysis models, layered composite materials in the scope of this methodology, and methods that have previously been used to measure these properties is provided in Chapters 2, 3, and 4. The evolution of the methodology and the observations of experiments that led to each incremental evolution are presented in chronological order. In addition to the

background information provided in Chapter 4, the experimental methods and analysis procedures advocated in this methodology are also presented. The finalized methodology is presented in general terms and is demonstrated on four layered composite materials (corrugated cardboard, low-pile carpet, a carbon fiber aerospace composite, and glass-reinforced polyester) in the form of individual, stand-alone case studies in Chapters 5 through 8. The final case study included here on fiberglass-reinforced polyester (Chapter 8) was conducted with support from the author by a colleague under the supervision and advisement of the author. That case study demonstrates the relative ease with which independent researchers and practitioners of fire models may implement this methodology to parameterize pyrolysis models as well as a demonstration of the potential predictive capabilities of pyrolysis models for the design of composite systems.

Chapter 2: Modeling

Section 2.1: Motivation to Study Pyrolysis

All deflagrations that occur in the built environment are fueled entirely or in part by combustible volatile species that are released from solid materials. Pyrolysis may be defined generally as simultaneous thermal degradation and heat and mass transport. In the context of fire science, pyrolysis may be defined as the set of processes that occur in the solid phase beginning with the onset of absorption of energy by the material, continuing on after ignition of the flammable gases produced by the material until the energy is no longer introduced to the solid. A complete and comprehensive understanding of pyrolysis has proven elusive over more than a century of research. One reason that the research community still lacks a comprehensive understanding of pyrolysis is the vastly different behavior of different classes of materials. As a simple example, the pyrolysis of intumescent charring polymers includes several additional complicating phenomena when compared to the pyrolysis of non-charring polymers including the formation of a thermally insulative layer of char, additional thermal degradation reactions, and potential effects from the transport of volatiles through the char matrix.

The advent and proliferation of generalized pyrolysis models has not only allowed predictions of the rate of production of gaseous volatiles from solid materials due to energy absorption, but has also provided tools for researchers to better understand the physics and importance of the processes that occur during pyrolysis. Comprehensive models have been constructed to incorporate all of the major physical phenomena that can possibly occur in the solid phase and they may be utilized to determine the sensitivity of all model predictions to the parameter that primarily defines each phenomenon. Models have also been used in

inverse analyses to determine the value of unknown parameters that are difficult to measure in a laboratory setting.

Comprehensive pyrolysis models are commonly used in research to better understand the complicated processes that comprise pyrolysis, but these models have also been coupled to gas phase solvers for a variety of applications. Pyrolysis models may be used during the design of the built environment to provide quantitative and qualitative information pertaining to the fire risk of the design. Models have been used extensively in forensic investigations to reconstruct a fire event based on the observations made in the aftermath of the event. It has also been hypothesized that pyrolysis models may be used independently or coupled to mechanical models when designing materials to produce a desired response to specified thermal conditions [9]. All of these applications have the capacity to prevent loss of life and property and require knowledge of the physics that dominate pyrolysis in general as well as the pyrolysis of materials encountered in the built environment.

Section 2.2: Pyrolysis Model Background

A promising potential alternative method to as well as an analytical tool that can supplement standard fire tests are computational fire models. These models may provide improved understanding of the fire risk of materials in the built environment over a range of orientations and scales and provides designers a basis from which to provide better-informed designs [10]. The current generation of computational fire models can account for radiation, multi-phase flow, combustion, and several other phenomena that occur in the gas phase. The solid phase of these models is generally coupled to the gas phase and each is solved separately with a different set of governing equations. The solid phase is

accounted for by a pyrolysis sub-model that relates the external heating conditions (determined by the gas phase sub-model) to the rate of production of combustible gaseous pyrolyzate. Pyrolysis sub-models have also been used as stand-alone models to investigate pyrolysis-related phenomena, improve the physical understanding of pyrolysis, and to aid in the design of materials to meet specific fire response requirements.

Pyrolysis models may be classified according to the assumptions made to simplify the scenario to be described as well as their solution method. A major distinction is between thermal models that rely on the assumption of infinite-rate reaction kinetics and comprehensive models that account for finite-rate reaction kinetics. Thermal models are called such because they are used to calculate the rate of production of volatile species by solving only an energy balance. These models are constructed under the assumption that pyrolysis occurs at a single temperature, effectively decoupling the thermal degradation reaction kinetics from other processes occurring during pyrolysis.

Thermal models may be sub-divided further into semi-empirical, analytical, and integral models [11]. Semi-empirical models are the simplest closed-form correlations between environmental conditions and the rate of pyrolyzate production that require several assumptions. Semi-empirical models rely on input parameters that can be determined directly from standard fire tests and generally require the fewest parameters to define a material. Analytical models are closed-form correlations that are formulated based on exact solutions to heat transfer equations. Integral models solve energy conservation equations according to an assumed form of the temperature profile and require a computational algorithm for solution.

Development of pyrolysis models for common building materials began in 1945 with the development of a simple analytical model for the pyrolysis of wood [12]. Even with the advent of computational technology, the utility of these simple models has not been overlooked and analytical formulations of pyrolysis models for very specific scenarios continued to be developed into the 1990s [13]. Though semi-empirical models are generally simpler than analytical models, these models appeared chronologically after the origin of analytical models. The biggest proponent of semi-empirical models developed a model in 1979 [14] that is still commonly used today in analysis of bench-scale standard test data. Integral models were developed to address the shortcomings of closed-form solutions, particularly the inability to apply the model to different heating conditions and materials. Integral models incorporated a more elegant solution into pyrolysis models, but also required the definition of many more pyrolysis models. A model developed by Quintiere [15] has been used extensively in his collaborations with other fire researchers [16].

Comprehensive models were developed because the assumption that chemical reactions occur much faster than diffusion processes is not always valid and predictions made with thermal models were found to be inadequate for the new generation of computational fire models in development. Comprehensive models use energy and mass conservation equations with a representation of the chemical kinetic reaction mechanism to calculate the rate of thermal degradation and generally attempt to represent all the important physics that occur in the solid material on the microgram-scale. The kinetic mechanism is used to describe the rates of reactions that occur during pyrolysis as a function of temperature and species concentration. The mechanism defines reaction

schemes that describe the various effective pathways through which the reactants form products. Each reaction is defined by a set of parameters that mathematically describes the rate at which solid reactants transform to solid and gaseous products of degradation. Comprehensive models general use the Arrhenius equation to calculate the reaction rate as a function of temperature.

The earliest versions of comprehensive models were developed by Kung et al. in the 1970s [17]. Various improvements on the physics described in the models came over the next few decades. Multiple reaction schemes were introduced to comprehensive models in the 1980s [18]. The 1990s brought modeling of changes in geometry with degradation [19] and the extension of comprehensive models to multiple dimensions [20]. Though the functionality of these models improved over years, each was still limited to fairly specific materials and possible external conditions that could be modeled. Generalized comprehensive models were developed to allow simulations of almost any material subjected to almost any external conditions. The most prominent examples of these models are the solid phase model for NIST Fire Dynamics Simulator (FDS) [8], GPyro [21], and the Thermal Kinetic Model of Burning (ThermaKin) [22].

The treatment of the physical processes that occur in the condensed phase during pyrolysis have a significant effect on the predictions made by the model. A variety of pyrolysis models have been used previously that are formulated with a range of assumptions about these processes. It is important that any researcher that utilizes the generalized methodology outlined in this document fully understand the assumptions made to model the physical phenomena that occur during pyrolysis and all of the simplifications associated with the experiments conducted as part of this methodology.

Section 2.3: ThermaKin

The pyrolysis model used in this work to conduct inverse analyses and to ultimately produce mass loss rate predictions is the ThermaKin modeling environment [22]. ThermaKin solves the non-steady energy and mass conservation equations accounting for chemical reactions described by Arrhenius reaction rates. The sample material is defined in ThermaKin geometrically as a series of layers with specified thicknesses and chemically as material components defined by specific thermodynamic and physical properties. ThermaKin has recently been expanded to model two-dimensional geometries [23] and the governing equations presented here are from the two-dimensional formulation. In the two-dimensional formulation, the material is represented as a series of one-dimensional modeled material (with depth denoted as x) layered in the direction of the additional dimension (denoted y). The ThermaKin modeling environment has been validated through several investigations on charring and non-charring polymers [23–25].

Chemical and physical properties are defined for each component material in the ThermaKin framework. These properties include the density, heat capacity, thermal conductivity, mass transport coefficient, emissivity, and absorption coefficient. The emissivity and absorption coefficient are assumed constant for each component. All other properties are defined as functions of temperature in Eq. 2.1 where the property is generically denoted p.

$$p(T) = p_1 + p_2 T + p_n T^n \tag{2.1}$$

Reactions are defined in ThermaKin as occurring between one or two components to produce between zero and two components. The energy evolved from each reaction can

be defined as a temperature-dependent quantity with Eq. 2.1. The reactions defined in the reaction mechanism are governed by Arrhenius reaction rates defined in Eq. 2.2. The reaction order is equivalent to the number of component concentrations defined in Eq. 2.2 and is most often defined in this work as first-order, although second-order reactions may also be modeled.

$$r_i = A_i \exp\left(\frac{-E_i}{RT}\right) \xi_j \, \xi_k \tag{2.2}$$

The pre-exponential factor, *A*, and activation energy, E_a, are the kinetic parameters specified to define the reaction rate as a function of temperature and the mass concentration of the reactant components denoted in the equation by ξ_l and ξ_k.

Mass and energy conservation equations are solved by ThermaKin assuming the heat exchange between the gases and the solid material of the sample is instantaneous. It is also assumed that the momentum from the gases transported in the solid material is negligible. The statement for the conservation of mass for component *j* (Eq. 2.3) includes contributions from reactions, mass transport, and expansion or contraction of the material.

$$\frac{\partial \xi_j}{\partial t} = \sum_{i=1}^{N_r} \nu_i^j r_i - \frac{\partial {J_j}^x}{\partial x} - \frac{\partial {J_j}^y}{\partial y} + \frac{\partial}{\partial x}\left(\xi_j \int_0^x \frac{1}{\rho}\frac{\partial \rho}{\partial t}\, dx\right) \tag{2.3}$$

The symbols in Eq. 2.3 are defined as follows: t is time, ν_i^j is the stoichiometric coefficient of component *j* in reaction *i*, J_j is the mass transport term for component *j* which can occur in the *x* and *y* direction, and ρ is density of the component mixture. Mass transport is assumed to be driven by concentration gradients. The expression for mass transport of gas g is provided as Eq. 2.4, where λ is defined as the mass transport coefficient.

$$J_g = -\rho_g \lambda \frac{\partial \left(\frac{\xi_g}{\rho_g}\right)}{\partial x} \tag{2.4}$$

The conservation of energy equation is solved accounting for heat generation from reactions, in-depth and in-plane conduction, radiation absorption, re-radiation, convection from gas transport in the solid, and energy flow associated with contraction or expansion of the material with respect to a stationary boundary (x = 0). The conservation of energy term solved in ThermaKin is provided as Eq. 2.5.

$$\sum_{j=1}^{N} \xi_j c_j \frac{\partial T}{\partial t} = -\sum_{i=1}^{N_r} h_i r_i - \frac{\partial q_x}{\partial x} - \frac{\partial q_y}{\partial y} - \frac{\partial I_{ex}}{\partial x} + \frac{\partial I_{rr}}{\partial x} - \sum_{g=1}^{N_g} c_g \left({J_g}^x \frac{\partial T}{\partial x} + {J_g}^y \frac{\partial T}{\partial y} \right) + c\rho \frac{\partial T}{\partial x} \int_0^x \frac{1}{\rho} \frac{\partial \rho}{\partial t} dx \tag{2.5}$$

The symbols in Eq. 2.5 are defined as follows: c_j is the heat capacity of component *j*, c is the mixture heat capacity, which is weighted according to the mass of components in the mixture, h_i is the heat absorbed in reaction *i*, q is heat flow due to conduction (Eq. 2.6), I_{ex} is the radiation flux from external sources traveling to and within the material (Eq. 2.7), and I_{rr} is re-radiation, potentially from in-depth (Eq. 2.8). κ_j is defined in the radiation term of Eq. 2.7 as the absorption coefficient of material *j*. The symbols of Eq. 2.8 are defined as the following: ϵ is the surface emissivity, σ is the Stefan-Boltzmann constant, and I_{ex}^0 is the net external radiation flux through the material boundary.

$$q = -k \frac{\partial T}{\partial x} \tag{2.6}$$

$$\frac{\partial I_{ex}}{\partial x} = -I_{ex} \sum_{j=1}^{N} \kappa_j \xi_j \tag{2.7}$$

$$\frac{\partial I_{rr}}{\partial x} = \frac{\epsilon \sigma T^4}{I_{ex}^0} \frac{\partial I_{ex}}{\partial x} \tag{2.8}$$

Boundary conditions are defined at the top and bottom surfaces of the computational domain. The boundaries can be defined with the capability of mass transport from the material to the surroundings. The mass transport at the boundary is specified with a linear function generally used to remove pyrolyzate gases from the solid sample at the top surface. Alternatively, an exponential function may be applied as the boundary condition to simulate surface reactions.

The heat transfer boundary condition must be specified for convective and radiant heat flow. The atmospheric temperature can be defined as a linear function of time to modify the convective heat flow boundary condition during simulation. The radiant heat flow boundary condition can be specified with up to two linear heat flux phases and may be specified as periodic to repeat the heat flux program. A critical mass flux for ignition can be defined to simulate flaming combustion of the solid sample. The critical mass flux causes the convective and radiant boundary condition to change to account for the excess heat flux caused by the presence of a flame on the material surface.

The ThermaKin program divides the computational domain into finite volumes (elements) in the shape of rectangular prisms and calculates the temperature and concentration of each component in all the elements at every time step. The conservation equations are solved for the x-dimension with a modified Crank-Nicolson scheme shown here as Eq. 2.9.

$$z_i^{t+\Delta t} = z_i^t + \frac{\left[F_i\left(z_i^t, z_j^t, z_k^t, \ldots\right) + F_i\left(z_i^{t+\Delta t}, z_j^{t+\Delta t}, z_k^{t+\Delta t}, \ldots\right)\right]}{2} \Delta t \tag{2.9}$$

Where the variable z_i^t is the mass or temperature of a component in the element being considered at time t and $z_i^{t+\Delta t}$ is the same property at time $t + \Delta t$. F_i in the above equation is the rate of change of the property denoted by i. The rates of change of the properties are functions of the component masses and element temperatures defined by the conservation equations provided by Stoliarov and Lyon [22]. The resulting equations for each element and each component are linearized and solved at each time step. The y-dimension terms in the conservation equations are solved through a simple explicit integration with all the details provided elsewhere [23].

The models constructed with the ThermaKin program can be divided in two categories based on the operating assumptions for each model. The models used to simulate the milligram-scale tests conducted in the STA apparatus were constructed assuming the sample was thermally thin. Under this assumption, the material heated instantaneously and evenly via convection from the atmosphere. The convection coefficient was sufficiently high to induce instantaneous heating. The model was defined such that heat was transferred to the sample purely through convection without a contribution from radiation. The models constructed in the thermally thin mode followed the same temperature program as the tests conducted with the STA apparatus.

The models constructed to simulate bench-scale tests required few assumptions a priori about the heat and mass transfer characteristics of the sample and test procedure. Heat was transferred to the material with a radiant boundary condition set to the external heat flux measured in the physical tests. As the sample material was heated, convective cooling from the atmosphere occurred on the top and bottom surface boundary. The

descriptions of measurements made to characterize convective cooling of the sample at its boundaries are described in a later section.

Section 2.3.1: Comparison to Other Comprehensive Pyrolysis Models

There are two additional comprehensive pyrolysis models that are commonly used in research and modeling because of their robustness and ability to represent myriad materials. These two models are the NIST Fire Dynamics Simulator (FDS) condensed phase model [26] and GPyro [7]. Each of these models was formulated with different assumptions and, as such, slightly different physical phenomena are represented in each or a slightly different mathematical representation of the phenomena is provided in each.

GPyro was developed with the assumption that there is no resistance to gas transport within the solid phase, although mass transport may be accounted for with invocation of the pressure solver option, in which case transport is dictated by Darcy's law. The heat equation takes into account conduction from the condensed phase, production due to reactions, convection from the gas phase to the condensed phase, in-depth radiation absorption, and radiation emission from the sample surface, although in-depth emission is considered negligible. The chemical reactions are described in GPyro with Arrhenius reaction parameters and the reaction scheme may take on any of a wide variety of possible reaction models, including nth-order reactions. GPyro has the additional advantage that it is coupled to an optimization algorithm that is capable of automatically determining unknown model parameters from a set of target data provided by the user. GPyro has the ability to be operated in one-, two-, or three-dimensions. The thermo-physical properties are defined with a temperature dependence by multiplying the property defined at a reference temperature by the ratio between the instantaneous temperature and the reference

temperature raised to a power. GPyro has been coupled to the gas phase solver in FDS to formulate a robust fire model [27].

The FDS condensed-phase model was constructed under the assumption that all volatiles generated in-depth are instantaneously transported to the top surface, so there is no need to track momentum or model mass transport. It is also assumed that any gases and solid are in thermal equilibrium at all times. The one-dimensional heat equation implemented in FDS takes into account conduction in the solid phase, production from reactions, radiation absorption, and in-depth emission of radiation. Solid-phase chemical reactions are defined in FDS with the Arrhenius reaction parameters and an nth-order reaction model is used to describe the kinetic mechanism, although only a single reactant may be defined for each reaction. The FDS solid phase model has the advantage of being coupled to the FDS gas phase solver, continuous development and support from NIST staff, and has been validated against several sets of experimental data. The FDS solid phase model has only been formulated for one-dimensional geometries. The thermo-physical properties may be defined in FDS according to any arbitrary temperature dependence in terms of discrete temperature/property pairs but the process of doing so can be tedious for non-linear dependencies. Limitations to the description of the solid phase in FDS include the inability to automatically calculate properties of mixtures and the inability to model reactions between multiple solid reactants. The FDS condensed phase model has been used extensively in research and modeling efforts [28,29].

The subtle differences in the formulation of the three comprehensive models described here yield slightly different results for simulations conducted to predict pyrolysis rates for various materials. Any model not described here with equivalent or more

sophisticated features could be parameterized by the standard methodology presented herein. It is important to understand the assumptions inherent to each model that may possibly be used to characterize a material through inverse analyses and the ultimate effect of each assumption on the final results.

Chapter 3: Materials

Section 3.1: Composites Background

Natural and artificial composite materials are ubiquitous in structures and other applications and have been for millennia, though recent improvements in technology have led to significant advances in technical sophistication and industrial and commercial relevance of artificial composites. Bricks composed of dried mud reinforced with straw were used by Sumerians in buildings as long ago as 5000 BC [30]. Wood, the material that is most commonly used in modern structural applications, is a composite that consists of cellulose fibers bound together in a matrix of lignin. Technological advances in high-strength fibers and polymer chemistry throughout the twentieth century have led to a prevalence of laminate composites in applications ranging from automobiles to spacecraft. These advanced composites now compete with, and in some industries, have completely displaced, traditional materials.

Composite materials are defined as a combination of two or more materials in which each constituent retains its mechanical, chemical, and thermo-physical properties, and the combination results in better overall properties than any of the individual components alone. The components in a structural composite can be classified as either reinforcement or matrix [31]. The reinforcing components provide strength and stiffness to the composite and the matrix components maintain the orientation of the reinforcement and protect the reinforcement from environmental conditions. These structural composites can be designed to withstand the stresses associated with physical loadings in the built environment with knowledge of the mechanical properties of the component materials.

Fiber-reinforced polymer (FRP) is a class of advanced structural composites that is subdivided by the type of reinforcing fiber and matrix polymer that compose the material.

Commonly the reinforcing fiber is composed of glass or carbon. Advanced structural composites that use fiberglass or carbon fiber as the reinforcement and various thermosets or thermoplastics as the matrix are common in aerospace and marine applications, as well as in automobiles, sporting goods, and consumer products due to a favorable strength to weight ratio [32]. Specifically in the aerospace industry, advanced composites have completely replaced metals in the design of parts in some aircraft.

Though manufacturing technology lagged behind the potential demand for advanced composites for decades, this technology has advanced such that production and use of structural composites is, at times, more advantageous than traditional building materials. It has been estimated that global demand for carbon fiber will consistently increase each year and reach approximately 80,000 metric tons by the year 2020 [33]. These annual increases are projected to span across all sectors and a marked surge is expected in alternative energy infrastructure.

Composite materials will remain an important topic for fire researchers as new components and combinations are developed and because they are currently favored in situations that require the most stringent flammability requirements including the aerospace and maritime industries. One of the most significant barriers to widespread use of advanced structural composites over metals and other low flammability traditional building materials is the unavoidable thermal decomposition, and inherent flammability, of these composites as well as a lack of knowledge concerning the flammability characteristics of such materials. Determining the flammability characteristics of composites is particularly difficult because the parameters that define the energetic and physical interactions between the components and layers are generally not well understood.

Section 3.2: Materials Studied

The subject of this work is a generalized methodology to characterize composites. There are varying degrees of complexity in the composites that are common to the built environment, and as such, the specific materials to which this methodology may be applied must be defined. The methodology is demonstrated on several composite materials that have been generically defined as macroscopic layered composites. These composites feature individual components in the form of layers and each layer is visible with the naked eye (thickness is greater than 1 μm). This definition also includes fiber-reinforced laminate composites that consist of alternating layers of fiber reinforcement and polymer matrix.

The samples of the material must be suitable for quasi-one-dimensional bench-scale testing and a one-dimensional pyrolysis model. The material must feature a layered orientation or an orientation that may be simplified through assumptions to a layered geometry. If each layer is not a homogeneous component, but rather a mixture of components, the analysis gets more complicated and uncertain, though the material may still be characterized. Examples of each of these have been studied during the development of the methodology presented here and the following sub-sections provide background about each material and the motivation to study that material. Challenges were confronted when applying the generalized methodology to each of the following materials and the solutions to these challenges were generalized and incorporated into the methodology to improve the robustness of its application.

Section 3.2.1: Corrugated Cardboard

Warehouse storage presents a potential fire hazard due, in part, to the orientation, configuration and nature of the stored commodities. Lignocellulosic materials, specifically

corrugated cardboard, are frequently used to produce storage containers and can comprise much of the fuel load for fires in warehouses and storage occupancies. In many storage facilities, commodities are stored closely together in combustible corrugated cardboard packaging on racks that can range up to 30 m high. A small fire can spread rapidly due to the proximity of combustible goods. The economic impact from warehouse fires is, on average, considerably higher than the economic impact of fires in residential and office buildings because it includes property damage and business interruption costs. On average, between 2007 and 2011, storage occupancies accounted for 20.6% of non-residential fires, 29.4% of civilian deaths in non-residential fires, and 20.2% of the dollar cost of direct property damage in non-residential fires ($614MM) annually [34].

By developing a comprehensive understanding of the ignition and pyrolysis of corrugated cardboard and similar composite packaging materials, it is possible to better understand fires in storage occupancies and propose new fire safety measures that effectively reduce the societal, economic, and environmental impacts of warehouse fires [35]

Lignocellulosic materials are mainly composed of cellulose, hemicelluloses, and lignin, which are organic polymers that act as the structural components of the cell wall of plant cells. Cellulose is characterized by long, unbranched chains and a crystalline structure. Hemicellulose refers to any of a group of polymers existing in plant cell walls that are characterized by relatively shorter, branched chains and an amorphous structure [36]. Lignin is made up of several complicated amorphous polymers. The lignin and hemicelluloses serve as the matrix and the cellulose chains serve as the reinforcement in plant cells. When cardboard is structured with alternating layers of planar and corrugated

sheets, the material may be defined as a layered composite. A picture of the specific corrugated cardboard samples tested as part of this research is provided in Figure 3.1.

Figure 3.1: Picture of a Corrugated Cardboard Sample

Recent studies on corrugated cardboard have focused on burning rate correlations [37] and flame spread over the surface of the material [38,39]. Several studies [40,41] have focused on determining an effective reaction mechanism for cardboard thermal degradation. However, these mechanisms vary considerably and it is not completely clear whether this variation reflects the differences in the material composition or the method of determination. Moghtaderi [11] provided a survey of existing pyrolysis models for lignocellulosic materials although corrugated cardboard was not identified as a material that has been characterized for a pyrolysis model.

The motivation for studying corrugated cardboard is not limited to the benefits afforded to warehouse and storage occupancy fire protection. Since 1960, corrugated cardboard production has increased by approximately 300% and its municipal solid waste market share has increased 27%. 31.9 million tons are produced annually, based on industry statistics from 2011 [42]. With the widespread use of corrugated cardboard, it is possible that the material may comprise a portion of the fuel load for a wide array of scenarios and it is advantageous to understand the flammability and create a pyrolysis model for such a material.

The corrugated cardboard characterized through this methodology presented a challenge because of the non-one-dimensional fluted layers in the composite. The fluted

layers could not be separated from the composite without compromising the structure of the entire composite so it was impossible to accurately independently characterize the flutes. A homogeneous representation of the composite was originally considered, although it had to be modified to include a lower density representative material in place of the flutes. Layers of the material also tended to delaminate and exfoliate during pyrolysis, which led to uncertainty in the heat transfer that occurred in depth. This led to later modification of the bench-scale gasification tests used in the experimental portion of this work to include a spatially-resolved temperature measurement.

Section 3.2.2: Low-pile Carpet

Carpet constructed with synthetic polymers is the most common floor covering material in the built environment although it has poor flammability characteristics compared to other flooring materials. Carpet and area rugs accounted for 50.7% of the U.S. floor covering market in 2013, which amounts to an estimated 985 million m^2 installed that year [43]. Modern carpet consists of a series of complicated layers made from several different polymers. Low-pile carpet tile, a modular form of the flooring material that is commonly found in commercial and institutional occupancies, particularly in high traffic areas, features at least three distinct layers of polymer mixtures. A picture of the low-pile carpet tiles characterized in this research is provided in Figure 3.2.

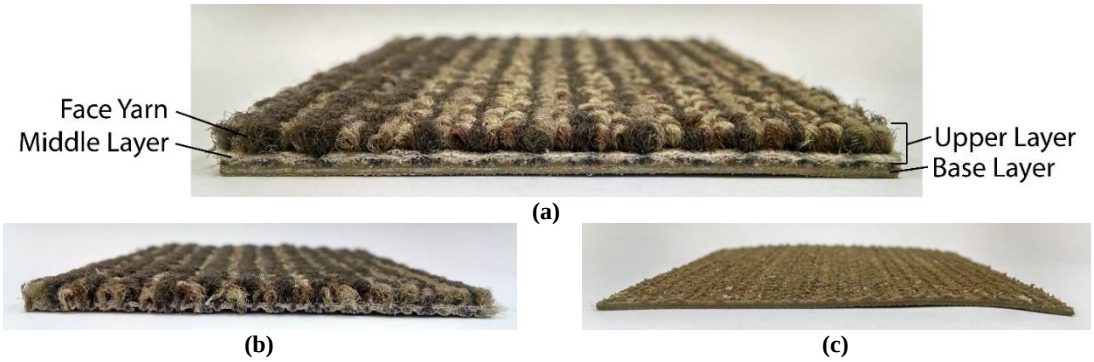

(a) **(b)** **(c)**

Figure 3.2. Pictures of (a) Full Carpet Composite, (b) Upper Layer, and (c) Base Layer

Currently the ignitability of carpeting and its ability to allow fire to spread over its surface is addressed by the Flammable Fabrics Act and is administered by the US Consumer Product Safety Commission (CPSC). A test specific to carpeting, commonly referred to as the "pill test," [44] provides a good indicator of the ability of a carpet sample to act as the point of ignition for an enclosure fire, but it does not provide information about the flammability characteristics of the floor covering when a fire ignites and grows elsewhere. The Flooring Radiant Panel Test [45] is an additional standard test used to simulate the scenario when an enclosure adjacent to a carpeted corridor is engulfed in a fully involved fire. This standard test provides a better indication of the flame spread characteristics of the floor covering in realistic fire scenarios than the pill test, but does not provide enough information to understand the fire spread and evolution as a function of the ambient conditions.

These standard test methods have been successfully used for decades to assign flammability classifications to the materials used to make consumer products or to collect data from which quantitative flammability characteristics may be inferred although numerous shortcomings have been identified. Major criticisms of these and other standard fire tests are the limitations on the scenarios that can be realized in a given apparatus and uncertainties in the physical parameters that define these scenarios. These limitations result in an inability to generalize the results and extrapolate beyond conditions of a given test method. A pyrolysis model with predictive capabilities may provide the variability required to simulate these standard fire tests as well as realistic fire scenarios.

Several of the polymers used to make the carpet tiles that were studied here were harvested from recycled materials and included auxiliary chemicals as stabilizers and fire-

retardant additives. The inexact chemistry of the materials generally used in carpet make the usefulness of literature values for the properties of these materials limited. As a result, all of the materials in the carpet samples required experimental testing to adequately determine the thermo-physical properties and reaction parameters that described the complete pyrolysis process. The layered structure of carpet, the variety of materials that may be used in each layer, and the significant differences in the structure of each layer led to significant difficulty in characterizing the carpet samples for fire models. Carpet may comprise a large fraction of the fire load in the built environment, and as such, a full understanding of its fire hazard and all of the processes involved in pyrolysis proves to be important. This complete understanding of the pyrolysis process cannot be attained through standard testing like the radiant panel, although it may be gained through development of a predictive pyrolysis model.

Section 3.2.3: Fiberglass Reinforced Polyester

Reinforced polymer composites are fabricated through the polymerization of a liquid resin in the presence of a chemical initiator within an interpenetrating fiber network. The commonly used resins include polyester, epoxy, and vinyl ester. Typical fiber reinforcement materials are fiberglass, carbon fiber, and KEVLAR. Polyester reinforced by fiberglass is the most common combination of fiber-reinforced composites in the world [33]. Fiberglass reinforced polymers are used extensively in structural and thermal protection applications for the maritime, aerospace, and offshore industries [46,47], but the uses for these composites has spread across many industries with the largest percentage utilized for transportation, construction, and in electronics. It has been shown that the weight of merchant ships can be decreased by up to 60% through the use of fiber-reinforced

polymers, which is advantageous because it decreases the energy required for transportation. The widespread adoption of these composites as they have become a cost-effective alternative to traditional building materials has outpaced the knowledge base in the research community of their inherent fire hazard.

Unsaturated polyester resin is one of the most flammable matrix polymers that are commonly used in composites and also produces a large yield of soot relative to its mass when it undergoes pyrolysis and combustion [48]. This soot contributes to dark smoke that compromises sight and timely egress in a fire scenario and may lead to asphyxiation. Dark, sooty smoke may also contribute to increased thermal radiation emission [49] which may decrease the time to flashover in an enclosure, effectively increasing the risk to people and property in the enclosure. Fiberglass reinforced polyester is manufactured in several possible configurations with various geometries and compositions of reinforcement material and matrix phase material. A picture of a typical sample of fiberglass reinforced polyester that was characterized in this work is provided in Figure 3.3.

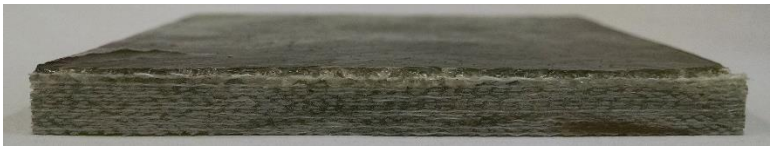

Figure 3.3: Picture of Typical Tested Fiberglass Composite

The majority of previous work to characterize reinforced polymer composites was performed on pure materials or composites of a single composition without addressing changes in the burning behavior with changes in the composition [50–52]. One study in which a constituent-based model was developed indicated that the determined material properties were not able to accurately describe the *MLR* measured in the pyrolysis of composites with a higher glass content [51], although the samples in that study were structurally more complicated than the current study. Zinchenko et al. conducted a study

with the main goal of predicting the thermal degradation rate of a carbon fiber reinforced polymer composite that is commonly used as a thermoprotective coating [53]. The authors adopted a methodology that relied on knowledge of the kinetic parameters and the mass fraction of each of the constituents in the composite. The ratio between the mass fraction of phenolformaldehyde resin and carbon fiber cloth was varied in the analysis and it was found that good agreement between the experimental thermogravimetric data and the model prediction was achieved when the specific properties of each material was well characterized. This study demonstrated the possibility of intelligently designing composites with well-known material and flammability properties by understanding the properties of each of the contributing components.

Many of the sectors that currently use fiber-reinforced polymers in structural applications require performance-based design to meet flammability metrics stipulated by safety standards. These composites may be designed with a specified ratio between the masses of reinforcement and polymer based on the desired mechanical and thermal performance. Because of the variety of uses for fiberglass reinforced polymers and the requirement of performance-based design, it was important to this work that the methodology provide the ability to predict the performance of composites as a function of their composition. A challenge that required modification of the generalized methodology was determining the thermo-physical properties of each individual component in such a way to facilitate prediction of the behavior of the composites.

Section 3.2.4: Carbon Fiber Structural Composite

The design of the structure and components as well as the manufacturability of carbon fiber laminate composites have experienced significant improvement in the last few

decades, and these improvements have led to increasing prevalence of these composites in a variety of common applications. The aerospace industry has experienced the most widespread adoption of carbon fiber laminates because of the favorable strength-to-weight ratio of carbon fiber compared to aluminum alloys that have been traditionally used in structural elements in aircraft. Carbon fiber structural composites have been used in aircraft since the mid-twentieth century and the uses for these composites in aircraft have increased since. The most recent commercial airplane models developed by Boeing and Airbus, the 787 and A380, respectively, have structures that comprise more than 50% of their mass from carbon fiber [54] and, more notably, the fuselage of the Boeing 787 is completely composed of carbon fiber laminates [55].

As the use of carbon fiber in airplanes has increased, manufacturing costs have decreased, which has allowed these structural composites to be used in a wide and varied range of applications. The structural advantages of carbon fiber composites over metal alloys that derive from their mechanical strength yield numerous advantages including increased fuel efficiency, improved fatigue and corrosion resistance, and the reduction of weight-based maintenance and fees [56]. These composites can currently be found in ground transportation vehicles, in building construction, and in a wide range of consumer goods.

Though there are numerous advantages to the use of composites over traditional aerospace materials, there are also unavoidable disadvantages that have slowed the replacement of traditional material components by advanced composites. The polymeric matrix materials that are currently used in laminate composites undergo thermal degradation at elevated temperatures. The fibrous reinforcement materials that compose

the laminae that may be made of aramid, carbon, or similar materials can also undergo thermal degradation and contribute to the heat released due to the combustion processes that occur in a fire event. In addition to the potential degradation of mechanical strength due to thermal degradation, the gaseous products of degradation may also create a toxic atmosphere that has historically led to more deaths than fires that start in airplane cabins [57]. As airplane manufacturers seek to benefit from the advantages of carbon fiber laminate composites, fire and associated hazards that contribute to loss of life must also be considered.

Carbon fiber laminate composites can be designed to withstand directional loadings more efficiently than metals. A disadvantage of composites over traditional building materials is the inherent flammability of the polymer matrix used in carbon fiber composites, the most common of which generally volatilize in the temperature range of approximately 580-680 K. An additional advantage of carbon fiber composites over metals in aerospace applications is that composites will maintain structural strength during decomposition of the matrix polymer and higher temperatures whereas metals exhibit degraded mechanical properties with increasing temperatures and will sustain damage beyond repair at a well-defined temperature.

A carbon fiber structural composite that was produced by Toray Composites and designated according to Boeing Material Specification 8-276 (BMS-8-276) was characterized as part of this investigation. A picture of the sample is provided as Figure 3.4. The layers of the composite could not be separated, so the composite was modeled as a homogeneous material. Although this simplified experiments and analysis, it was determined that the degradation process alternated between exothermic and endothermic,

resistance to mass transport was hypothesized to effect experimental results, the effect of oxidation on the unreacted and residual components was investigated, and the effect of orthotropic thermo-physical properties on the pyrolysis process was also investigated.

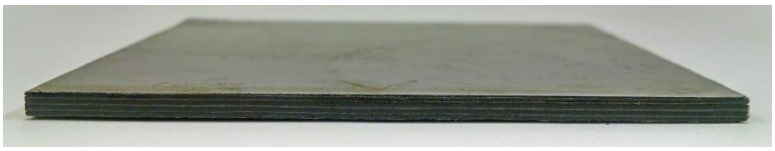

Figure 3.4: Picture of Tested Carbon Fiber Composite Sample

Research to characterize carbon fiber composites in fire-like conditions was conducted by researchers at Sandia National Laboratories [54] that consisted entirely of experimental testing. The investigation involved several configurations of composites and concluded that there was no evidence of oxidation in any of the tests that were conducted and that there were possibly edge effects in the experiments due to the relatively small sample dimensions. Quintiere et al. conducted an extensive investigation to determine the thermo-physical properties and fire response of the same carbon fiber composite that is the subject of this work [58].

The thermal conductivity of the composite was measured with a homemade apparatus although the authors recommended that the thermal conductivity of the composite be measured with a more accurate method. The properties that were measured and the observations made during burning experiments provide a data set for comparison with the current study. A thermal model was developed based on the data collected and subsequent analysis performed by Quintiere et al. that accounted for pyrolysis reactions, heat and mass transfer, and material swelling [59]. It was concluded after formation of the model that the treatment of swelling is important to the model, the treatment of the mass transport condition at the back boundary of the sample is important, and the definition of

the permeability of the sample appears to significantly affect the quantitative agreement between the experimental and modeled *HRR* curves.

Regulations set by the Federal Aviation Administration (FAA) that dictate the flammability requirements for cabin materials focus primarily on post-crash fire scenarios, where loss of life most commonly occurs. These regulations, which are specified in FAR 25.853, require materials to pass several standard fire tests including maximum flame spread after application of a flame to samples in a vertical orientation (FTMS 191, Method 5903), horizontal orientation (FTMS 191, Method 5903), and at a 45° angle from the horizontal, and additionally not exceed a critical heat release rate in tests conducted in the OSU Apparatus [60]. The regulations are intended to increase the amount of time to flashover in the airplane cabin to effectively provide more time for evacuation in a post-crash fire scenario. A specific concern with post-crash fires is smoldering of carbon fiber structural composites because this form of burning tends to produce more smoke, carbon monoxide, and unburned pyrolysis products, and smoke inhalation and carbon monoxide poisoning cause the largest percentage of deaths in fires [49].

These tests are capable of providing pass/fail determinations, though it has been noted that they do not provide enough information to make a full characterization of the fire hazard of a material [58]. It has been estimated that cabin materials for airplanes cost approximately $300 per pound and production requires large initial investment by the manufacturers [57]. Due to these relatively high costs for airplane cabin materials, it is advantageous for manufacturers in the aerospace industry to completely understand the fire response of materials that may be used to build airplanes before investing into large-scale production and full-scale fire testing. Fully parameterized pyrolysis models for the carbon

fiber composite can improve the understanding of fire dynamics and material degradation when carbon fiber laminates are involved.

Chapter 4: Experimental Methods

Section 4.1: Properties Required for Pyrolysis Models

This work is focused on developing a generalized methodology to determine thermo-physical properties and model parameters for composite materials that are otherwise difficult to determine. The methods used in this study have been designed to directly and indirectly measure the required properties while conducting as few physical tests as possible. An efficient methodology to completely characterize composite materials for pyrolysis models represents a marked improvement on state of the art parameterization methods that rely on techniques to measure single properties, use literature values, or multi-variable curve fitting algorithms.

Techniques to individually measure single properties are inefficient and may require a multitude of costly tests. Property values that are taken from literature will likely not correspond to the exact material of interest and can lead to inaccurate predictions if the differences between the material tested in the literature and the material of interest are not understood. Multi-variable curve fitting algorithms can be used to determine effective property values to accurately predict pyrolysis behavior [61], although there is uncertainty about the applicability of these properties outside the range of calibration conditions. Ultimately, there is a better probability that the predictions made with the model constructed with measured properties may be extrapolated to different orientations, scales, and a wider range of ambient conditions.

The need for more accurately estimated material properties drives a need for better measurement techniques and a better understanding of how each material property and each constituent material in a composite affect the model predictions [7,35,47]. Several sensitivity analyses have been conducted to identify the parameters that must be accurately

characterized and the parameters in which uncertainty causes little change in the model prediction. The procedures and major conclusions from these sensitivity analyses are provided in Sec. 4.1.2.

Section 4.1.1: Sensitivity Analyses

A pyrolysis model is generally evaluated on its ability to produce predictions that agree well with mass loss rate (*MLR*) and surface temperature data or in-depth temperature profiles measured in physical tests. Accepted practice suggests that a sensitivity analysis or parametric investigation be conducted when solving a multivariable problem in an attempt to quantify the uncertainty in the solution. Pyrolysis simulations are multivariable problems that require sensitivity analyses to properly define the total uncertainty in the final predictions. It is imperative to understand the effect each input parameter has on the model response when using the method of manually iterative optimization utilized in this study.

Stoliarov et al. conducted an analysis to determine the effect of variation of several thermo-physical properties on predictions of fire response parameters for a typical generic non-charring engineered polymer using the ThermaKin modeling environment [62]. Due to the lack of a comprehensive understanding of the charring process, the only parameter related to charring that was investigated was the typical char yield. A survey of literature data was used to define a mean value as well as an upper and lower bound on the range for each parameter that encompassed all of the property values in the literature. The authors determined that the prediction of the time to mass loss is sensitive to all thermo-physical properties and kinetic parameters with the exception of the heat of decomposition and the char yield, and was most sensitive to the reaction kinetics.

The time to the peak *MLR* and the overall shape of the *MLR* curve was also found to be sensitive to all the input parameters. The magnitude of the peak *MLR* as well as the average *MLR* were most sensitive to the parameters that define the reaction mechanism, including the heat of decomposition, the reaction kinetics, and the char yield. The average *MLR* was also sensitive to the absorption coefficient. This analysis concluded that all the defining features for the *MLR* curve are most sensitive to the parameters that define the reaction mechanism, slightly sensitive to the optical properties of the material, and largely insensitive to the remaining thermo-physical properties. It was also noted that the charring process can generally decrease the peak and average *MLR* by as much as 80% and that the properties of the char influence the effect of the properties of the char on the *MLR* predictions. These observations are consistent with the claim that any changes in polymer chemistry and the accompanying effect on the material properties profoundly affect the time to ignition and the shape of the *MLR* curve.

Linteris investigated the effect of variations in model inputs on the time history of the *MLR* and time to ignition for the thermal decomposition of PMMA predicted by both ThermaKin and FDS [63]. The heat capacity of the material was found to have a strong positive correlation with the time to ignition at high heat fluxes and to a larger extent at low heat fluxes. Thermal conductivity was also found to have a positive correlation with the time to ignition at all heat fluxes. The heat of reaction had the most significant effect on the time history of the *MLR* with a decrease in the heat of reaction resulting in an overall increase in the *MLR*. Adjusting the thermal conductivity of the material resulted in changes in the shape of the *MLR* curve, but did not significantly affect the average *MLR* or the peak *MLR*. Absorption coefficient was found to affect the shape of the *MLR* curve, and the peak

and average values of the *MLR* decreased with increasing values of absorption coefficient. The heat capacity had little effect on the *MLR* curve at low heat fluxes and only affected the shape, shifting the peak later in time, while at high heat fluxes, increasing the heat capacity resulted in lower average and peak *MLR*. It must also be noted that the material in this investigation, PMMA, does not produce char, and though the conclusions on the sensitivity of each input parameter may likely be applied to any material simulated with these models, the conclusions do not definitely apply to all materials.

Linteris et al. conducted a brief sensitivity analysis as part of a modeling effort for the gasification of four polymers [64]. The magnitude of the perturbations for each parameter was chosen to reflect the uncertainty in determining the parameter. The parameters that impacted the predictions, in order of sensitivity, were the activation energy, pre-exponential factor, heat capacity, and absorption coefficient. The thermal conductivity was found to have very little effect on the *MLR* profiles for all of the polymers and the heat of decomposition had the most significant effect on the *MLR* curve. The brief sensitivity analysis concluded that uncertainties in the measured parameters created variations in the predicted *MLR* curves that were greater in magnitude than the error between the predicted curves and the experimental curves. Since the variations in the parameters were on the order of the uncertainty in determining each parameter, this conclusion implies that an emphasis must be placed on reducing the uncertainty in parameter estimation and measurement.

Bal et al. conducted a study to assess the complexity required in pyrolysis models [65]. This study was motivated by the trend that models require the definition of more parameters as the complexity of the models increases, which requires a more extensive

experimental effort and increases the computational cost of modeling. The authors defined the optimal complexity of the model as the number of input parameters that yields equivalent prediction errors due measuring thermo-physical parameters and to neglecting physical phenomena (e.g. reducing the number of independent input parameters). Three models for the pyrolysis of PMMA were assessed to illustrate the breadth of variations available to predict the pyrolysis of a single material and each used a different set of governing equations in the pyrolysis model and different methods to determine the parameters to define the sample in the models.

The assumptions that the heat of decomposition was negligible, the thermo-physical properties had no temperature dependence, and there was no in-depth radiation absorption resulted in large errors for the surface temperature prediction. Some of the major conclusions included a relatively small error in the surface temperature prediction can be achieved with a large reduction in the number of parameters used to define the heat transfer physics and all complexity associated with mass transport within the solid appeared to be negligible. It was demonstrated through this study that the chemical mechanism had a significant impact on the *MLR*, single-step reaction kinetics led to a large increase in the *MLR* error, and that a good prediction of the energy distribution throughout the solid and any heat losses must be well quantified to produce accurate *MLR* predictions. Though several of these conclusions may be applied generally to pyrolysis models, it must be noted that this study was focused on models for PMMA, which undergoes pyrolysis with the least complicating factors, and it is no surprise that much of the complexity in these models was found to be extraneous.

Chaos conducted a sensitivity analysis on a simplified version of GPyro claiming that previous sensitivity analyses examined specific materials or situations and lacked generality [66]. Chaos investigated the model response based on both a non-charring and a charring virtual material with properties representative of common thermoplastics. For the charring material, the *MLR* was most affected by the virgin and char emissivities and the reaction parameters at low heat flux. At high heat flux, the same trends were observed up to the first *MLR* peak and thereafter the char and virgin thermal conductivities dictated the *MLR* due to the insulating layer at the top surface. The surface temperature rise was affected by the thermal conductivity, density, and heat capacity of the virgin material and the emissivities of the virgin and char components. For high and low heat flux conditions, the ignition time was most sensitive to virgin emissivity, reaction parameters, virgin heat capacity, and virgin density. The peak and average *MLR* were most sensitive to the virgin and char emissivities and the virgin density.

Kim et al. examined the effect of the complexity of the reaction mechanism chosen to describe the resins in two different fiberglass-reinforced polymer composites on the *MLR* curve and temperature profiles predicted by GPyro [67]. Six different kinetic schemes with a range of complexity were investigated and it was concluded that, with the exception of a single zeroth order reaction scheme, the kinetic mechanism defined in the model produced minimal changes in the *MLR* in 1D bench-scale simulations. It was concluded that the samples with a high glass content did not require a geometric description with alternating layers of glass and resin in the 1D model, and doing so added unnecessary complexity to the model.

All the analyses were in agreement that the reaction kinetics and the heat absorbed during the pyrolysis process had the most significant effect on the *MLR* curve. The absorptivity and absorption coefficient also tended to have a marked effect on the *MLR* curve as well as the sample temperature distribution. The time to the onset of mass loss was affected most significantly by the reaction kinetics and the heat capacity of the material. The thermo-physical properties of the virgin material appeared to affect the initial rise of the temperatures throughout the sample, but did not significantly affect the overall *MLR* curve. Chaos et al. found that for charring materials, the emissivity and thermal conductivity of the char tended to have a profound effect on the *MLR* after the onset of mass loss.

Bal et al. emphasized the importance of temperature-dependent thermo-physical properties but Linteris concluded that constant values of heat capacity and thermal conductivity, evaluated at the average temperature between ambient and decomposition, and temperature-dependent values of the same properties yielded similar results in bench-scale thermal degradation simulations. Stoliarov et al. made a similar conclusion, stating that density, heat capacity, and thermal conductivity are of little importance when predicting the peak and average *MLR* and the mean value of these parameters from a literature review may be used in lieu of direct measurement.

The range of methods used to conduct these sensitivity analyses and the conflicting conclusions drawn from each demonstrates the complexity and nonlinearity of the mathematics of pyrolysis. It is clear from the review of the analyses in this section that the sensitivity of the pyrolysis process to each thermo-physical property and kinetic parameter is dependent on the test conditions, the sample material, and the structure of the sample.

Because of this and because few of the materials investigated in these sensitivity analyses were charring or had complicated composite geometries like the materials defined in the scope of this work, few of the conclusions specific to non-charring polymers can be applied to the current study, although several of the general conclusion regarding the time to mass loss and the thermo-physical properties of the unreacted components may be applicable.

Section 4.2: Experimental Methodology and Philosophy

The methodology developed through this work is presented in this section. The general philosophy that led to the specific steps in the methodology is explained, followed by several subsections that are divided into the properties and parameters that must be characterized through the methodology. Alternative experimental methods and analyses that are available and have previously been used to determine each specific parameter are presented, followed by experimental procedures and analyses that were conducted to characterize materials in this work. The methodology presented here is intended to provide general direction for engineers, scientists, and fire model practitioners to determine thermo-physical properties that are required for the study and modeling of pyrolysis. Applications of the methodology to characterize several composites that are common to the built environment is demonstrated in chapters 5 through 8.

In light of several of the studies described in Sec. 4.1.1. that were conducted to assess the required complexity for accurate pyrolysis model predictions, this methodology is built on the philosophy that additional complexity is only included in the model when it has been demonstrated that the additional complexity will significantly improve the accuracy of model predictions. A common complaint about fully characterizing materials for pyrolysis models, particularly complicated composites, is the extensive experimental

effort and breadth of measurement techniques required. The philosophy adopted in the current investigation is to measure and infer as many properties as possible while making as few assumptions that will introduce error into the predictions as possible. An additional attribute that was considered essential was the ability to determine several parameters from each experimental method or apparatus, effectively reducing the number of experiments that must be conducted.

Pyrolysis models are commonly used as a tool to analyze data collected in thermal analysis and bench-scale test methods in inverse analyses. By defining the experimental conditions of the specific test method as the boundary conditions in the model, specific parameters of interest may be determined by mathematically replicating target experimental data. This method of inverse analysis is most effective when the replicated experiment has been designed to isolate an individual parameter or set of parameters. The experiments conducted to demonstrate this methodology and to test its scope and robustness were designed to isolate the condensed phase processes from the gas phase processes, but also to isolate individual thermo-physical properties or parameters associated with thermal degradation reactions.

Inverse analyses conducted as part of this methodology are comprised of three general steps that may be repeated as many times as necessary. The first step involves determining an appropriate functional form to model the parameter of interest. Taking into account the overall philosophy adopted for this methodology, the simplest functional form is initially chosen. The second step involves simulating the experiment using the model parameterized with an initial guess of the desired parameter. The third step is to adjust any coefficients in the model by iteratively assessing the agreement between the model

prediction and the target experimental data and modifying the coefficients. If an inadequate agreement, defined according to predefined acceptance criteria, is achieved between the model prediction and the target data regardless of the coefficients chosen, the functional form of the model for the parameter is made slightly more complicated and the process is repeated.

When applying this methodology to a composite, the first task is to collect as much existing information about the material and similar materials as possible. Of particular importance in this preliminary phase is whether research has been published on the material, if the distinct components have been identified and further researched, and whether the material melts, chars, or undergoes other morphological changes during pyrolysis. The information accrued in this preliminary research may potentially inform the design of several of the experiments conducted later in the characterization methodology and will inform the analyses of data collected in experiments.

After conducting preliminary research, the geometry of the material must be assessed by identifying the number of distinct layers present and determining whether these distinct layers may be separated from the composite structure or individually procured to be studied independently. If it is determined that there are distinct layers that may be separated from the composite, these layers are separated and the remainder of experiments are conducted on each distinct layer. Inverse analyses are used extensively in this work, so the dimensions and mass of the entire composite as well as any separated layers must be measured prior to testing to identify the density and thickness of the representation in the pyrolysis model.

The experimental effort presented here is divided between milligram-scale samples to determine the effective reaction kinetics and thermodynamics (Sections 4.2.1-3) and bench-scale samples to determine the thermal transport properties (Sections 4.2.4-5) just as the pyrolysis model is divided between a zero-dimensional (thermally-thin) sub-model and a one-dimensional (thermal transport) sub-model. The presentation in the following section of the methodology used to characterize these materials is done in a chronological order because the successive experiments and analysis require the foundation provided by the parameters determined in preceding measurements and analyses.

Section 4.2.1: Thermal Degradation Kinetics

The treatment of the kinetic parameters has been shown to be important in the construction of pyrolysis models in several of the sensitivity analyses of Sec. 4.1.1 as well as other investigations [68]. Thermogravimetric Analysis (TGA) [69,70] is the most commonly used standard testing method for collecting data from which the reaction kinetics may be determined. In TGA, the mass of a sample is measured as the environmental temperature follows a user-specified temperature program in a well-defined gas atmosphere. TGA tests are completed with various heating programs, generally in an inert atmosphere to gather data on the total sample mass as a function of temperature. These data may be replicated with mathematical formulae that relate the rate at which the sample mass volatilizes at the elevated temperatures to the temperature and composition of the sample.

The sample mass for TGA experiments must be small (3-10 mg) to reduce temperature and concentration gradients to effectively eliminate heat and mass transfer within the sample. The gas atmosphere is well-defined and continuously purged with high

precision mass flow controllers to remove any gaseous byproducts formed in heterogeneous reactions, reduce the possibility of secondary reactions, and to continuously cool the apparatus. The total gas flow rate is typically on the order of 100 mL min^{-1}, and may be reactive or non-reactive according to the desired test conditions. The temperature in the vicinity of the sample is controlled by a furnace that is capable of isothermal operation and dynamic heating and/or cooling and can operate at heating rates ranging from 0 K min^{-1} to as high as 500 K min^{-1}. In material flammability research, the temperature program generally includes a constant heating rate in the range of 3 to 30 K min^{-1}. The sample is contained in a crucible that may have a lid to improve the uniformity of the temperature in the crucible or may not have a lid to improve interaction between the sample and the atmosphere and to facilitate the exhaust of gaseous byproducts of the reactions.

Individual mass loss events are considered reactions and the rates of reactions are commonly described using the Arrhenius equation, which was presented as Equation 2.2. TGA test data are analyzed to determine the reaction parameters, A and E, that describe the condensed phase reactions that take place over the range of temperatures investigated as well as the kinetic scheme that consists of the stoichiometric coefficients for the pyrolyzate gas and solid pyrolysis products generated through each reaction. In homogeneous kinetics terms, the activation energy represents the minimum energy threshold beyond which chemical bond redistribution can take place and the pre-exponential factor represents the maximum frequency at which a reaction will take place, which is related to the vibration frequencies of a molecule. There are a multitude of methods for determining reaction parameters from thermogravimetric data, and there is no single, universally accepted

standard method in the fire protection community, which can lead to a disparity between kinetic parameters determined by different investigators.

There is a debate about the use of TGA based on the lack of standard calibration, testing, and analysis procedures. Calibration generally consists of comparing the measured temperature of the sample to a well-defined temperature (generally a melting point or Curie point), but the calibration curve is highly sensitive to the heating rate. There is no standard heating rate at which data is collected, and often data is collected at several heating rates. A related debate exists about whether application of the Arrhenius equation to heterogeneous reactions may be justified. Several fire researchers and practitioners of pyrolysis models claim that the Arrhenius reaction parameters are fitting parameters and that the physics of heterogeneous reactions are of no consequence when defining the kinetic mechanism for a material [71].

Data collected with microscale combustion calorimetery (MCC) (See Section 4.2.3) [72] and data collected with differential scanning calorimetry (DSC) (See Section 4.2.2) [73] have been analyzed to extract kinetic reaction parameters as an alternative to TGA data. These methods are limited to specific materials that display *HRR* and heat flow rate curve maximums that correspond to the maximum *MLR*. These limitations make it unlikely that the thermal degradation of composite materials would be adequately described through these methods and further discussion of them is not warranted.

Though there is a strong contingent of researchers that use Arrhenius kinetics to describe the thermal degradation process of solid phase materials, modeling efforts have illuminated a deficiency in the understanding of solid phase reactions. It has been observed that the kinetics that describe solid phase processes are highly dependent on the

experimental conditions, which leads some researchers to believe kinetic parameters cannot be characterized as distinct properties of the material [74]. There is also evidence of a kinetic compensation effect, whereby several different sets of Arrhenius parameters describe a curve that accurately depicts experimental thermogravimetric data [75,76]. Despite the physical interpretation of the reaction rates, the applicability of the Arrhenius equation, and the myriad techniques used to determine kinetic parameters, previous investigations have demonstrated semi-global reaction kinetics may be adequately represented with the Arrhenius equation.

The analysis methodologies to determine reaction kinetics are so numerous and varied that it is impossible to concisely summarize all of them, although some of the most common techniques are briefly explained here. Generally, analysis of thermogravimetric data requires the transformation of the mass data collected as a function of temperature to a non-dimensional variable that represents the fractional reaction or conversion, α, defined in Eq. 4.1, where the subscript 0 denotes the initial mass, f denotes the final (residual) mass, and no subscript indicates the instantaneous mass.

$$\alpha = (m_0 - m)/(m_0 - m_f) \tag{4.1}$$

The Arrhenius equation and it relationship to the rate of mass loss of the sample is modified from the form presented as Equation 2.2 to Equation 4.2. The form of Equation 2.2 is specific to first- and second-order reactions and the generic form of equation 4.2 may take on several different theoretical models, denoted $g(\alpha)$, that relate the instantaneous mass (or conversion) to the rate of change of the mass (or conversion). Each theoretical model has a foundation in physical phenomena including nucleation and growth, diffusion processes, reaction order, and geometric considerations for the progress of the reaction

front. The functional form of the theoretical model is generally an unknown parameter that must be determined in addition to the pre-exponential factor and activation energy when analyzing thermogravimetric data [71].

$$\frac{d\alpha}{dt} = A \exp\left(\frac{E}{RT}\right) g(\alpha) \tag{4.2}$$

When data is collected at a single heating rate, the functional form of the reaction model must be assumed so that the other two unknowns may be determined. Analysis of TGA data with the differential form of the rate expression requires the transformation from a time derivative to a temperature derivative provided generically in Eq. 4.3, and manipulation to Eq. 4.4 to achieve a functional form that easily allows determination of *A* and *E* by graphical means. In these equations, φ is the heating rate, α is the conversion, t is time, T is temperature, and R is the universal gas constant. Several simplifications and modifications to the relationship provided as Eq. 4.4 that are applicable to specific scenarios have been made by many researchers [77]

$$\frac{d\alpha}{dT} = \left(\frac{d\alpha}{dt}\right)\left(\frac{dt}{dT}\right) = \left(\frac{d\alpha}{dt}\right)\left(\frac{1}{\varphi}\right) = \left(\frac{A}{\varphi}\right) e^{-E/RT} g(\alpha) \tag{4.3}$$

$$\ln\left[\left(\frac{d\alpha}{dT}\right)/g(\alpha)\right] = \ln\left(\frac{A}{\varphi}\right) - \left(\frac{E}{R}\right)\left(\frac{1}{T}\right) \tag{4.4}$$

Related analyses rely on data collected at multiple heating rates and form the set of isoconversional methods. These methods are based on the relationship between the activation energy and temperature at constant values of conversion collected at several different heating rates. A multitude of isoconversional methods have been used to determine the kinetic scheme and reaction parameters [78]. One such method was proposed by Friedman [79] that uses a slightly manipulated form of Eq. 4.4, in which the activation

energy is determined as the slope of a graph of 1/T vs. $\ln\left(\frac{d\alpha}{dT}\right)$. The theoretical model is assumed to take the form of an nth-order reaction shown in Eq. 4.5, which may be manipulated to Eq. 4.6 and plotted for the pre-exponential factor and order of the reaction, *n*, to be determined.

$$f\left(\frac{m}{m_0}\right) = \left[\left(\frac{m - m_f}{m_0}\right)\right]^n \tag{4.5}$$

$$\ln\left[Af\left(\frac{m}{m_0}\right)\right] = \ln A + n\ln\left[\left(\frac{m - m_f}{m_0}\right)\right] \tag{4.6}$$

Another common isoconversional method is the Ozawa/Flynn/Wall method [70], which requires the assumption that decomposition can be described with first-order reactions and requires at least four tests conducted on samples at heating rates ranging from 1 to 10 K min^{-1}. This method uses the general form of the Arrhenius rate equation given as Equation 4.3, with the theoretical model defined for first-order reactions, $g(\alpha) = (1 - \alpha)$. The equation is manipulated to an expression for the activation energy as a function of $\frac{\Delta \log \varphi}{\Delta(1-T)}$, which can easily be evaluated as the slope of data points of constant conversion on a semi-log plot of heating rate against $(1 - T)$. Determination of the activation energy and pre-exponential factor requires an iterative process that makes use of tabulated values of integration parameters provided in the standard [80,81].

Investigators have employed optimization software or graphical methods to determine the kinetic parameters that provide the best fit for experimental TGA and bench-scale *MLR* data [40,41,82]. In the studies that used optimization techniques, the reaction scheme was generally formulated based on schemes available in the literature or on qualitative analysis of the data. The most common optimization algorithms for highly dimensional problems like extracting the parameters of the reaction mechanism from a set

of thermogravimetric data are evolutionary algorithms that are based on natural selection. These algorithms begin with a diverse group of parameter sets (called individuals) and the sets that produce the best fitness to the experimental curve survive and pass on property values that produce the most accurate prediction to the next population of parameter sets. Over many iterations, all of the property values in the set take on their optimal values.

Evolutionary algorithms, including genetic algorithms and the stochastic hill climber algorithm, have been used extensively to determine thermo-physical properties and reaction parameters for materials. Generally, an evolutionary algorithm begins with the determination of an initial set of property value and an assessment of the fitness of curve(s) predicted by the property value set. A second set of property values is created by random mutation of the first set of property values. The magnitude of the mutations are decreased with each iteration of the algorithm until the fitness of the predicted curve cannot be improved any further. A genetic algorithm will have a large population of individual property value sets and the mutated sets are created by combining values of properties from two different individual well-performing sets [21]. With a genetic algorithm, the mutated property sets always replace the parent property sets that were combined to produce them. A unique feature of the stochastic hill-climber algorithm is that there are only a parent and offspring individual in the population at one time and the parent property set passes on to the next iteration if the mutated offspring property set does not provide a better fit to the target data [6].

Optimization codes can be useful for determining the kinetic parameters of a chemical reaction but a physical understanding of the effect of varying the kinetic parameters remains the most important requirement for fitting data. A variety of

optimization algorithms have been used with varying degrees of success, though in one study several of the optimized parameters were outside the range of physical possibility [40]. And it was also shown that the properties determined through an evolutionary optimization algorithm predicted cone calorimeter data well from a single heat flux but did not extrapolate predictions well to other heat fluxes [6]. Bruns proposed a methodology to determine the kinetic parameters for pyrolysis reactions using Bayesian inference to compute probability density functions (PDFs) from Markov Chain Monte Carlo Simulations intended to fit experimental TGA data [29]. By determining PDFs for the kinetic parameters of pyrolysis reactions, the uncertainty in each parameter may be inferred, which facilitates the determination of uncertainty in bench-scale simulations in which all important physics are represented. It was found that the kinetic parameters determined through this method did not always extrapolate well to other heating rates, and this was attributed to overly complicated reaction models. It was found that some of the parameters that fit experimental TGA data tended to provide qualitatively poor predictions for the experimental *HRR* curves.

Each of the methods outlined in this section had unavoidable drawbacks, required complicated optimization algorithms, or required a battery of tests at a range of heating rates. Although isoconversional methods require analysis of data collected at several heating rates, there has been little discussion about the ability of isoconversional methods to accurately predict data measured at a range of heating rates without modification to the kinetic parameters determined through analysis. Additionally, there have been several researchers that have noted the high computational expense of optimization algorithms for fitting thermogravimetric data [83] that have also demonstrated a deficiency in the ability

of the algorithms to predict data outside the calibration conditions and at larger scales. Optimization algorithms take most of the engineering judgement out of the determination of kinetic parameters, which eliminates the opportunity to make common sense modifications to the fit. The method utilized in this work is advantageous because it requires relatively few tests conducted at a single heating rate and analysis of the data only requires a computational pyrolysis modeling tool.

Section 4.2.1.1: Experimental Procedure and Analysis

Simultaneous Thermal Analysis (STA) is a generic term for a class of thermal analysis methods that are simultaneously conducted in the same apparatus. In this methodology, TGA and DSC tests are conducted together to reduce the number of tests that must be conducted to accurately characterize a material. These tests were conducted in the Netzsch 449 F3 Jupiter STA. There were some minor deviations from the standard STA procedure outlined here, and those differences are indicated in the following chapters. Simultaneous measurement of mass and heat flow rate is advantageous over individual measurement because the energetic and gravimetric responses of a material to a given thermal event are correlated, whereas individual measurements would inevitably be affected by a temperature offset [71].

STA tests were conducted on each of the distinct materials extracted from the composite. The sample material was ground to a powder or cut to be sufficiently small such that the total mass of the sample ranged from 3 to 10 mg. It was preferable to keep the structure of the sample intact when preparing samples, and powders were only prepared when necessary. The sample was compacted into a platinum crucible so that the sample was flat against the bottom of the crucible. Thermal contact between the sample and the

crucible proved to be an important variable and it was determined that reliably repeatable data was only obtained when the sample was positioned in the crucible in a consistent manner. All STA tests were conducted with the crucible lid covering the sample to ensure a uniform temperature in the crucible. There was an opening in the center of the crucible lid to allow pyrolyzate gases to escape the crucible.

The temperature program was designed with an initial conditioning period when the temperature of the sample was held constant at 313 K for a minimum of 20 minutes to ensure the sample was purged of oxygen and residual moisture before dynamic data was collected. The conditioning period was followed by linear heating at a rate of 10 K min^{-1} to approximately 100 K above the highest temperature at which mass loss was observed (usually about 900 K). The test chamber was constantly purged with nitrogen flowing at a rate of 50 mL min^{-1} (70 mL min^{-1} for materials that released high molecular weight pyrolyzate products) which was within the range recommended by the manufacturer. Conducting STA tests in a nitrogen atmosphere allowed the pyrolysis processes to be decoupled from possible oxidation and other heterogeneous reactions as well as heat and mass transport within the sample. A temperature calibration was routinely conducted to ensure the accuracy of the temperature measurement. The calibration consisted of several tests on metals or anhydrous salts in which the samples were heated above their melting point and the measured onset of melting was compared to well-defined literature values.

The heating rate of 10 K min^{-1} was chosen because it is the most prevalent heating rate used in the literature [24,25,40,41,84,85]. This heating rate is low enough that the sample does not experience significant temperature or mass gradients, making the effects of mass and heat transfer negligible and validating the assumption that the material may be

described as thermally thin. It has been noted [47] that a larger error is observed when using kinetics determined at high heating rates where the thermally thin assumption may be invalid than the error associated with extrapolating the kinetics determined at a low heating rate to a situation in which a wide range of heating rates are observed. A heating rate of 10 K min^{-1} is also high enough that portions of the sample could experience this heating rate in the bench-scale tests. Additional STA tests were conducted on each of the sample materials with a different heating rate to validate the reaction scheme and kinetic parameters determined from data collected with a heating rate of 10 K min^{-1}.

A thermally thin model was constructed using the ThermaKin modeling environment to conduct inverse analyses to determine the thermal degradation kinetic parameters. In this model, the convection coefficient at the sample boundaries was defined sufficiently high to force the boundaries of the sample to adhere to the ambient temperature. The mass flow boundary conditions were defined such that the gaseous pyrolyzate instantaneously escaped the sample. The sample thickness was defined small enough to guarantee uniformity of the sample temperature and component concentrations throughout the sample. Transient changes in the heating rate initially caused all modeled thermal analysis methods to deviate from the conditions realized in the measurements. A time-dependent function that is provided as Equation 4.7 approximated the temporal evolution of the measured heating rate was defined at the boundary to force the sample temperature to the approximate measured temperature.

$$\frac{dT}{dt}(t) = b_1\left(1 - (\exp(-b_2 t))(\cos b_3 t + b_4 \sin b_3 t)\right) \tag{4.7}$$

One of the assumptions that must be made when conducting an analysis on thermogravimetric data collected at a single heating rate is the functional form of the

theoretical reaction model. The analysis of the TGA data that is used in this methodology assumes a first or second order reaction model as shown in Eq. 2.2. First and second are the only reaction orders with physical justification for the solid phase. The number of apparent reactions is determined through a visual inspection of the TGA and DSC data to locate the maxima in the *MLR* curve in combination with background information gathered in preliminary research on the material. Generally the number of maxima in the TGA data curves provides an initial basis for the number of distinct thermal degradation reactions.

When analyzing each data set to determine the Arrhenius parameters, the reaction mechanism evolves from a single reaction, global scheme to a multi-step semi-global scheme. The single reaction scheme is initially used in an attempt to minimize the number of unknown parameters that require measurement or fitting. It is generally clear from analysis of the single-reaction scheme and comparison to the TGA data whether a more representative fit can be determined with the inclusion of more reactions.

The first reaction to be attempted for curve fitting corresponds to the *MLR* peak at the lowest temperature. A manually-iterated method was used to determine the reaction parameters that describe an adequate agreement to the experimental data that has been illustrated in Figure 4.1. The procedure for fitting the thermogravimetric data to determine the kinetic parameters A and E required estimation of the temperature at which the peak mass loss rate occurred, the peak mass loss rate, and the residual mass. An initial estimate of the activation energy was calculated from Eq. 4.8, which is an approximate solution to the first order Arrhenius equation for decomposition under linear heating conditions [86]. An approximation of the stoichiometric coefficient may be determined using the graph of

the normalized mass and assuming the half of the mass loss associated with the reaction occurs prior to the temperature at which the peak appears.

$$E = \frac{eRT_{peak}^2 \frac{MLR_{peak}}{m_0}}{(1-\nu)\frac{dT}{dt}} \tag{4.8}$$

The symbols in Eq. 4.8 are defined as follows: R is the universal gas constant, T_{peak} is the temperature at the peak of interest, MLR_{peak} is the magnitude of the *MLR* curve at the peak of interest, m_0 is the initial mass, and ν is the residual mass fraction for the specific reaction. The pre-exponential factor corresponding to the initial estimate of the activation energy was calculated using Eq. 4.9, where $m(T_{peak})$ denotes the mass measured at the temperature corresponding to MLR_{peak}.

$$A = \frac{MLR_{peak}}{\left(\frac{m(T_{peak}) - m_0\nu}{1-\nu}\right)} e^{\frac{E}{RT_{peak}}} \tag{4.9}$$

After the initial estimate, the agreement between specific traits of the predicted curve and the experimental curve are evaluated. These traits include the error in the peak magnitude of the *MLR* curve, error in the temperature of the peak of the *MLR* curve, and mean instantaneous relative error between the prediction and experimental curve of the normalized mass curve. The activation energy and pre-exponential factor are iteratively modified until acceptable agreement is achieved. Acceptable agreement was generally defined as a maximum error of 10% in the magnitude of the peak *MLR*, a maximum error in the temperature of the peak of 3 K, and a mean instantaneous error of less than 2% in the normalized mass curve. A brief sensitivity analysis was conducted to determine the

effect of these criteria on bench-scale model predictions and the results are presented in Section 4.3.

Though this process becomes quicker with experience, general guidelines exist to expedite the process. By increasing the pre-exponential factor, the magnitude of the peak of the curve tends to increase, the temperature at which the peak occurs decreases, and the temperature range of the curve decreases. Increasing the activation energy tends to shift the curve to higher temperatures and decreases the magnitude of the peak without a significant effect on the temperature range of the mass loss feature. The integral of the mass loss rate curve is associated with the total mass lost during the reaction, and can be influenced by adjusting the stoichiometry of the reaction. Upon determining the kinetic parameters that provide the most representative fit, it may be evident that additional reactions are required to accurately describe the thermal degradation of a material. An identical process is used for each individual reaction in a multi-reaction mechanism, although the reaction rate may be influenced by parallel or consecutive reactions that are added to the mechanism.

The reaction mechanism defines the initial, unreacted components present in the sample, the rates of transition of those components to solid products of thermal degradation, and the evolution of the mass of all components with respect to time and temperature. The solid products of degradation may be the final products, usually termed char, or may be intermediate products that eventually degrade to the final products. It is important to note that the reaction mechanism and the components included in the mechanism are not likely to represent actual reactions or individual chemical components. The mechanism is intended to mathematically mimic the mass and mass loss rate data in

the simplest form possible and relies on model-specific kinetics to reproduce the experimental curve. Understanding the composition changes of the solid sample throughout degradation as a function of temperature allows analysis and eventual prediction of the DSC data.

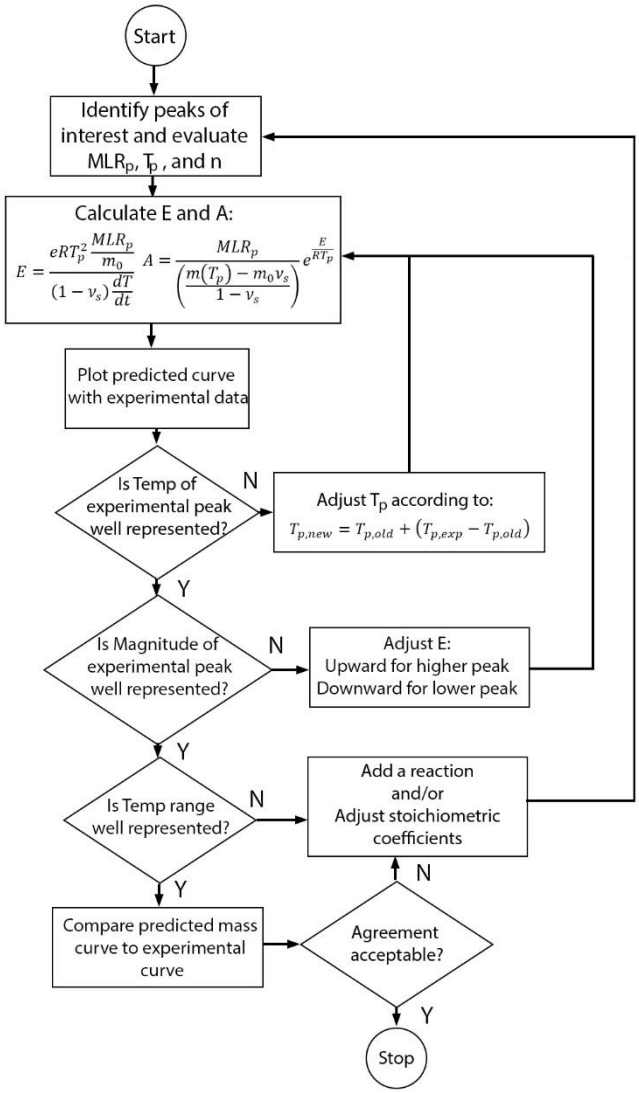

Figure 4.1: Flow Chart Depicting the Inverse Analysis Procedure for Determining the Kinetics of Thermal Degradation

The uncertainty in each kinetic parameter for the carbon fiber composite in Chapter 7 was determined by iteratively varying the parameter independent from the other

parameters while assessing the effect of the parameter on prediction of the *MLR* and the evolution of the mass. The activation energy and pre-exponential factor for each reaction were varied upward and downward by a percentage and the mean relative error between the *MLR* curve predicted by the model and the experimental curve was calculated. The percentage of the change in each kinetic parameter was iteratively decreased until the mean error between the prediction and the mean experimental data was equivalent to the scatter in the experimental data. This analysis yielded a calculated uncertainty in the pre-exponential factor of ± 20% and an uncertainty in the activation energy was calculated of ± 1% and these have been adopted as the uncertainties for all kinetic parameters determined through this method. It should be noted that each parameter was varied independently and this analysis did not consider the compensation effect or modification of multiple parameters simultaneously. It was hypothesized that large variations in the stoichiometric coefficients would yield similar simulation results provided the variations were balanced between positive and negative variations. It was estimated that the uncertainty in the stoichiometric coefficients was ± 5%. The uncertainty in the same parameters have been estimated previously as ± 50% for the pre-exponential factor and ± 3% for the activation energy.

Section 4.2.2: Heat Capacity and Thermal Degradation Energetics

The heat capacity of all sample material components through all states of degradation must be determined to fully characterize a composite. These have been particularly difficult to measure in the past due to the inability to isolate components that have been partially degraded and to quantify the degree to which such samples have been degraded. The heats of degradation reactions and phase transitions must also be determined

before the parameters associated with heat and mass transport can be included in the pyrolysis model. A common method that has been used to quantify the heat capacities and energetic flows associated with the pyrolysis process is Differential Scanning Calorimetry (DSC).

Differential Scanning Calorimetry [87] derives its name from measuring the differential between the heat flow rate to the sample and the reference crucible as the temperature of the atmosphere is scanned along a well-defined program. All DSC apparatuses consist of a twin measuring system in which environmental changes imposed on the system in terms of temperature and gas atmosphere will affect both the sample to be measured and the reference. The sample and reference are both contained in crucibles that generally have a lid to improve the uniformity of the temperature profile within the sample or reference. The sample mass must be small (3-10 mg) to reduce temperature and concentration gradients to effectively eliminate heat and mass transfer within the sample. The reference is most commonly an empty crucible although any well characterized material could be used.

There are two common types of DSC apparatuses, the major distinction arising from the method by which the heat flow rate difference between the sample and reference is measured. In heat flux DSCs, the primary measurement is the difference in temperature between the sample and the reference crucible. The temperature difference is related to the heat flow rate to the sample relative to the heat flow rate to the reference. Power-compensation DSCs consist of two identical furnaces in which the sample and the reference are positioned to maintain thermal isolation. The two furnaces provide an identical heat flow, but as the sample absorbs sensible enthalpy or enthalpy associated with a reaction or

phase change, the temperatures of the furnaces diverge, which provides a signal to the control mechanism to supply more power to the furnace containing the sample. This power signal provides a direct measurement of the heat flow rate to the sample [88]. It has been observed that the heats of reactions of a material are more accurately determined with a heat flux DSC in which both crucibles are fully immersed in the furnace than a power-compensation DSC [89]. The STA apparatus utilized in this methodology uses the principles of heat flux DSC to measure the heat flow rate.

Recently, fire scientists have used DSC as a standard method to determine the heat capacities of materials and the energetics of heterogeneous reactions at the range of temperatures comparable to those in fire environments [89–91], but there remains some skepticism surrounding the use of DSC in fire science. Some debate exists about the validity of DSC because of the lack of standard procedures for evaluating the temperature and sensitivity calibrations, as well as the limits of applicability of the measured data and the sources of uncertainty and systematic errors. There are also no accepted standard heating rates at which tests are conducted and the heating rates that are generally used do not necessarily correspond to fire conditions. These factors must be kept in mind by the researcher conducting tests and analyzing DSC data to ensure accurate parameter measurements. Since DSC provides a direct measurement of the heat flow rate to the sample as a function of temperature, interpretation of the data is dependent on knowledge of the sample material and the discretion of the practitioner.

Although DSC has become the most common method for determining heat capacity and heats of thermal degradation reactions, alternative methods have been used in past studies. A commonly used method before the widespread adoption of DSC was proposed

by Tewarson and Pion and involved the measurement of the heat of gasification from a series of bench-scale quasi-one-dimensional radiant heating tests [1,92]. This method is incapable of completely isolating heat and mass transfer processes from the absorption of energy due to sensible enthalpy and decomposition and is limited in applicability to only homogeneous materials. The heat capacity of a material may also be extracted from the Thermal Response Parameter (TRP) [14], a metric that relates the time to ignition to the thermo-physical properties, which is generally measured in one-dimensional radiant heating tests.

Each of these methods requires significant prior knowledge of thermo-physical properties or several additional tests to provide the heat capacity of the material or the heat absorbed during thermal degradation. To effectively determine the heat capacity from the TRP requires measurement or prior knowledge of the thermal conductivity, density, and the ignition temperature to account for thermal transport through the material, which would require an extensive experimental and analytical effort to determine a single parameter. Each is also limited in the geometry and composition of the materials that may be characterized, which effectively eliminates these options for composite materials. The limitations on these alternative methods and the ability to determine heat capacities and heats of reaction while simultaneously collecting data to determine the kinetic parameters of the reactions are major reasons DSC conducted with an STA was chosen for this methodology.

Section 4.2.2.1: Experimental Procedure and Analysis

The heat flow rate to each material from the composite that required characterization as a function of temperature was measured in STA tests. The sample

preparation, temperature program, and gas atmosphere for the STA tests were described in Sec. 4.2.1.1. All heat flow rate data that was used in analysis was collected in STA tests conducted at a heating rate of 10 K min^{-1}. A sensitivity calibration was periodically conducted to relate the heat flow rate to the sample to the temperature difference between the sample and reference crucible. This sensitivity calibration consisted of comparing the integral of the voltage difference between the sample and reference thermocouples to the well-defined heats of fusion of several anhydrous salts that melted over a wide temperature range.

The heat flow rate data collected in STA tests may be manipulated according to Eq. 4.10, which describes the rate of heat flow to a sample, $\dot{q}$ [W m^{-3}], in terms of the sensible enthalpy and heat flow due to reactions and physical transitions. The same symbols defined in Section 2.3 have been used here for clarity.

$$\dot{q} = \sum_{j=1}^{N_c} \left(\xi_j c_j \frac{\partial T}{\partial t} + \sum_{i=1}^{N_r} \nu_j^i r_i h_i \right) \tag{4.10}$$

It is clear from Eq. 4.10 that when there is no heat flow due to phase changes or degradation reactions occurring, the heat flow rate is dictated solely by the sensible enthalpy of the material and the rate at which the environmental temperature changes. Because of this, the heat capacity of the initial, unreacted material and the final, residual material may be extracted from the heat flow rate data at the temperature range before any reactions occur and after all reactions have completed. The apparent heat capacity was calculated by dividing the heat flow rate by the observed heating rate in temperature ranges where a single component comprised the majority of the sample mass.

To comply with the philosophy of this methodology and maintain the simplest representation of each species, a constant term for the heat capacity was initially attempted for the functional form of the heat capacity for both the unreacted species and the residual species. If it appeared that the constant value did not adequately represent the calculated apparent heat capacity of either species, a linear relationship was attempted and if the relationship was still deemed inadequate, an additional term was added to the expression while maintaining the form of Equation 2.1. The heat capacities of any intermediate species were generally defined as a linear combination of the heat capacity of the initial and residual components.

A thermally-thin model was constructed according to the description provided in Section 4.2.1.1. The experimentally measured heating rate was fit was Equation 4.7, and the resulting coefficient was defined in the model to ensure the sample in the model adhered to the observed temperature program. It has been determined in previous studies that the thermo-physical properties, particularly the heat capacity, can significantly affect the onset of mass loss [63,66], and so it is important to determine a well-resolved heat capacity for the material throughout the temperature range where degradation is observed, but particularly at relatively low temperatures where mass loss begins. It was determined that the mean error between the model-predicted and experimental heat flow rate curves for the carbon fiber aerospace composite presented in Chapter 7 decreased from approximately 16.2% to 8.4% and the mean relative error in the time-dependent integrals of the heat flow rate decreased from 5.5% to 1.9% by instituting the time-dependent heating rate expression in the ThermaKin model in place of a constant ideal heating rate.

The inverse analysis procedure that was used to determine the heat capacity of each solid component and the heat absorbed in each reaction is presented as a flow chart in Figure 4.2. The model was used to construct a baseline heat flow rate curve that corresponded to the sensible enthalpy of the sample through degradation from modeled evolution of the mass of each component as well as the determined heat capacities. With the sensible enthalpy baseline constructed, the only other contributions to the heat flow rate are due to reactions and phase transitions (h_i in Eq. 4.10). The heat evolved during these chemical and physical changes to the sample specimen were determined as the integral between the experimental curve and the sensible enthalpy baseline over the range of temperatures at which the reaction or phase change occurred. Because the DSC data is normalized by the initial mass, the integrals that correspond to the heats evolved during reactions must be corrected to the mass of the reactant present when the reaction occurs. Though the experimental and predicted heat flow rate curves do not always completely coincide, the integral of each must be equal to verify the energy evolved in the model is equivalent to the energy evolved in the experiment. The criterion for acceptance of the energetic parameters determined through the method described here requires that the mean instantaneous error between the time-dependent integrals of the model-predicted heat flow rate curve and the experimental curve remain below 5%. The effect of this acceptance criterion on bench-scale model predictions was investigated and is presented in Section 4.3.

The uncertainty in the heat capacity of virgin and melt components calculated through the method described here was determined as ± 10% by varying the heat capacity definition to generate a heat flow rate curve prediction that was within the scatter of the

experimental data. The heat capacity of char components that were determined through this method were calculated from data with relatively larger scatter, and the uncertainty was calculated as approximately ± 20%. The graphical method used to determine the heats of reaction yielded heats of reaction with uncertainties of approximately ± 20%.

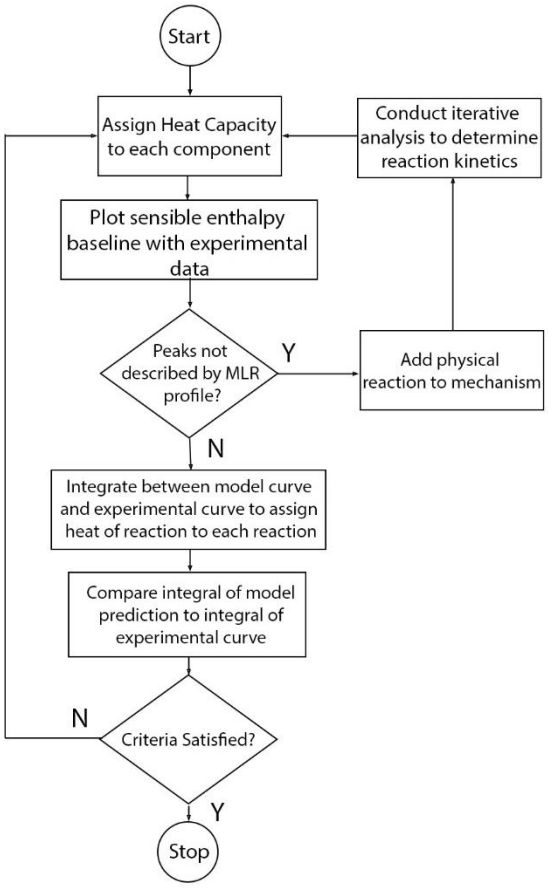

Figure 4.2: Flow Chart Depicting the Inverse Analysis Procedure for Determining the Heat Capacity of Each Solid Component and the Energetics of Thermal Degradation

Section 4.2.3: Heat of Combustion of Pyrolyzate Gases

The heat of combustion of the gaseous species produced during pyrolysis effectively relates the solid-phase processes to the gas-phase processes that occur in a fire. This link between the solid- and gas-phase processes is vital to understanding the effect of pyrolysis of a building material on its surroundings in a fire scenario. Microscale combustion calorimetry (MCC) [93] is a standard thermal analysis method that is capable

of measuring the heat release rate due to complete combustion of a material as a function of temperature and it was used in this methodology to measure the heats of complete combustion and also to verify that the complexity of the combustion of pyrolyzate species was fully captured by the kinetic model developed through analysis of STA data. MCC data may also provide additional information about the relative importance of each reaction to the overall fire response of the material.

The sample is contained in an open, ceramic crucible to ensure the gaseous pyrolyzate escapes the pyrolysis chamber with no resistance to flow. The mass of the sample is typically in the range 3 to 5 mg based on a constraint that oxidation of the pyrolyzate consume less than half the oxygen in the combustion chamber at any time. The sample is pyrolyzed in an inert atmosphere at a well-defined heating rate generally between 12 and 120 K min^{-1} (0.2 and 2 K s^{-1}). The gaseous pyrolyzate is allowed to mix with excess oxygen at a relatively low temperature in a mixing chamber and flows to a combustion chamber at a temperature of 1173 K (900°C) where complete combustion takes place. The heat release rate due to combustion of the pyrolyzate is measured using oxygen-consumption calorimetry.

Various other methods have been used to measure the heat release rate and to provide data from which heats of combustion of gaseous volatiles produced through pyrolysis may be extracted. Oxygen bomb calorimetry [94] was used by Walters et al. [95] to measure the heat of combustion of several polymers with known chemistry. The measurement of the heat released in oxygen bomb calorimetry is made based on the change in sensible enthalpy of distilled water surrounding the combustion chamber. A drawback

to oxygen bomb calorimetry is the inability to assign a distinct heat of combustion to each reaction that has been identified in the kinetic mechanism.

Several similar methods exist for determining the heat release rate of a burning material in which the temperature of air flowing through the test chamber is measured before and after coming in contact with the burning sample and change in enthalpy is related to the heat released in combustion [96]. The OSU calorimeter is a measurement apparatus that determines the heat release rate according to the change in sensible enthalpy, although there has been significant criticism about the errors incurred and overall execution of this test method [97]. More common are methods that use the principle of oxygen consumption calorimetry, including the cone calorimeter [98], fire propagation apparatus [99], and the intermediate scale calorimeter [100]. These methods all require coupon-sized samples and can only provide a single effective heat of combustion value for the pyrolyzate species from composite materials. These methods are inferior to the MCC because the combustion efficiency in each is lower than one, but it is not well-defined and can change depending on the conditions. The MCC not only provides heats of complete combustion, but also does so for each pyrolyzate species produced through thermal degradation, so the complexity of the pyrolysis process is not a limiting factor.

Section 4.2.3.1: Experimental Procedure and Analysis

Samples for MCC tests were prepared identically to the samples for STA tests described in Section 4.2.1.1. The sample mass, which ranged from approximately 2 to 5 mg was recorded and the sample was placed in a ceramic crucible. The small sample size makes the MCC ideal for determining the heats of combustion of the pyrolyzate species produced in the degradation of composite materials when each component can be tested

independently. The tests in the MCC were conducted without lids on the crucibles to allow all pyrolyzate gases to escape the sample unimpeded. The sample crucible was introduced to the pyrolysis chamber and allowed to reach equilibrium at approximately 348 K (75°C). Upon reaching equilibrium, the temperature of the pyrolysis chamber was increased according to a well-defined constant heating rate of 10 K min^{-1} to the final temperature of approximately 900 K. The heating rate chosen for MCC tests conducted in this work changed over the development of the methodology presented here. Initially, the heating rate recommended in the standard, 60 K min^{-1}, was used to determine the heats of combustion associated with the pyrolyzate species from the corrugated cardboard. As the methodology developed, it was determined that a better analysis of the heats of combustion could be achieved by conducting MCC tests at 10 K min^{-1}, the same heating rate as all other thermal analysis techniques conducted in this work.

The temperature measurement in the MCC apparatus was calibrated according to the melting temperature of several metals over the typical temperature range at which most polymers decompose. The oxygen sensor was calibrated against a standard air mixture to ensure accurate heat release rate measurements. The mass flow controllers for oxygen and nitrogen flow into the combustion and pyrolysis chambers were calibrated against an independent flow meter.

An analysis of the heat release rate data that utilized the reaction kinetics determined through analysis of TGA data provided a basis from which to determine the heat of complete combustion of the pyrolyzate species evolved during thermal degradation of the sample. The thermally-thin pyrolysis model was used to simulate the mass loss process in the MCC test with the heating rate profile observed in the tests and described by

Equation 4.7. Generally, a shift between the modeled mass loss rate and the experimental heat release rate was evident that was most likely due to the difference in the heat transport characteristics to and within the crucibles in these two instruments. This analysis was based on an assumption that the STA provided a more reliable sample temperature control than the MCC.

An inverse analysis was conducted in which a unique heat of combustion for each pyrolyzate species was multiplied by the model-predicted mass flux associated with each reaction to yield a *HRR* curve. The simulated *HRR* curve was compared to the experimental *HRR* curve and the values of each heat of combustion were adjusted until acceptable agreement was achieved. Though qualitative agreement between the simulated and experimental *HRR* curves was important, the only formal acceptance criterion was that the total integrals of the simulated and experimental curves agree within 5%.

The uncertainty in each of the heat of combustion values was determined as approximately ± 10%. The uncertainty was determined by independently adjusting two of the heats of combustion determined for the carbon fiber composite (Chapter 7) to minimize the difference between the experimental and modeled *HRR* curves while stipulating that the third heat of combustion be defined such that the integral of the predicted *HRR* curve assume the upper and lower bounds dictated by the acceptance criterion. In previous, related studies, the uncertainty in the heats of combustion was approximated as ± 20%.

Section 4.2.4: Optical Properties

The review of sensitivity analyses in Section 4.1.1 concluded that the optical properties of a material may significantly affect the pyrolysis model predictions of the temperature distribution through the material and the *MLR* profile. The measurement of

sample temperatures and the inverse analysis technique adopted for application of the methodology presented in this work to determine the thermal conductivity (Section 4.2.5.1) depends on well-defined optical properties at the top and bottom boundary. The optical properties that are most important to the pyrolysis process are the surface emissivity and the absorption coefficient.

Composites are generally composed of several polymers, which may possess a wide range of absorption coefficient values. It is also evident that the emissivity of a particular composite may not be adequately described by literature values. In many other research efforts, emissivity and absorption coefficient values for materials characterized in pyrolysis models are usually either taken from literature or determined indirectly through a comparative method.

The optical properties have been measured directly and indirectly through several standard test methods described in this section, although these methods require specialized apparatuses, each of which has limitations. Typically the surface reflectivity of a sample material is easier to measure than the emissivity or absorptivity. Radiant heat transfer problems may be simplified by assuming material surfaces are opaque or optically thick. This simplification allows for the following relationship between the absorptivity (α) and reflectivity (ρ) of a surface: $\alpha + \rho = 1$. By assuming the material surfaces are gray emitter-absorbers, Kirchhoff's law may be invoked to equate the absorptivity to the emissivity (ϵ) of the material, resulting in the following equation: $\epsilon + \rho = 1$ [101]. This simplifications has been used by researchers to describe the optical properties of synthetic polymers and composites [102,103].

Hubbard et al. measured the surface emissivity of several carbon fiber composite formulations using a directional hemispherical reflectometer [54]. While the sample was irradiated, the reflectometer allowed the directional total emissivity to be measured at two angles of incidence as well as the hemispherical total emissivity. A reflectometer is a form of spectrophotometer that measures the radiant energy reflected from a material usually within a specific spectral band. Several laboratories use an integrating sphere to measure optical properties [64,104]. An integrating sphere is a device used to collect reflected or transmitted radiation from a sample to a hemisphere. The electromagnetic radiation gets captured in the hemisphere and the entirety of the energy is measured by spectrophotometers on the sphere. The integrating sphere allows the measurement of spectral as well diffuse optical properties and can accommodate the measurement of the optical properties of a wide range of materials [105]. The specialized equipment used in these studies generally cannot withstand large temperatures, so it is evident that the changes in the optical properties that occur due to thermal degradation of the sample may not be assessed with these methods.

Matsumoto et al. measured the emissivity of graphite as a function of temperature up to 3000 K [106]. The sample was held between two electrodes in a cylindrical vacuum chamber and a gold coated hemispherical mirror was positioned centered on the middle of the sample surface. A radiation thermometer that was calibrated against a blackbody measured the surface temperature of the sample through an aperture in the hemispherical mirror. The spectral emissivity was determined by comparing the voltage measured from the radiation thermometer with and without the hemispherical mirror. This method is so specialized that it is not applicable to any composites that undergo thermal degradation.

Though the emissivity measured by Matsumoto et al. is used in this methodology often to define char species, the method of measurement was completely ruled out.

Linteris et al. used a method in which a well-defined thickness of polymer was exposed to radiation from a heater with a well-defined emission spectrum to measure the transmitted radiation with a heat flux gauge [102] to effectively determine the absorption coefficient. Similar methods have also been used by other researchers [107,108]. A slight modification of this method was used in this methodology. The method only required a heater that irradiated through a broad spectrum and a heat flux gauge, which made it ideal for the minimalist approach presented in this work.

Section 4.2.4.1: Experimental Procedure and Analysis

Early in the development of this methodology, the surface emissivity of corrugated cardboard was determined through a comparative method that utilized an inverse analysis on data collected on two samples with a well-defined emissivity due to paint and an unknown emissivity, with all other properties identical. The heat flow into the depth of the sample was tracked by thermocouples that were inserted at several depths. An inverse analysis was conducted on the data from the sample with the well-defined emissivity to determine the thermal conductivity. After the thermal conductivity was determined, an identical inverse analysis was conducted on the sample of unknown emissivity to determine the emissivity.

Though this comparative method was effective when used to characterize the emissivity of the corrugated cardboard, it was hypothesized that the paint affected absorption of radiation at the surface of the material. This effect was insignificant with corrugated cardboard because it was non-transparent to radiation before the paint was

applied and because the difference in emissivity between the painted and unpainted samples was relatively large. When this method was attempted with other materials studied in this work, the differences in temperature and *MLR* profiles between the painted and unpainted samples were not significant enough to confidently conclude that the emissivity of the material was different than the paint. Literature values were relied upon to define the emissivity of these materials.

The method used in this work to measure the absorption coefficient for each layer of the composites material was adapted from Linteris et al. [102]. A rendering of the general measurement technique is provided in Figure 4.3. The radiant heat flux transmitted through a sample of a well-defined thickness, subjected to a well-defined heat flux from the cone heater, was measured with a Schmidt-Boelter heat flux gauge. The sample was irradiated for up to ten seconds, at which point the sample was removed and the heat flux directly to the gauge was measured for one minute. Eq. 4.11 (Adapted from [103]) was used to calculate the effective absorption coefficient based on the data from this measurement. In Eq. 4.11, κ is the absorption coefficient, γ is the reflection loss coefficient, and τ_0 is the transmission coefficient defined in Eq. 4.12 as the fraction of radiation allowed to pass through the film thickness, δ. In Eq. 4.12, the radiant energy incident to the sample surface, $I_{x=0}$, was approximated as the radiant energy directly incident to the gauge. Linteris et al. found that this method of determining the absorption coefficient produced consistent results to those measured with an integrating sphere.

$$\kappa = \frac{[2\ln(1-\gamma) - \ln\tau_0]}{\rho\delta} \tag{4.11}$$

$$\tau_0 = \frac{I_{x=\delta}}{I_{x=0}} \tag{4.12}$$

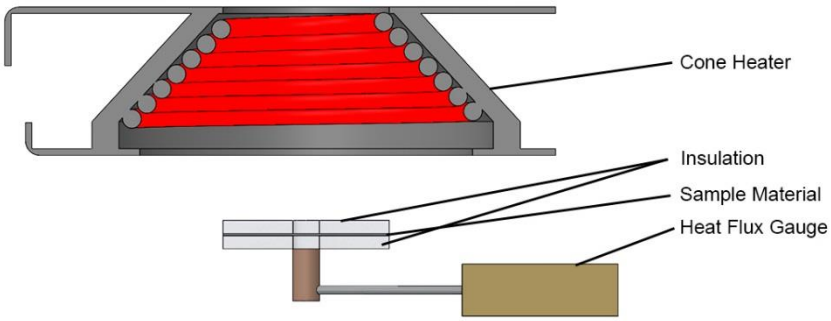

Figure 4.3: Rendering of Technique Used to Measure Absorption Coefficient

The reflection loss coefficient, γ, accounts for reflection of incident radiation at the interface between the material and the gaseous atmosphere. In this methodology, this coefficient was assumed to be 0.05 for all materials unless there was evidence of a more representative value. This value is the approximate mean of the reflection loss coefficients for common polymers tabulated by Tsilingiris [109] and supported by the work of Linteris et al. [102] and Försth and Roos [104].

Linteris et al. estimated that the uncertainty in the measurement of the absorption coefficient using this method was approximately ± 5%, although variations in calculated absorption coefficients determined from measurements made in this work indicate that the uncertainty in all absorption coefficient definitions is approximately ± 25%.

Section 4.2.5: Determination of Thermal Conductivity

Measurement of thermal conductivity can be difficult and is further complicated when the material to be measured undergoes thermal degradation during the measurement. This is a common occurrence because thermal conductivity values are required for all components at the range of temperatures that are encountered in the test to be simulated. Several standard methods and apparatuses exist for the measurement of thermal

conductivity for a wide range of material classes and a wide range of conditions, although each method is limited in its scope. The main distinction between these methods is whether the system may be dynamic or must be in operated in steady-state.

The guarded-hot-plate apparatus [110] and the heat flow meter apparatus [111] are steady-state methods that are limited to homogeneous samples with parallel sides with dimensions that do not change during the tests. Because of the requirement that the system be in steady state (isothermal), a single test can last for hours because of the time required for the system to reach steady conditions. When thermal conductivity values are required over a range of temperatures, tests must be conducted at several temperatures, which compounds the amount of time required to collect meaningful data and implies that the thermal conductivity of the materials may not be measured as the material degrades.

The flash method [112] was designed to measure the thermal diffusivity of non-porous, homogeneous, isotropic materials that are opaque to thermal radiation. The range of thermal diffusivities that may be measured is from 0.1 to 1000 $mm^2\ s^{-1}$ and the temperatures that the apparatus can accommodate are in the range of 75 to 2800 K. This method allows determination of the thermal conductivity as long as the density and the specific heat of the material is known. It may also be used to measure the heat capacity of a material relative to other materials. The flash method must be conducted at a specific temperature, and if data is required over a temperature range, the tests must be conducted at several discrete temperatures over the desired range, which brings about the criticisms aired about the other steady-state methods. Harada et al. used the flash method to determine the thermal conductivity, heat capacity, and thermal diffusivity of wood up to 543 K for the purpose of studying the charring process for the wood samples [113].

The transient plane source technique [114] is intended to measure the thermal conductivity of materials that may have orthotropic properties. A flat coil of heating wire acts as both the heating element and temperature sensor. The sensor is clamped between two planar samples with known dimensions and a known amount of heat is introduced to the specimen. The thermal conductivity can be calculated from the voltage and resistance measurements over the surface of the sensor as a function of time. The transient plane source method has been used by Suleiman et al. to measure the thermal conductivity and diffusivity of several wood samples at temperature up to 373 K [115] and by Bentz to measure thermal properties of fire resistive materials at room temperature, although slug calorimetry was used in the same study to determine thermal conductivity at elevated temperatures [116]. This method is limited by the maximum sample temperature at which thermal conductivities may be measured that do not allow materials that undergo degradation to be accurately characterized.

Myllymäki and Baroudi conducted an investigation that demonstrated the merit of inverse analyses and showed that a direct measurement is not always necessary when determining thermo-physical properties [117]. Bentz did a study that demonstrated that it is possible to predict the thermal conductivity of a complicated composite material by measuring the thermal conductivity of each of the individual components and applying knowledge about the geometry of the composite and heat transfer through composites [118].

Quintiere et al. measured the thermal conductivity of a carbon fiber aerospace composite using a method similar to the transient plane source method calorimeter [58]. A flat power source was sandwiched between two plates of the composite and the temperature

difference between the power source and each plate was measured as a function of time. The power was increased throughout the duration of the measurement in steps and the system was allowed to reach thermal equilibrium. The temperature difference, thickness of the sample, and power supplied to the system were used to calculate the temperature-dependent thermal conductivity for the composite. The authors estimated that the uncertainty in the measurement was approximately ± 20% and recommended that a more rigorous measurement be made.

Many of the testing methods described in this section do not facilitate the measurement of the thermal conductivity of layered composite materials or of materials that are undergoing thermal degradation. Additionally, they all require specialized equipment and the methods that have the widest temperature range are steady-state methods that must be conducted isothermally and time-consuming. Common to all the transient methods is the generation of a temperature gradient through the material and two or more temperature or heat production measurement points at well-defined locations in the sample. All of these methods require some analysis of the collected temperature and heat data to determine the thermal conductivity of the material and may be significantly affected by poor thermal contact.

Section 4.2.5.1: Experimental Procedure and Analysis

The method adopted in this investigation to determine the thermal conductivity of the sample specimen relies on temperature measurements collected during one-dimensional radiant heating and an inverse analysis that utilizes a pyrolysis model that has been completely parameterized, with the exception of the thermal conductivity. Two methods of temperature measurement that are demonstrated in this work include embedded

thermocouples, which may be impractical for many commonly encountered materials, and infrared thermometry to measure the back surface temperature of the samples, which is essentially capable of measuring surface temperatures for any material.

Infrared thermometry is a form of non-invasive temperature measurement that relies on the emission of electromagnetic radiation from a source object to determine the temperature of the source object, although it can be complicated by uncertainty in defining the surface optical properties of the target specimen. Though there are several types of infrared thermometers, the infrared thermometer used in this study, a thermal imager, is the only thermometer capable of determining the spatial distribution of electromagnetic radiation emitted from a surface that has a well-defined emissivity [119].

Most of the one-dimensional bench-scale tests conducted in this work utilized a gasification apparatus designed at the University of Maryland that augments the standard cone calorimeter called the controlled-atmosphere pyrolysis apparatus (CAPA). The study conducted on corrugated cardboard utilized the cone calorimeter and embedded thermocouples, and the experimental procedure is completely described in Chapter 5. Analysis of the temperature data was identical regardless of the measurement method. The CAPA was developed to generate a well-defined oxygen concentration in the vicinity of the sample material while the sample is subjected to a well-defined heat flux from the cone heater. The basic design of the CAPA consists of two concentric, square, metal ducts with a sample holder inside the inner duct. The sample holder is completely isolated from the gas flow chamber to ensure there is no interference between the two that may result in unphysical mass loss data. The annular space between the two ducts features a gas flow path through a low pressure drop area followed by approximately 1 inch of glass beads to

homogenize the gas flow that is injected into the gas flow chamber. This design was implemented to uniformly distribute the gas along the edges of and over the surface of the sample. The CAPA makes possible simultaneous measurement of the back surface temperature for determination of the thermal transport parameters, and the mass of the sample for model validation. Simultaneous measurement improves the efficiency with which a material may be characterized, which may be very important for complicated layered composites.

The interior volumes of the inner duct and sample holder have square cross sections with sides measured 120 mm and 115 mm, respectively. The gap between these two is blocked by a lip installed on the sample holder (see Figure 4.4). The lip is located 1 mm above the upper edge of the inner duct, ensuring that the sample holder is suspended on the balance and does not make contact with the CAPA ducts to prevent interference with the mass measurement.

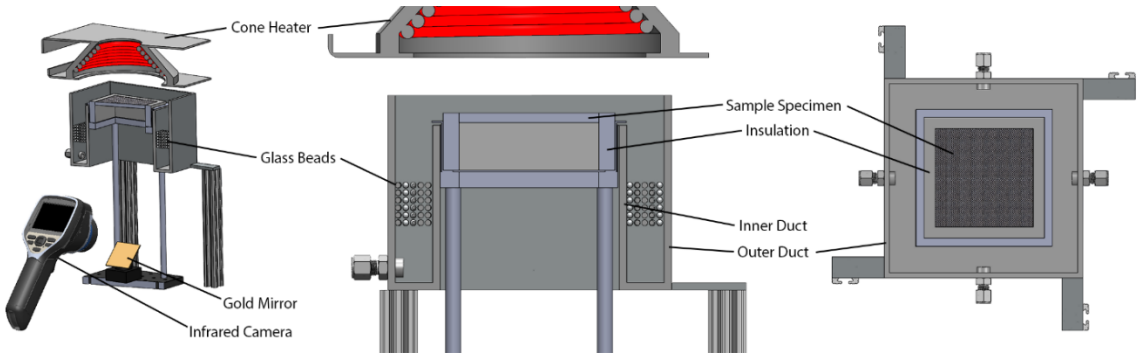

Figure 4.4: Rendering of Controlled Atmosphere Pyrolysis Apparatus (CAPA)

CAPA tests were conducted on square samples with a side of 0.08 m at a range of heat fluxes that are commonly encountered in enclosure fires. Samples were located in the center of a square sheet of 0.00625 m thick Kaowool PM board with an edge dimension of 0.105 m for a total of 0.0125 m of insulation at each face of the sample orthogonal to the heated surface. The method for measuring the back surface temperature with infrared

thermometry required a well-defined emissivity at the surface to be measured. This definition was achieved by applying a highly emissive paint to the back surface of the sample, or resting the sample on aluminum foil with the surface facing the camera painted. The aluminum foil was deemed necessary only when it was evident that oxygen introduced to the back surface of the sample affected pyrolysis. A picture of the sample holder is provided in Figure 4.5.

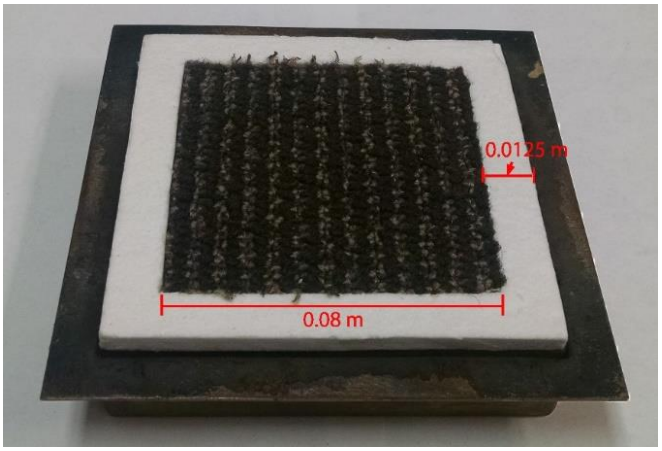

Figure 4.5: Picture of a Sample of Carpet Composite Mounted to the CAPA Sample Holder and Surrounded by Kaowool PM Insulation Board

A Schmidt-Boelter heat flux gauge was positioned at a location corresponding to the geometric center of the top sample surface, 40 mm below the bottom of the cone heater, to set the radiant heat flux to the sample. A feedback control system internal to the cone calorimeter automatically adjusted the temperature of the heater based on the signal from the heat flux gauge. The uniformity of the heat flux at the sample surface was examined with a separate heat flux gauge and found to be satisfactory (< 7% maximum deviation from the set point).

The tests conducted in this work with the CAPA had nitrogen introduced to the gas flow chamber at a rate of 225 SLPM unless otherwise noted. At this flow rate, the mean oxygen concentration was measured as 2.2 ± 0.4 vol.% over nine points approximately 1

mm from the surface of the sample. It was found that this oxygen concentration prevented autoignition for all samples tested and appeared to make any effects of oxidation on temperature profiles and mass loss rates inconsequential.

Analysis with ThermaKin required construction of a thermal transport sub-model to systematically determine thermal transport parameters from sets of data collected in CAPA tests. The model required a one-dimensional assumption and the spatially-resolved temperature data was reduced to a single representative value of the T_{back}. The T_{back} data was recorded at a rate of 7.5 Hz. In each frame, the image was divided into three regions. Region 1 consisted of the central 0.04 m × 0.04 m square, region 2 consisted of the central 0.06 m × 0.06 m square less region 1, and region 3 consisted of the entire 0.08 m × 0.08 m sample surface less regions 1 and 2. The mean T_{back} was calculated in each frame using four randomly selected locations from regions 1 and 2, and two randomly selected locations from region 3. The T_{back} was generally uniform, with the maximum deviation from the mean value on the order of 5%.

To quantify convective heat losses from the top surface, a 3 mm thick copper plate of sample dimensions was placed in the CAPA in place of a sample. Copper was chosen because its thermal conductivity, heat capacity, and density are well defined in literature [120]. The plate was painted black for a surface emissivity of 0.95, which allowed a fully parameterized one-dimensional heat transfer model to be constructed, leaving the convection coefficient as the only unknown parameter that could not be directly measured. The plate was instrumented with two embedded thermocouples. Tests were performed at incident heat fluxes of 20, 40, and 60 kW m^{-2}. The temperature of the nitrogen flowing through the CAPA was measured at the level of the sample upper surface in the middle of

the annular space between the ducts using a 0.13 mm diameter type K thermocouple. The temperature changed linearly from 330 to 370 K as the heat flux increased from 20 to 60 kW m^{-2}. It was assumed the same linear temperature dependency could be interpolated and extrapolated up to 80 kW m^{-2}. Defining the convection coefficient as 5 W m^{-2} K^{-1} was found to produce the best agreement between the experimental and simulated temperatures. Specific details of this convection coefficient determination procedure are provided elsewhere [121].

The boundary conditions for the top surface of the sample were defined with a radiant heat flux identical to the heat flux set point for the CAPA tests, the convective heat transfer coefficient was defined as 5 W m^{-2} K^{-1}, and the ambient temperature at the front surface was defined according to the aforementioned linear dependence. The mass transport at the boundary was defined to provide no impedance to the escape of gaseous pyrolyzate produced during degradation.

Chaos et al. found heat loss from the back boundary can significantly affect the results predicted by a bench-scale model [122,123], which indicates the importance of an accurate definition of the back boundary condition. The back surface was defined to be impenetrable to mass transport. The convective boundary condition at the back surface of the sample was defined with a heat transfer coefficient of 4 W m^{-2} K^{-1} and an ambient temperature of 310 K. A radiant heat flux of 500 W m^{-2} was applied to the back surface to simulate radiation from the internal walls of the test apparatus (which were assumed to be at ambient temperature). The absorption coefficient of the back surface was defined such that all incident radiation was absorbed at the surface. The emissivity of the back surface was defined as 0.95 to simulate the presence of high emissivity paint on the back surface

of the tested samples or on the aluminum foil on which the samples rested. A default value for the mass transport coefficient was defined for all components (2×10^{-5} m^2 s^{-1}). This value was determined as high enough to allow all gaseous pyrolyzate to escape the condensed phase with no impedance to flow, and low enough that it would maintain the stability of the integration [24].

The material was geometrically defined in the thermal transport sub-model according to the measured thickness, composition, and temperature of each layer. Each component was defined with its measured density, state of matter, and its specific heat capacity determined through analysis of milligram-scale data, and its emissivity and absorption coefficient. The mass transport coefficient was initially assigned a value based on the assumption that no component provides any impedance to the flow of pyrolyzate through the material, though this assumption was relaxed if sufficient justification was available.

The initial conditions and the boundary conditions for the bench-scale test were defined in the model and the thermo-physical properties of the tested material were determined through several iterative inverse analyses that used the sample temperature data as the target for the analyses Temperature profile data collected at the lowest tested heat flux for each material were generally used to determine the thermal transport parameters. These data were chosen to determine the thermo-physical properties of the material because they were collected under the best defined boundary conditions. Additionally, by using only temperature data to determine the thermal transport properties, the mass and mass loss rate predictions were completely decoupled from the process of property determination and served as independent validation data sets.

It has been observed [124] that the structure of the unreacted material at room temperature changes as the material degrades, and with the changing structure of the material come changes in the properties of the material. The changes in the structure and properties of the material are captured in the model as species defined as solid products of degradation reactions. During the process of conducting inverse analyses to determine the thermal transport parameters, it proved advantageous to focus the analysis on specific time periods in the data to isolate individual species. In this way, the entire material could be parameterized incrementally for its most accurate mathematical representation.

The thermal transport sub-model was used to conduct an inverse analysis on the back temperature data to determine the only remaining unknown thermal transport parameters, the thermal conductivities of the solid components. A flow chart that represents the inverse analysis is presented as Figure 4.6. The temperature data that was collected at the back surface of the sample through infrared thermometry were analyzed in relatively small time increments to first isolate the unreacted species. The focus when fitting temperature data for the unreacted species was the time to the initial rise and slope of the initial rise in the temperature. In maintaining the philosophy in which additional complexity was only included in the model when necessary, the thermal conductivity of each species was initially defined as a constant and additional terms were included in the expression while maintaining the form of Equation 2.1 when it was demonstrated that doing so would improve agreement with the experimental data. Common sense limits have been applied to the thermal conductivity values determined in the case studies presented in Chapters 5-8 along with justification for each limit definition.

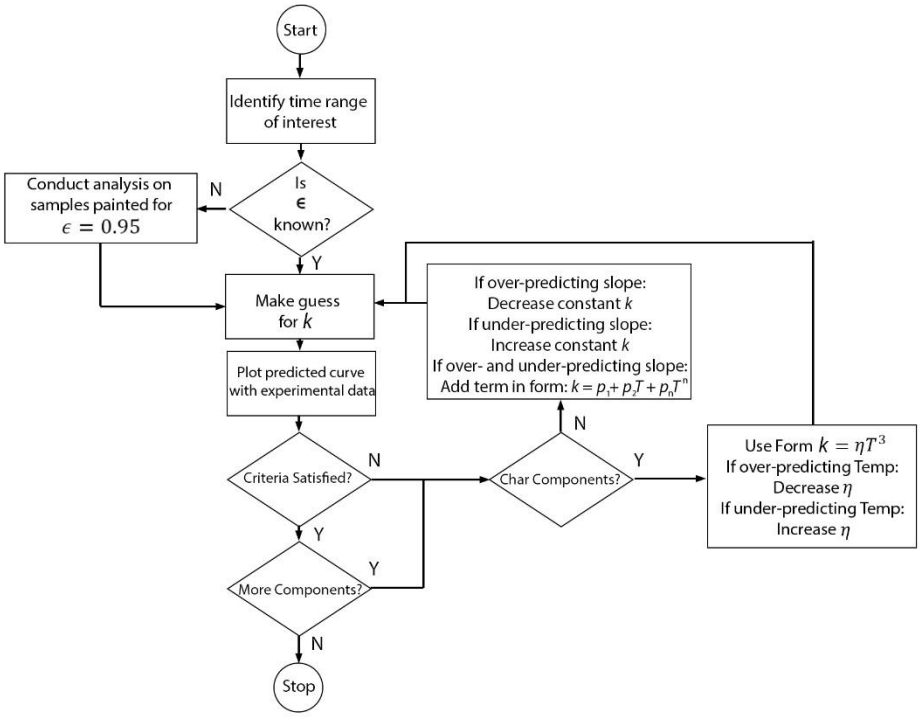

Figure 4.6: Flow Chart Describing the Inverse Analysis Procedure for Determining the Thermal Conductivity of Each Solid Component.

The heat transfer through multi-layered composites is a complicated process that is difficult to accurately model. The highly emissive paint that was applied to the sample has been observed to degrade in the temperature range of approximately 650 K, which makes data above this threshold range unreliable. These complicating factors make the most important criterion for acceptance of a thermal conductivity definition a qualitative agreement with the experimental back temperature data curve. A quantitative criterion that has been used in this work is a mean instantaneous error not greater than the scatter in the mean back surface temperature measurement up to approximately 600 K. The effect of this criterion on bench-scale model predictions was investigated and is presented in Section 4.3.

The second time range at which an inverse analysis was conducted was the final portion of the CAPA test in which the residual species composed the greatest fraction of the sample. The temperatures at which this analysis was conducted were generally close to the threshold above which the measurements were considered unreliable, although one of the reasons the data collected at the lowest heat flux was used for target data in inverse analyses was the relatively low maximum temperature measured in these tests.

The residual species were generally characterized by a highly porous structure and low densities. The temperatures at which the char forms were sufficiently high that radiation was assumed to be the dominating form of heat transfer in the porous char layers. The radiation-diffusion approximation was invoked to describe the radiant heat transfer in terms of an effective thermal conductivity. The radiation-diffusion approximation [125] is stated in the following equations, where k is thermal conductivity, σ is the Stefan-Boltzmann constant, k' is the effective thermal conductivity which is described by the coefficient to the temperature-dependent term, η.

Fourier's law for conductive heat transfer is defined as Eq. 4.13 and represents the diffusion of energy along a spatial temperature gradient. The spatial temperature gradient can be approximated as a finite temperature difference over a finite distance instead of the infinitesimal temperature difference for the differential defined in the equation.

$$q'' = -k\frac{\partial T}{\partial x} \approx -k\frac{\Delta T}{\Delta x} \tag{4.13}$$

The Stefan-Boltzmann law for radiant heat transfer is provided as Eq. 4.14. The radiant heat transfer is proportional to the fourth power of the temperature of the radiating surface.

$$q'' = \epsilon\sigma T^4 \tag{4.14}$$

By manipulating the Stefan-Boltzmann law and Fourier's law and introducing an effective thermal conductivity, k', to approximate the radiant heat transfer by the conductive heat transfer equation, Eq. 4.15 is derived.

$$k'\Delta T \approx \epsilon\sigma T^4 \Delta x \tag{4.15}$$

The effective thermal conductivity that describes the radiant heat transfer with Fourier's law is defined by simplifying Eq. 4.15 and approximating ΔT as T to yield Eq. 4.16.

$$k' \approx (\epsilon\sigma\Delta x)T^3 = \eta T^3 \tag{4.16}$$

The agreement between the model-predicted back temperature profiles and the experimental data was assessed for the entire duration of the tests and the thermal conductivity definitions for the intermediate species were adjusted as a linear combination of the unreacted and residual species if modification was required. The properties of the gaseous volatiles had little impact on the model because transport of the pyrolyzate was assumed to be fast and the mass of the solid phase components was much larger than the mass of the gases. The heat transfer due to advection of gases through the solid phase fuel had a minor effect on heat transfer in the solid and the heat capacity of the pyrolyzate gas was the only factor that was found to affect the model predictions.

An important observation that was made during investigation of the low-pile carpet and the fiberglass-reinforced polyester composite was the influence of interfacial effects on thermal transport within the material. Each layer of these composites was characterized independently, and it was shown that the reconstruction of each independently-characterized layer into a model of the composite did not adequately reproduce mass or

temperature data collected on the composite. The solution that was incorporated into the methodology consisted of reparametrizing the most uncertain thermal conductivity definitions from back temperature data collected on the full composite, which essentially determines the thermal transport parameters with the interfacial effects built in. The most uncertain thermal conductivity must be determined while adhering to the guiding philosophy of this methodology, which, in essence, seeks to relate the properties of well-defined species to the properties of less well-defined species to maintain the fewest independent parameters in the model that require determination.

The thermal conductivities determined through this method of inverse analysis are considered to have an uncertainty of approximately ± 15%. The uncertainty was determined by varying the thermal conductivity definition for the component of interest and observing the change in the back temperature prediction relative to the scatter in the experimental data. This uncertainty was the largest variation in the thermal conductivity expression that yielded a back surface temperature prediction that was within the limits of error of the mean experimental data.

Section 4.2.6: Bench-scale One-Dimensional Pyrolysis Tests

As mentioned in Sec. 4.2.5.1, the bench-scale one-dimensional radiant heating test that was used to collected sample temperature data for analyses and *MLR* data for model validation changed over the development of this methodology. The cone calorimeter was initially used, and an apparatus that augmented the cone calorimeter, the CAPA, was also utilized as the bench-scale apparatus for this work. These apparatuses serve to demonstrate the generality of this methodology and show that almost any bench-scale apparatus with well-defined boundary conditions for the sample may be substituted here to determine the

thermal transport parameters and may provide validation data for the constructed model. Some alternatives are discussed in the following section.

Common bench-scale testing methods including the cone calorimeter, FPA (Fire Propagation Apparatus), and NIST gasification device provide mass loss data for samples that are irradiated with a well-defined heat flux incident to a single face to simulate one-dimensional pyrolysis behavior. The mass loss rate data may be used as a target for inverse analyses conducted to determine thermo-physical properties as well as validation for fully-parameterized pyrolysis models. These bench-scale tests have relatively simple configurations that allow for the assumption of quasi-one-dimensional behavior.

Cone calorimetry is a type of calorimetry that is common in fire science that uses the oxygen-consumption concept to measure heat released during burning of solids. The cone calorimeter is designed with a cone-shaped coil of wire that heats through electrical resistance. The distance between the heater and the sample is kept constant throughout a test and the heat flux from the heater to the sample depends on the temperature of the heater coil. The temperature of the heater, and effectively the heat flux from the heater, is set based on feedback from a Schmidt-Boelter heat flux gauge mounted 25 mm from the heater surface in the standard test [98]. The heater is oriented such that an approximately uniform heat flux falls incident on the surface of the sample. The sample is usually placed on a holder that rests atop a balance to track the mass of the sample over the course of the test. A spark igniter is held over the sample at the beginning of a test to induce piloted ignition and the igniter is removed upon ignition. A ventilation system is included in the apparatus with a well-defined flow rate of 0.024 $m^3 s^{-1}$. A pump is connected to the ventilation system to sample the gases in the exhaust and feed the sampled gas to a gas analyzer.

The oxygen consumption calorimeter is called such because ventilation gas sampling is conducted primarily to detect the concentration (volume fraction) of oxygen in the exhaust gas. By comparing the concentration of oxygen in the exhaust gases during combustion of the sample to the exhaust gases sampled during a baseline measurement when there is no sample present, the mass of oxygen consumed in the combustion process can be determined. It has been hypothesized, observed, and validated in experiments that the mass of oxygen consumed in the combustion process is directly proportional to the rate of heat release from a burning material [126,127].

One of the major characteristics of the cone calorimeter is the size of the samples for which it was designed. As a bench-scale test, the materials generally have masses of the order of tens of grams. The tests are conducted under a ventilation hood that does not isolate the sample from the surrounding atmosphere, resulting in test samples that are subjected to an oxygen concentration equivalent to ambient air. A major advantage of using the cone calorimeter is the ability of the user to easily modify the test to measure additional variables that affect burning.

Several researchers have made modifications to the standard cone calorimeter to integrate the ability to dictate the oxygen concentration in the vicinity of the sample specimen, which eliminates the solid-gas interactions and further simplifies analysis of the mass loss data. With these modifications made to the cone calorimeter, the gas analyzer and the spark igniter become extraneous and only the mass of the sample is measured during tests. The Fire Propagation Apparatus and the NIST gasification device have the capability to continuously purge the gas atmosphere with an inert gas to provide well-defined boundary conditions at the top and bottom surface. As mentioned previously, in

addition to using the cone calorimeter as a method for measuring the heat release rate due to flaming combustion of pyrolyzate species, it has also been utilized to measure the heat of combustion and time to ignition and to determine the heat of gasification and thermo-physical properties for the material [1].

The Fire Propagation Apparatus (FPA) [99], developed by FM Global, is a standard bench-scale test apparatus that is used to characterize the propensity of a material to support fire propagation in a manner similar to the cone calorimeter. A distinguishing feature between the cone calorimeter and the FPA is a test section duct in the FPA that isolates the sample from the ambient atmosphere and allows the gas atmosphere to be well-defined throughout the test. The FPA has an infrared heating system that is capable of producing heat fluxes up to 510 kW m^{-2} at the heater surface. It has been shown that the heating system in the FPA does not radiate as an ideal black or gray body and emits closer to the visible and near infrared ranges, whereas the cone heater radiates as a near perfect blackbody [108,128]. The FPA is instrumented with a load cell to measure the mass loss history of the sample during burning or gasification, as well as a gas analyzer to measure the concentrations of oxygen and other gases in the vicinity of the sample in the test section duct.

The FPA allows researchers to assess the effects of oxygen concentration, gas pressure, convection coefficient, as well as other atmosphere-related variables on the mass loss rate of the sample material during pyrolysis and combustion [35]. As with the cone calorimeter, the samples tested with the FPA have masses on the order of tens of grams. Modifications to the standard apparatus can also be made to collect additional data

pertaining to the sample material, including thermometry to measure the temperature of the surfaces of the sample.

The NIST gasification apparatus [129] was designed to control the oxygen concentration of the atmosphere as a solid or liquid sample was subjected to a uniform heat flux. The heater, sample holder, and the balance are contained within a sealed cylindrical chamber that is continuously purged with the desired gas mixture. The inner walls are painted black and the surface of the chamber features a water cooling circuit that maintains the temperature of the walls at room temperature to reduce reflection and radiation from the walls to the sample. The heater is constantly maintained at a temperature of 750°C and the heat flux to the sample is specified according to the distance between the heater and the sample. By maintaining the temperature of the heater at a constant value, the spectral distribution of the radiation incident to the sample also remains constant.

Several gasification apparatuses have been constructed for the purpose of subjecting materials to a radiant heat flux in an atmosphere with an oxygen concentration sufficiently low to eliminate all oxidation and gaseous combustion. These devices are generally capable of measuring the mass loss and possibly temperature profiles of the sample during pyrolysis, while others can collect and analyze the composition of the gaseous pyrolysis products. The main motivation behind development of a gasification apparatus is to eliminate the flame on the surface of the sample and the effects of all other gas phase phenomena while simultaneously simulating the response of the sample material to the heat flux from the flame and other radiating sources. The advantage of such a test over the cone calorimeter is that the boundary conditions of the sample are better defined by eliminating the fluctuating behavior of the flame, resulting in a condition that is more

easily modeled than the conditions encountered in flaming cone calorimeter tests. A disadvantage of testing with a gasification apparatus is the lack of standardized test parameters and the resulting inability to compare data collected in different apparatuses.

Babrauskas et al. developed a controlled-atmosphere cone calorimeter (CACC) to test the fire response of sample materials subjected to a range of oxygen concentrations above and below ambient conditions [3]. The specimen holder was encased in a high-temperature glass enclosure. The joints of the enclosure were sealed to prevent any inflow or outflow of gases which would affect the measurements. The desired mixture of gases that comprise the test atmosphere were introduced to the glass enclosure from the bottom to take advantage of buoyancy. The gas mixture was designed to flow through a manifold system, through a layer of glass beads intended to homogenize the flow, and into the enclosure housing the test specimen. The authors acknowledged the advantage a controlled atmosphere test has over the standard cone calorimeter for characterizing polymers and developing improved materials.

Marquis et al. conducted an extensive investigation on the gas flow rate in to the test section of a modified CACC and its effect on the burning rate of the condensed phase sample as well as the combustion of pyrolyzate gases downstream of the testing enclosure [130]. The authors stated that due to the design of the open CACC, with a chimney between the test chamber and the ventilation intake, it is possible to achieve a flame outside the test chamber that will not affect pyrolysis of the sample specimen. It was concluded that the flow of a gas mixture into the bottom of the testing enclosure does not have a cooling effect on condensed phase pyrolysis. The authors advocated the definition of standard testing

protocol for controlled atmosphere pyrolysis tests and referred to potential discussion with the International Organization for Standardization (ISO).

Lattimer et al. recently developed a small-scale thermal decomposition apparatus (TDA) capable of irradiating square samples with a characteristic dimension as large as 0.2 m and up to 12 kg with a cylindrical ceramic heater [131]. The apparatus measures the mass of a sample in a well-defined gas atmosphere as the temperature of the heater is either maintained constant or changed over time along a predefined temperature program. The apparatus was designed such that the sample specimen is in a vertical orientation to allow for natural convection to exhaust the gaseous pyrolyzate. Testing in a vertical orientation provides the unintentional possibility that gaseous pyrolyzate influences the pyrolysis of the sample specimen downstream of the flow. The TDA does not feature any means to homogenize the gas flow introduced to the testing chamber, which could produce locations in the test chamber with oxygen concentrations and flow conditions that are not well characterized.

Lattimer et al. used the TDA to measure the thermal conductivity, heat capacity, and density as a function of temperature for several composite materials. The authors also attempted to determine the Arrhenius reaction parameters and the heat of decomposition through bench-scale tests. A model capable of calculating the heat transfer through a degrading material was utilized in an inverse analysis on front and back surface temperature data and mass loss rate data collected in the TDA. The data was collected in a series of tests in which the temperature of the heating element was increased over a predefined temperature program as well as tests in which the temperature of the heater was held constant. TGA and DSC tests were conducted to validate the findings from the thermal

decomposition apparatus. Though the overall procedure in this investigation was considerably different than the procedure used in the current methodology, the work of Lattimer et al. provides precedence for estimating parameters through bench-scale tests.

Section 4.3: Justification for Acceptance Criteria

An analysis was conducted to determine the effect of the acceptance criteria on the final bench-scale gasification test *MLR* predictions. The analysis specifically examined the effect of independent variations in the pre-exponential factors, activation energies, heat capacities, heats of reaction, and thermal conductivity on the final model predictions for the carbon fiber composite that is the subject of Chapter 7. (Please note that an attempt was made to generalize the results, but for a specific understanding of the material, it is advised that this section is read after Chapter 7)

Because criteria were defined for the peak *MLR* and the temperature at which the peak *MLR* occurred for acceptance of the kinetic parameters for each of the reactions, the kinetic pairs were adjusted to independently investigate each of the limits of the acceptance criteria. The criteria defined a maximum deviation of 10% from the magnitude of the design *MLR* and a maximum deviation of 3 K between the design temperature at which the peak *MLR* occurred and the predicted temperature at which the peak *MLR* occurred. Kinetic pairs were generated that independently assumed the approximate positive and negative limits in temperature and magnitude of *MLR* while the other criterion was held within its defined limits with an attempt to minimize any change in the other criterion. In each case, the effect on the complete predicted STA *MLR* curve was assessed as was the effect on the bench-scale *MLR* predictions at two incident heat flux conditions. The results of this sensitivity analysis on the acceptance criteria are presented in Tables 4.1 and 4.2.

Table 4.1. Results of Sensitivity Analysis Investigating the Effect of the Acceptance Criteria for the Kinetic Parameters on the Agreement Between Experimental and Predicted Mass and *MLR* data from STA Tests

	Mean Instantaneous Error in Normalized Mass [%]	**Mean Instantaneous Error in Normalized *MLR* [%]**	**Error in Maximum *MLR* [%]**	**Error in Temperature at Maximum *MLR* [K]**
Final	0.4	7.2	-4.7	-1
Reaction 1				
Minimum Allowable *MLR* (1M-)	0.2	11.0	+5.4	-3.4
Maximum Allowable *MLR* (1M+)	0.2	10.9	-6.0	-3.3
Minimum Allowable T_{peak} (1T-)	0.2	10.9	-5.9	-3.3
Maximum Allowable T_{peak} (1T+)	0.2	10.9	-6.7	-3.2
Reaction 2				
Minimum Allowable *MLR* (2M-)	0.4	8.9	-5.8	-7.3
Maximum Allowable *MLR* (2M+)	0.4	7.5	+4.6	+1.5
Minimum Allowable T_{peak} (2T-)	0.4	12.1	+5.8	+4.7
Maximum Allowable T_{peak} (2T+)	0.4	9.2	-11.5	-6.3
Reaction 3				
Minimum Allowable *MLR* (3M-)	0.4	7.1	-1.8	-1.3
Maximum Allowable *MLR* (3M+)	0.4	8.4	-10.8	-7.2
Minimum Allowable T_{peak} (3T-)	0.4	11.2	-22.8	-3
Maximum Allowable T_{peak} (3T+)	0.4	9.8	+5.8	-1.2
Reaction 4				
Minimum Allowable *MLR* (4M-)	0.5	10.6	-7.0	-4.5
Maximum Allowable *MLR* (4M+)	0.3	8.4	-5.7	-3.3
Minimum Allowable T_{peak} (4T-)	0.5	14.5	-8.0	-4.8
Maximum Allowable T_{peak} (4T+)	0.3	9.5	-5.5	-2.5

The data presented in Table 4.1 shows the effect of accepting kinetic parameters for each individual reaction at the extreme allowable values. In the table, ‘M’ represents the mass acceptance criterion and ‘T’ represents the temperature criterion. In general, the mean instantaneous error in the normalized mass curve was not significantly affected by the changes to individual reactions. This indicates that the acceptance criterion for the normalized mass may be made more stringent without an increase in the analysis time. The

Mean Instantaneous Error in the Normalized *MLR* increased from approximately 7.2% to a mean of 10% at the acceptance limits. The prediction of the maximum *MLR* was only significantly affected by the reactions in closest proximity to the total peak *MLR* and the temperature at which the peak experimental *MLR* was almost uniformly affected by the limits outside of the acceptance limits for the entire kinetic mechanism.

Though the limits of the acceptance criteria for the kinetic parameters were found to have a profound effect on the agreement between the normalized mass and *MLR* predictions from the thermally-thin model, the data presented in Table 4.2 shows that they did not significantly affect the bench-scale *MLR* predictions. The error between experimental and predicted *MLR* curves at 40 kW m^{-2} was increased uniformly but only by as much as 4.5% and the error for the *MLR* curves at 80 kW m^{-2} were either unaffected or decreased. The predicted magnitude of the *MLR* and the time to the peak *MLR* was not uniformly degraded at either heat flux and the time to the peak *MLR* at 40 kW m^{-2} appeared to most significantly affected by the peak *MLR* of the first reaction.

These data appear to indicate that the acceptance criteria may be relaxed without a significant decrease in the agreement between bench-scale model predictions and experimental data. These results also indicate that the definition of the acceptance criteria that resulted in this four reaction mechanism established a process for adding reactions whereby every reaction was important to the final prediction. In other words, the acceptance criteria defined for the kinetic parameters for this material yielded the simplest mechanism that described all phenomena associated with degradation. The results of this analysis also indicate that each reaction defined in a multiple reaction scheme is important to the final model prediction regardless of the magnitude of the mass loss associated with

the reaction. It was shown that the first reaction in the scheme for the composite modeled here that accounted for a total mass loss of approximately 1% of the total mass of the composite had the most profound effect on the qualitative shape of the bench-scale *MLR* predictions.

Table 4.2. Results of Sensitivity Analysis Investigating the Effect of the Acceptance Criteria for the kinetic Parameters on the Agreement Between Experimental and Predicted Bench-scale *MLR* data

	Mean Instantaneous Error in *MLR* [%]	**Error in Maximum *MLR* [%]**	**Error in Time to Maximum *MLR* [s]**	**Mean Instantaneous Error in *MLR* [%]**	**Error in Maximum *MLR* [%]**	**Error in Time to Maximum *MLR* [s]**
	40 kW m^{-2}			**80 kW m^{-2}**		
Final	28.8	-0.8	-4	18.2	-32.1	+2
1M-	29.9	+0.7	-10	16.9	-32.4	-1
1M+	31.4	-0.5	+15	19.7	-32.5	+3
1T-	30.8	+0.7	+1	18.5	-32.3	+2
1T+	30.0	+1.2	-4	17.8	-32.6	+1
2M-	29.5	+1.2	-4	17.9	-32.6	+1
2M+	31.4	+0.3	-2	18.4	-32.2	+1
2T-	31.9	+0.0	-4	18.3	-32.2	+1
2T+	32.4	+1.4	-5	18.2	-32.4	+2
3M-	29.7	+1.2	-5	17.9	-32.5	+2
3M+	31.1	+0.7	-3	18.3	-32.3	+1
3T-	33.0	+0.4	-3	18.1	-32.5	+2
3T+	32.5	+1.3	-5	18.3	-32.3	+1
4M-	30.9	-0.7	-5	18.2	-31.4	+3
4M+	30.0	+2.4	+1	18.2	-33.4	0
4T-	33.3	-1.6	-5	18.2	-31.2	+3
4T+	32.4	+2.5	+1	18.2	-33.0	0

The acceptance criteria for the heat capacities and heats of reaction stipulated that the mean instantaneous agreement between the experimental and predicted integral of the heat flow rate remain less than 5%. The heat capacity of the unreacted components, the residual mass component, and the heats of all reactions were independently proportionally modified to yield heat flow rate curve predictions that were at the positive and negative limits of the acceptance criteria. These values were used to parameterize a bench-scale model and the resulting agreement between the model prediction and mean experimental data from heat fluxes of 40 and 80 kW m^{-2} were assessed. The results of this sensitivity analysis are presented in Table 4.3.

Table 4.3. Results of Sensitivity Analysis Analysis Investigating the Effect of the Acceptance Criteria for the Heats of Reactions and the Heat Capacities on the Agreement Between Experimental and Predicted Bench-scale *MLR* data

	Final	c_{virgin}^{+}	c_{virgin}^{-}	$c_{residual}^{+}$	$c_{residual}^{-}$	Δh_r^-	Δh_r^+
Mean Instantaneous Error in heat flow rate curve [%]	8.4	9.7	10.4	19.2	17.5	13.9	18.0
	40 kW m^{-2}						
Mean Instantaneous Error in *MLR* [%]	28.8	24.4	28.8	24.4	27.8	23.1	34.8
Error in Maximum *MLR* [%]	-0.8	3.4	-4.1	2.8	-3.1	6.2	-11.1
Error in Time to Maximum *MLR* [s]	-4	-10	+5	0	-9	-7	+2
	80 kW m^{-2}						
Mean Instantaneous Error in *MLR* [%]	18.2	17.3	20.8	18.5	20.6	18.3	22.6
Error in Maximum *MLR* [%]	-32.1	-34.8	-28.9	-33.8	-29.6	-34.7	-27.4
Error in Time to Maximum *MLR* [s]	+2	0	+4	+2	+1	+1	+4

At the low heat flux condition, an increase in the heat capacity was found to improve the mean instantaneous error in the *MLR* curve and a decrease improved the agreement for the high heat flux scenario. An increase in the heats of reaction was found to have the most significant effect on the bench-scale *MLR* by increasing the mean instantaneous error by 6% at 40 kW m^{-2} and 4.4% at 80 kW m^{-2}. The time to the peak *MLR*

for both heat flux conditions was largely unaffected by changes in the energetic parameters, with the most significant effect coming from the upper limit of the heat capacity of the unreacted component and the lower limit of the heat capacity of residual component. The effect of varying the energetic parameters to the limits of the acceptance criterion indicates that the criterion is likely appropriate for this particular case.

The criterion for acceptance of the thermal conductivity definition in the inverse analysis described in Section 4.2.5.2 dictates that the mean relative error between the experimental and predicted back surface temperature must remain within the mean scatter of the experimental temperature data. The thermal conductivity definitions for the unreacted component and the residual mass component were modified to the limits of scatter in the back surface temperature data and the effect on the model predictions at all tested heat fluxes was assessed. The thermal conductivity values for the unreacted components were increased by 2.5% and decreased by 3% and the values for the residual component were increased and decreased by 5% to achieve the limits of the acceptance criterion. Table 4.4 shows the results of the analysis.

By increasing the thermal conductivity of the unreacted component to its upper limit, the mean instantaneous error in the *MLR* prediction was increased at 40 and 60 kW m^{-2} by 4.9% and 7.4%, but agreement was improved at 80 kW m^{-2} by 0.3% and the opposite effect appeared to occur when decreasing the thermal conductivity of the unreacted components to its lower limit. The thermal conductivity of the residual components had little effect on the *MLR* predictions and the mean instantaneous error in the sample back temperature was largely unaffected by modifications to the thermal conductivities. The deviations from the final model produced when modifying the thermal conductivities are

reasonable and this indicates that the acceptance criterion for the thermal conductivities is justified.

Table 4.4. Results of Sensitivity Analysis Analysis Investigating the Effect of the Acceptance Criteria for the Heats of Reactions and the Heat Capacities on the Agreement Between Experimental and Predicted Bench-scale *MLR* data

	Final	k^{+}_{virgin}	k^{-}_{virgin}	$k^{+}_{residual}$	$k^{-}_{residual}$
	40 kW m^{-2}				
Mean Instantaneous Error in *MLR* [%]	28.8	33.7	27.1	28.5	28.6
Error in Maximum *MLR* [%]	-0.8	-5.9	5.2	-1.7	0.2
Error in Time to Maximum *MLR* [s]	-4	-1	-11	-7	-1
Mean Instantaneous Error in T_{back} [%]	0.8	1.0	0.8	0.8	1.0
	60 kW m^{-2}				
Mean Instantaneous Error in *MLR* [%]	21.5	28.9	21.9	22.4	21.0
Error in Maximum *MLR* [%]	-15.9	-12.3	-20.1	-14.9	-16.9
Error in Time to Maximum *MLR* [s]	-10	-9	-8	-11	-5
Mean Instantaneous Error in T_{back} [%]	4.2	4.4	4.7	4.7	3.6
	80 kW m^{-2}				
Mean Instantaneous Error in *MLR* [%]	18.2	17.9	19.6	18.3	18.4
Error in Maximum *MLR* [%]	-32.1	-29.5	-35.1	-31.4	-32.8
Error in Time to Maximum *MLR* [s]	+2	+1	+4	+1	+2
Mean Instantaneous Error in T_{back} [%]	5.9	6.1	5.6	6.6	5.2

Section 4.4: Previous Studies to Construct Complete Pyrolysis Models

The importance of the pyrolysis process has not been lost on a large contingent of the fire research community. Though gas-phase phenomena have been studied overwhelmingly more often than solid-phase phenomena, there have been several extensive efforts to study the major processes that dictate pyrolysis that have included construction and parameterization of pyrolysis models. Many such studies have been completed, drawing from several of the researchers referred to in preceding sections of this chapter and those that made the most significant contributions have been discussed in this section.

Salvador et al. developed a one-dimensional model to describe the combustion of a porous homogeneous medium composed of cardboard and polyethylene [132]. To facilitate the construction of the model, the investigators made several assumptions. The main assumptions built in to the model were that local thermal and chemical equilibrium was achieved and oxidation did not occur in the condensed phase material. The investigators also chose to neglect the heat flux contribution from the flame. The target data identified in this study was the mass loss rate profile collected in cone calorimeter tests. The model was validated by comparing predictions to the temperature profiles collected during cone calorimeter tests.

Chaos et al. conducted an investigation to construct complete pyrolysis models for single-wall corrugated cardboard and chlorinated poly-vinyl chloride (CPVC) [122]. The investigation consisted of FPA tests on coupon-sized samples of each material at heat fluxes of 20, 60, and 110 kW m^{-2}. Mass loss rate data for each of the materials was used as target data in a curve-fitting procedure that used a Shuffled Complex Evolution (SCE)

algorithm to determine eleven parameters required to model pyrolysis of each material. The density of the undegraded material was directly measured, and the thermal conductivity, heat capacity, and emissivity of the virgin material and the char, the density of the char, and four parameters associated with the kinetics and energetics of thermal degradation were determined with the optimization algorithm. Surface temperature measurements were found to be in satisfactory agreement with the model predicted surface temperatures at the heat fluxes tested. This study employed the common approach of applying a genetic algorithm to curve-fit mass loss rate data and extract effective properties for a pyrolysis model. A common criticism of this and similar methodologies is the uncertainty about whether it is possible to apply the effective properties determined with the optimization algorithm to situations outside the calibration conditions.

Stoliarov et al. conducted an investigation to develop complete pyrolysis models for two common charring polymers, bisphenol A polycarbonate (PC) and poly-vinyl chloride (PVC) [25]. The investigation employed TGA and DSC data to determine the reaction kinetics and energetics for the pyrolysis process, MCC to determine the heat of complete combustion of the gaseous pyrolyzate, and cone calorimeter tests to supply heat release rate curves for validation of the constructed models. A single reaction was used to describe the thermal degradation of PC, and two consecutive first-order reactions described the thermal degradation of PVC. TGA tests were conducted at heating rates of 10 and 30 K min^{-1}. It was determined that significantly different kinetic parameters accurately described each of the curves, but the authors showed that these differences in the kinetic parameters had little effect on the predicted cone calorimeter heat release rate curves.

The densities of the polymers were directly measured, and the thermal conductivities, heat capacities, reflectivities, and absorption coefficients were determined through an extensive literature review. The heat capacity and thermal conductivity values used in the model were calculated as the average in the temperature range between room temperature and the decomposition temperature and it was determined that substituting constant values for temperature-dependent property values had no effect on the simulations. The structure of the char was assumed to be similar to graphite, and the heat capacity and reflectivity was defined as an average value of char in the range of 700 to 1100 K, while the density and thermal conductivity of the char were determined through inverse analyses of cone calorimeter heat release rate curves. The models constructed for each polymer were able to predict results of cone calorimetry tests conducted on charring and intumescing polymers at a range of conditions outside those used to calibrate the models. This study provides precedence for several of the assumptions made in the current investigation and proves the usefulness of a generalized methodology in parameterizing predictive pyrolysis models.

Marquis et al. conducted an investigation that involved the development of a CFD solver-coupled pyrolysis model for a balsa wood and fiber reinforced polymer (FRP) sandwich structure composite material [10]. The kinetic reaction parameters and energetics of the degradation were determined with a genetic algorithm applied to data collected in TGA and DSC tests. The thermo-physical properties used to describe each component were inferred from individual standard test methods. Simulations were conducted to predict the mass loss rate and heat release rate of the material at five scales, ranging from sample sizes on the order of 10 mg up to full scale (more than 50 kg). The authors found deficiencies in

the model when attempting to predict flame spread for intermediate to large scale geometries because of the increased influence of non-one-dimensional behavior at larger scales. The model captured the overall fire growth in a full-scale test up to the point of flashover, which the authors attributed to an accurate representation of the thermal degradation kinetics. This study exhibits the powerful prediction capability of a model for a composite, in which each component was characterized individually. The implication of this investigation as it pertains to the current study is the possibility that full-scale model predictions can be made by characterizing a complicated composite at the milligram- and bench-scale.

A recent study by Tsoi et al. attempted to develop a model to capture the thermal degradation of FRP composites and validate the model with experimental data collected with the cone calorimeter [9]. The authors developed a single-layer, homogeneous model as well as a zonal model with alternating layers of polyester resin and resin-infused glass mat. Both models were based on a pyrolysis model formulation from literature, and all the property values were adopted from the same reference with few modifications. The cone calorimeter experiments were conducted according to the standard test method, which resulted in a condition with flame covering the surface of the sample through most of the test, which served to complicate the agreement between the model and the experimental data. By slightly modifying the model, the authors were able to predict the upper surface and midplane temperatures collected in the experiments well, although agreement between the measured and modeled mass loss rate and back surface temperatures were not consistent. It is likely that better model predictions could have been achieved by parameterizing the model with thermo-physical property values specific to the sample

material and by defining finite-rate reaction kinetics to describe the thermal degradation of the FRP composite.

Li et al. have conducted studies in which complete pyrolysis models were parameterized for charring [133] and non-charring polymers [121]. The kinetics and thermodynamics of thermal degradation were determined through inverse analyses of experimental data collected in differential scanning calorimetry and thermogravimetric analysis tests conducted simultaneously. The reaction mechanisms determined in these analyses included one to four consecutive reactions. The thermal conductivity of each of the polymers was determined throughout degradation through inverse analyses of back temperature data collected in bench-scale gasification tests. The predictions produced with the fully parameterized models agreed well with experimental data, although there were some complications with intumescence for some of the charring polymers that affected agreement.

The studies explored in this section demonstrated a range of techniques to determine the full set of parameters required to define a material in a comprehensive pyrolysis model. Some of the measurement and estimation techniques mentioned in these studies are utilized in the current investigation in addition to some techniques that have not been used previously. An alternative to direct and indirect measurement of properties presented in this section is the use of genetic algorithms to determine property values from target bench-scale mass and temperature data. Though these methods appear to be more efficient than measurements, there are also well-known issues with these techniques that prevent them from being adopted as a standard method for parameterizing pyrolysis models that have been elucidated by Webster et al. [6].

Chapter 5: Corrugated Cardboard

Section 5.1: Introduction

This chapter presents the development of a one-dimensional pyrolysis model for corrugated cardboard and the contents of this chapter were modified from a more detailed publication [134]. One of the major obstacles faced when investigating this material was the complicated, non-one-dimensional geometry. An objective of this study was to determine the level of geometric complexity required in the model to adequately describe the complicated pyrolysis behavior of the material. Data collected in milligram-scale tests were analyzed to determine an effective reaction mechanism, the thermodynamic properties of the material components, and the energetics associated with the thermal degradation process. An iterative inverse analysis was conducted on data obtained in cone calorimeter experiments to infer the thermal transport properties for the corrugated cardboard and its products of degradation. These measured and inferred properties were used as parameters to define the corrugated cardboard material in the pyrolysis model.

Analysis of the collected data and the subsequent definition of the model parameters are presented through a logical progression in which a single parameter (or a set of related parameters) is determined through each experimental method. These parameters are used to develop a model aimed at predicting the results of cone calorimeter tests [135] with incident heat flux set points ranging from 20 to 80 kW m^{-2}. Validation of the constructed pyrolysis model is provided through a comparison against the mass loss rate (*MLR*) and heat release rate (*HRR*) histories collected in these tests. It is important to note that these histories are not utilized in the model parameterization.

The ThermaKin modeling environment [22] was used in this investigation during analysis of experimental data to extract chemical and thermo-physical property values and

was ultimately employed to construct a one-dimensional pyrolysis model to predict the results of cone calorimetry tests. Heat was transferred to the material with a radiation boundary condition set to the external heat flux of the cone calorimeter tests. As the sample surface was heated, convective cooling to the atmosphere occurred, which was defined by a convection coefficient of 10 W m^{-2} K^{-1} and a constant ambient temperature of 300 K [136]. The cooling was turned off and additional heat flux was turned on when the mass flux at the boundary reached a critical value representing piloted ignition of the sample. The values of parameters describing the ignition process are provided as they become relevant.

Section 5.2: Experiments and Analysis

Section 5.2.1: Material and Sample Preparation

The samples specific to this study were double-wall cardboard designated as 69-23B-69-23C-69. Figure 5.1 displays a schematic representation of these samples. The numbers in the cardboard designation refer to the areal density of the layer in lb per 1000 ft^2. The letters signify the flute designation. B-flute is characterized by 160 ± 10 flutes per m and a layer height of 2.1 ± 0.2 mm. C-flute is characterized by 132 ± 10 flutes per m and a layer height of 3.4 ± 0.2 mm.

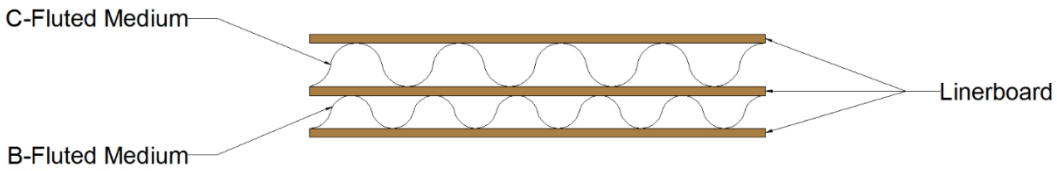

Figure 5.1. Schematic representation of the corrugated cardboard samples used in the current investigation

The thickness of the linerboards was measured as 0.64 ± 0.03 mm. The density of the linerboards (ρ_{LB}) was calculated as approximately 520 kg m^{-3}. The composite density of the fluted layers was defined as the mass of the fluted medium over the volume of the entire layer. The composite density of the C-fluted section (ρ_{CFL}) was measured as 49 kg

m^{-3} and the density of the B-fluted section (ρ_{BFL}) was measured as 74 kg m^{-3}. The uncertainty in the densities of the linerboard and fluted layers was estimated as ± 10%.

STA and MCC tests comprise the milligram-scale experiments conducted during this investigation. These experiments require approximately homogeneous samples with masses between 2 and 10 mg. A thoroughly cleaned file was used to grind the edge of a corrugated cardboard specimen to generate powder, which was subsequently compacted into a thin (< 1 mm), flat disk to form these samples. Preliminary STA tests performed on samples prepared from individual cardboard layers indicated that these layers have identical chemical composition (same mass loss versus temperature profiles). Therefore, all thermal analysis results reported in a later section were obtained for a mixture of the linerboards, C-fluted medium and B-fluted medium.

All bench-scale tests were conducted in a cone calorimeter and used octagonal corrugated cardboard samples oriented such that the C-fluted layer was closest the cone heater. Figure 5.2 shows a schematic of the plan view of a sample prepared and mounted for bench-scale testing with the dimensions of the sample provided. The octagonal samples were used instead of standard square samples [135] to minimize the impact of spatial variation in radiant heat flux from the cone heater. The cardboard samples used in all tests (including milligram-scale experiments) were allowed to dry in a desiccator in the presence of Drierite for a minimum of 48 hours before testing to obtain measurements with little contribution from moisture.

The cone calorimetry samples were wrapped in heavy gauge aluminum foil such that one face of the sample could accept a radiant heat flux. The sample was placed on top of 30 mm of Kaowool PM insulation and positioned 25 mm from the cone heater surface.

Kaowool PM insulation was chosen as the backing for bench-scale tests because its thermo-physical properties are well-established [137]. Steel wires were used at each of the corners of the samples to mount the sample to the holder. The choice to use these wires is discussed in a later section.

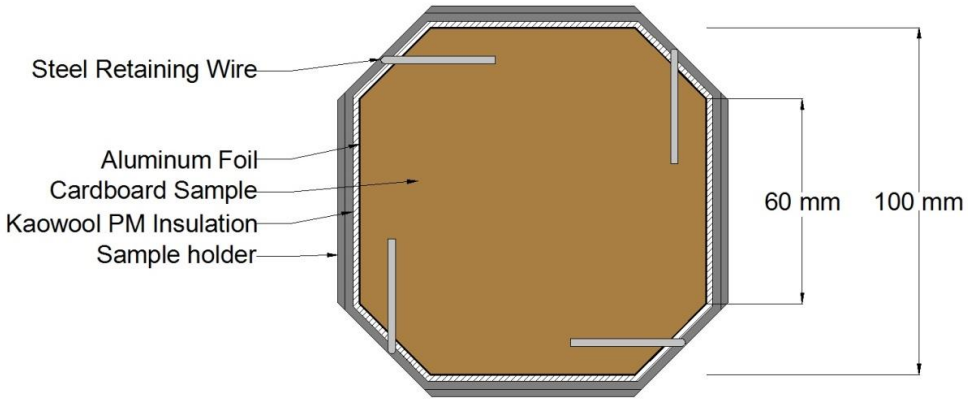

Figure 5.2. Plan view drawing of sample prepared and mounted for bench-scale testing

Section 5.2.2: Milligram-scale Testing

MLR and heat flow rate data were collected on the corrugated cardboard samples as a function of temperature through STA tests following the procedure described in Section 4.2.1.1. The temperature program for the STA tests consisted of a conditioning period when the temperature of the sample was held constant at 313 K for 20 min, followed by heating to 1113 K at a rate of 10 K min^{-1}. The heat of the overall degradation process and the heat capacities of the virgin cardboard material and solid degradation products (char) were determined from heat flow rate data collected in STA tests. Three additional tests were conducted with a heating rate of 5 K min^{-1} and the same heating program temperatures to examine the generality of the reaction mechanism derived from the 10 K min^{-1} tests.

MCC tests were conducted to determine the heats of complete combustion of the gaseous pyrolyzate produced in each thermal degradation reaction observed in the STA tests. The sample masses were around 4 mg for the MCC experiments to minimize the effects of mass and temperature gradients in the samples. Five MCC tests were conducted in nitrogen with a heating program from 373 to 1073 K and a heating rate of 60 K min^{-1}.

Section 5.2.3: Bench-scale Testing

A cone calorimeter allows a set, constant radiant heat flux to be applied to a tile-like material specimen while the *MLR* and *HRR* of the sample are recorded. Govmark CC-1 cone calorimeter was utilized in this investigation. This apparatus was calibrated before each day of testing according to the standard procedure [135]. All bench-scale tests employed a spark igniter 12 mm from the surface of a horizontally mounted sample unless otherwise noted. Five tests were conducted to measure the *HRR* and *MLR* of the cardboard samples at each heat flux of 20, 40, 60, and 80 kW m^{-2}.

The radiant heat flux incident to the sample was automatically set for each test according to a feedback control system built into the calorimeter. A Schmidt-Boelter heat flux gauge was oriented such that its sensing surface was the same distance from the heater as the upper surface of the sample during testing (25 mm). The control system for the heater adjusted the temperature of the heater based on the signal from the heat flux gauge.

It was observed during preliminary tests that layers of the corrugated cardboard tended to peel away from the sample as the adhesive binding the layers degraded at high temperatures. Delamination and exfoliation of layers resulted in poor reproducibility of *MLR* data. Several solutions were considered to eliminate exfoliation or minimize its effect during testing. It was decided that the method of preventing exfoliation that introduced the

smallest mass to the system and obscured the sample surface least would also introduce the smallest amount of uncertainty and error. The method adopted for all tests consisted of the sample held in place with four 1.7 mm diameter steel wires located at the corners of the sample.

A 6.4-mm diameter water-cooled Schmidt-Boelter heat flux gauge was embedded in the corrugated cardboard for several bench-scale tests. The intended purpose of these tests was to measure the heat flux generated by the flame that was incident to the cardboard surface. The magnitude of the flame heat flux is a parameter required for the modeling of flaming combustion. The heat flux gauge was oriented such that the surface of the gauge was flush with the sample surface. Three tests were conducted at cone heater fluxes of 20 and 60 kW m^{-2} and the heat flux gauge in two locations to provide insight about the spatial variation of the heat flux fed back to the sample surface due to the presence of the flame. The heat flux gauge was positioned in the center of the sample and close to the edge of the sample. *MLR* and *HRR* data were not collected during the tests with the heat flux gauge embedded in the samples because preliminary tests indicated that the presence of the gauge resulted in unreliable mass loss information.

Tests were conducted to determine whether the cardboard material transmitted thermal radiation according to the procedure described in Section 4.2.4.1. A single (0.64 mm thick) linerboard layer was inserted between the cone heater set to produce a heat flux of 40 kW m^{-2} and a free-standing heat flux gauge to measure the transmitted radiant heat flux.

Bench-scale tests were conducted with 0.25 mm diameter, grounded type K thermocouples inserted in each of the three linerboard sections at a central point such that

the bead of the thermocouple was located at the approximate middle of the double-wall cardboard specimen and the thermocouple wire was perpendicular to the main direction of heat flow. Five tests were conducted on the unaltered samples at each incident heat flux of 20 kW m^{-2} and 60 kW m^{-2}. Five tests were also conducted on samples with the surface painted black to define the surface emissivity as 0.95 at an incident heat flux of 20 kW m^{-2}. High emissivity spray paint supplied by Medtherm was used in these experiments. The spark igniter was not used in the tests with the surface painted in an effort to increase the amount of time the thermocouples collected meaningful data before structural degradation led to the displacement of the thermocouples. *MLR* and *HRR* data was not collected during the tests with thermocouples.

Section 5.3: Analysis and Model Development

Section 5.3.1: Milligram-scale Data Analysis and Model Construction

Figure 5.3 presents the mean thermogravimetric data collected in five TGA tests conducted with a heating rate of 10 K min^{-1}. The mass and *MLR* data are normalized by the initial sample mass, m_0. The mass loss rate was consistent between individual tests with an average of 3% instantaneous deviation. The deviations appeared to be random noise partially amplified by the numerical differentiation of the total mass data to produce the mass loss rate plots.

Three distinct processes can be observed in the TGA data. The first occurred in the range of 325 – 385 K and was attributed to the evaporation of residual moisture from the sample. Residual moisture is defined in this study as the moisture retained by the sample after drying in the desiccator. The second process was evidenced by the large peak in the *MLR* curve ranging 500 – 650 K which corresponded to volatilization of the majority of the mass of the sample. The final process started at approximately 650 K and finished at

approximately 850 K, generating a tail that slowly approached a mass loss rate of zero as the sample pyrolyzed to yield a final char in the amount of approximately 18.5% of the original mass.

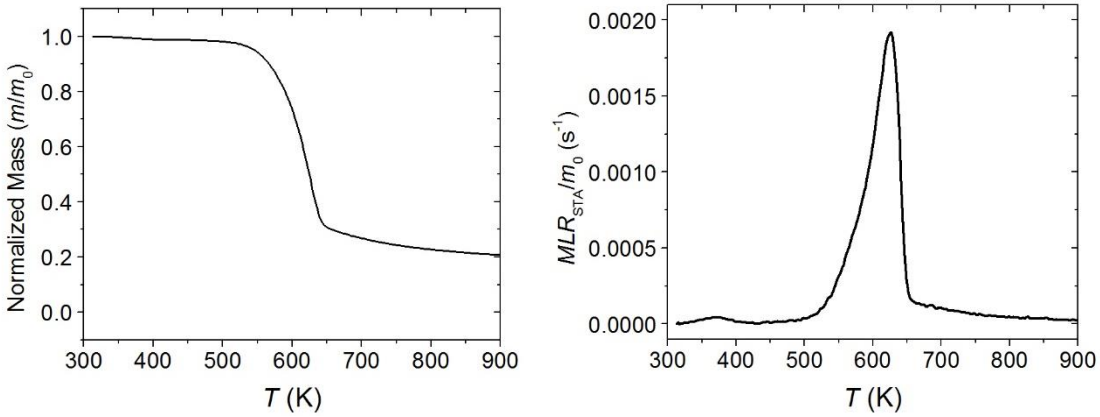

Figure 5.3. Experimental TGA data collected in nitrogen at a heating rate of 10 K min^{-1} presented as (a) normalized total mass (b) normalized mass loss rate

The TGA data were analyzed to determine the reaction mechanism of the thermal degradation process. The reaction mechanism was assumed to consist of sequential, first-order reactions with one solid and one gaseous product. The reaction parameters (E, A, and ν) were obtained by fitting the TGA data with the ThermaKin model of mg-scale experiments. A detailed explanation of this fitting procedure is provided in Section 4.2.1.1. The reaction mechanism was intended to mathematically mimic the m_{TGA} and MLR_{TGA} data using the minimum number of reactions possible. No attempt was made to identify the actual chemical species produced in the cardboard degradation.

A four-reaction mechanism was found to reproduce the experimental TGA curves. The quality of the agreement is demonstrated by Figure 5.4. The average deviation between the experimental and predicted mass loss rate was found to be 13%. Table 5.1 displays the fitted reaction kinetics and other reaction parameters. The values of the heat of reaction (h_r) and the heat of combustion (h_c) given in the table were determined from the analysis presented later in this section.

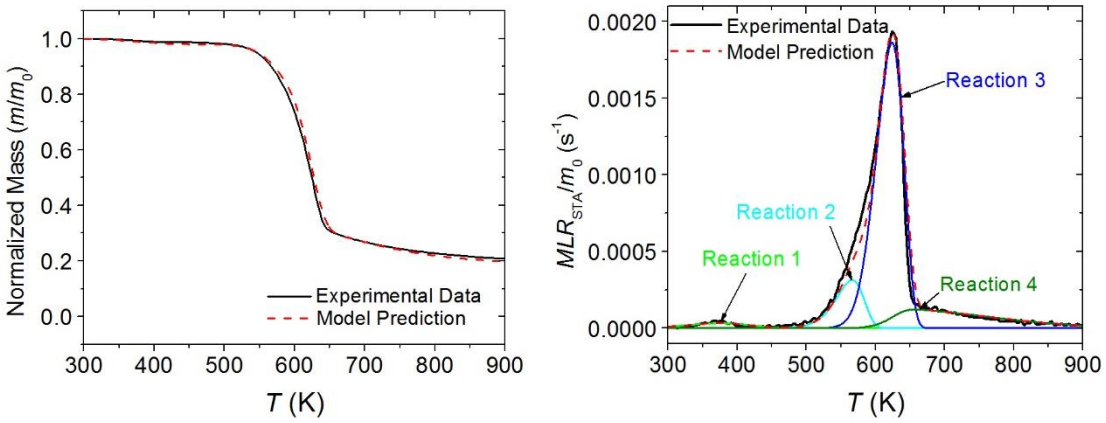

Figure 5.4. Experimental (solid lines) and simulated (dashed lines) TGA data collected in nitrogen at a heating rate of 10 K min^{-1} and presented as (a) normalized total mass and (b) normalized mass loss rate.

Table 5.1. Parameters of cardboard degradation reactions

Reaction	A (s^{-1})	E (J mol^{-1})	ν	h_r (J kg^{-1})	h_c of gas product (J kg^{-1})
1	6.14	2.35×10^4	0	-2.45×10^6	0
2	7.95×10^9	1.30×10^5	0.90	0	1.85×10^7
3	2.00×10^{11}	1.60×10^5	0.37	-1.26×10^5	1.36×10^7
4	2.61×10^{-2}	1.70×10^4	0.59	0	1.40×10^7

Figure 5.4 also displays contributions of individual reactions to the total mass loss. Reaction 1 corresponds to the liberation of residual moisture in the virgin material. According to the TGA data, about 2% of the initial material mass is H_2O. Reactions 2 and 3 describe the large peak in the MLR_{TGA} curve. The solid material produced in reaction 2 is described by a generic intermediate species that is consumed in reaction 3 to produce an intermediate char. These intermediate species are identified in this chapter with the subscripts *int* and *char*1, respectively. Reaction 4 corresponds to the gradually decreasing tail of the MLR_{TGA} curve in which the intermediate char is degraded to the final char, which is identified with the subscript *char*2.

To examine generality of the formulated reaction mechanism and kinetic parameters, they were used to simulate TGA experiments performed with a heating rate of 5 K min^{-1}. A comparison of the results of these simulations with the mean of three

experiments performed at the same heating rate is shown in Figure 5.5. The average instantaneous deviation between the prediction and the experimental data is below 2%, which indicates that the reaction mechanism instituted in the model is valid over a range of heating rates. No higher heating rate TGA experiments were performed to test the reaction model because, even after compacting, the cardboard samples were highly porous and resistant to heat flow and it was hypothesized that high heating rate tests would not yield accurate *MLR* curves

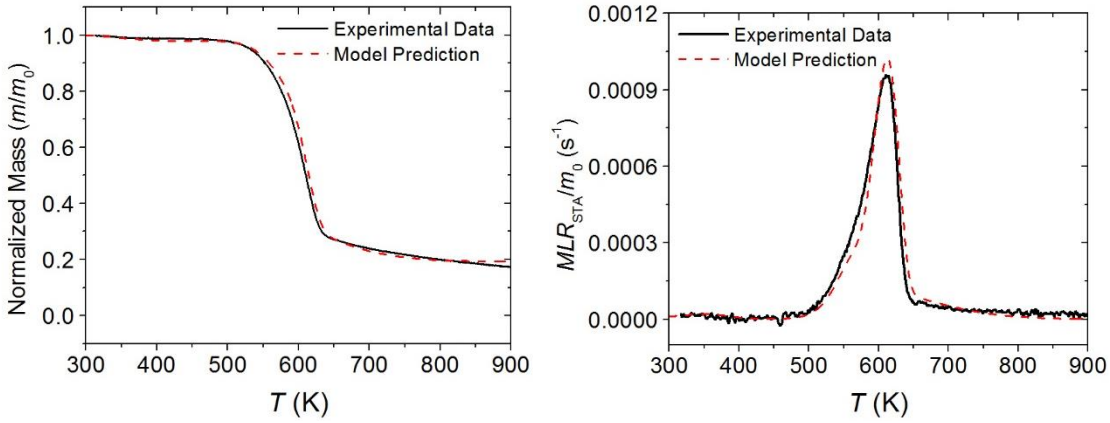

Figure 5.5. Experimental (solid lines) and simulated (dashed lines) TGA data collected in nitrogen at a heating rate of 5 K min^{-1} and presented as (a) normalized total mass (b) normalized mass loss rate

Figure 5.6 shows the mean heat flow data from five DSC tests. This data represents sensible enthalpy changes and reaction heats associated with the thermal degradation process. The initial drop in the heat flow, at 313 – 350 K, is a result of a gradual increase in the STA furnace heating rate to its set point value (10 K min^{-1}). The average scatter between the five tests was significant, approaching 25% of the instantaneous mean. The reason for this scatter is essentially the same as the reason why higher heating rate TGA experiments were avoided in this study: the nature of the material made it very difficult to ensure a good thermal contact between the sample and the crucible and within the sample. The DSC measurements are highly sensitive to the quality of this contact [88].

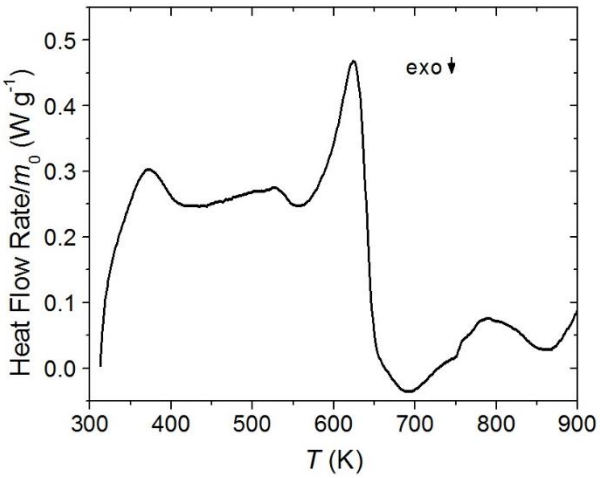

Figure 5.6. Experimental DSC data collected in nitrogen at a heating rate of 10 K min^{-1}. Exo is down.

The DSC heat flow curve was normalized by the instantaneous heating rate. A region of this curve between the release of moisture and the onset of the first degradation reaction, 400 – 540 K, was identified as the most representative range to describe the heat capacity of the dried virgin cardboard (c_{CB}). The value of c_{CB} was assumed to be independent of temperature and was assigned the mean of the normalized heat flow in this range, 1.8 J g^{-1} K^{-1}. The normalized heat flow values in the range of 700 – 870 K were considered the steadiest portion of the DSC data when only char (primarily *char*2) was present. The mean of the heat flow in this range renormalized by residual mass was specified as the heat capacity of the char: $c_{char1} = c_{char2} = 1.3$ J g^{-1} K^{-1}.

The heat capacity of the intermediate solid species (c_{int}) could not be determined from the DSC test data because this intermediate existed only during the chemical degradation, at 500 – 650 K (see Figure 5.4). Therefore, this heat capacity was assumed to be the mean of the virgin cardboard and char heat capacities. The heat capacities of liquid water (representing residual moisture in the virgin cardboard) and water vapor were taken from the literature [138]. The heat capacities of the gaseous volatiles produced in the degradation reactions (Reactions 2-4) were assumed to be equivalent to the heat capacity

of the char. The values of these heat capacities had no impact on the modeling of milligram-scale experiments and a minor impact on the modeling of bench-scale tests because of the fast transport assumption implemented in these models.

The heat of overall degradation of the corrugated cardboard was determined from the DSC data as follows. A baseline curve was constructed to represent the sensible enthalpy of the material through the procedure described in Section 4.2.2.1. Figure 5.7 shows the baseline as well as the integral of the heat flow curve that was defined as the heat of the overall degradation process. The abscissa of Figure 5.7 has a time scale as opposed to a temperature scale to make the baseline and integral easier to calculate.

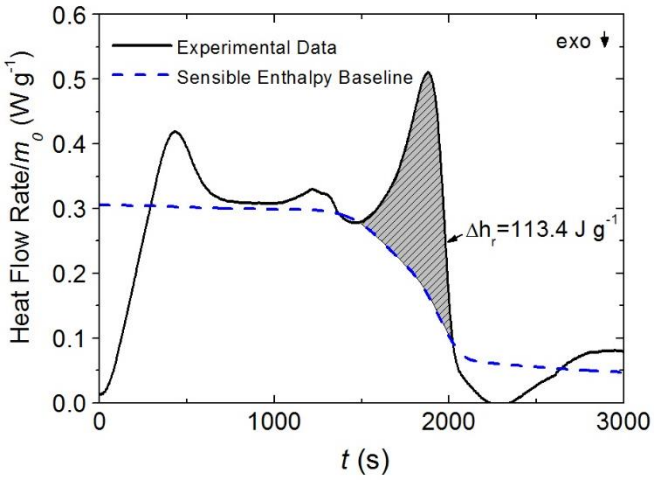

Figure 5.7. Experimental DSC heat flow data (solid line) and modeled sensible heat baseline (dashed line). Exo is down. The area corresponding to the heat of overall degradation is highlighted

The heat of the overall degradation process was renormalized by the total mass of the solid intermediate species produced by Reaction 2 and assigned to Reaction 3 because this reaction was responsible for the majority of the mass loss. The reaction corresponding to the evaporation of moisture (Reaction 1) was assigned a heat of reaction equal to the enthalpy of vaporization for water [138]. The remaining decomposition reactions were assumed to have zero reaction enthalpies. The reaction heats are listed in Table 5.1.

Figure 5.8 displays a comparison between the experimental heat flow and the curve generated by the ThermaKin program, accounting for the reaction mechanism, heat capacities for each component, and the heats of reaction. The predicted heat flow curve overestimates the total energy transferred to the sample heated from 313 to 900 K by approximately 4%.

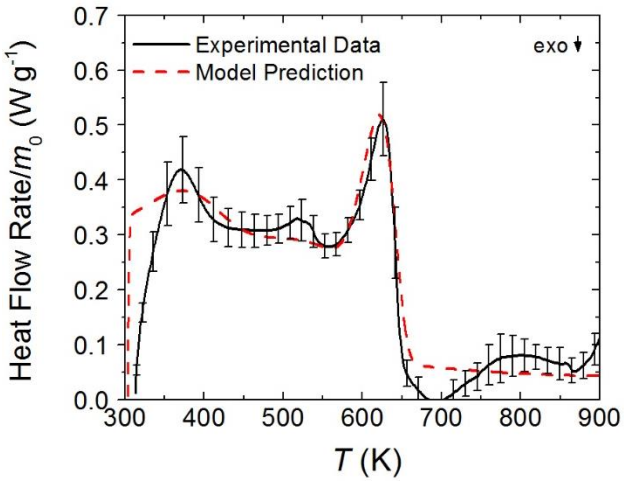

Figure 5.8. Comparison of the experimental (solid line) and simulated (dashed line) DSC heat flows collected in nitrogen at a heating rate of 10 K min^{-1}. Exo is down

The MCC data was also analyzed using the reaction model developed on the basis of STA experiments. ThermaKin was employed to simulate 60 K min^{-1} linear heating of the MCC tests. The analysis procedure used to determine the heats of complete combustion of the pyrolyzate species was described in Section 4.2.3.1. An effort was made to generate similar *HRR* shapes, while keeping the integral of the experimental curve equal to that of the model prediction instead of attempting to precisely reproduce the experimental *HRR* curve. The resulting heats of combustion are provided in Table 5.1.

Figure 5.9 shows the mean *HRR* obtained by averaging the results of five MCC tests and the predicted curve. The average scatter between the experiments was approximately 12% of the instantaneous mean. Although there was a significant scatter in

the instantaneous HRR_{MCC} values, the integrals of individual curves were within less than 5% of each other.

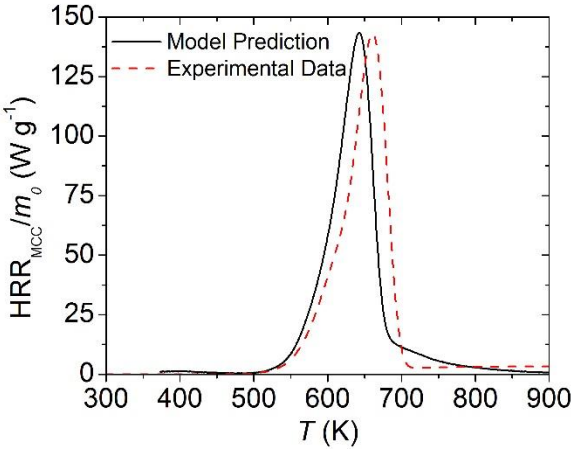

Figure 5.9. Comparison of experimental (solid line) and simulated (dashed line) MCC experiments performed at a heating rate of 60 K min^{-1}.

Section 5.3.2: Bench-scale Data Analysis and Model Construction

The structure of corrugated cardboard presents a modeling challenge because of the presence of complex, low-density layers consisting of the non-planar fluted medium (see Figure 5.1). In an initial attempt to circumvent this complexity, the model of bench-scale experiments was formulated using a homogeneous representation of the cardboard samples. The samples were assumed to be a mixture of uniformly distributed cardboard component (*CB*) and residual moisture (H_2O_ℓ). These samples were characterized by a single, effective density. The results obtained with this model led to the conclusion that the experimental in-depth temperature profiles (discussed later in this section) could not be captured without accounting for the density differences between the linerboard and fluted layers. Therefore, a non-homogeneous model was developed.

In the non-homogeneous model, the geometry of the sample was defined with three initial components: the linerboard (*LB*), C-fluted medium (*CFL*) and B-fluted medium (*BFL*). The densities of these components were set to be equal to the composite densities

of the corresponding layers (reported in Section 5.1.1). Figure 5.10 shows a schematic of the geometry of the sample including a representation of the backing material (Kaowool PM). Each of the cardboard layers defined in this model was also specified to contain 2% of H_2O_ℓ component, which was assumed not to contribute to the material volume. The amount of moisture was determined from the TGA measurements discussed in the previous section. The presence of aluminum foil between the linerboard and Kaowool PM was simulated implicitly by setting all gas transport within the Kaowool to zero.

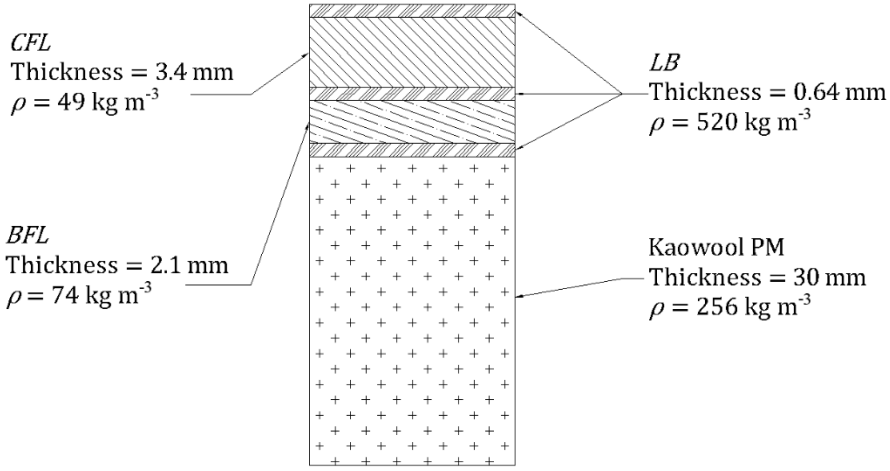

Figure 5.10. Schematic of the virgin cardboard sample defined in the model of bench-scale experiments

The decision to represent cardboard layers with individual components led to an expansion of the thermal degradation mechanism. Each cardboard component that existed after the initial removal of moisture (*LB*, *CFL* and *BFL*) degraded according to the same three-reaction sequence but generated solid intermediate products with different densities, resulting in one reaction for drying and nine degradation reactions. The density of the solid products of degradation of each component was assumed to be equal to the density of the reactant multiplied by the stoichiometric coefficient of the product. This assumption was consistent with the observation that thicknesses of the layers and entire sample did not

change significantly over the duration of the cone calorimetry experiments. The reactions that define the expanded kinetic mechanism are provided as equations 5.1-10. The reaction index (the number over arrow) denotes the corresponding reaction number in Table 5.1.

$$\mathrm{H_2O}_{\ell} \xrightarrow{1} \mathrm{H_2O}_{g} \tag{5.1}$$

$$LB \xrightarrow{2} 0.9LB_{int} + 0.1CB_{vol1} \tag{5.2}$$

$$LB_{int} \xrightarrow{3} 0.37LB_{char1} + 0.63CB_{vol2} \tag{5.3}$$

$$LB_{char1} \xrightarrow{4} 0.59LB_{char2} + 0.41CB_{vol3} \tag{5.4}$$

$$CFL \xrightarrow{2} 0.9CFL_{int} + 0.1CB_{vol1} \tag{5.5}$$

$$CFL_{int} \xrightarrow{3} 0.37CFL_{char1} + 0.63CB_{vol2} \tag{5.6}$$

$$CFL_{char1} \xrightarrow{4} 0.59CFL_{char2} + 0.41CB_{vol3} \tag{5.7}$$

$$BFL \xrightarrow{2} 0.9BFL_{int} + 0.1CB_{vol1} \tag{5.8}$$

$$BFL_{int} \xrightarrow{3} 0.37BFL_{char1} + 0.63CB_{vol2} \tag{5.9}$$

$$BFL_{char1} \xrightarrow{4} 0.59BFL_{char2} + 0.41CB_{vol3} \tag{5.10}$$

The cone radiation transmission experiments indicated that even a relatively thin sample of cardboard material (a single linerboard) absorbed all of the non-reflected radiation. Therefore, all cardboard components were defined as non-transparent to the radiation in the model (i.e., all radiation was set to be either absorbed or reflected at the material boundary). Confirmation that the corrugated cardboard did not transmit radiation allowed the surface of the sample to be painted to define its emissivity without concern that applying paint would also affect the in-depth absorption characteristics of the material.

The temperature data with the surface of the sample painted black for an emissivity of 0.95 was collected at a heat flux of 20 kW m^{-2} to isolate the thermal conductivity of the initial components (k_{CB}) as the only unknown parameter that affected the temperature profiles. Although the linerboard layers were physically different from the fluted layers, it was assumed that all the initial components (*LB*, *CFL*, and *BFL*) could be described by a single, temperature-independent thermal conductivity value. Only the data before the onset of mass loss was considered to ensure that only the initial cardboard components were present and all parameters describing the system could be considered invariant. The temperature profile predictions generated by the model were used to infer the thermal conductivity by adjusting the thermal conductivity value to reproduce the experimental temperature curves.

The results of this fitting procedure are shown in Figure 5.11. The discrete data points in the plot correspond to the mean experimental data collected in five tests and the error bars represent two standard deviations of the mean. The solid lines correspond to the model prediction obtained with $k_{CB} = 0.1$ W m^{-1} K^{-1}. The uncertainty in the position of the temperature measurement, ± 0.15 mm, is reflected in the dashed lines. This uncertainty is associated with the difficulty determining precise locations of the thermocouples after their insertion into the linerboard. This convention for uncertainties and error bars is adopted for all plots of temperature shown later in this chapter.

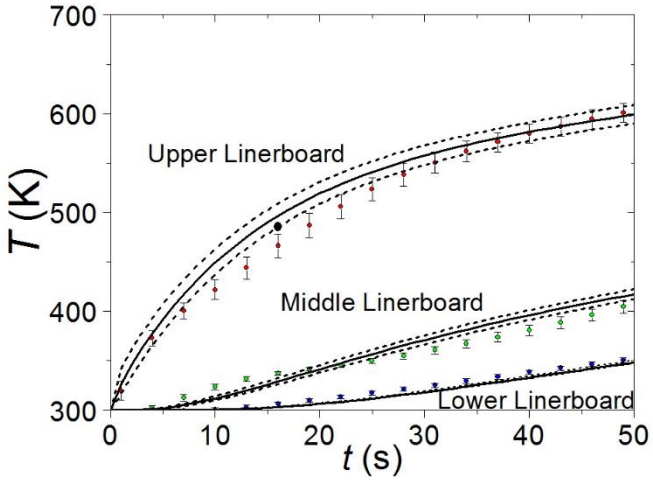

Figure 5.11. Experimental (points with error bars) and simulated (lines) temperature profiles collected in bench-scale tests at an incident heat flux of 20 kW m^{-2}. The sample surface was painted black for an emissivity of 0.95

The same experimental conditions were used to collect temperature data for samples which surfaces were unaltered. These data were employed to obtain the emissivity of the initial components (ϵ_{CB}). ϵ_{CB} = 0.7 was found to provide the best agreement between the experiments and simulations. The quality of this agreement is demonstrated by Figure 5.12.

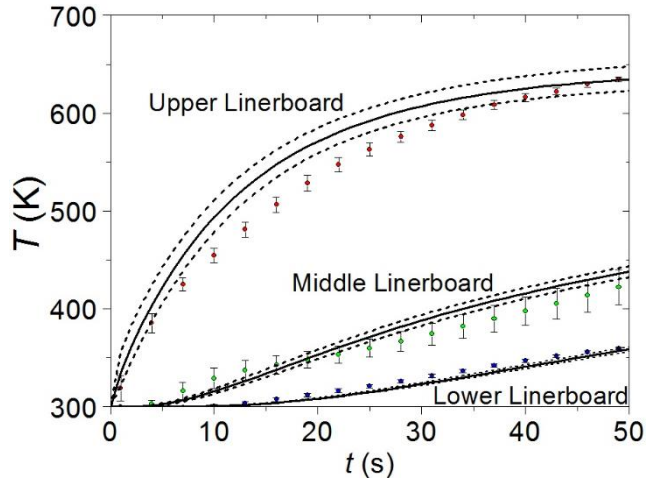

Figure 5.12. Experimental (points with error bars) and simulated (lines) temperature profiles collected in bench-scale tests at an incident heat flux of 20 kW m^{-2} on unaltered samples

Further analysis of the bench scale experiments required that a piloted ignition criterion and changes in the heat flux to the sample associated with the appearance of flame are defined in the model. The ignition was defined using the notion of critical heat release

rate [139] which was converted to the critical mass flux in ThermaKin using given gaseous effluent composition and the heats of combustion reported in Table 5.1. Previous studies indicated that, in horizontal cone calorimetry tests, the critical heat release rate for piloted ignition varies between 10 kW m^{-2} [24] and 20 kW m^{-2} [25]. In this work, the value of 16 kW m^{-2} was adopted because it provided the best match between experimental and simulated temperature profiles discussed later in this section.

The change in the upper surface boundary condition at the point when piloted ignition occurred and the flame covered the surface of the sample was characterized in the model according to the measurements made with a heat flux gauge embedded in the sample. An average curve for the total heat flux incident on the sample surface as a function of time from ignition was generated from the collected data. There was no significant difference between the data collected at the center of the sample and at the edge of the sample. The steady incident heat flux measured before ignition was subtracted from the heat flux evolution profile to obtain the contribution of heat flux from the flame incident on the sample surface. Figure 5.13 shows this contribution obtained at cone heat flux set points of 20 and 60 kW m^{-2} as well as a simplified model representation of the flame flux discussed below.

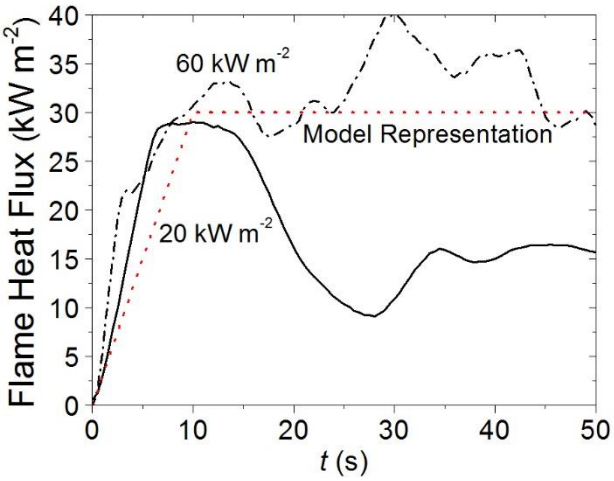

Figure 5.13. Experimental flame heat flux data collected at cone heat fluxes of 20 and 60 kW m^{-2} and model representation of this flame heat flux

Each experimental data set contained a gradual increase to the first peak succeeded by a relatively steady period. The graduate increase approximately reflected the process of flame spreading over the sample surface. The data collected had a notable scatter of about 10% of the instantaneous mean (on average). Observations of the tests conducted at 20 kW m^{-2} of cone heat flux led to the conclusion that the decrease in the flame heat flux occurring at 15-25 s after ignition did not correspond to physical changes observed in the flame structure and was most likely caused by an obstruction of the heat flux gauge with partially delaminated upper cardboard layers. The fluctuations in the flame heat flux observed in the 60 kW m^{-2} experiments after about 10 s after ignition did not exhibit a systematic trend and also lacked any connection to the visual appearance of the flame. Therefore, both of these features were ignored in the construction of the flame representation.

The flame was defined in the model by turning off convective, pre-ignition cooling (see the discussion of ThermaKin in Section 2.3) and applying incident radiative heat flux that was ramped from 0 to 30 kW m^{-2} over 10 s and remained steady until extinction. 30 kW m^{-2} was used for the plateau region because it was the mean experimental heat flux measured between 10 and 50 s after ignition in the 60 kW m^{-2} experiments. This flux was

assumed to be radiative in nature because the flame observed in the cone calorimetry tests was essentially non-transparent and was lifted from the sample surface.

It was hypothesized that at the temperatures where char components (LB_{char1}, LB_{char2}, CFL_{char1}, CFL_{char2}, BFL_{char1} and BFL_{char2}) form during combustion, the heat transfer within these highly porous substances is dominated by radiation. The radiation-diffusion approximation [125] was invoked to describe this transfer using conduction mathematics by defining an effective thermal conductivity as a function of T^3. The coefficient in front of this term was assumed to be inversely proportional to the density of each component. The ratio of densities between the linerboards and the fluted sections was approximated as 10:1 resulting in $k_{LB_{char1}} = k_{LB_{char2}} = \eta T^3$ and $k_{CFL_{char1}} = k_{CFL_{char2}} = k_{BFL_{char1}} = k_{BFL_{char2}} = 10\eta T^3$, where η is an adjustable parameter.

Based on apparent high carbon content of degraded cardboard, the emissivity of all char components was defined as 0.85, which was the emissivity of graphite in the temperature range at which these components were formed [106]. The thermal conductivity and emissivity of the intermediate components (LB_{int}, CFL_{int} and BFL_{int}) were set to be equal to the mean of the thermal conductivities and emissivities of the corresponding char and virgin cardboard components. The only unspecified heat transport parameter, η, was fit to the temperature profile data collected during flaming combustion in bench-scale experiments at a cone heat flux of 20 kW m^{-2}. The fitting results, obtained with $\eta = 1.5\times10^{10}$ W m^{-1} K^{-4}, are shown in Figure 5.14. Note that no attempt was made to fit temperature readings once they exceeded 800 K. At this temperature, the structural stability of the sample was clearly compromised and the thermocouple was likely to be shifted significantly from its original position.

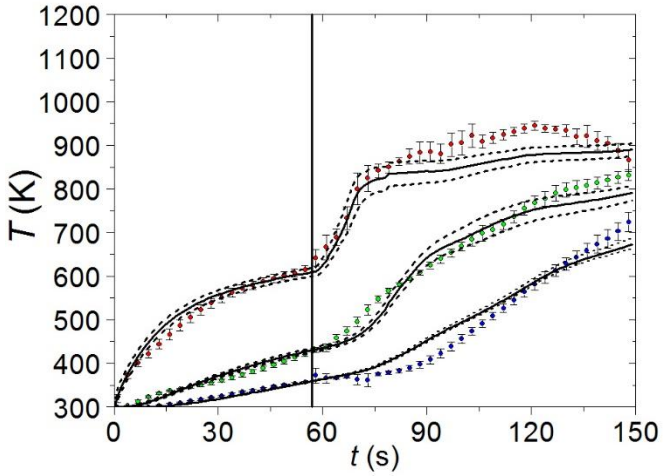

Figure 5.14. Experimental (points with error bars) and simulated (lines) temperature profiles collected in bench-scale tests at a cone heat flux of 20 kW m^{-2} on unaltered samples. The solid vertical line in the plot indicates the time of piloted ignition observed in experiments

The thermal transport property set was validated by simulating bench-scale experiments performed under significantly different heating conditions. The modeled temperature histories obtained at a cone heat flux of 60 kW m^{-2} are compared to the corresponding experimental observations in Figure 5.15. The average instantaneous difference between the model and experiment was less than 8%. This difference is less than 5% for the 20 kW m^{-2} temperature data (shown in Figure 5.14). The consistency between the model prediction and the experimental temperature profiles at both heat fluxes indicated that the thermal transport properties determined through analysis of the bench-scale data were reasonably accurate.

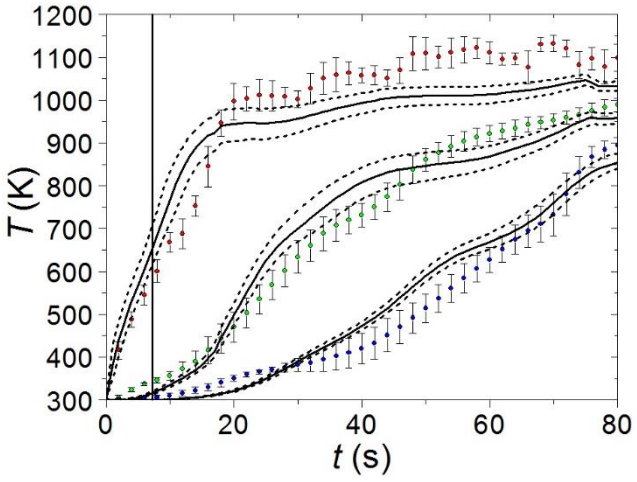

Figure 5.15. Experimental (points with error bars) and simulated (lines) temperature profiles collected in bench-scale tests at a cone heat flux of 60 kW m^{-2} on unaltered samples. The solid vertical line in the plot indicates the time of piloted ignition observed in experiments

A summary of thermo-physical properties describing pyrolysis of the corrugated cardboard is presented in Table 5.2. Although there are 54 property values defined in this table, simplifying constraints imposed on the problem limit the number of independent properties to 14. Note that all independent properties, with the exception of those describing residual moisture, Kaowool PM, and the emissivity of the charring components (which were obtained from the literature), were directly measured or inferred from the data collected in this study. Component properties that are not defined in the table were not utilized in the simulations.

Table 5.2. Thermophysical properties of cardboard components and Kaowool PM

Component	ρ (kg m^{-3})	c (J g^{-1}K^{-1})	k (W m^{-1}K^{-1})	ϵ
H_2O_ℓ	--	$5.2 - 6.7 \times 10^{-3}T + 1.1 \times 10^{-5}T^2$	--	--
H_2O_g	--	$2.4 - 1.6 \times 10^{-3}T + 2.0 \times 10^{-6}T^2$	--	--
LB	520	1.8	0.10	0.70
LB_{int}	470	1.55	$0.05 + 7.5 \times 10^{-11}T^3$	0.78
LB_{char1}	170	1.3	$1.5 \times 10^{-10}T^3$	0.85
LB_{char2}	100	1.3	$1.5 \times 10^{-10}T^3$	0.85
CFL	49	1.8	0.10	0.70
CFL_{int}	44	1.55	$0.05 + 7.5 \times 10^{-10}T^3$	0.78
CFL_{char1}	16	1.3	$1.5 \times 10^{-9}T^3$	0.85
CFL_{char2}	9.4	1.3	$1.5 \times 10^{-9}T^3$	0.85
BFL	74	1.8	0.10	0.70
BFL_{int}	67	1.55	$0.05 + 7.5 \times 10^{-10}T^3$	0.78
BFL_{char1}	25	1.3	$1.5 \times 10^{-9}T^3$	0.85
BFL_{char2}	15	1.3	$1.5 \times 10^{-9}T^3$	0.85
CB_{vol1-3}	--	1.3	--	--
Kaowool PM	256	1.07	$0.052 - 4 \times 10^{-5}T + 1 \times 10^{-7}T^2$	--

Section 5.4: Model Validation

Figure 5.16 shows the experimental cone *MLR* data collected at four heat flux settings between 20 and 80 kW m^{-2}. The data obtained in each individual test are plotted as discrete points to show the scatter between tests with a solid line representing the mean of five experiments. The plots display data collected from the beginning of radiant exposure to the point of time when the surface of the sample was no longer covered with

the flame. No attempt was made to model smoldering of the corrugated cardboard char, which took place after flaming.

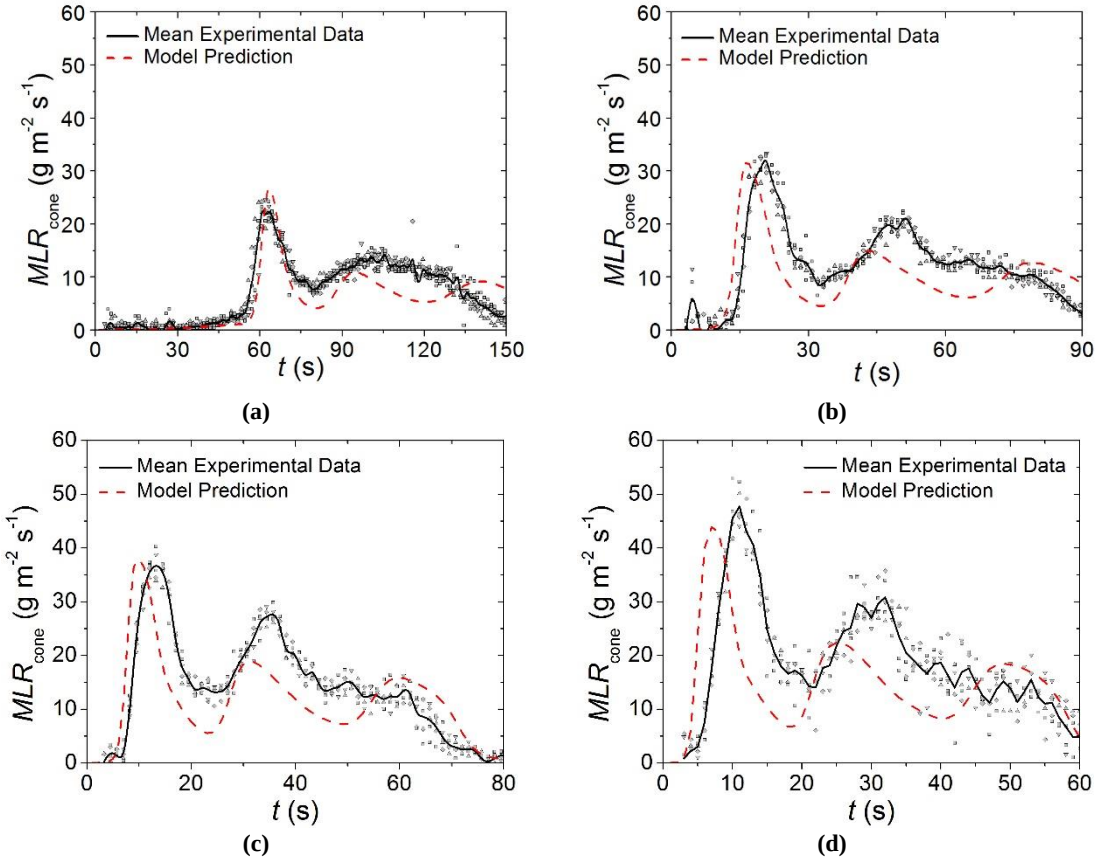

Figure 5.16. Experimental (points and solid lines) and simulated (dashed lines) mass loss rate cuves collected in cone calorimetery tests at an incident heat flux of (a) 20 kW m^{-2} (b) 40 kW m^{-2} (c) 60 kW m^{-2} (d) 80 kW m^{-2}

The mass loss rate curves predicted by the model are plotted as dashed lines in Figure 5.16. A three-peak structure of these curves reflects the presence of three high-density linerboards in the corrugated samples. Table 5.3 summarizes the characteristic values and times associated with the experimental MLR_{cone} and model predictions. The uncertainties defined in the table are two standard deviations of the mean. The model accurately predicted the time to ignition (which is also the time to onset of mass loss), the height of the first (and highest) peak *MLR* and the timing of this peak. The model systematically under-predicted the magnitude and timing of the second peak.

Table 5.3. Characteristic parameters of experimental and predicted mass loss rate curves collected in cone calorimetry tests at heat fluxes ranging 20 – 80 kW m^{-2}

Characteristic Parameter	20 kW m^{-2}		40 kW m^{-2}		60 kW m^{-2}		80 kW m^{-2}	
	Exp.	Model	Exp.	Model	Exp.	Model	Exp.	Model
Time to Ignition [s]	56.2 ± 3.4	57	14.2 ± 1.8	11	7.3 ± 1.0	6	5.8 ± 1.0	4
Peak *MLR* [g m^{-2} s^{-1}]	24.1 ± 1.0	27	32.6 ± 2.0	32	37.3 ± 4.6	38	48.9 ± 1.5	44
Time to Peak *MLR* [s]	59.3 ± 2.9	63	18.5 ± 1.1	16	10.5 ± 1.4	10	9.4 ± 1.0	7
Second Peak *MLR* [g m^{-2} s^{-1}]	15.1 ± 0.7	11	21.4 ± 0.7	15	28.3 ± 1.1	19	31.8 ± 0.7	22
Time to Second Peak *MLR* [s]	98.8 ± 2.5	95	47.8 ± 1.9	43	32.0 ± 1.0	31	27.4 ± 1.0	25

The total mass lost during the flaming portion of the cone calorimetry tests was also under-predicted by the model by 19%, on average. This disagreement suggested that chemical processes were not fully accounted for in the simulations. One process, which was not captured by the model, was a direct oxidation of solid cardboard components by atmospheric oxygen. This oxidation may have occurred in the second half of the tests where flame was still present on the sample but did not always cover its entire surface. A recent study found that accounting for surface oxidation in a cardboard pyrolysis model is essential for an accurate prediction of flame spread on this material [140]. An expansion of the current model to include oxidation will be a subject of future work.

The mass production rate of each volatile product of cardboard degradation was multiplied by the corresponding heat of combustion (given in Table 5.1) to compute predicted HRR_{cone} histories. These histories are compared with the mean experimental results in Figure 5.17. The experimental HRR_{cone} were obtained in the same tests as the mass loss rate data discussed above. The experimental data were consistent between individual tests with an average of 7% instantaneous deviation.

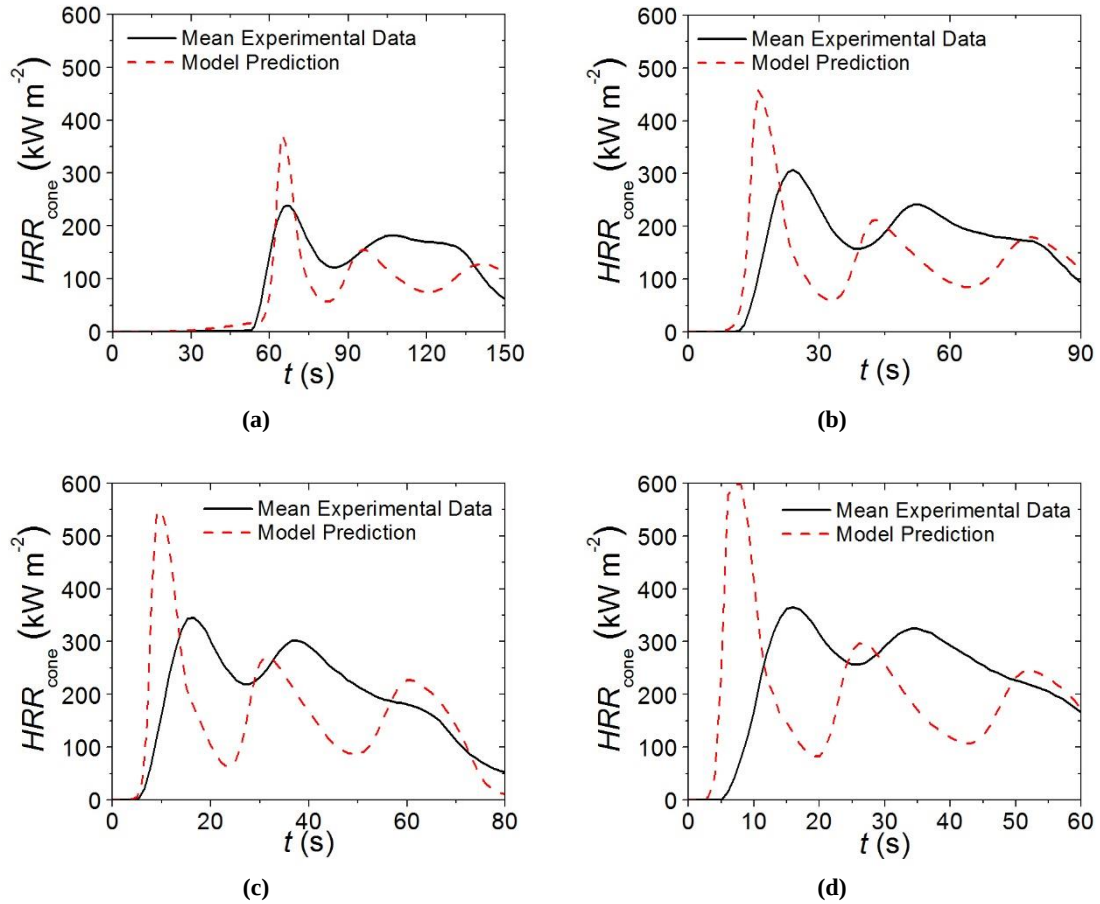

Figure 5.17. Experimental (solid lines) and simulated (dashed lines) heat release rate cuves collected in cone calorimetery tests at an incident heat flux of (a) 20 kW m^{-2} (b) 40 kW m^{-2} (c) 60 kW m^{-2} (d) 80 kW m^{-2}

Unlike in the case of MLR_{cone}, the first peak HRR_{cone} was systematically and significantly over-predicted by the model. This over-prediction was most likely a consequence of the fact that, in the experiments, the flame covered only a fraction of the sample surface for several seconds after ignition resulting in a significant portion of the volatiles escaping uncombusted. The time evolution of the flame heat flux shown in Figure 5.13 supports this observation. The total heat released during the flaming portion of the cone calorimetry tests was still under-predicted by the model by about 13%.

Section 5.5: Conclusions

This investigation demonstrated a general procedure to determine the parameters required to build a pyrolysis model for double-wall corrugated cardboard. Milligram-scale experiments were conducted to determine the kinetics and thermodynamics of the cardboard thermal degradation and combustion. Temperature and heat flux measurements performed in bench-scale experiments were utilized to characterize heat transfer inside the degrading cardboard structure. The model was shown to provide reasonably good predictions of the material burning rate over a wide range of heat exposures. Considering the complex nature of the studied material, the quality of predictions serves to demonstrate that this procedure can be successfully applied to a wide range of material systems.

Building on the results of this study, future work will be focused on improving the bench-scale measurements. It is expected that by controlling the gaseous atmosphere in cone-calorimetry-like experiments, it will be possible to eliminate the flame and reduce uncertainties in the heat transfer characterization. A controlled atmosphere pyrolysis apparatus, similar to the NIST Gasification Device, would also enable determination of the rate of solid oxidation, which is thought to be at least partially responsible for the discrepancies between the experimental and predicted burning rates obtained in this work.

Chapter 6: Low-Pile Carpet Tiles

Section 6.1: Introduction

This chapter demonstrates the characterization of a multilayer low-pile carpet flooring system using the model parameterization methodology presented in this work. This demonstration includes the construction of a model for each individual layer to identify its contribution to the pyrolysis dynamics of the full composite. A complete understanding of the contribution of each layer to the response of the composite provides the possibility to engineer composite materials to meet specific flammability performance metrics. The complicated structure and composition of the low-pile carpet system presented a significant challenge that required modifications to methods and analyses of the existing methodology. The ThermaKin numerical pyrolysis modeling environment was used in this work to conduct inverse analyses on experimental data to indirectly measure thermo-physical properties and reaction parameters to describe the thermal degradation of the carpet samples. ThermaKin was also used to generate gasification mass loss rate (*MLR*) and temperature predictions for the sample material to validate the measured properties and constructed models.

Section 6.2: Experiments and Analysis

Section 6.2.1: Materials

EcoWorx style low-pile carpet tiles produced by the Shaw Contract Group were characterized in this work according to the methodology presented in the following sections. A schematic of a carpet tile sample is provided in Figure 6.1. The approximate mass of each polymer contributing the largest mass to each layer of the carpet was provided by the manufacturer. The face yarn is made of 0.42–0.57 $kg \cdot m^{-2}$ of woven polyamide-6 (PA6) with auxiliary polymers. The primary backing, which is composed of a mesh through

which the face yarn is interwoven, includes approximately 0.11 $kg \cdot m^{-2}$ of a PA6 and polyethylene terephthalate (PET) bicomponent mixture. The precoat is made from approximately 0.42 $kg \cdot m^{-2}$ of highly-filled vinyl-acetate ethylene (VAE) with other auxiliaries. The base layer consists of approximately 1.18 $kg \cdot m^{-2}$ of highly filled very-low-density polyethylene (LDPE) (labeled as "thermoplastic compound" in Figure 6.1) with auxiliary additives as well as 0.05 $kg \cdot m^{-2}$ of nonwoven fiberglass mat.

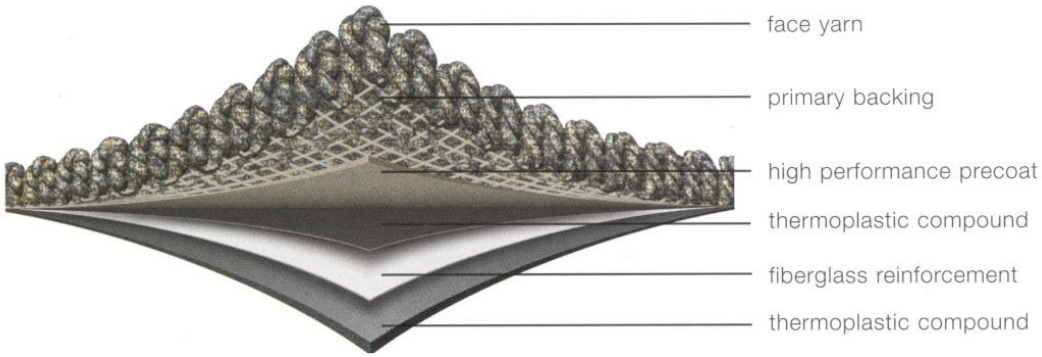

Figure 6.1. Schematic of the EcoWorx carpet tile [141].

The tile was separated by pulling the composite into two layers denoted as the upper layer and the base layer. Coupon-sized samples of the two individual layers were tested in bench-scale experiments to characterize thermal transport through the composite. The two layers tested in bench-scale experiments are displayed in Figure 6.2b,c together with a photograph of the full carpet sample Figure 6.2a.

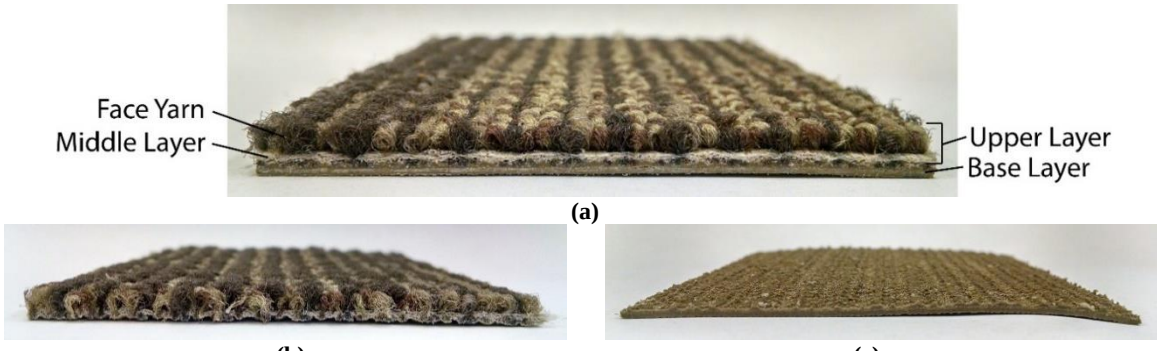

(a)

(b) **(c)**

Figure 6.2. Photographs of (a) full carpet composite; (b) upper layer; and (c) base layer.

Samples of each of the three individual layers sized on the order of several milligrams were harvested and tested to characterize the thermal degradation reaction kinetics, energetics, and combustibility of the gases evolved during thermal degradation. These three layers were the face yarn, the middle layer, which consisted of the primary backing and the precoat, and the fiberglass-reinforced base layer. Because of their small size, these samples were easily cut from the upper layer and base layer while keeping the structure of each layer intact.

The masses and thicknesses of coupon-sized samples (0.08 m × 0.08 m) of the entire carpet, the upper layer, and the base layer were measured to verify the geometric and gravimetric definitions of the individual layers in the successive analyses and to confirm the additive nature of each layer to the composite. The thickness of the face yarn in the upper layer sample was measured, all the face yarn was carefully removed from the sample, and the mass and thickness of the remaining middle layer portion was measured to determine the relative masses of the face yarn and middle layer in the upper layer. The areal density of the face yarn was calculated as the compliment to the areal density of the middle layer in the upper layer samples.

The areal density of the base layer was measured as 1.770 ± 0.060 $kg \cdot m^{-2}$ and the thickness of the layer was measured as 0.0017 ± 0.0001 m. The areal density of the face yarn layer was measured as 0.350 ± 0.050 $kg \cdot m^{-2}$ and the thickness of the layer was 0.0030 ± 0.0002 m. The areal density of the middle layer was measured as 0.970 ± 0.050 $kg \cdot m^{-2}$ and the thickness was measured as 0.0016 ± 0.0003 m. These measurements led to the following definitions for the density of each virgin component: The $\text{Face Yarn}_{\text{virgin}}$ component density was defined as 125 $kg \cdot m^{-3}$, the $\text{Middle}_{\text{virgin}}$ component density was

defined as 582 kg·m^{-3}, and the $\text{Base}_{\text{virgin}}$ component density was defined as 1060 kg·m^{-3} in individual layer models constructed as described in Section 6.2.2.4.

The areal densities of the individual layers were additive to within the uncertainty of the measured areal density of the composite, but the thicknesses did not add to within the uncertainty of the thickness of the composite. The disparity between these two measurements originated from a textured interface between the base layer and the precoat component in the middle layer (see Figure 6.2). The thickness of the middle layer was measured as approximately 0.0011 ± 0.0001 m as a layer in the composite and the thickness of the base layer was measured as 0.0015 ± 0.0001 m as a layer in the composite.

The densities of the base layer and middle layer components defined in the individual layer models were modified during construction of the full carpet composite model to maintain consistency with the measured masses and to account for the reduced thicknesses of these layers in the tested composite. The density definitions for the middle layer and base layer were modified to the following values: the $\text{Middle}_{\text{virgin}}$ component density was defined as 750 kg·m^{-3}, and the $\text{Base}_{\text{virgin}}$ component density was defined as 1200 kg·m^{-3} in the full carpet composite models. Construction of the model that required these geometric and gravimetric definitions is outlined in Section 6.2.2.4.

Section 6.2.2: Experimental Methods

Section 6.2.2.1: Simultaneous Thermal Analysis

Ten STA tests were conducted on samples of each of the three layers to accumulate the necessary statistics following the procedure described in Section 4.2.1.1. Analysis of STA data required a model constructed in the ThermaKin modeling environment that simulated the STA tests as described in Section 4.2.1.1. The criteria for acceptance of the kinetic mechanism was defined as a maximum error of 10% in the prediction of the

magnitude of MLR_{peak}, a maximum absolute error in the prediction of T_{peak} of 3 K, and a mean error of less than 2% in the normalized mass versus temperature curve. The resulting reaction schemes are presented in Section 6.3.1.1.

The heat capacity was calculated from the STA heat flow rate data according to the procedure presented in Section 4.2.2.1. The range of data analyzed corresponded to the initial, unreacted components. The heat capacity of the char components was assumed based on the mean heat capacity determined for seven common charring polymers [133]. The intermediate components that were produced and consumed in reactions during degradation were assumed to have the mean heat capacities of the component that reacted to produce the intermediate and the component that was produced when the intermediate was consumed. A baseline heat flow rate curve that accounted for the sensible enthalpy as a function of temperature throughout degradation was constructed and the heat of phase transitions and degradation reactions were determined according to the procedure in Section 4.2.2.1.

The preceding analysis yielded all the parameters required to predict the heat flow rate to the sample as a function of temperature. The STA experiment was simulated and the predicted heat flow rate curve was compared to the mean experimental curve to ensure that all heat flow events were adequately described by the reaction mechanism. Modifications were made to the heat capacities or the reaction mechanism if the comparison indicated that the predictions yielded from this analysis were unacceptable. The acceptance criterion for this analysis required that the mean instantaneous relative difference between the time-dependent integrals of the predicted heat flow rate curve and the experimental curve remain less than 5% to verify the total energy absorbed by the

sample in the model was equivalent to the total energy absorbed by the sample in the experiment throughout decomposition.

Section 6.2.2.2: Microscale Combustion Calorimetry

Three MCC tests were carried out on samples of each of the face yarn, middle layer, and base layer. Samples for MCC tests were prepared identically to the samples tested in the STA. The sample mass, which ranged from approximately 2 to 5 mg was recorded and the sample was placed in a ceramic crucible. The tests were conducted according to the procedure from Section 4.2.3.1 programmed for a heating rate of 10 $K \cdot min^{-1}$ and a final temperature of 1023 K. The heating rate used in this investigation is outside the range of heating rates recommended in the standard, but was chosen to provide data collected under conditions comparable to those used in the STA tests.

A predicted *HRR* curve was generated by simulating the mass loss process in the MCC experiment and applying the heat of combustion value to each distinct gaseous species. The predicted *HRR* curve was compared to the experimental *HRR* curve. Modifications were made to the heat of combustion values until the predicted and experimental curves agreed to within the acceptance criterion. Though qualitative agreement between the experimental and modeled *HRR* curves was important for determining the heat of combustion for each modeled gaseous species, the only formal acceptance criterion required that the total integrals of the predicted curve and the experimental curve agree to within 2%.

Section 6.2.2.3: Absorption Coefficient Measurement

A crude measurement method described in detail in Section 4.2.4.1 was used to measure the broadband radiant flux transmitted through a thin sample. As described in

Section 4.2.4.1, the measured transmitted radiant flux was used in conjunction with Eq. 4.14 to estimate the absorption coefficient of each of the layers in the carpet composite.

Section 6.2.2.4: Gasification Experiments and Analysis

The CAPA, described in Section 4.2.5.1, was used to collected data on the mass and back surface temperature (T_{back}) while each sample material was subjected to radiant heat flux in well-controlled atmospheric conditions. The tests conducted in this work on the carpet materials with the CAPA had nitrogen introduced to the gas flow chamber at a rate of 225 SLPM (measured at 1 atm and 298 K). The CAPA tests were conducted on samples of the upper layer, the base layer, and the full carpet composite subjected to radiant heat flux of 30, 50, and 70 $kW \cdot m^{-2}$. Each test was repeated three times to accumulate statistics. Inverse analyses of the data were conducted with the ThermaKin modeling environment as described in Section 4.2.5.1 to determine the parameters that define thermal transport at the surface and within the condensed phase.

Samples were prepared in a square geometry with a side of 0.08 m. They were located in the center of a square sheet of 0.00625 m thick Kaowool PM board with an edge dimension of 0.105 m. In the tests on the face yarn and the full composite, the sample rested on a square piece of aluminum foil that was painted on the side facing away from the sample for an emissivity of 0.95 to provide a well-defined surface emissivity for the infrared camera. The base layer samples were tested without aluminum foil and their back surfaces were painted for an emissivity of 0.95. It was observed that the paint partially degraded above approximately 600 K, compromising the well-defined emissivity, and data collected above this threshold was considered unreliable and was not used in inverse analyses. It was observed during preliminary CAPA tests that the edges of the face yarn

samples curled toward the center of the sample immediately upon heating and decreased the exposed area of the sample. The face yarn samples prepared for subsequent CAPA tests were secured to the holder with wires to combat deformation of the samples.

Section 6.3: Results

Section 6.3.1: Data Analysis for Property Evaluation

Section 6.3.1.1: Thermal Degradation Kinetics and Energetics Determination

The STA data collected on each of the individual carpet layers was analyzed according to the procedures outlined in Section 4.2 to determine the kinetics and energetics of the thermal degradation process as well as the heat capacity of the condensed phase components. The heating rate measured in each of the tests had reproducible time-dependency that was approximated in ThermaKin by Equation 4.7. The parameters of this equation were adjusted until it matched the experimental data. The agreement between the experimentally observed and modeled heating rate profiles is evident in Figure 6.3.

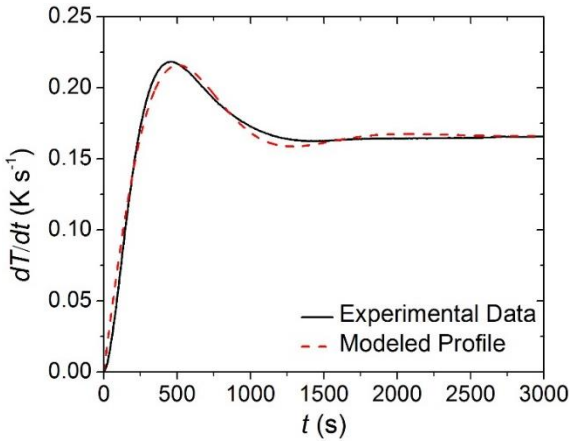

Figure 6.3. Experimentally observed and modeled heating rate histories typical of the Simultaneous Thermal Analysis (STA). The coefficients for Equation 4.7 that describe the modeled curve are the following: b_1= 0.166 K s^{-1}, b_2 = 0.0024 s^{-1}, b_3 = 0.004 s^{-1}, b_4 = −0.0623.

It was assumed that a mechanism with consecutive reactions would be suitable for the face yarn and the base layer. Analysis of the face yarn layer resulted in a mechanism with one phase transition reaction and two thermal degradation reactions. The mechanism

determined for the base layer also featured a single phase transition and two thermal degradation reactions. A parallel scheme was assumed for the middle layer because it was known prior to the analysis that the middle layer was composed of at least four distinct polymers that degraded independently. The pyrolysis mechanism for the middle layer included two parallel phase transitions and four parallel thermal degradation reactions. The effective reaction mechanism determined for each layer is provided in Table 6.1.

Table 6.1. Effective reaction mechanisms for each layer of the carpet composite and the heats of reactions. Positive heats represent endothermic processes.

#	Reaction Equation	A (s^{-1})	E (J mol^{-1})	h (J kg^{-1})
	Face Yarn			
1	$\text{Face Yarn}_{\text{virgin}} \rightarrow \text{Face Yarn}_{\text{melt}}$	6.0×10^{38}	3.80×10^{5}	6.1×10^{4}
2	$\text{Face Yarn}_{\text{melt}} \rightarrow 0.92\text{Face Yarn}_{\text{int.}} + 0.08\text{Face Yarn}_{\text{volatiles}}$	1.0×10^{9}	1.41×10^{5}	5.3×10^{4}
3	$\text{Face Yarn}_{\text{int.}} \rightarrow 0.06\text{Face Yarn}_{\text{char}} + 0.94\text{Face Yarn}_{\text{volatiles}}$	3.0×10^{14}	2.30×10^{5}	5.3×10^{5}
	Middle Layer			
1	$\text{Middle}_{4,\text{virgin}} \rightarrow \text{Middle}_{4,\text{melt}}$	9.0×10^{38}	3.84×10^{5}	8.0×10^{4}
2	$\text{Middle}_{3,\text{virgin}} \rightarrow \text{Middle}_{3,\text{melt}}$	1.0×10^{28}	3.00×10^{5}	6.0×10^{4}
3	$\text{Middle}_{1,\text{virgin}} \rightarrow 0.334\text{Middle}_{\text{char}} + 0.666\text{Middle}_{\text{volatiles}}$	1.0×10^{12}	1.55×10^{5}	2.7×10^{6}
4	$\text{Middle}_{2,\text{virgin}} \rightarrow 0.334\text{Middle}_{\text{char}} + 0.666\text{Middle}_{\text{volatiles}}$	1.0×10^{20}	2.62×10^{5}	0
5	$\text{Middle}_{3,\text{melt}} \rightarrow 0.334\text{Middle}_{\text{char}} + 0.666\text{Middle}_{\text{volatiles}}$	5.0×10^{8}	1.42×10^{5}	3.5×10^{5}
6	$\text{Middle}_{4,\text{melt}} \rightarrow 0.334\text{Middle}_{\text{char}} + 0.666\text{Middle}_{\text{volatiles}}$	1.0×10^{10}	1.70×10^{5}	2.0×10^{5}
	Base Layer			
1	$\text{Base}_{\text{virgin}} \rightarrow \text{Base}_{\text{melt}}$	1.0×10^{21}	1.72×10^{5}	6.0×10^{3}
2	$\text{Base}_{\text{melt}} \rightarrow 0.92\text{Base}_{\text{int.}} + 0.08\text{Base}_{\text{volatiles}}$	5.0×10^{6}	1.15×10^{5}	4.0×10^{4}
3	$\text{Base}_{\text{int.}} \rightarrow 0.71\text{Base}_{\text{char}} + 0.29\text{Base}_{\text{volatiles}}$	1.0×10^{16}	2.58×10^{5}	1.5×10^{5}

The STA normalized mass and normalized *MLR* data for all carpet layers is plotted in Figure 6.4 along with the curves predicted by the reaction mechanism shown in Table 6.1. In Figure 6.4, m_0 indicates initial mass of the sample. In general, the reaction mechanisms determined in the work presented in this chapter generated curves that agreed

well with the experimental *MLR* and total mass curves. All error bars displayed in this chapter correspond to two standard deviations of the mean.

The heat flow rate data collected in STA tests on each layer were analyzed to determine the temperature-dependent heat capacity for all the virgin carpet components. Two linear temperature-dependent relationships were found for the Face $Yarn_{virgin}$ and Face $Yarn_{melt}$ components. The heat capacity of all the $Middle_{virgin}$ components was adequately described with a single temperature-dependent term. It was impossible to assign a heat capacity value to each individual $Middle_{virgin}$ component, and all were assigned the same value. The base layer sample melted shortly into the tests, and it proved impossible to determine the heat capacity of the $Base_{virgin}$ component from the collected heat flow rate data. The heat capacity of the $Base_{melt}$ component was determined with a linear temperature-dependence and it was assumed that the same expression could adequately describe the heat capacity of the $Base_{virgin}$ component.

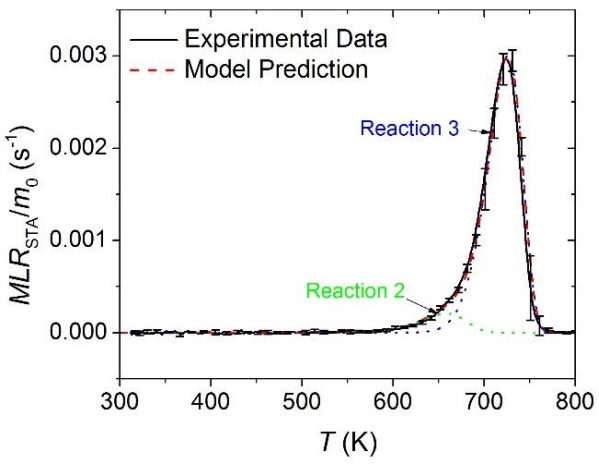

(a)

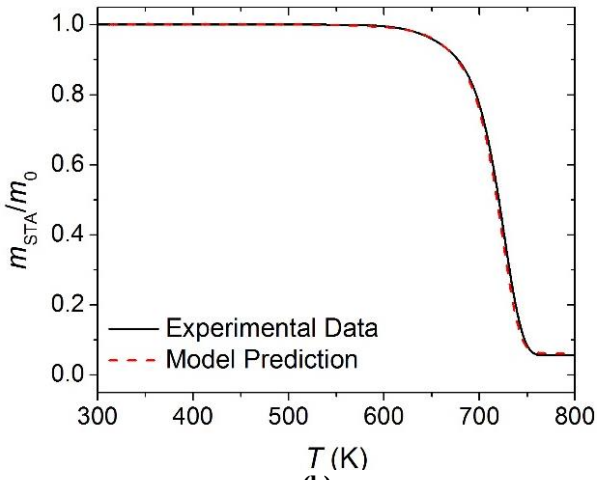

(b)

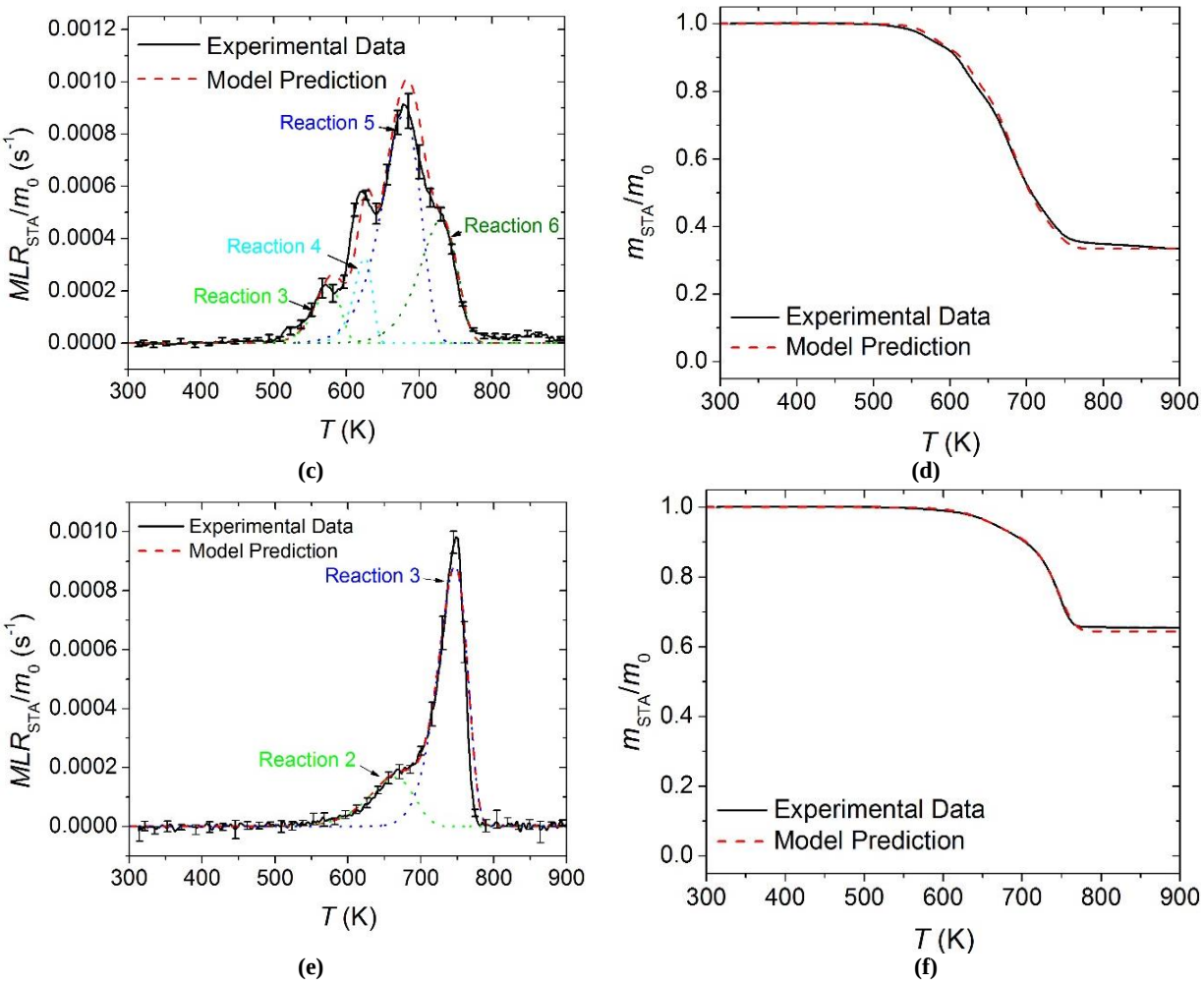

Figure 6.4. Normalized mass loss rate (*MLR*) and normalized mass data collected in STA experiments and model predicted curves for: (a) and (b) face yarn layer; (c) and (d) the middle layer; and (e) and (f) the base layer. Error bars indicate two standard deviations of the mean experimental data.

The Face Yarn$_{char}$ and Middle$_{char}$ components were characterized by low masses and a porous structure that compromised the thermal contact between the sample and the crucible and yielded unreliable heat flow rate measurements. These char components were assigned a single heat capacity that was measured as the mean value for the chars produced by seven common polymers [91]. The heat capacity of the Base$_{char}$ component was determined by conducting independent tests on the char produced from thermal degradation of the base layer sample. The heat capacity of the char did not follow a recognizable functional form, so the arithmetic mean of the data over the entire tested temperature range was defined as the heat capacity of the Base$_{char}$ component.

The heat capacity of the Face $Yarn_{int.}$ component was defined as the mean between the heat capacities of the Face $Yarn_{melt}$ component evaluated at 560 K and the Face $Yarn_{char}$ component. The heat capacity of the $Middle_{3,melt}$ and $Middle_{4,melt}$ components was defined as the mean between the heat capacity of the $Middle_{virgin}$ components evaluated at 500 K and the $Middle_{char}$ component. The heat capacity of the $Base_{int}$ component was defined as the mean between the heat capacities of the $Base_{melt}$ component evaluated at 600 K and the $Base_{char}$ component. The heat capacity of the reactant was evaluated at a different temperature for each layer based on the temperature at which the intermediate was produced and subsequently reacted.

The heat capacity of the gaseous volatiles produced during thermal degradation of the carpet samples was assumed to be well approximated by hydrocarbons ranging in length from one to eight carbon atoms in the temperature range of 400 K to 500 K. This resulted in the specific heat capacity of all gaseous volatiles defined as 1800 $J \cdot kg^{-1} \cdot K^{-1}$. The expressions determined for the heat capacity of each component are provided in Table 6.2.

Table 6.2. Heat capacity values for each component in the carpet composite.

Component	c [J kg^{-1} K^{-1}]	Method
Face $Yarn_{virgin}$	$8.2T - 1180$	STA
Face $Yarn_{melt}$	$3.6T + 580$	STA
Face $Yarn_{int.}$	2150	Assumed
Face $Yarn_{char}$, $Middle_{char}$	1700	[91]
$Middle_{1,virgin}$, $Middle_{2,virgin}$, $Middle_{3,virgin}$, $Middle_{4,virgin}$	$4.2T$	STA
$Middle_{3,melt}$, $Middle_{4,melt}$	1900	Assumed
$Base_{virgin}$	$2.0T + 1000$	Assumed
$Base_{melt}$	$2.0T + 1000$	STA
$Base_{int.}$	1525	Assumed
$Base_{char}$	850	STA
Face $Yarn_{volatiles}$, $Middle_{volatiles}$, $Base_{volatiles}$	1800	Assumed

The integral between the experimental heat flow rate curve and the sensible enthalpy baseline was defined as the enthalpy absorbed by the sample undergoing phase transition or thermal degradation. Each heat of reaction was assigned to the reaction that occurred at the temperature range corresponding to the heat flow rate peak. It was difficult to differentiate between the two thermal degradation reactions in the heat flow rate curve for the face yarn and the base layer and the total integral of the peak was divided between the two reactions in approximate proportion to the total mass volatilized in each reaction. The resulting heat flow quantities associated with each reaction are provided in Table 6.1. The experimental heat flow rate curves are plotted in Figure 6.5 along with the model predictions generated with the parameters summarized in Tables 6.1 and 6.2.

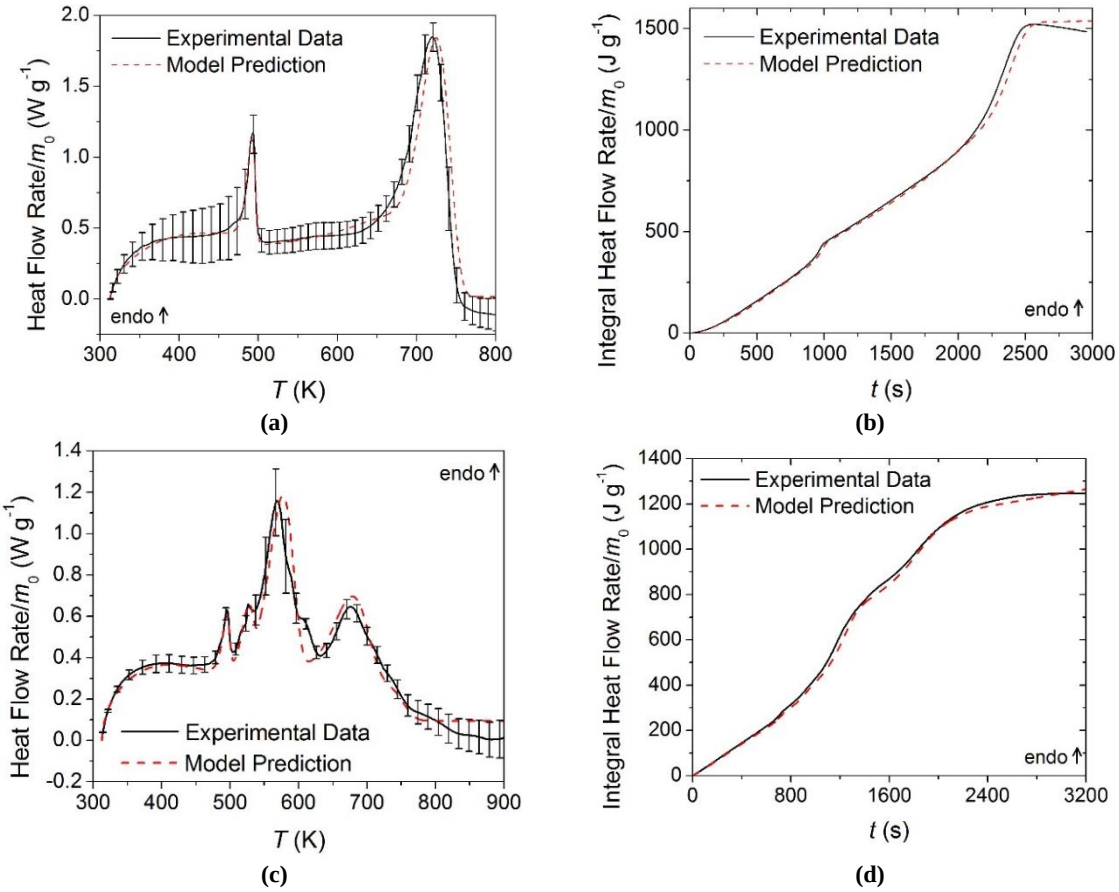

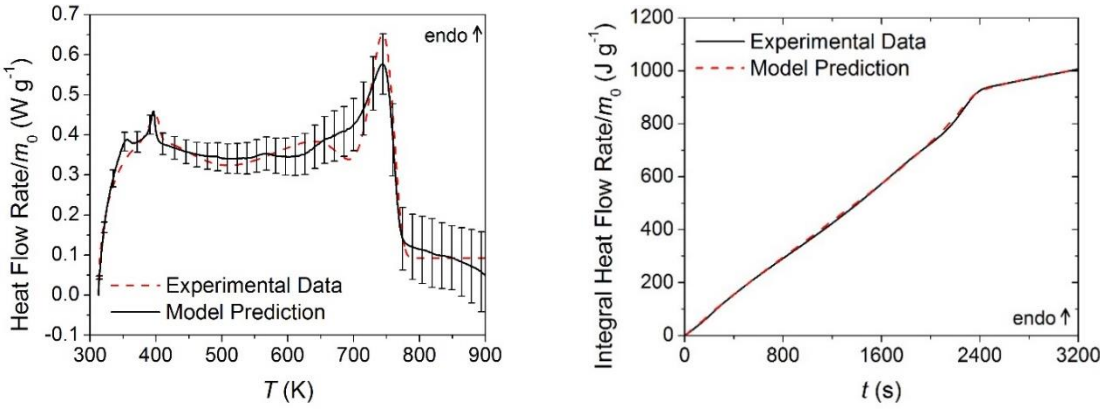

(e) **(f)**

Figure 6.5. Normalized heat flow rate and integral heat flow rate data collected in STA experiments and model predicted curves for: (a) and (b) face yarn layer; (c) and (d) the middle layer; and (e) and (f) the base layer. Error bars indicate two standard deviations of the mean experimental data.

Section 6.3.1.2: Heat of Combustion Determination

The MCC data collected on each of the carpet layers at a set heating rate of 10 K min^{-1} (0.167 K s^{-1}) were analyzed using the degradation kinetics determined from analysis of STA data. The heating rate profile observed in MCC experiments was different than the profile observed in STA experiments, but was adequately described by the form of Equation 4.7. The agreement between the experimentally observed and modeled heating rate profiles is displayed in Figure 6.6.

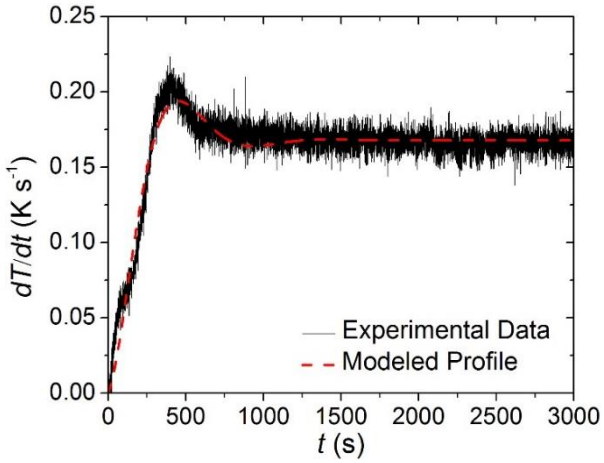

Figure 6.6. Experimentally observed and modeled heating rate histories typical of the Microscale Combustion Calorimetry (MCC) experiments conducted in this work. The coefficients for Equation (14) that describe the modeled curve are the following:
b_1= 0.168 K s^{-1}, b_2 = 0.0039 s^{-1}, b_3 = 0.0065 s^{-1}, b_4 = 0.256.

The mean *HRR* curve measured for each layer was shifted in temperature to properly align with the *MLR* curve predicted with the corresponding reaction mechanism. The magnitude of the shift in the data for each layer was based on the principle that heat release required a concurrent mass loss. By applying this shift, the *MLR* curves agreed well with the rising and falling edges of the *HRR* curves. The face yarn *HRR* curve was shifted upward in temperature by 14 K, the middle layer curve was shifted upward in temperature by 15 K, and the base layer was shifted upward in temperature by 5 K.

The heats of combustion determined through this analysis are provided in Table 6.3 and the experimental and predicted *HRR* curves and integral *HRR* curves are provided in Figure 6.7. The MCC data was highly repeatable for all materials, and error bars were omitted because the magnitude of the scatter was insignificant for the scale plotted. Contrary to the convention used to define the heats of reaction, positive values in Table 6.3 correspond to exothermic processes.

The *HRR* curve collected on the middle layer was shifted such that the falling edge of the curve corresponded to the falling edge of the *MLR* curve. After applying this offset in the temperature scale, the first thermal degradation reaction appeared to correspond to a zero magnitude heat release. This led to the conclusion that the volatile species produced in this reaction had no associated heat of combustion. The other values determined for the heats of combustion of volatile species were within a reasonable range for common fuels.

Table 6.3. Effective heat of combustion values for the volatile species released in each reaction. Positive heats of combustion are exothermic.

Volatile Species	h_c (J kg^{-1})
Face Yarn$_{\text{volatiles,reaction 2}}$	2.4×10^7
Face Yarn$_{\text{volatiles,reaction 3}}$	2.9×10^7
Middle$_{\text{volatiles,reaction 3}}$	0
Middle$_{\text{volatiles,reaction 4}}$	1.6×10^7

$Middle_{volatiles,reaction\ 5}$	2.4×10^7
$Middle_{volatiles,reaction\ 6}$	5.0×10^7
$Base_{volatiles,reaction\ 2}$	3.4×10^7
$Base_{volatiles,reaction\ 3}$	5.9×10^7

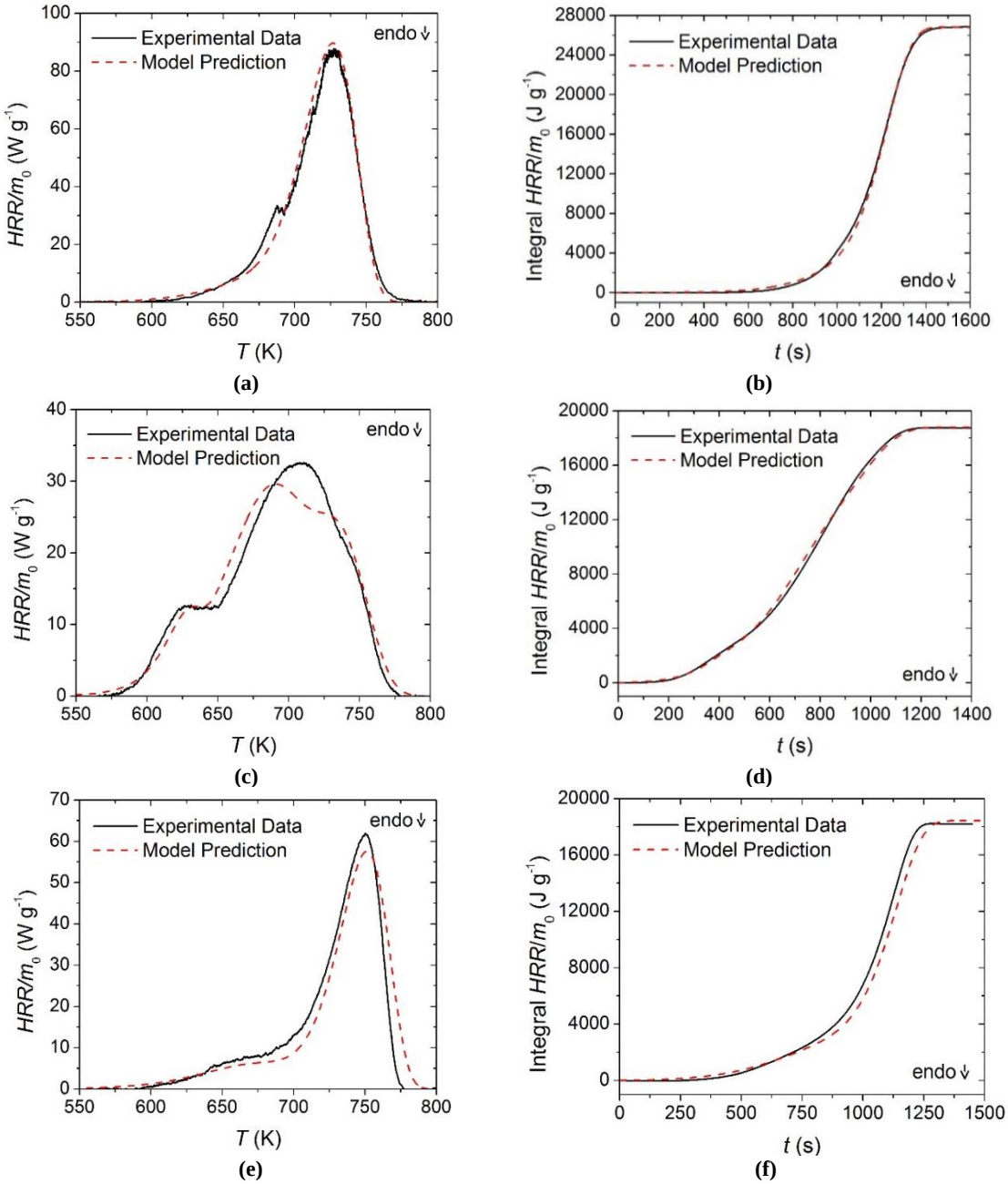

Figure 6.7. Normalized heat release rate and integral heat release rate data collected in MCC experiments and model predicted curves for: (a) and (b) the face yarn layer; (c) and (d) the middle layer; and (e) and (f) the base layer. Error bars were omitted due to small magnitude scatter.

Section 6.3.1.3: Absorption Coefficient and Emissivity Determination

The data collected in transmitted heat flux measurements on all the sample materials and used to calculate the absorption coefficients are provided in Table 6.4. Since the virgin face yarn was observed to melt shortly after the beginning of radiant heating, the absorption coefficient of the melted face yarn was measured instead of the virgin face yarn. The density of the melted face yarn used in the calculation is discussed later in this section.

Table 6.4. Measurements used to calculate the absorption coefficient for each virgin and melt component.

Layer	$\left(\frac{I_{x=0}}{I_{x=\delta}}\right)$	δ (m)	ρ (kg m^{-3})	k (m^2 kg^{-1})
Face Yarn Melt	0.025	0.0008 ± 0.0001	625	7.17
Middle Layer	0.026	0.0013 ± 0.0001	582	4.69
Middle Layer	0.020	0.0016 ± 0.0001	582	4.09
Base Layer	0.010	0.0010 ± 0.0001	1060	4.25
Base Layer	0.005	0.0010 ± 0.0001	1060	4.90

Because the radiant flux transmitted through the melted face yarn was measured, the density used to model the $\text{Face Yarn}_{\text{melt}}$ component was also used to calculate the absorption coefficient. The densities of the middle layer and the base layer defined in the individual layer models were used to calculate the absorption coefficient of each of those layers. The mean of the individual measurements of the absorption coefficient for each layer was calculated to define the absorption coefficient in the models. Approximate values were assigned to each component based on the transmitted heat flux measurements (7 $m^2 \cdot kg^{-1}$ for the face yarn, 4.4 $m^2 \cdot kg^{-1}$ for the middle layer, and 4.6 $m^2 \cdot kg^{-1}$ for the base layer). The absorption coefficients of the melt and intermediate components were assigned the same absorption coefficient as the virgin component for all layers.

It was observed during gasification tests on the upper layer that the char components were optically dark and appeared to be graphitic. To make the simulations consistent with this observation, the absorption coefficient of the char components was defined such that

all radiation was absorbed at the surface of the sample (100 $m^2 \cdot kg^{-1}$). The char formed during thermal degradation of the base layer did not appear to be optically dark. The absorption coefficient for the $Base_{char}$ component was assumed to be equal to the absorption coefficient of all other base layer components.

The relationship between the reflection loss coefficient and emissivity of optically thick materials (must add to unity) led to the definition of the emissivity of all of the virgin and melt components in each of the carpet layers as 0.95. Due to observations of the samples in gasification tests on each of the layers, the char components were assumed to have lower emissivities than the virgin components. It was assumed that the char components had high carbon content, and the emissivity of all chars was expected to be similar to graphite. The emissivity of graphite was measured at elevated temperatures as approximately 0.86 [106] and was defined as the emissivity of the char components. These definitions are consistent with results of a study by Försth and Roos, who conducted experiments on various colors of PVC and vinyl carpets and found that in some instances, the emissivity tended to decrease as the samples degraded [104]. The emissivity of the intermediate components was defined as the mean value between the virgin components and the char components ($\epsilon = 0.905$).

Section 6.3.1.4: Thermal Conductivity Determination

It was observed that the thickness of the face yarn decreased by a factor of approximately five upon melting. This observation was difficult to confirm in gasification tests because the surface of the sample was completely covered with rapidly regenerating bubbles shortly after melting occurred. However, it was reproduced in a furnace with the temperature set to the melting point of the face yarn (approximately 490 K). A small mass

of porous char was produced by the face yarn during degradation, though the thickness of the face yarn layer did not change significantly after melting. The density of the Face $Yarn_{melt}$ component was defined five times larger than the density of the Face $Yarn_{virgin}$ component, and the density of the Face $Yarn_{int}$ and Face $Yarn_{char}$ components were defined proportional to the stoichiometric coefficient for the condensed phase product of each reaction to simulate a constant thickness for the layer after melting.

All $Middle_{virgin}$ components were defined with the same density because it was impossible to identify and separate each individual initial component. Two of the middle layer components underwent phase changes that did not affect the geometry of the sample, so the $Middle_{melt}$ components were defined with the same density as the $Middle_{virgin}$ components. The $Base_{virgin}$ component went through a phase change without the geometry of the layer changing considerably and the density of the $Base_{melt}$ component was defined equivalent to the virgin component density. The overall thickness of the middle layer and the base layer remained approximately constant throughout the CAPA tests. The densities of the $Middle_{char}$, $Base_{int}$ and $Base_{char}$ components were defined proportional to the associated stoichiometric coefficients in the reaction mechanism to maintain a constant thickness in the simulations. The definitions for the densities of all components are provided in Table 6.5.

The thermal conductivities of the components in each layer of the carpet composite were the only remaining undefined parameters that affected the pyrolysis model predictions. Inverse analyses were conducted on the T_{back} data collected in the CAPA tests using the ThermaKin modeling environment. The initial rise of the T_{back} data curve was chosen as the target for the virgin and melt components because these were the only

components that affected the T_{back} curve early in the tests. The model prediction for the upper layer (face yarn and middle layer) is compared to the experimental data in Figure 6.8. The temperature prediction was not sensitive to the thermal transport parameters of the char and intermediate components for the time range that corresponded to the initial rise of T_{back}.

Table 6.5. Full set of thermophysical properties used in the individual upper layer model and base layer model.

Component	ρ [kg m^{-1}]	k [W m^{-1} K^{-1}]	ϵ	κ [m^2 kg^{-1}]
Face Yarn				
Face Yarn$_{virgin}$	125	0.05	0.95	7
Face Yarn$_{melt}$	625	0.05	0.95	7
Face Yarn$_{int.}$	575	$0.025 + 6.5 \times 10^{-10}T^3$	0.905	7
Face Yarn$_{char}$	34.5	$11 \times 10^{-10}T^3$	0.86	100
Middle Layer				
Middle$_{1,virgin}$, Middle$_{2,virgin}$, Middle$_{3,virgin}$, Middle$_{4,virgin}$, Middle$_{3,melt}$, Middle$_{4,melt}$	582	0.05	0.95	4.4
Middle$_{char}$	194.4	$11 \times 10^{-10}T^3$	0.86	100
Base Layer				
Base$_{virgin,}$ Base$_{melt}$	1060	$0.25 - 2.85 \times 10^{-4}T$	0.95	4.6
Base$_{int.}$	975.2	$0.125 - 1.425 \times 10^{-4}T + 3.5 \times 10^{-10}T^3$	0.905	4.6
Base$_{char}$	692.4	$7 \times 10^{-10}T^3$	0.86	4.6

It was found that a single, constant value for the thermal conductivity (k = 0.05 W·m^{-1}·K^{-1}) of the Face Yarn$_{virgin}$, Middle$_{virgin}$, Face Yarn$_{melt}$ and Middle$_{melt}$ components was adequate to describe the rising edge of the T_{back} curve. There was no evidence in the data of a change in the thermal conductivity from the virgin components to the melt components. Though this thermal conductivity value is low for a mixture of solid polymers and is more typical of air at elevated temperatures (650 K), the structure of the carpet upper layer supports a thermal conductivity value lower than the typical range for polymers. The face yarn was made of fibrous filaments woven into a yarn and the majority of the volume of the defined face yarn layer was air (or, in the case of the gasification tests, nitrogen). Furthermore, the face yarn melted shortly after exposure to the cone heater and the melted face yarn was characterized by rapidly regenerating bubbles. The middle layer was

structured as a mesh interwoven with face yarn and although the density of the middle layer was larger than the face yarn, gases still made a large contribution to the volume of the layer.

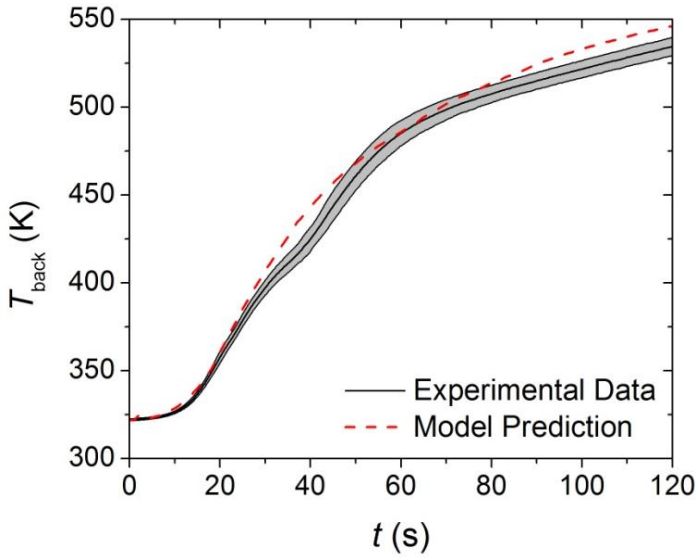

Figure 6.8. First 120 s of experimental T_{back} curve measured in Controlled Atmosphere Pyrolysis Apparatus (CAPA) tests and corresponding model predicted curve for the upper layer exposed to a radiant flux of 30 kW·m^{-2}. The shaded region corresponds to two standard deviations of the mean experimental data.

Although the thermal conductivity determined for the upper layer is the only value that provides an adequate agreement between the predicted curve and the experimental data, it is probable that some physical phenomena that occurred during testing are not represented in the model. As mentioned in Section 6.2.2.4, the edges of the upper layer sample tended to curl inward during CAPA tests, and the method of securing the sample to the holder was only partially effective in reducing the deformation. It is possible that the decrease in exposed area may have caused the samples to deviate from one-dimensional behavior. The back surface of the upper layer samples was textured which may have compromised the thermal contact between the ample and the aluminum foil, resulting in inaccurate T_{back} profiles.

An inverse analysis was conducted on the T_{back} data collected on the upper layer subjected to a heat flux of 30 kW·m^{-2} to determine the thermal conductivities of the char components. The target data for the inverse analysis was chosen as the slowly rising portion of T_{back} that was observed after 120 s in the gasification tests. Due to the high porosity of the chars produced in each layer, radiation was assumed to be the dominant mode of heat transfer through the char and the radiation diffusion approximation [125] was invoked to describe the thermal conductivity of all the char components. It was determined that a single value of β adequately described the T_{back} profile in the final 480 s of the curve. The thermal conductivities of all the intermediate components were defined as the mean of the thermal conductivities of the corresponding virgin component and char component. For the face yarn intermediate, this produced an expression with a constant term and a T^3 term. The agreement between the T_{back} predictions and the experimental data collected on the upper layer at a heat flux of 30 kW·m^{-2} are shown in Figure 6.9. The full set of parameters that were determined for the upper layer of the carpet composite to describe thermal transport to and within the solid sample are provided in Table 6.5.

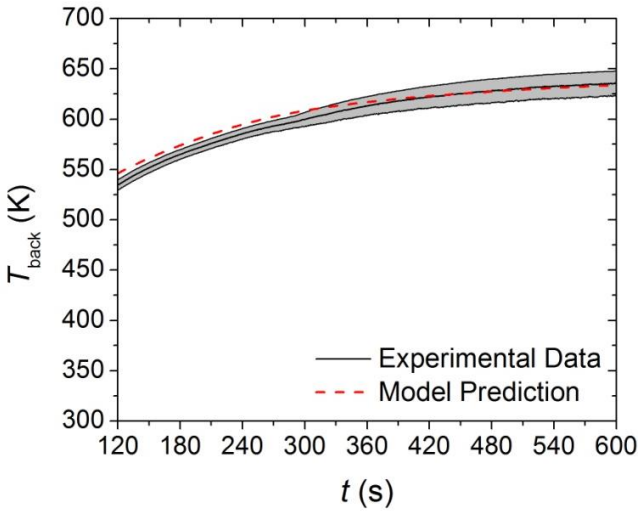

Figure 6.9. Final 480 s of experimental T_{back} curve measured in CAPA tests and corresponding model predicted curve for the upper layer exposed to a radiant flux of 30 kW·m^{-2}. The shaded region corresponds to two standard deviations of the mean experimental data.

An inverse analysis to determine the thermal conductivity of the virgin and melt components was conducted on the data collected in CAPA tests on the base layer at a heat flux of 30 kW·m^{-2}. The target data was identified as the slope of the initial increase in the T_{back}. Inadequate agreement between the model prediction and the experimental data was produced with a single, constant value for the thermal conductivity of the virgin and melt components. A linearly decreasing thermal conductivity for the $\text{Base}_{\text{virgin}}$ and $\text{Base}_{\text{melt}}$ components was able to adequately predict both the fast and slow rising portions of the initial 150 s of the T_{back} curve. The agreement between the experimental curve and the model prediction are provided in Figure 6.10.

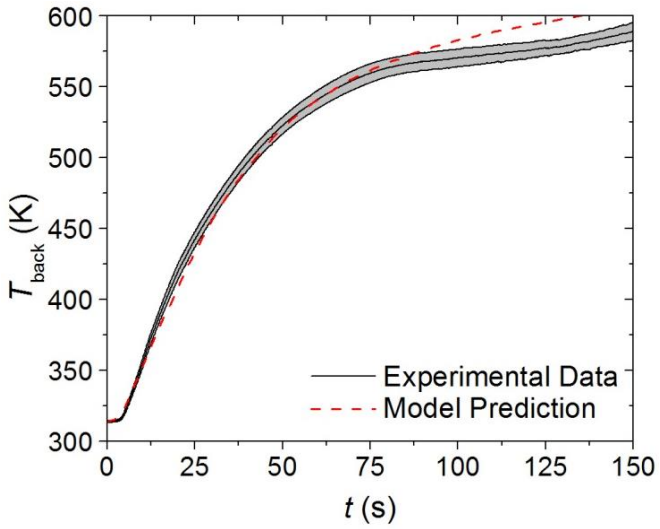

Figure 6.10. First 150 s of experimental T_{back} curve measured in CAPA tests and corresponding model predicted curve for the base layer exposed to a radiant flux of 30 kW·m^{-2}. The shaded region corresponds to two standard deviations of the mean experimental data.

The data collected in the CAPA tests on the base layer were analyzed to determine the thermal conductivity of the $\text{Base}_{\text{char}}$ component. The resulting experimental and predicted curves for the T_{back} of the base layer are provided in Figure 6.11. A single, constant value

of β in the βT^3 expression adequately described the T_{back} profile in the final 450 s of the curve. The thermal conductivity of the $Base_{int}$ component was defined as the mean between the $Base_{virgin}$ and $Base_{char}$ components, which resulted in a form with a constant, linear, and T^3 term. The full set of parameters that define the base layer thermo-physical properties are provided in Table 6.5.

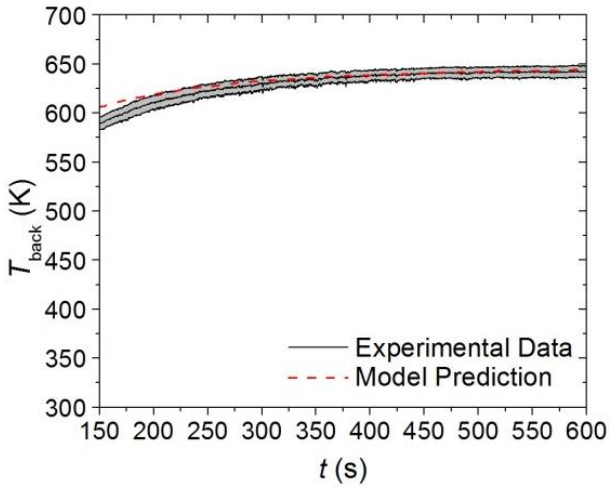

Figure 6.11. Final 450 s of experimental T_{back} curve measured in CAPA tests and corresponding model predicted curve for the base layer exposed to a radiant flux of 30 kW·m^{-2}. The shaded region corresponds to two standard deviations of the mean experimental data.

Section 6.3.2: Individual Layer Model Predictions

Section 6.3.2.1: Upper Layer (Consisting of Face Yarn and Middle Layer)

The model constructed from the parameters presented in Tables 6.1, 6.2 and 6.5 was independently validated against T_{back} data collected at incident heat fluxes of 50 and 70 kW·m^{-2} as well as *MLR* curves collected in CAPA tests conducted at incident heat fluxes of 30, 50, and 70 kW·m^{-2}. The model predicted curves and the experimental data are provided in Figure 6.12.

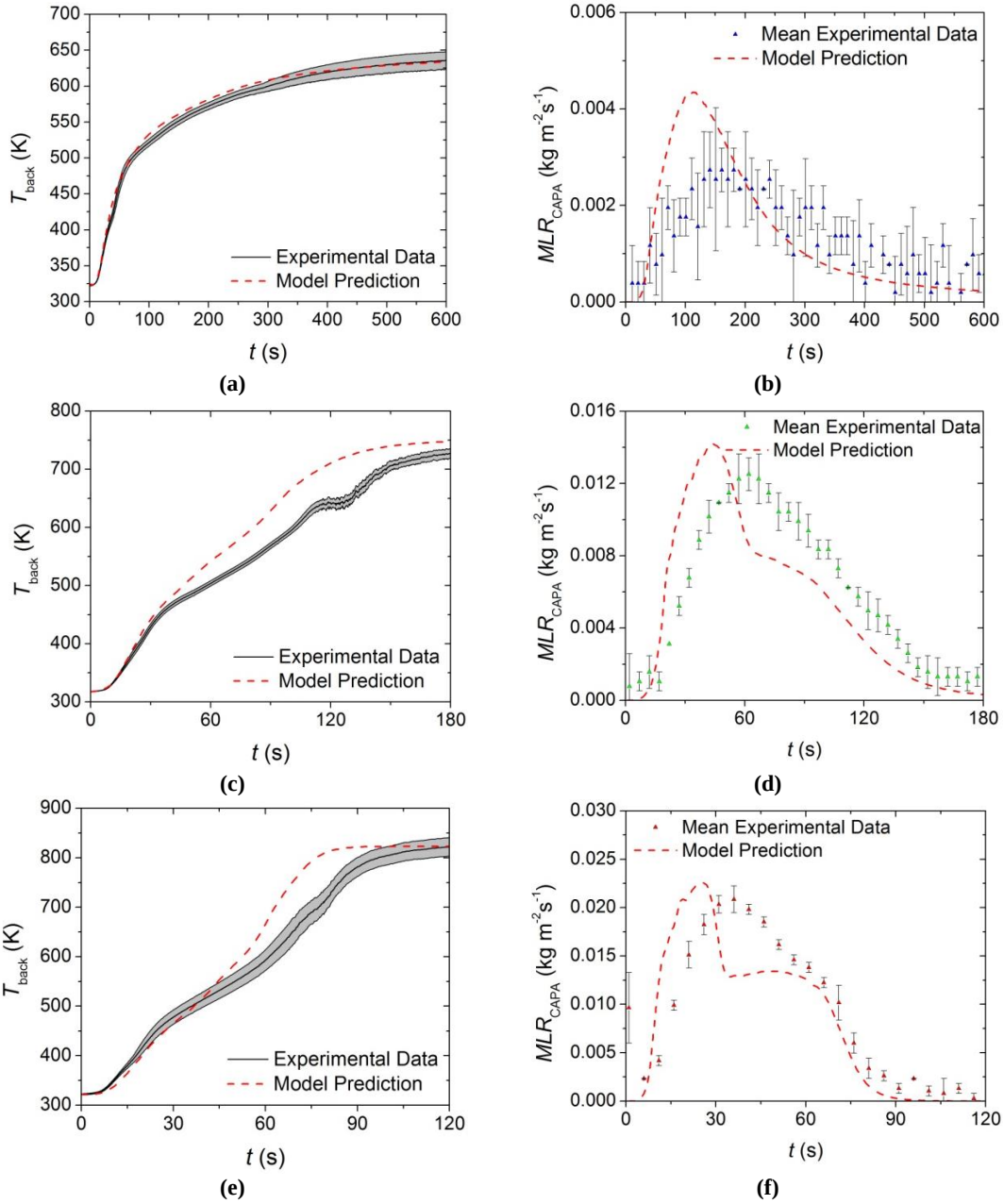

Figure 6.12. Experimental T_{back} and *MLR* curve collected in CAPA tests and corresponding model predicted curve for the upper layer exposed to radiant fluxes of (a) and (b) 30 kW·m^{-2}; (c) and (d) 50 kW·m^{-2}; and (e) and (f) 70 kW·m^{-2}. The shaded region and error bars correspond to two standard deviations of the mean experimental data.

The model for the upper layer captures the time to the initial increase of the T_{back} profile as well as the slope of the initial increase for all incident heat fluxes. The model also accurately predicts the final steady temperature at each heat flux. The model overpredicts the T_{back} from approximately 40 to 180 s at a heat flux of 50 kW·m^{-2} and overpredicts the T_{back} from 45 to 90 s at a heat flux of 70 kW·m^{-2}, although the qualitative

shape of each temperature prediction agrees with the experimental data. This overprediction may be attributed to systematic errors in the measurement of T_{back} due to sample deformation of the upper layer and poor thermal contact between the back surface of the sample and the aluminum foil. It may also be due to uncertainty in the measurement because of degradation of the high emissivity paint on the back surface of the foil above 600 K.

The model was able to accurately predict the total mass lost at all heat fluxes and the qualitative shapes of each *MLR* curve. The approximate time to initial mass loss and the approximate peak *MLR* were also well predicted at each heat flux. The model systematically overpredicted the rising edge of the *MLR* curve and underpredicted the time to the peak *MLR*. There was also a portion of the predicted curve after the peak *MLR* that underpredicted the experimental data at all heat fluxes.

The disagreement between the predicted *MLR* curves and the experimental curves may be attributed to possible compensation effects between the absorption coefficients and the thermal conductivities for the face yarn components. The measurements made to determine the absorption coefficient of the face yarn were conducted on a melted sample that had solidified, but the melted face yarn observed in the tests was characterized by rapidly regenerating bubbles that may have influenced the actual absorption coefficient and thermal conductivity of the layer. Though there was a possible compensation effect, and considering the complexity of the layer, the predictions provide adequate agreement with the experimental data over a range of conditions outside of the calibration conditions.

6.3.2.2. Base Layer

The model constructed from the parameters for the base layer presented in Tables 6.1, 6.2, and 6.5 was independently validated against T_{back} data collected at incident heat fluxes of 50 and 70 kW·m^{-2} as well as *MLR* curves collected at incident heat fluxes of 30, 50, and 70 kW·m^{-2}. The model predicted curves and the experimental data are provided in Figure 6.13.

The model tends to predict the experimentally observed time to the initial temperature rise and the slope of the initial temperature rise well at all incident heat fluxes. The model tends to overpredict T_{back} after about 50 s at heat fluxes of 50 and 70 kW·m^{-2}, although the temperatures measured at times later than 50 s into the tests for the higher heat fluxes correspond to temperatures significantly above 600 K, so there is some uncertainty about the validity of that data due to degradation of the high emissivity paint on the back surface of the sample. It is also possible that the glass reinforcement, which comprises a large fraction of the residual mass in the base layer and has a relatively low emissivity, compromised the well-defined emissivity at the back surface. A decrease in the emissivity of the measured surface manifests as artificially low T_{back} measurements.

The predicted *MLR* profiles tend to capture the overall trends in the experimental data at all heat fluxes. The initial rise to the peak *MLR* for the predicted curves follows the slope of each of the experimental curves with a slight lag in the time to the initial increase. The peak value is slightly underpredicted in each case, although the time to the peak *MLR* is captured well by the model.

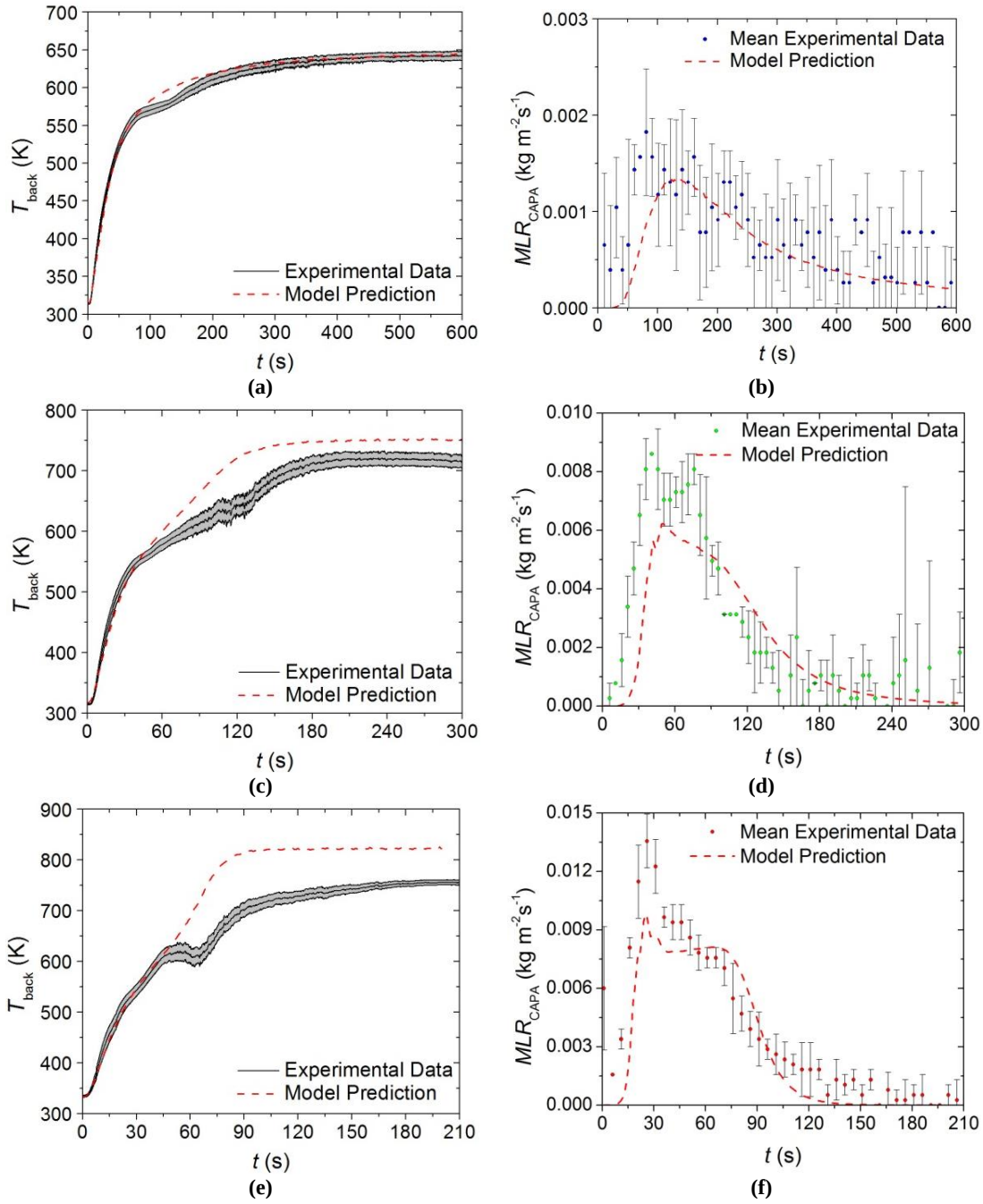

Figure 6.13. Experimental T_{back} and *MLR* curves collected in CAPA tests and corresponding model predicted curves for the base layer exposed to radiant fluxes of (a) and (b) 30 kW·m^{-2}, (c) and (d) 50 kW·m^{-2}, and (e) and (f) 70 kW·m^{-2}. The shaded region and error bars correspond to two standard deviations of the mean experimental data.

Section 6.3.3: Full Carpet Model Predictions

The individual upper layer and base layer model parameters that were validated against T_{back} and *MLR* data from CAPA tests were combined in a full carpet model to evaluate their

ability to predict the pyrolysis behavior of the full carpet composite. The thicknesses and densities of the middle layer and the base layer were modified based on a discrepancy in thickness measurements discussed in Section 6.2.1. The density definitions for the full carpet composite model are provided in Table 6.6.

Table 6.6. Thermal conductivity and density values for Final Full Carpet model. Modifications to property values from individual layer models are shown in bold.

Component	ρ [kg m^{-1}]	k [W m^{-1} K^{-1}]
Face Yarn		
Face Yarn$_{virgin}$	125	**0.12**
Face Yarn$_{melt}$	625	**0.12**
Face Yarn$_{int.}$	575	$\mathbf{0.06 + 3.5 \times 10^{-10} T^3}$
Face Yarn$_{char}$	34.5	$\mathbf{7 \times 10^{-10} T^3}$
Middle Layer		
Middle$_{1,virgin}$, Middle$_{2,virgin}$, Middle$_{3,virgin}$, Middle$_{4,virgin}$, Middle$_{3,melt}$, Middle$_{4,melt}$	**750**	**0.12**
Middle$_{char}$	**250.5**	$\mathbf{7 \times 10^{-10} T^3}$
Base Layer		
Base$_{virgin,}$ Base$_{melt}$	**1200**	$0.25 - 2.85 \times 10^{-4} T$
Base$_{int.}$	**1104**	$0.125 - 1.425 \times 10^{-4} T + 3.5 \times 10^{-10} T^3$
Base$_{char}$	**783.8**	$7 \times 10^{-10} T^3$

The T_{back} and *MLR* data predicted by the model of the full carpet constructed from the combination of the individually parameterized upper and base layer representations are labeled in Figure 6.14 as "Initial Model Prediction". The model was able to predict the qualitative trends in the experimental T_{back} curves at all heat fluxes. The approximate steady T_{back} was well predicted at 30 and 50 kW·m^{-2} and slightly overpredicted at 70 kW·m^{-2}. The shape of the *MLR* curve was well predicted at 30 kW·m^{-2}, but the agreement between the predicted curve and the experimental curve degraded at the higher heat fluxes. Though the model was able to predict the qualitative trends in the experimental data, the quantitative agreement required improvement.

All predicted temperature and *MLR* curves had a tendency to be lower than the experimental curves. This tendency may be attributed to the difficulties encountered with

testing and modeling the upper layer that led to a low thermal conductivity defined for the virgin face yarn and virgin middle layer components. It is also evident that, by separating the layers, the physical structure of the composite was compromised and the thermal transport within the sample was affected. To investigate the extent to which the structure of the carpet and interaction between layers affects thermal transport in the composite, the upper layer thermal transport was re-parameterized in the context of the full carpet composite.

The full carpet samples did not deform significantly during tests and the texture of the back surface of the full carpet samples guaranteed proper thermal contact between the sample and the aluminum foil. The target data for the inverse analysis to re-parameterize the upper layer was the T_{back} profile collected on the full carpet samples in CAPA tests conducted at a heat flux of 30 $kW \cdot m^{-2}$. It was hypothesized that the individually parameterized base layer model provided sufficient description of the actual tested base layer and the only independent parameters that were adjusted to improve agreement between the experimental data and the model prediction were the thermal conductivities of the upper layer components. The curves that were predicted when the thermal transport parameters were adequate to describe the target experimental data are plotted as "Final Model Prediction" in Figure 6.14. The changes made to the thermal conductivity definitions provided in Table 6.5 to generate the "Final Model Prediction" are provided in Table 6.6.

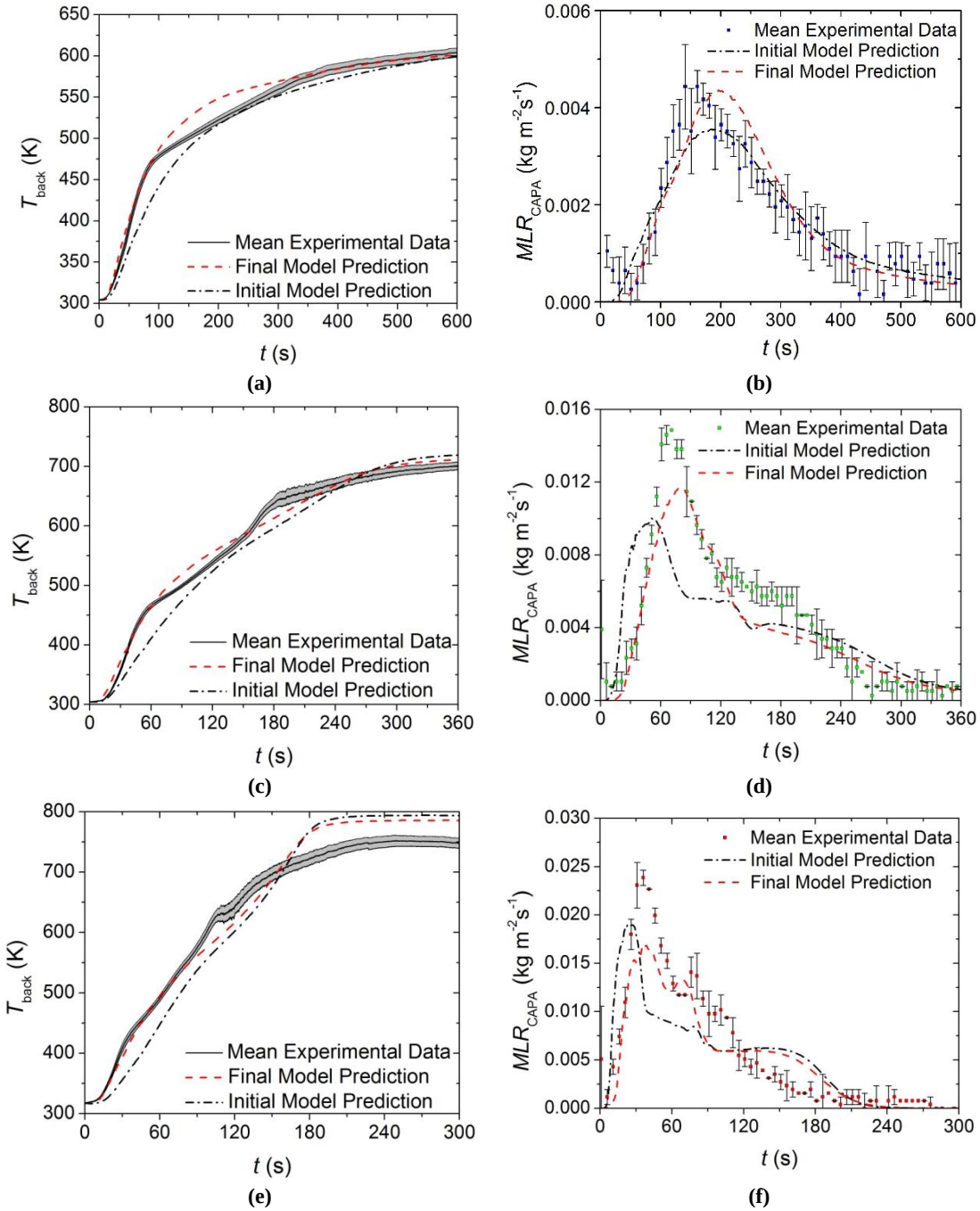

Figure 6.14. Experimental T_{back} and *MLR* curve collected in CAPA tests and corresponding model predicted curves for the full carpet composite exposed to radiant fluxes of (a) and (b) 30 kW·m^{-2}, (c) and (d) 50 kW·m^{-2}, and (e) and (f) 70 kW·m^{-2}. The shaded region and error bars correspond to two standard deviations of the mean experimental data.

There is an obvious improvement in the model predictions from the combination of the individually parameterized layers to the re-parameterization of the upper layer in the context of the full carpet composite. The temperature profiles predicted with the final full

composite model captured the time to the initial increase in the T_{back} and the slope of the initial increase at all heat fluxes. The entire T_{back} curve was well predicted at heat fluxes of 30 and 50 kW·m^{-2}, and alternated between underpredicting and overpredicting the T_{back} above 600 K at a heat flux of 70 kW·m^{-2}. An interesting observation is that the experimental T_{back} of the base layer and the full composite never reached temperatures higher than approximately 750 K, which corresponds to the peak *MLR* in the base layer TGA data. This temperature indicates the point in the tests at which the largest fraction of the volatile mass of the base layer is liberated from the solid, which leaves a matrix of fiberglass as residue. It is possible that a more comprehensive definition of the base layer that includes the properties of the fiberglass reinforcement would improve the agreement between the experimental data and the model predictions for the full carpet composite.

The initial increase in the *MLR* curve was predicted well by the model at all heat fluxes. The peak *MLR* was well predicted at 30 kW·m^{-2}, but the time to the peak was over predicted by approximately 50 s. At the higher heat fluxes, the time to the peak *MLR* was better predicted, but the peak value was underpredicted by larger percentages with each increase in the incident heat flux. The qualitative shape of the predicted curve at 30 and 50 kW m^{-2} agree with the experimental curve. The curve predicted at a heat flux of 70 kW m^{-2} showed a slowly decaying plateau from approximately 120 to 210 s that did not occur in the experiments. The mean error between the predicted *MLR* and the mean experimental *MLR* was calculated as 13% for 30 kW m^{-2} (mean *MLR* value of 0.00171 kg m^{-2} s^{-1}), 18% for 50 kW m^{-2} (mean *MLR* value of 0.00427 kg m^{-2} s^{-1}), and 28% for 70 kW m^{-2} (mean *MLR* value of 0.00850 kg m^{-2} s^{-1}). The mean error between the predicted *MLR* and the

mean experimental *MLR* was within the mean experimental uncertainty for all tested heat fluxes.

Section 6.4: Conclusions

This work presents several improvements to a relatively new methodology to parameterize pyrolysis models [142] and extends this methodology to a multilayered composite system. To the knowledge of the authors, this is the most complicated material system ever to be fully parameterized for a pyrolysis model. The developments to the existing methodology presented here include a focus on characterizing each layer of the composite individually, modeling STA data according to an approximation of the observed heating rate profiles, and the use of MCC tests to incorporate heat release rate predictions into the capabilities of the pyrolysis models.

The carpet sample was divided into three separate layers and the thermal degradation of each was characterized independently. The kinetics and energetics of the thermal degradation process were determined through an inverse analysis of STA data. The heats of combustion of the gaseous species produced in each degradation reaction were determined through analysis of data collected in MCC tests. The absorption coefficient of each layer of the initial material was calculated from data on the radiant flux transmitted through thin film samples. The carpet was divided into two layers for bench-scale gasification tests. These layers were independently investigated to characterize the thermal transport through the carpet composite by conducting inverse analyses on the back surface temperature data collected in these tests.

The models for the two individual layers of the carpet that were tested in the gasification experiments generated *MLR* and T_{back} predictions that agreed well with the

experimental data. The combination of these two layers produced predictions that had a fair agreement with experimental data collected on the full carpet composite. It was likely that, by separating the layers of the carpet and effectively compromising the structure of the composite, the thermal transport characteristics of the layers were affected. Qualitatively and quantitatively improved predictions were produced by re-parameterizing the thermal conductivity of the upper layer components in the context of the full carpet composite.

The previously used parametrization methodology enhanced by the aforementioned improvements produces pyrolysis models that are capable of predicting the fire response for highly complicated materials subjected to a wide range of conditions. It was shown that individual layer parameterization works to a significant degree and provides the ability to extrapolate results to different material structures, provided the properties of the additional material elements are available. It was also shown that the interfaces between macrostructural elements affect the overall heat transfer within the condensed phase, and high fidelity models require additional measurements on the structures that include any such interfaces for accurate characterization.

Chapter 7: Carbon Fiber/Epoxy Aerospace Composite

Section 7.1: Introduction

The primary test method for suitability of materials to act as airplane cabin materials relies on flame spread over an inclined surface of the material. By developing an accurate comprehensive pyrolysis model of the material, the test may be modeled and a greater insight and understanding about the physics that dominate flame spread may be extracted from test data. This improved understanding will aid in the design of future carbon fiber laminates intended for aerospace applications and may act as a screening method to determine the suitability of a material for airplane cabins. The methodology presented in this work has been has demonstrated in this chapter on a carbon fiber structural composite that is used in aerospace applications.

The carbon fiber laminate composite investigated in this chapter had many densely packed layers of carbon fiber tape that have been previously hypothesized to affect mass transport through the material. An objective of this investigation was to assess the degree to which the transport of gaseous volatiles was retarded by the high density of the carbon fiber layers. An additional objective was to investigate whether this complicated composite could be modeled as a homogeneous material to simplify the model and reduce computational expense.

The ThermaKin numerical pyrolysis modeling environment was used in this work to conduct inverse analyses on experimental data to indirectly measure thermo-physical properties and reaction parameters to describe the thermal degradation of the carbon fiber composite samples. ThermaKin was also used to generate gasification mass loss rate (*MLR*) and temperature distribution predictions for the sample material to validate the measured properties. By developing a fully parameterized model, it was possible to use the two-

dimensional formulation of ThermaKin to investigate the effect of in-plane conduction due to the laminate structure of the carbon fiber composite. A direct comparison has been made between the model developed through the procedures described in this chapter and a model developed for the same material by Quintiere et al. [58].

Section 7.2: Experiments and Analysis

Section 7.2.1: Material

The material that is the subject of this work is a carbon fiber laminate composite produced by Toray Co. in compliance with Boeing Material Specification (BMS) 8-276. The layup is made of 16 plies with an orientation defined by $[-45,0,45,90]_{2s}$, which results in a composite with orthotropic thermo-physical properties. The laminae are composed of continuous carbon fibers and the matrix material is an epoxy resin. The composite is produced in the form of a preimpregnated panel and is cure toughened at 450 K to satisfy BMS 8-276. Figure 7.1 displays the carbon fiber composite samples characterized through this investigation. Note from the figure that the composite has one face with a smooth surface finish and the other face has a rough surface finish due to the manufacturing process.

Figure 7.1. Picture that Includes All Surfaces of the Toray Co. BMS 8-276 Aerospace Composite [58]

Section 7.2.2: Experimental Methods

Section 7.2.2.1: Simultaneous Thermal Analysis

STA tests were conducted to measure the sample mass and heat flow rate to the sample as a function of temperature and time as the material underwent thermal degradation. The calibration and experimental testing procedures for the all STA tests conducted on the carbon fiber composite are described in Section 4.2.1.1. The STA tests used to collect data from which the thermal degradation kinetic and energetic parameters were determined were conducted with a heating rate of 10 K min^{-1} to a maximum temperature of approximately 1000 K. The test chamber was constantly purged with nitrogen flowing at a rate of 50 mL min^{-1} to investigate thermal degradation while eliminating oxidation and other unwanted heterogeneous reactions. Seven STA tests were conducted on carbon fiber composite samples to accumulate statistics and assess repeatability of the data sets. The samples for the STA tests were cut to a size such that the total mass of the sample ranged from 3 to 10 mg and the layered structure of the laminate was maintained.

The mass and *MLR* data collected in STA tests were analyzed through a manually iterative inverse analysis procedure using the ThermaKin modeling environment described in Section 4.2.1.1 to determine the thermal degradation kinetic mechanism. Acceptable agreement was defined for the carbon fiber composite as a maximum error of 10% in the prediction of the magnitude of MLR_{peak}, a maximum absolute error in the prediction of T_{peak} of 3 K, and a mean error of less than 2% in the normalized mass versus temperature curve. The resulting reaction schemes are presented in section 7.3.1.1.

The energetic parameters were determined through analysis of the heat flow rate data collected in STA tests described in Section 4.2.2.1. The range of data analyzed to determine the heat capacity corresponded only to the initial, unreacted components. Since the final residual mass was primarily composed of carbon fibers, the heat capacity of the char component was assumed equivalent to the heat capacity of graphite. The intermediate components that were produced and consumed in reactions during degradation were assumed to have the mean heat capacities of the component that reacted to produce the intermediate and the component that was produced when the intermediate was consumed. The acceptance criterion for this analysis required that the instantaneous relative difference between the time-dependent integrals of the predicted heat flow rate curve and the experimental curve remain less than 5% to verify the total energy absorbed by the sample in the model was equivalent to the total energy absorbed by the sample in the experiment throughout decomposition.

Section 7.2.2.2: Microscale Combustion Calorimetry

MCC tests were conducted according to the procedures described in Section 4.2.3.1. Three MCC tests were carried out on samples of the carbon fiber composite.

Samples for MCC tests were prepared identically to the samples tested in the STA. The sample mass, which ranged from approximately 2 to 5 mg was recorded and the sample was placed in a ceramic crucible. The tests were conducted at a heating rate of 10 K min^{-1} up to a final temperature of approximately 900 K.

The mean data collected from the three tests conducted on the carbon fiber composite required a shift of 11.5 K to higher temperatures to calculate a mean that was consistent with the mass loss process due to pyrolysis. The heats of combustion of the gases produced during thermal degradation of the carbon fiber composite samples were determined through an analysis of MCC data outlined in Section 4.2.3.1. Though qualitative agreement between the experimental and modeled *HRR* curves was important for determining the heat of combustion for each modeled gaseous species, the only formal acceptance criterion required that the total integrals of the predicted curve and the experimental curve agree to within 3%.

Section 7.2.2.3: Gasification Experiments and Analysis

CAPA tests were conducted on samples of the carbon fiber composite by following the procedure described in Section 4.2.5.1 with the rough surface and the smooth surface facing the heater subjected to radiant heat fluxes of 40, 60, and 80 kW m^{-2} with nitrogen used as the purge gas at a flow rate 225 SLPM. The number of samples available for this investigation was limited, so two tests were conducted with each surface facing the heater at heat fluxes of 40 and 60 kW m^{-2}, although only a single test with each surface facing the heater was conducted at a heat flux of 80 kW m^{-2}. An additional test was conducted at a heat flux of 40 kW m^{-2} with the surface that faced the heater painted for an emissivity of 0.95. Samples were prepared in a square geometry with a side of 0.08 m and were

positioned in the center of a square sheet of 0.00625 m thick Kaowool PM board with an edge dimension of 0.105 m. The well-defined emissivity provided by the paint applied to the back surface of the carbon fiber samples appeared to deteriorate at approximately 550 K. It was hypothesized that the surface finish of the composite changed a this temperature and the paint was unable to adhere to either surface above that temperature.

Due to the laminate structure of the carbon fiber composites studied in this investigation, it was hypothesized that the rate of in-plane heat conduction was larger than in-depth heat conduction. This hypothesis is consistent with measurements that have been made on carbon fiber/epoxy laminate composites [143,144]. An experiment was conducted to assess the importance of in-plane conduction relative to in-depth conduction in which a sample was irradiated under the cone heater while half of the surface was covered with 0.0127 m thick Kaowool PM insulation board. A picture of the prepared sample is provided in Figure 7.2.

The back surface temperatures were monitored throughout the test to facilitate an inverse analysis to determine the in-plane thermal conductivity. The rate of in-plane heat conduction was investigated with the two-dimensional formulation of the ThermaKin model in which the material and the Kaowool insulation that covered the sample were modeled. A low-density, low-heat capacity, high thermal conductivity layer approximately 10% the thickness of the sample was introduced to the geometric center of the sample and the thermal conductivity was adjusted as part of an inverse analysis on the back temperature data to determine the rate of heat conduction in-plane relative to the heat conduction in-depth.

Figure 7.2. Sample Prepared to Investigate In-Plane Heat Conduction

Several tests that utilized a variety of mixtures of nitrogen and oxygen were conducted to investigate the oxidation characteristics of the carbon fiber composite. One test was conducted with a heat flux of 40 kW m^{-2} in which the gas mixture that was introduced to the CAPA nominally consisted of 15 vol.% O_2 while the total flow rate of gas remained 225 SLPM (33.8 SLPM O_2/191.2 SLPM N_2). The oxygen concentration approximately 0.001 m from the front surface of the sample was measured as 15.0 ± 0.5 vol.% O_2 during this flow condition.

Four additional tests were conducted in which the residual mass from tests in nitrogen conducted at 60 kW m^{-2} were subjected to heat fluxes of 40 and 60 kW m^{-2} while 225 SLPM of nitrogen was injected into the CAPA for approximately ten minutes followed by ten minutes of laboratory air (approximately 21 vol.% O_2). The oxygen concentration approximately 0.001 m from the front surface of the sample was measured as 20.9 ± 0.5 vol.% O_2 during this flow condition. Three type K thermocouples were inserted in each sample to measure the temperature distribution throughout the tests. The successive phases of nitrogen and air flow were intended to yield a steady *MLR* in the first phase while producing a noticeable increase in sample temperature and *MLR* with the addition of oxygen to the test atmosphere.

Inverse analyses were conducted on the T_{back} data collected in CAPA tests conducted in nitrogen following the analysis procedure described in Section 4.2.5.1 to determine the parameters that define thermal transport at the surface and within the condensed phase. The T_{back} was generally uniform, with the maximum deviation from the mean value on the order of 5%. A default value for the mass transport coefficient was initially defined for all components ($2 \times 10^{-5}\ m^2\ s^{-1}$) in the model constructed in ThermaKin. This value was determined as high enough to allow all gaseous pyrolyzate to escape the condensed phase with no impedance to flow, and low enough that it would maintain the stability of the integration [24]. The mass transport coefficient was modified due to additional analysis after all other thermo-physical properties were determined (See Sec. 7.4.1.1.).

Section 7.3: Results

Section 7.3.1: Data Analysis for Property Evaluation

Section 7.3.1.1: Thermal Degradation Kinetics and Energetics Determination

The STA data collected on the carbon fiber composite samples was analyzed to determine the kinetics and energetics of the thermal degradation process as well as the heat capacity of the condensed phase components. The mean heating rate profile measured in the all of the STA tests on the carbon fiber was approximated by Equation 4.7 in ThermaKin simulations. The agreement between the experimentally observed and modeled heating rate profiles is evident in Figure 7.3.

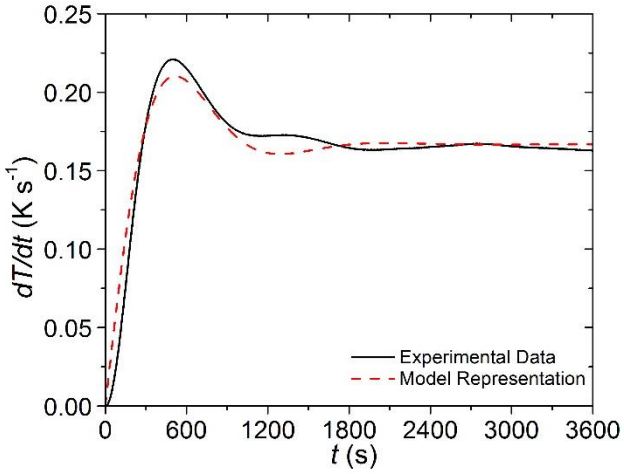

Figure 7.3 Experimentally observed and modeled heating rate histories typical of the Simultaneous Thermal Analysis (STA). The coefficients for Equation 4.7 that describe the modeled curve are the following: b_1 = 0.167 K s^{-1}, b_2 = 0.0025 s^{-1}, b_3 = 0.0041 s^{-1}, b_4 = −0.534.

It was assumed that the reaction mechanism that described thermal degradation of the carbon fiber composite consisted completely of consecutive reactions because only the epoxy resin underwent degradation. Analysis of the mass loss rate data and the heat flow rate data for the composite initially resulted in five consecutive thermal degradation reactions. Though there was only a single distinct peak in the mass loss rate data curve, the heat flow rate data curve had a complicated shape that necessitated several additional reactions. The final reaction mechanism determined through analysis of STA mass loss data is summarized in Table 7.1 and the experimental and simulated mass loss curves corresponding to the pyrolysis of carbon fiber are plotted in Figure 7.4, where the error bars correspond to two standard deviations of the mean. The mean relative error due to scatter between the individual tests was approximately ± 9%. During the analysis, it was determined that the final of five reactions could be eliminated if the fourth reaction was defined as a second-order reaction. Reduction of the reaction mechanism by one reaction was advantageous in terms of computational expense.

Table 7.1. Effective reaction mechanisms for each layer of the carpet composite and the heats of reactions. Positive heats represent endothermic processes (absorb energy during the reaction).

#	Reaction Equation	A (s^{-1})	E (J mol^{-1})	h (J kg^{-1})

1	$\text{Carbon Fiber}_{\text{virgin}} \rightarrow 0.989\text{Carbon Fiber}_{\text{int,1}} + 0.011\text{Carbon Fiber}_{\text{volatiles}}$	4.09×10^5	9.18×10^4	1.8×10^4
2	$\text{Carbon Fiber}_{\text{int,1}} \rightarrow 0.902\text{Carbon Fiber}_{\text{int,2}} + 0.098\text{Carbon Fiber}_{\text{volatiles}}$	6.16×10^{19}	2.78×10^5	3.8×10^4
3	$\text{Carbon Fiber}_{\text{int,2}} \rightarrow 0.911\text{Carbon Fiber}_{\text{int,3}} + 0.089\text{Carbon Fiber}_{\text{volatiles}}$	1.23×10^{21}	3.01×10^5	-1.8×10^4
4	$0.5\ \text{Carbon Fiber}_{\text{int,3}} + 0.5\ \text{Carbon Fiber}_{\text{int,3}} \rightarrow 0.888\text{Carbon Fiber}_{\text{residue}} + 0.112\text{Carbon Fiber}_{\text{volatiles}}$	8.00×10^5	1.50×10^5	-1.0×10^4

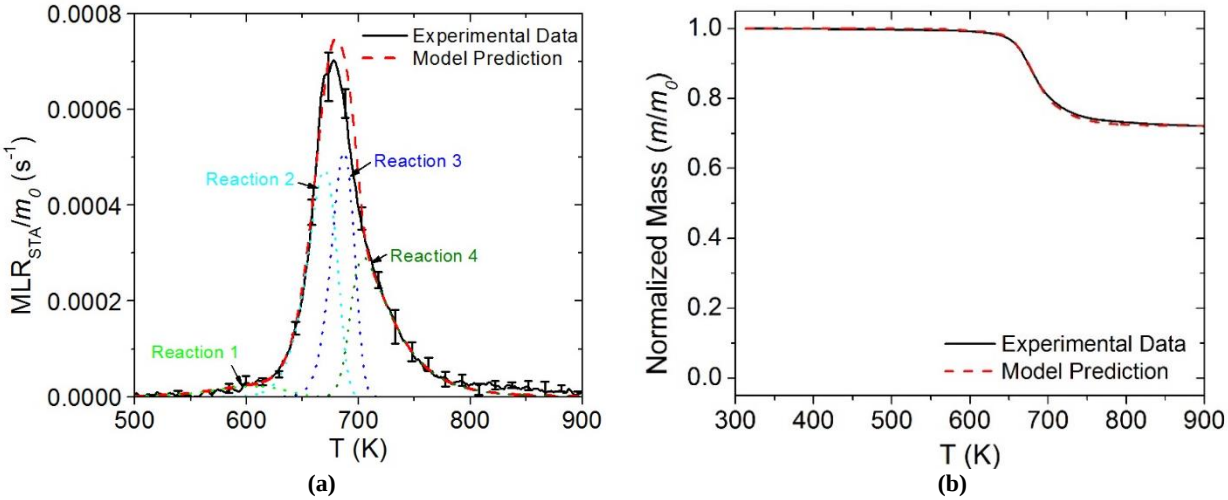

Figure 7.4. Normalized mass loss rate (MLR) and normalized mass data collected in STA experiments and model predicted curves for the carbon fiber composite.

Criticism has been levied against methods that analyze data collected at a single heating rate with claims that 10 K min^{-1} is not representative of fire conditions. Common thought follows that since materials are subjected to a wide range of heating rates in fire scenarios, only kinetics determined through isoconversional analyses on multiple heating rate data sets are able to extrapolate to a range of heating rates. *MLR* predictions made with the model parameterized in this chapter and a previous study on the carbon fiber composite [58] which utilized a model-free method to analyze data collected at several heating rates are compared to experimental data in Figure 7.5. Figure 7.5a displays both predicted curves and the experimental data at a heating rate of 10 K min^{-1} and Figure 7.5b shows the same curves at a heating rate of 30 K min^{-1}.

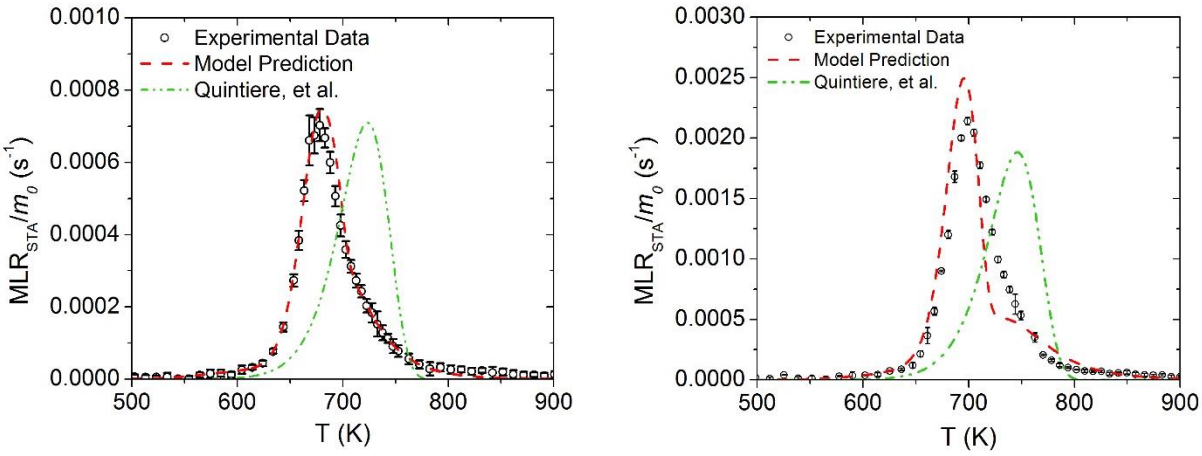

Figure 7.5. Normalized mass loss rate (*MLR*) and normalized mass data collected in STA experiments and model predicted curves for the carbon fiber composite.

The discrepancy between the experimental data and the prediction of the *MLR* curve at a heating rate of 30 K min^{-1} is likely due to the propagation of small errors in each of the four reactions defined in the kinetic mechanism. As the difference between the experimental heating rate and the calibration heating rate is increased, the mass loss associated with each reaction shifts slightly in temperature. Superposition of the reactions due to this shift caused an over-prediction of the maximum *MLR* measured at 30 K min^{-1} and a subsequent under-prediction of the falling edge of the *MLR* curve. Although the mean instantaneous error between the predicted and experimental *MLR* curves at 30 K min^{-1} was 28%, the mean instantaneous error in the predicted normalized mass curve was 0.4%, which indicates that the prediction of the overall thermal degradation process is well captured at all temperatures at a heating rate of 30 K min^{-1}.

The curve predicted by Quintiere et al. captures the qualitative shape of the experimental data curve at both heating rates although the temperature at which the maximum *MLR* occurs in each case is over-predicted by approximately 50 K. The maximum experimental *MLR* was captured at 10 K min^{-1} by the model produced by

Quintiere et al. although the maximum *MLR* measured at 30 K min^{-1} was under-predicted by approximately 10%. The consequences of over-predicting the temperature at which the maximum *MLR* occurs and under-predicting the magnitude of the maximum *MLR* can potentially include a gross under-prediction of the severity of a fire event, particularly in the early stages of the fire. The disagreement between the model produced by Quintiere et al. and the model produced in this work is likely the result of the method used to determine the kinetics of the degradation process, and possibly also because of differences in experimental data caused by variations between the apparatus used to conduct TGA in each study.

A linear temperature-dependent relationship was found for the heat capacity of the Carbon $Fiber_{virgin}$ component. The uncertainty due to scatter in the heat flow rate data over the entire temperature range tested was approximately ± 19%, although it was approximately ± 8% in the temperature range from which data was analyzed to determine the heat capacity of the unreacted component.

The residual mass that remained at temperatures above approximately 800 K was characterized by a porous structure that compromised the thermal contact between the sample and the crucible and yielded unreliable heat flow rate measurements. Compounding the issues caused by the structure of the sample was the decreased sensitivity of the heat flow rate measurement at high temperatures. This was exemplified by a rapid increase in the heat flow rate from 800 K to approximately 1100 K that did not correspond to a physically realistic process. The Carbon $Fiber_{residue}$ component was assigned a linear, temperature-dependent heat capacity that was calculated from a least-squares linear

regression conducted by Butland and Maddison on a survey of data for the heat capacity of graphite [145].

The intermediate components that were produced and consumed during thermal degradation of the sample material could not be isolated for direct measurement of the heat capacity. The heat capacities of Carbon Fiber$_{int,1}$, Carbon Fiber$_{int,2,}$ and Carbon Fiber$_{int,3}$ were defined as a linear combination of the heat capacity defined for the Carbon Fiber$_{virgin}$ and Carbon Fiber$_{residue}$ components evaluated between 500 and 750 K. The heat capacity of the Carbon Fiber$_{int,2}$ component was defined as the mean of the heat capacities of Carbon Fiber$_{virgin}$ evaluated at 500 K and Carbon Fiber$_{residue}$ evaluated at 750 K. The heat capacity of Carbon Fiber$_{int,1}$ was defined as the mean of the heat capacity of Carbon Fiber$_{virgin}$ evaluated at 500 K and the heat capacity of Carbon Fiber$_{int,2}$. The heat capacity of Carbon Fiber$_{int,3}$ was defined as the mean of the heat capacity of Carbon Fiber$_{residue}$ evaluated at 750 K and the heat capacity of Carbon Fiber$_{int,2}$. The heat capacity of each component defined in the reaction mechanism are provided in Table 7.2.

Table 7.2. Heat capacity values for each component in the carbon fiber composite.

Component	c [J kg^{-1} K^{-1}]	Method
Carbon Fiber$_{virgin}$	2.4T + 160	STA
Carbon Fiber$_{int,1}$	1415	Assumed
Carbon Fiber$_{int,2}$	1470	Assumed
Carbon Fiber$_{int,3}$	1525	Assumed
Carbon Fiber$_{residue}$	0.7T + 1054	[145]

The heat flow rate data collected in the STA tests is plotted in Figure 7.6 along with the sensible enthalpy baseline constructed from the heat capacities from Table 7.2 and component masses modeled by the mechanism provided in Table 7.1. The curve features local minima at 515 K and 663 K and a maximum at approximately 690 K. It is clear from the Figure 7.6 that the experimental heat flow rate curve is below the sensible enthalpy baseline curve between 500 and 680 K and the maximum that occurs at 690 K is above the

baseline. The convention adopted for this work is that values that are negative with respect to the sensible enthalpy baseline represent exothermic processes and values that are positive represent endothermic processes. Though the entire process of thermal degradation of the carbon fiber composite is endothermic (positive heat flow rates), there are exothermic processes that contribute to its thermal degradation. Though this behavior is unusual for materials that undergo non-oxidative pyrolysis, this phenomenon has been observed for materials with high char yields by Li and Stoliarov [91].

The integral between the experimental heat flow rate curve and the sensible enthalpy baseline was defined as the enthalpy absorbed by the sample undergoing thermal degradation. Each heat of reaction was assigned to the reaction that occurred at the temperature range corresponding to the heat flow rate peak. The local minimum that appeared at the lowest temperature in the heat flow rate curve did not correspond to a mass loss event and the magnitude of the feature was relatively small, so the minimum was ignored in analysis. The single reaction that described the mass loss rate curve maximum was split into two reactions (Reaction # 2 and 3 defined in Table 7.1), each of which had a maximum mass loss rate that corresponded to one of the two local extrema that were observed at 663 and 690 K. This allowed an exothermic heat of reaction to be assigned to the reaction with the peak at 663 K and an endothermic heat of reaction at the reaction corresponding to the peak at 690 K to account for the unusual shape of the heat flow rate curve. The remainder of the analysis yielded an exothermic heat of reaction for the first reaction and an endothermic heat of reaction for the final reaction.

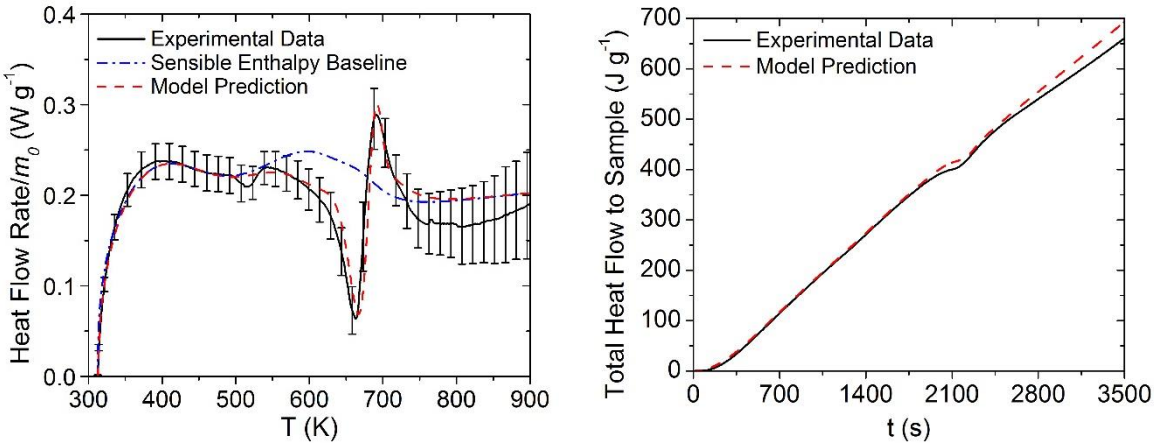

Figure 7.6. Normalized heat flow rate and integral heat flow rate data collected in STA experiments and model predicted curves for carbon fiber composite

The heat absorbed during the thermal degradation reaction defined by Quintiere et al. [58] was considerably larger than the heats of all of the reactions defined in the current investigation. The heat flow rate curves predicted in the current investigation and the investigation conducted by Quintiere et al. are plotted in Figure 7.7 with the experimental heat flow rate data. Note that since the maximum heat flow rate predicted by Quintiere et al. is approximately one order of magnitude greater than the peak predicted in the current investigation, the data has been plotted on semi-logarithmic axes.

The heat of gasification for the carbon fiber composite was measured with two techniques by Quintiere et al. The value determined through analysis of cone calorimeter data was 1.8 x 10^6 J kg^{-1} and the value determined in DSC tests was 2.85 x 10^6 J kg^{-1}, although the integral of the heat flow rate curve predicted with the parameters defined in that investigation up to 900 K was approximately 3.6 x 10^6 J kg^{-1}. With all of the heats of gasification defined here in terms of the original mass of the sample. The discrepancy between the measured and predicted values in that investigation is significant and the reason for the discrepancy is unclear. The integral of the heat flow rate curve measured in the current work up to 900 K was approximately 6.6 x 10^5 J kg^{-1} and the value predicted

by the model parameterized through this work was 7.0 x 10^5 J kg^{-1}, both of which are defined in terms of the original sample mass. It is possible that the disagreement between the heat of gasification values measured in these two studies was caused by the type of DSC apparatus utilized for each. It has been noted that the heats of reactions are more accurately determined with the apparatus used in this investigation, a heat flux DSC apparatus, than with a power-compensation DSC apparatus, the apparatus used by Quintiere et al.

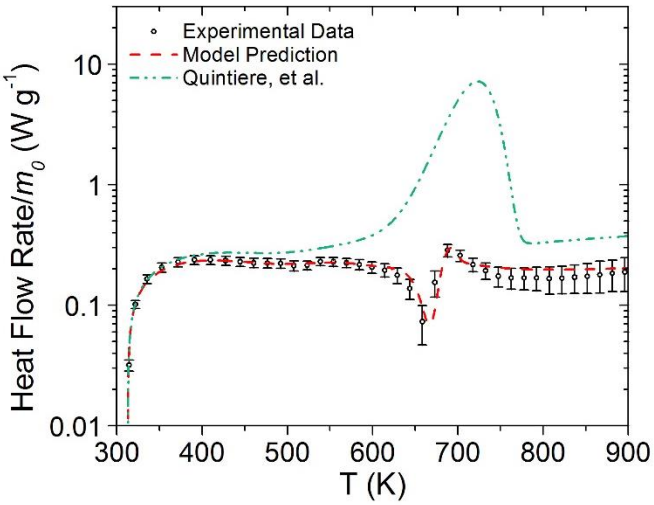

Figure 7.7. Normalized heat flow rate and integral heat flow rate data collected in STA experiments and model predicted curves for carbon fiber composite

Section 7.3.1.2: Heat of Combustion Determination

The MCC data collected on the carbon fiber composite at a set heating rate of 10 K min^{-1} (0.167 K·s^{-1}) were analyzed using the degradation kinetics determined from analysis of STA data. The heating rate profile observed in MCC experiments was different than the profile observed in STA experiments, but was adequately described by the form of Equation 4.7. The agreement between the experimentally measured and the heating rate profile instituted in the ThermaKin model for the MCC is displayed in Figure 7.8.

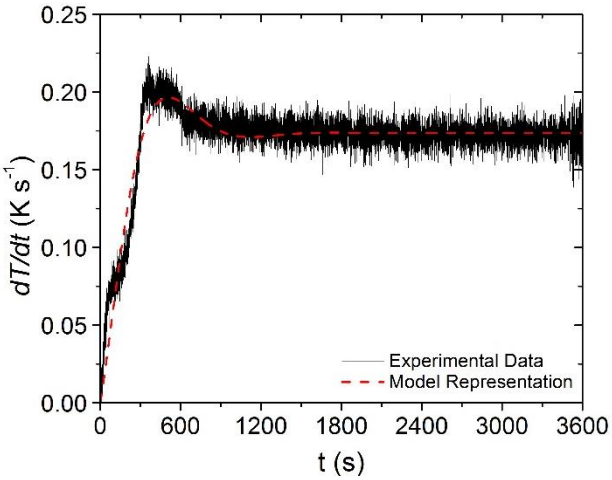

Figure 7.8. Experimentally observed and modeled heating rate histories typical of the Microscale Combustion Calorimetry (MCC) experiments conducted in this work. The coefficients for Equation 4.7 that describe the modeled curve are the following: b_1 = 0.174 K s^{-1}, b_2 = 0.0036 s^{-1}, b_3 = 0.0052 s^{-1}, b_4 = 0.091.

The mass loss associated with the first thermal degradation reaction appeared to correspond to a zero magnitude heat release and the heat of combustion was defined as zero to maintain agreement between the experimental and simulated *HRR* curves. The heats of combustion of the remaining three thermal degradation reactions were determined as nonzero values that are displayed in Table 7.3. Contrary to the convention used to define the heats of reaction, positive values in Table 7.3 correspond to exothermic processes.

The experimental and predicted *HRR* curves and integral *HRR* curves are provided in Figure 7.9. The error bars in the *HRR* curve are defined as two standard deviations of the mean. The mean relative error corresponding to the error bars is approximately ±9%. The heats of combustion defined in Table 7.3 produce a curve with an integral in the range of 600-900K that is within 0.1% of the integral of the experimental curve. The aggregate heat of combustion determined in this investigation was calculated from these data as 2.7 $\times 10^7$ J kg^{-1} of volatiles, compared to the value measured by Quintiere et al. [58] which was 2.65 $\times 10^7$ J kg^{-1} of volatiles. These values are within the uncertainty associated with reproducibility of measurements made with the MCC apparatus (6%).

Table 7.3. Effective heat of combustion values for the volatile species released in each reaction. Positive heats of combustion are exothermic.

Volatile Species	h_c (J kg^{-1})
Carbon Fiber$_{\text{volatiles,reaction 1}}$	0
Carbon Fiber$_{\text{volatiles,reaction 2}}$	2.4×10^7
Carbon Fiber$_{\text{volatiles,reaction 3}}$	2.3×10^7
Carbon Fiber$_{\text{volatiles,reaction 4}}$	3.7×10^7

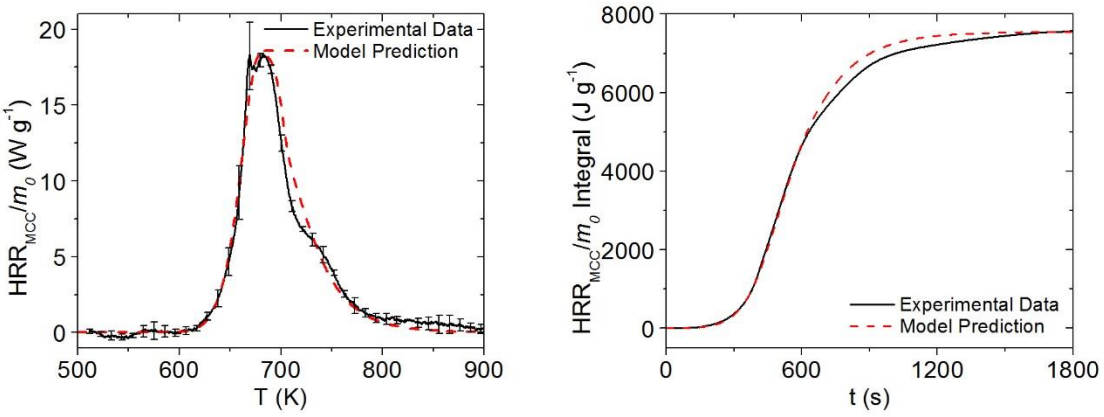

Figure 7.9. Normalized heat release rate and integral heat release rate data collected in MCC experiments and model predicted curves for the carbon fiber composite.

Section 7.3.1.3: Thermal Transport Parameter Determination

The thermal conductivity of all of the components defined in this pyrolysis model for the carbon fiber composite were determined through the inverse analysis procedure described in Section 4.2.5.1. The structure and stability of the composite eliminated the possibility of separating the individual layers to decrease the thickness to facilitate direct measurement of the absorption coefficient with the method described in Section 4.2.4.1. It was observed during gasification tests on the composite that all components were optically dark, nontransparent to visible light, and it was known that these components were graphitic. To make the simulations consistent with this observation, the absorption coefficient of all components was defined sufficiently high to ensure no radiation was allowed to transmit through the surface of the sample (100 m^2·kg^{-1}).

It was known prior to modeling that the char components were comprised almost entirely of carbon, and the emissivity of Carbon Fiber$_{residue}$ was expected to be similar to graphite. The emissivity of graphite was measured at elevated temperatures as approximately 0.86 [106] and was defined as the emissivity of the Carbon Fiber$_{residue}$ component. This value has been used to describe the emissivity of char components in several previous related studies [134,146].

The emissivity of the carbon fiber composite was not directly measured in this work. The surface emissivity of carbon fiber composites composed of a several different types of reinforcements and matrix polymers has been measured by researchers at Sandia National Laboratories [54]. The measurements included spectrally-averaged measurements of the irradiation with angles of incidence classified as near-normal and near-grazing as well as a hemispherical total emissivity. The orientation of the radiation source in the measurement of the spectrally-averaged total hemispherical emissivity is the most representative of the heating scenario for a post-flashover enclosure fire, but it is not the most representative for the heating scenario in the gasification tests presented here. The heating scenario that agrees most closely with the gasification tests was realized in the measurement of the spectrally-averaged emissivity with near normal irradiation (20° angle of incidence).

The composite measured in the study conducted at Sandia that is most similar to the material in this work in terms of component materials and structure had a near normal emissivity measurement of 0.86 for the smooth surface and 0.90 for the rough surface. By comparing the experimental data that was collected with the rough surface and the smooth surface facing the heater, it was determined that the difference in surface finish did not

significantly affect the T_{back} or *MLR* data. In an effort to simplify the model, the emissivity of the Carbon Fiber$_{virgin}$ component, as well as all the Carbon Fiber$_{int.}$ components, was defined as 0.86.

The thickness of the carbon fiber composite sample was observed to increase in gasification tests as individual layers partially delaminated from the composite. This increase in thickness occurred gradually over the course of the gasification tests, and the observation of this increase is consistent with observations made in previous work conducted on carbon fiber composites [54,58,59]. Though there was scatter in the measured increase in thickness, the measurements have been approximated for this model as an increase of 100% of the original thickness of the sample regardless of the radiant heat flux to the sample, which resulted in a sample that was approximately 6.4 mm thick at the end of the simulated gasification. Figure 7.10 shows pictures of the virgin carbon fiber composite prior to and after testing to emphasize the change in thickness observed to occur through bench-scale gasification tests.

Figure 7.10. Comparison of the Thickness of the Virgin Carbon Fiber Composite to the Residual Composite after Cooling from a Radiant Heating Gasification Test at 60 kW m^{-2}

ThermaKin has the ability to model intumescence by scaling the contribution of gases to the overall volume by a factor related to the local composition. To simulate this increase in the thickness of the entire sample, the density of each component produced through a thermal degradation reaction was defined to decrease systematically from the density of the reactant that decomposed to form the product. The thickness was defined to increase by 25% over the course of each reaction. The product density was decreased from the reactant density by a factor equal to the stoichiometric coefficient corresponding to the reaction divided by the factor by which the thickness increased, e.g. the density for Carbon $\text{Fiber}_{\text{int,1}}$ was calculated as $(1521\ \text{kg m}^{-3})\left(\frac{0.989}{1.25}\right)$. The definitions for the densities of all components are provided in Table 7.4. The gases were assumed not to contribute to the volume of the sample in all simulations conducted in this work.

Table 7.4. Full set of thermo-physical properties defined in the carbon fiber composite pyrolysis model.

Component	ρ [kg m^{-3}]	k [W m^{-1} K^{-1}]	ϵ	κ [m^2 kg^{-1}]
$\text{Carbon Fiber}_{\text{virgin}}$	1521	$0.59 - 0.00065T$	0.86	100
$\text{Carbon Fiber}_{\text{int,1}}$	1203.4	$0.295 - 0.000325T + 2.75 \times 10^{-10}T^3$	0.86	100
$\text{Carbon Fiber}_{\text{int,2}}$	904.6	$0.295 - 0.000325T + 2.75 \times 10^{-10}T^3$	0.86	100
$\text{Carbon Fiber}_{\text{int,3}}$	706.3	$0.295 - 0.000325T + 2.75 \times 10^{-10}T^3$	0.86	100
$\text{Carbon Fiber}_{\text{residue}}$	548.8	$5.5 \times 10^{-10}T^3$	0.86	100

The thermal conductivities of virgin and residual components in the carbon fiber composite were determined through inverse analyses conducted on T_{back} data collected in the CAPA tests conducted with an incident heat flux of 40 kW m^{-2} using the ThermaKin modeling environment. The initial rise of the T_{back} data curve was chosen as the target for the $\text{Carbon Fiber}_{\text{virgin}}$ component because this was the only component that affected the T_{back} curve early in the tests. The model prediction for the composite is compared to the experimental data in Figure 7.11. The shaded region in the experimental T_{back} curves represents two standard deviations of the mean. The temperature prediction was not

sensitive to the thermal transport parameters of the residual and intermediate components for the time range displayed in the figure and all components were defined with the same thermal conductivity for this portion of the analysis.

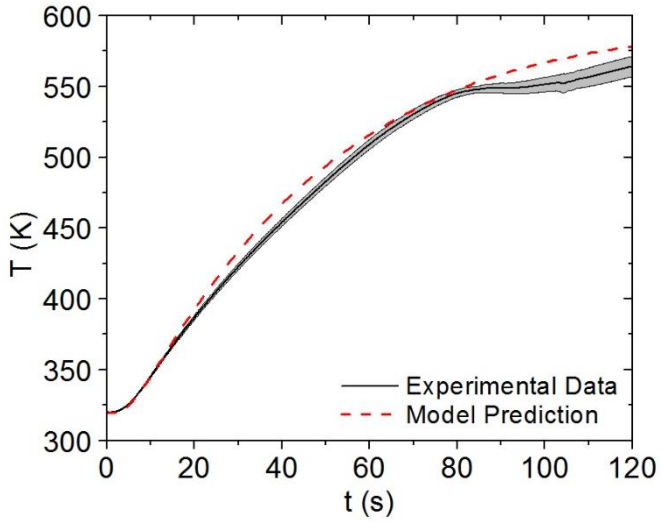

Figure 7.11. First 120 s of experimental Tback curve measured in CAPA tests and corresponding model predicted curve for the carbon fiber composite exposed to a radiant flux of 40 kW·m^{-2}. The shaded region corresponds to two standard deviations of the mean experimental data.

The target data for the inverse analysis to determine the thermal conductivity of the residual components was chosen as the portion of T_{back} that was collected after 120 s in to the gasification tests, with a particular focus on the final 200 s. Due to the high porosity and emissivity of the carbonaceous residual mass, radiation was assumed to be the dominant mode of heat transfer through the sample when Carbon Fiber$_{residue}$ was the major component and the radiation diffusion approximation was invoked to describe the thermal conductivity of the residual mass. The full set of parameters that were determined for the composite to describe thermal transport to and within the solid sample are provided in Table 7.4.

Section 7.3.2: Model Validation

Predictions of the T_{back} and *MLR* of the carbon fiber composite from the fully parameterized pyrolysis model are plotted in Figure 7.12 against the experimental data. The error bars for the experimental *MLR* data represent two standard deviations of the mean data. The figure also includes predictions from models parameterized with the property values determined by Quintiere et al. [58].

All of the experimental T_{back} data curves have a noticeable discontinuity that occurred when the temperature reached approximately 550 K. Above this temperature, the data measured at heat fluxes of 60 and 80 kW m^{-2} were noisy and the shape of the curves was irregular. The temperature 550 K did not appear to correspond to any features in the *MLR* curves or the STA data and it was hypothesized that it was associated with decomposition of the highly emissive paint applied to the back surface of the sample. As a result of this hypothesis, the data collected above the 550 K threshold was considered unreliable. The rise in temperature up to this threshold was highly repeatable at all temperatures and was well predicted at 40 and 60 kW m^{-2}. The slope of the initial rise in temperature predicted at 80 kW m^{-2} was well predicted although the time to the onset of temperature rise was slightly over-predicted.

The experimental *MLR* data collected at all heat fluxes are characterized by a single distinct peak as well as a local maximum/inflection point approximately 60 to 180 s after the peak. The *MLR* data gradually decreased to zero following the shoulder in the data. All of the *MLR* predictions made with the default mass transport definition ($\lambda = 2.0 \times 10^{-5}$ $m^2 s^{-1}$) captured the rising edge of the experimental curve. The peak of the experimental curve

was well predicted at 40 kW m^{-2} and over-predicted by greater margins with increasing heat flux. The qualitative shape of each predicted curve does not agree with the corresponding experimental curve. The curves predicted at each heat flux tended to over-predict the magnitude of the peak of the experimental curve and the points collected between the peak and the shoulder feature. The predicted curves all tended to under-predict the magnitude of the *MLR* curve from the shoulder until the end of the test.

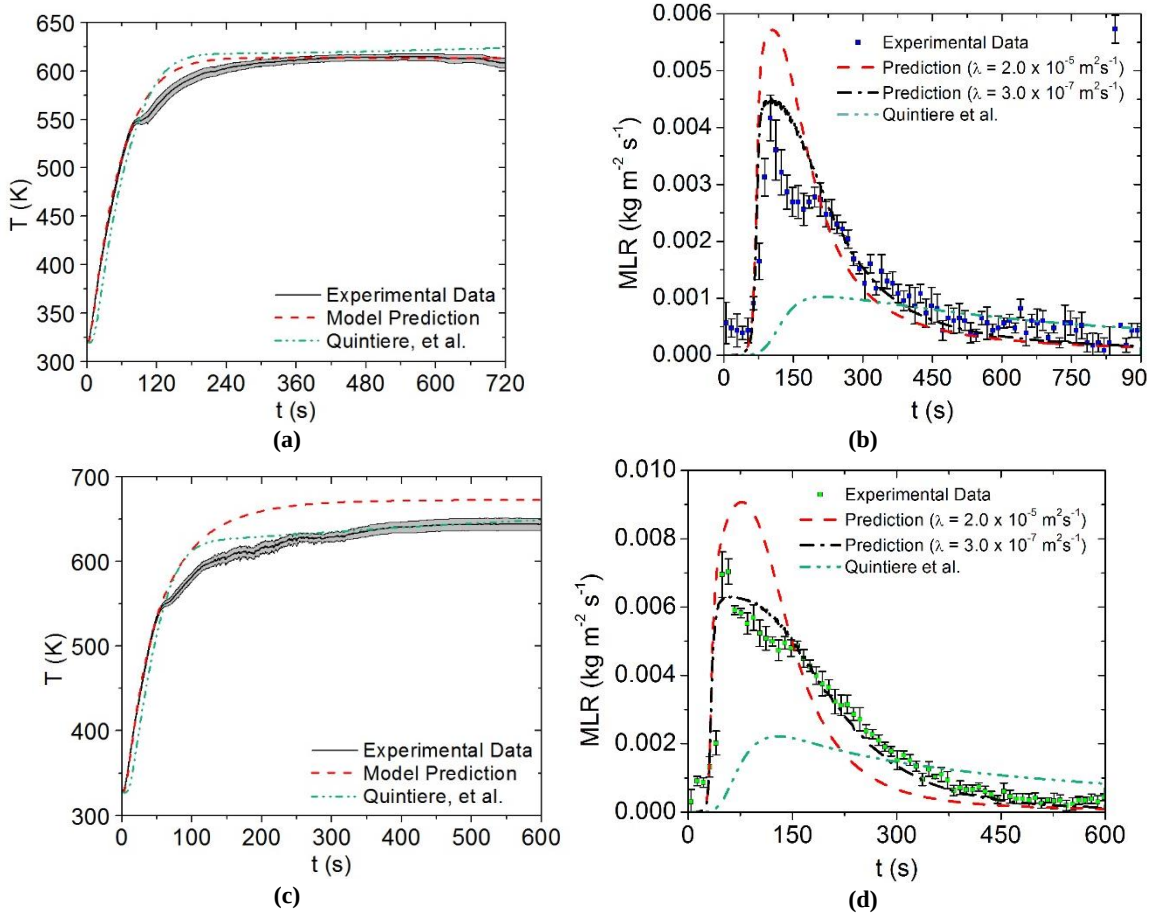

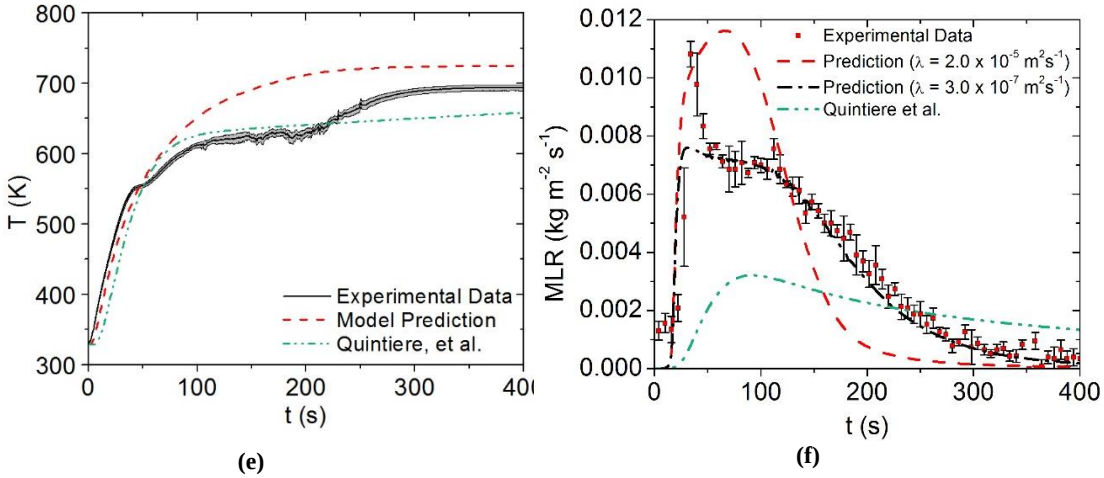

(e) **(f)**

Figure 7.12. Model-predicted and experimental Tback and *MLR* data collected in CAPA tests at incident heat fluxes of: (a) and (b) 40 kW m^{-2}, (c) and (d) 60 kW m^{-2}, and (e) and (f) 80 kW m^{-2}. Shaded Regions and error bars indicate two standard deviations of the mean experimental data.

The back temperature profile predicted by the model parameterized with the values determined by Quintiere et al. has a slightly worse agreement than the model parameterized in this work at 40 kW m^{-2} and a better agreement at the higher heat fluxes. These agreements are misleading because the data collected above 550 K is of limited reliability. It appears that the initial thermal conductivity is similar to the value determined in this work because predictions from both models match the initial increase in temperature, although due to the slightly delay in the initial increase of the temperature, it is likely that the initial heat capacity defined by Quintiere et al. is too large. Even though the model predictions agree with the experimental data from this work, the *MLR* curves are not well predicted. The shortcomings of the property set determined by Quintiere et al. may be caused by the simplicity of the kinetic mechanism, but it is much more likely that the seemingly incorrectly determined heat of reaction was too large and decreased the magnitude of the *MLR* curves.

Section 7.3.2.1: Investigation of Mass Transport Effects

Whereas the pyrolysis of common polymers is characterized by the entire irradiated surface releasing pyrolyzate gas, the gasification of the carbon fiber composite featured few localized points on the surface where pyrolyzate gas escaped from the solid. This observation indicated that the structure of the carbon fiber composite contributed to mass transport effects, which has been shown to be affected in highly cross-linked polymers like the epoxy in the composites studied in this work [147]. The effect of a reduced mass transport coefficient on the measured *MLR* was verified during modeling by adjusting the default mass transport coefficient downward to account for resistance to the free flow of pyrolyzate within the sample. The mass transport coefficient that made the predicted *MLR* curves achieve quantitative and qualitative agreement with the experimental *MLR* curves collected at all heat fluxes was 3.0×10^{-7} $m^2 s^{-1}$. The *MLR* curve predicted by the model parameterized with the lower mass transport coefficient is plotted in Figure 7.12. Of note is that the temperature predictions were unaffected by the adjusted mass transport coefficient.

It is evident in Figure 7.12 that the qualitative shape of the tail of the experimental *MLR* curves are predicted by the model at each heat flux. The time to the peak *MLR* is well represented by the model at all heat fluxes, although the magnitude of the peak is under-predicted for the 60 and 80 kW m^{-2} cases. The overall agreement between the model predictions and the experimental *MLR* data was improved with the mass transport coefficient defined as 3.0×10^{-7} $m^2 s^{-1}$. The mean instantaneous error between the predicted curve and the experimental curve was 28.8% at 40 kW m^{-2}, 21.5% at 60 kW m^{-2}, and was 18.2% at 80 kW m^{-2}. The time to the maximum *MLR* was predicted to within 10 seconds at each heat flux and the magnitude of the maximum *MLR* was predicted to within 1% at

40 kW m^{-2}, although the prediction of the maximum *MLR* deteriorated at higher heat fluxes as a compromise with overall agreement.

A first-order approximation calculation of the internal pressure due to gas buildup in the composite during pyrolysis was performed using the gas concentrations calculated with ThermaKin parameterized with the decreased mass transport coefficient. According to the simulation, the maximum pyrolyzate gas concentration found in the sample was approximately 28 kg m^{-3} at a temperature of 670 K. The mean molar mass of the gaseous species produced during pyrolysis of epoxy resin and similar polymers is approximately 0.28 kg mol^{-1} [148–150]. The pressure approximated through this crude calculation was on the order of 5 x 10^6 Pa. Measurements of the internal pressures in carbon fiber laminate composites have been as high as approximately 1.013 x 10^6 Pa (10 atm) [151] and the tensile strength of the Toray composite tested in this work has been measured as 2.7 x 10^9 Pa [152] at room temperature. The internal pressure caused by the reduced mass transport coefficient is reasonable because it is of the same order of magnitude but lower than the peak internal pressure that has been previously measured and it is orders of magnitude lower than the tensile strength of the material, which is consistent with the absence of mechanical failure during observations of the gasification tests.

Section 7.3.2.2: Investigation of In-Plane Conduction

The T_{back} data collected from the tests to investigate the effect of in-plane conduction relative to in-depth conduction are plotted as discrete points in Figure 7.13. Each data point represents the mean value from four points across the length of the back surface of the sample (parallel to the edge of the insulation on the sample surface). These data points were collected at sixteen locations across the back surface of the sample

(perpendicular to the edge of the insulation). The inverse analysis on these data resulted in the highly conductive layer defined as 10% the thickness of the sample that had a thermal conductivity of 50 W m^{-1} K^{-1}. Though the agreement between the model prediction and the experimental data shown in Figure 7.13 is not perfect, the prediction provides a reasonable estimate for the in-plane thermal conductivity of the composite. Using the well-known expression for the conductivity of materials layered in parallel to the direction of heat flow, Equation 7.1, the thermal conductivity of the mixture that has been simulated may be calculated. The symbols in Equation 7.1 are the following: $\boldsymbol{k_j}$ is the thermal conductivity of component $\boldsymbol{j}$, $\boldsymbol{V_j}$ is the volume fraction of component $\boldsymbol{j}$, and $\boldsymbol{k}$ is the effective thermal conductivity of the mixture.

$$k = \sum_{j=1}^{N} V_j k_j \tag{7.1}$$

The in-plane thermal conductivity of the carbon fiber composite is approximately 4.8 W m^{-1} K^{-1}. This value appears to be reasonable because literature values for the in-plane thermal conductivity for carbon fiber composites range from ten to fifteen times larger than the in-depth thermal conductivity [143,144]. A mean value of the thermal conductivity of the unreacted component evaluated over the temperature range of 300-600 K is approximately 0.32 W m^{-1} K^{-1}. The ratio between the in-plane thermal conductivity determined here and the in-depth thermal conductivity is 15. A one-dimensional simulation was conducted with the additional highly conductive layer with a thickness of 10% the thickness of the composite to identify the effect of the layer on in-depth conduction. The T_{back} profiles produced by the one-dimensional model were identical with and without the

highly conductive layer, which confirmed that the presence of this additional layer did not affect in-depth conduction.

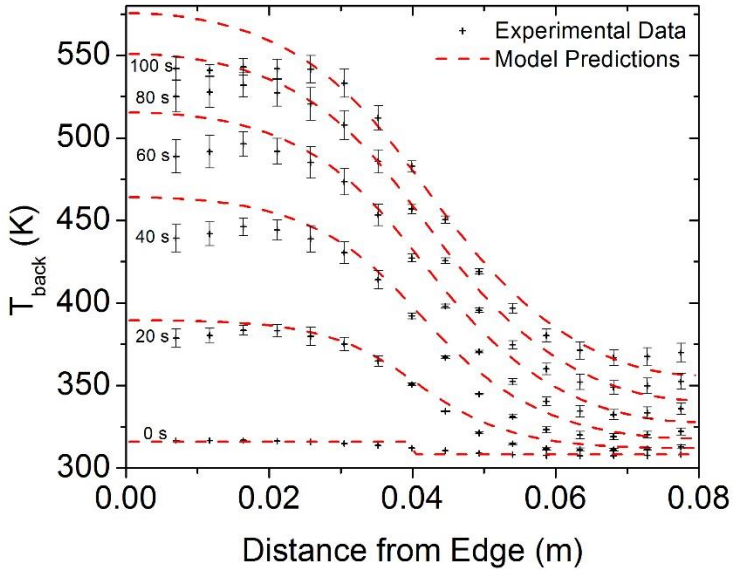

Figure 7.13. Experimental Data and model Predictions of Temperature Distribution Across the Back Surface of the Sample at Various Times After Radiant Exposure. Error Bars Are Associated with Two Standard Deviations of the Mean Experimental Data.

Section 7.3.2.3: Investigation of Oxidation

The test that was conducted in a 15% oxygen atmosphere at a heat flux of 40 kW m^{-2} was intended to provide insight about the sensitivity of pyrolysis of the carbon fiber composite to oxidation. Since the reinforcement fibers in the composite were made of carbon, which is susceptible to oxidation at high temperatures, it was hypothesized that the presence of oxygen would affect the *MLR* and T_{back} data curves. The T_{back} and *MLR* data curves collected in 15% oxygen and the mean data collected in nitrogen are displayed in Figure 7.14. The shaded region in Figure 7.14a and the error bars in Figure 7.14b correspond to two standard deviations of the mean. The scatter in the T_{back} data collected in 15% O_2 had approximately the same magnitude as the scatter in the mean data collected in 100% N_2 although it has not been plotted to ensure clarity of the figure.

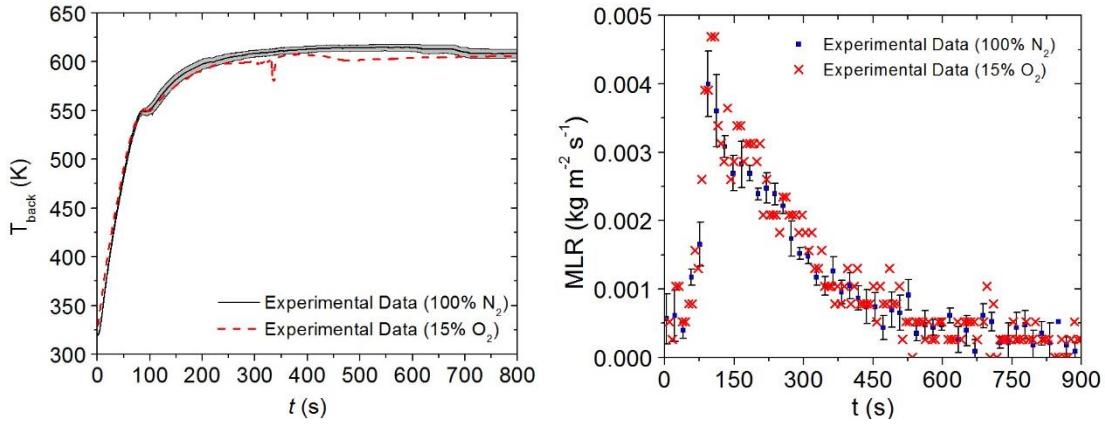

(a) **(b)**

Figure 7.14. Tback and MLR curves for the carbon fiber composite collected at 40 kW m^{-2} in 100% N_2 and 15% O_2 atmosphere.

It is evident from the figure that the introduction of oxygen to the gasification test on the undegraded sample did not significantly change the temperature distribution through the sample or the *MLR* history at 40 kW m^{-2}. The point of discontinuity in the T_{back} curve that occurred at approximately 325 s was likely caused by degradation of the highly emissive paint on the back surface of the sample and was not associated with oxidation. The expected effect of oxidation was an increase in both T_{back} and *MLR*. The T_{back} data collected in 15% O_2 was similar to the data collected in 100% N_2 and *MLR* collected in 15% O_2 was generally within the scatter of the data collected in 100% N_2.

The tests conducted on the residual mass samples in an air atmosphere at 40 and 60 kW m^{-2} were intended to determine the effect of oxidation of the carbon fiber reinforcement on the temperature distribution and *MLR* history after the majority of the epoxy resin had volatilized. An attempt was made to determine the oxidation kinetics from these experimental data, although it was ultimately concluded that oxidation had only a subtle effect on the pyrolysis process. The *MLR* and T_{back} data collected at 60 kW m^{-2} are displayed in Figure 7.15. The error bars represent two standard deviations of the mean of

the data collected from the three thermocouples. These variations are due to the distances from the surface of the sample to each thermocouple.

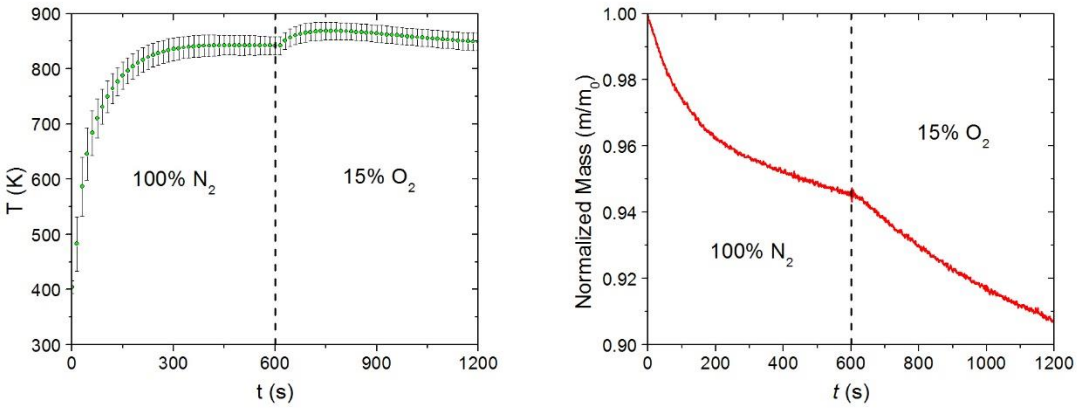

(a) **(b)**

Figure7.15. Tback and MLR curves for the carbon fiber composite collected at 60 kW m^{-2} in tests with 600 s of 100% N_2 followed by 600 s of 21% O_2/79% N_2 atmosphere.

The plots of Figure 7.15 show that a change in the pyrolysis process occurred approximately 600 seconds into the test which manifested as a temperature increase and a more rapid decrease in the sample mass. The increase in the mass loss rate is due to an increase in the reaction rate caused oxidation and the increase in the temperature is caused by additional energy in the sample because of the exothermicity of the oxidation reaction. The increase in the *MLR* and the back surface temperature due to the presence of oxygen was relatively small at both heat fluxes. It may be concluded from these data that oxidation does not significantly affect the pyrolysis process when residual carbon fiber samples are subjected to heat fluxes up to 60 kW m^{-2}. This result is consistent with observations made during radiant heating tests of carbon fiber composite samples [54], which concluded that the carbon fiber surface temperature must be approximately 1173 K for oxidation to occur.

Section 7.4: Conclusions

A complete set of thermo-physical properties and reaction parameters were determined for a carbon fiber structural composite through the systematic methodology presented throughout this dissertation. STA tests were conducted on samples of the composite and analysis was conducted to determine the reaction mechanism, heats of reaction, and the heat capacity for all identified components. The reaction mechanism was independently validated against *MLR* data collected at 30 K min^{-1}. Analysis of MCC data provided the heats of combustion for the volatile species evolved in each thermal degradation reaction and verified the complexity of the reaction mechanism.

Several bench-scale gasification tests were conducted on the composite with the CAPA in which the T_{back} and *MLR* data were collected. Inverse analyses on the T_{back} data allowed the extraction of thermal transport parameters for the composite. There did not appear to be a difference imposed on the collected data due to whether the smooth or textured face of the composite was facing the heater during the gasification tests. Resistance to mass transport within the sample was observed due to the structure of the carbon fiber reinforcement and the highly cross-linked epoxy resin which was accounted for by reducing the mass transport coefficient for all components by almost two orders of magnitude. By modifying the mass transport coefficient, the agreement between the model prediction and experimental data improved significantly.

Additional CAPA tests were conducted to investigate the effect of oxygen in the test atmosphere on the pyrolysis process. A 15% oxygen atmosphere had no effect on the data collected at 40 kW m^{-2} and appeared to have a small effect on data collected in tests on residual mass in an approximately 21 vol.% oxygen atmosphere. These data agreed with

previous observations that the temperature required for surface oxidation was not achieved with an irradiance of 60 kW m^{-2}. The in-plane thermal conduction was approximated by analyzing data from a test with partially obstructed radiant flux to the top surface of the sample using the two-dimensional formulation of ThermaKin. It was determined that in in-plane thermal conductivity was approximately fifteen times larger than the in-depth thermal conductivity in the temperature range of 300 to 600 K.

With the exception of the heats of combustion of the volatile species produced through degradation of the carbon fiber composite, all of the parameters that defined the model were validated against data collected outside the calibration conditions. Though the set of parameters determined through the methodology presented in this work were not validated at other orientations or larger scales, it is expected that similar results will be achieved as long as all boundary conditions are well defined.

Chapter 8: Fiberglass Reinforced Polyester Composite

Section 8.1: Introduction

An important application of comprehensive pyrolysis models is in the design of building materials that have a specific and predictable fire response. This application is particularly important for advanced composites for which quantification of flammability properties through destructive testing may be prohibitively expensive. The work presented in this chapter is focused on application of the methodology to a fiberglass reinforced unsaturated polyester (UP) laminate composite, which has been identified as the most common combination of reinforcement and matrix phases [153] for laminate composites. An objective of this application was to individually characterize each constituent to demonstrate the ability to develop a constituent-based model that was capable of simulating the results of gasification tests conducted on composite materials with arbitrary composition. Through this methodology, a single set of material properties was developed for each constituent and subsequently validated. The resulting model was extrapolated to various composition ratios and evaluated for the ability to predict the experimentally measured *MLR* from radiation-driven gasification experiments at various thermal exposures. This application demonstrates the possibility of using a comprehensive pyrolysis model to predict the fire response of combinations of well-defined components, which may be used in the composite manufacturing industry to tune the fire response of materials according to their composition.

Section 8.2: Modeling

The ThermaKin modeling environment was used in inverse analyses and to predict the results of gasification tests. The material behavior was modeled as zero-dimensional

for STA and MCC experiments. A one-dimensional model was produced to conduct inverse analyses to determine the thermal transport parameters and for the final *MLR* predictions from bench-scale gasification tests.

An additional feature of the ThermaKin modeling environment that was not explained in Chapter 2 is the treatment of the dependence of the thermal conductivity and the mass transport coefficient of mixtures of components on the concentration and relative orientation of the components. A mixture of components may be modeled in ThermaKin as layers oriented normal to the direction of the flow of heat or mass or parallel to the direction of flow for the purpose of determining an effective property value for the mixture using the form of Equation 8.1. In the equation, V_i is the volume fraction of species i, k_i is the thermal conductivity of species i, and θ is a user-defined input value for the mixture in the range from zero to one that defines the fraction of the material that is modeled as oriented parallel to the flow direction. The default value of θ (θ = 0.5) was defined for all of the other models presented in this manuscript.

$$k = \theta \sum_{i=1}^{N} V_i k_i + (1-\theta) \frac{1}{\sum_{i=1}^{N} \frac{V_i}{k_i}} \tag{8.1}$$

This expression, and the associated treatment of the properties of mixtures, is important for the FRP composite studied here because the structure of the composite was not explicitly defined in the model. Rather, the material was modeled as a homogeneous mixture of the components to reduce unneeded complexity in the model which was observed by Kim et al. [67]. The contrast between the thermal conductivity values for the constituent materials necessitated some freedom to account for deviations from the idealized default mixture rule. The heat transfer weight factor, θ, was set to zero in all

models that represented the composites in bench-scale tests to establish the heat transfer processes as occurring across layers of the homogeneous material oriented perpendicular to the material surface.

Section 8.3: Experiments and Analysis

Section 8.3.1: Materials

Samples were prepared using wax-free, general purpose unsaturated polyester (UP) resin and 10 ounce, style 7500, E-glass fabric with a plain weave. The resin was formulated to cure when combined with methyl ethyl ketone peroxide (MEKP) in the amount of 1.25% of the mass of the resin. All materials were purchased from Fiber Glast Developments Corporation.

The hand lay-up technique was selected for fabrication of the composite samples. A mold that was 21.5 inches by 9.5 inches and 0.5 inches deep was used to ensure each fabricated sheet had the same dimensions. A layer of wax was applied to the mold to ensure that the sample could be removed from the mold without compromising the sample structure. Each sample consisted of 16 layers of fiber reinforcement to achieve an overall thickness ranging from 5 to 7 mm. The orientation of the reinforcement layers was not varied between alternating layers. The fabrication method required an individual layer of reinforcement to be placed in the mold followed by manual application of the resin liquid system which was allowed to permeate through the fiberglass. This process was repeated until all of the reinforcement layers were included in the composite. The sample was allowed to cure at room temperature for 24 hours followed by a 1 hour oven post-cure at the glass transition temperature of the polyester resin (343 K). The glass transition temperature was determined through analysis of STA data conducted on uncured resin samples.

This fabrication method proved to be relatively crude, and the measured composition of the fabricated composites deviated from the design compositions of 40, 50, and 60 wt% resin by approximately ± 6 wt%. The actual compositions were determined by measuring the mass of the composite samples and factoring out the mass of the glass, which was independently measured. The composite fabricated using the hand lay-up technique with the most ideal and uniform distribution of resin that exhibited complete saturation of the fiber reinforcement was achieved with an equal mass of resin and reinforcement.

Deviations from this ideal composition resulted in minor imperfections in the samples such as the formation of small air pockets and non-uniform distribution of resin through the composite for samples with excess glass and resin, respectively. The measured composition ratios of the fabricated samples were 41, 48, and 54 wt% resin. The composite samples were 5.6 (±0.3), 6.3 (±0.1) and 6.9 (±0.4) mm thick, respectively. The density of the samples was measured at room temperature as 1600 (±12), 1620 (±16), and 1640 (±31) kg m^{-3}, respectively. An example of the fabricated composite samples is shown in Figure 8.1. The surface of the sample that was exposed to the ambient air during the room temperature cure possessed a glossy finish while the surface in contact with the mold had a matte finish.

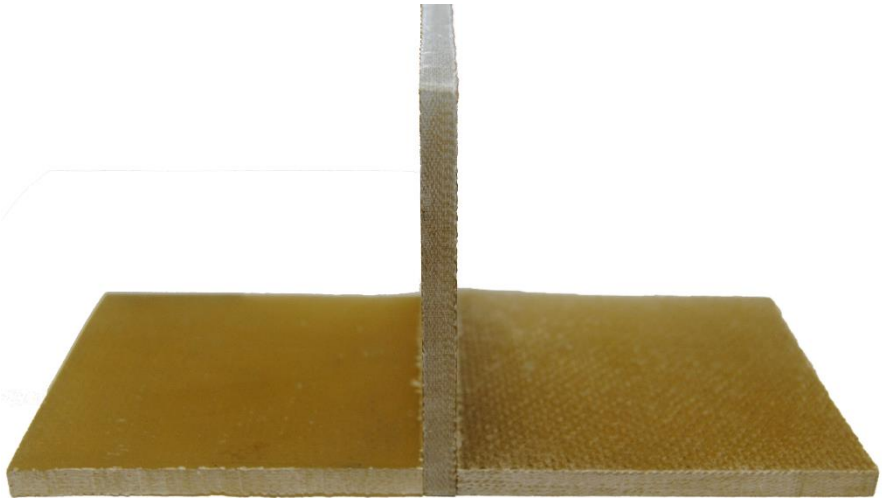

Figure 8.1. Fiberglass sample fabricated using a hand lay-up method with woven fabric and unsaturated polyester resin (top/side/bottom).

Pure UP resin samples were fabricated for independent material property evaluation. The UP resin prepared for bench-scale testing was 5.6 (±0.1) mm thick with a density of 1240 (±9) kg m^{-3}. Sheets of UP resin with thicknesses in the range of 0.9 to 1.4 mm were fabricated by curing the UP resin on a sheet of aluminum foil for milligram-scale testing and broadband radiation absorption determination to facilitate the assumptions regarding the heat transfer mechanisms within each measurement technique.

The density of the E-glass was calculated as the compliment to the resin density in the composite samples. This calculation required the previously determined values for the mass and measured density of the UP resin, the mass of E-glass in each sample, and the mass and volume of the composite samples. The effective density of the glass phase was calculated as 2260 (±140) kg m^{-3}, which was slightly lower than literature values that typically report the density of E-glass between 2500-2600 kg m^{-3} [154]. The difference was probably due to incomplete saturation of the fiberglass reinforcement during fabrication that resulted in air pockets within the sample. The uncertainty in the density calculation was due to error propagation from measurements of samples of all the compositions.

Section 8.3.2: Experimental Methods

Section 8.3.2.1: Simultaneous Thermal Analysis

STA tests were conducted on samples of the pure, cured UP resin following the testing and calibration procedures described in Section 4.2.1.1. The furnace was continuously purged with 50 mL min^{-1} of nitrogen to maintain an anaerobic environment throughout the STA experiments. UP resin samples were prepared with masses between 6 and 10 mg and were pressed into the bottom of the sample crucible to ensure adequate thermal contact. The samples were stored in a desiccator for a minimum of 48 hours after oven curing and prior to testing to minimize the effects of moisture content on the experimental data. The temperature program consisted of linear heating at a constant heating rate of 10 K min^{-1} to a maximum temperature of 900 K. The experimental procedure was repeated seven times to evaluate the reproducibility of the results.

The UP resin lost 93% of the initial mass over the course of the heating profile. The apparatus was known to lose sensitivity at elevated temperatures, which was compounded by the loss of thermal contact as the sample decomposed and resulted in unphysical heat flow rate data when only the char species were present in the sample. Seven additional STA tests were performed on char samples harvested from bench-scale gasification tests conducted at 70 kW m^{-2} in order to obtain accurate experimental measurements. Samples of the E-glass fibers used as the reinforcement in the composites were also tested although apparent issues with thermal conductivity led to unrealistic heat flow rate measurements.

The heat flow rate data collected in DSC tests were analyzed according to the procedure described in Section 4.2.2.1 to calculate the apparent heat capacity and the heats of the thermal degradation reactions. The specific heat capacity was determined from the experimental curve for the portions of the profile where no reactions occurred. This direct

analysis was employed for the initial UP resin prior to onset of thermal degradation and for the fully decomposed char. The heat capacities of the intermediate species were specified based on assumed expressions that related the properties of the intermediates to the properties of the virgin and char components.

The curve that represented the heat flow to the sample was integrated to produce a profile for the total heat flow to the sample as a function of time. The final value was representative of the energy required to fully decompose the material, the heat of gasification. The total heat flow profile was used as an optimization target for determination of the heats of decomposition. The characterized model was deemed adequate when the mean instantaneous relative error between the experimental and model-predicted total heat flow to the sample were within 1%.

Section 8.3.2.2: Microscale Combustion Calorimetry

MCC tests were conducted on the UP resin to determine the heats of complete combustion of the gaseous volatiles produced during thermal degradation of the resin. Samples of the UP resin were prepared in an identical way to the samples for STA tests. The MCC calibration and testing procedures from Section 4.2.3.1 were followed for the tests on UP resin. The tests used a constant heating rate of 10 K min^{-1} to a final temperature of 900 K. The test procedure was repeated five times for UP resin samples to ensure the repeatability of the results.

The mean heat release rate data collected on the resin was shifted by 23 K lower in temperature to ensure the HRR data was correlated with the mass loss process predicted by model constructed with ThermaKin. The resulting profile for the normalized heat release rate and integral of the heat release rate were targeted during an inverse analysis to

determine the heat of complete combustion for each reaction. The analysis followed the procedure from Section 4.2.3.1 using the ThermaKin modeling environment. The characterized values were determined to be adequate when the agreement between the integral of the predicted and experimental *HRR* curves were within 1%.

Section 8.3.2.3: Broadband Infrared Radiation Absorption Coefficient Determination

The broadband infrared radiation absorption coefficient was quantified according to the experimental technique described in Section 4.2.4.1 to measure the radiant heat flux transmitted through a thin resin sample. UP resin samples were fabricated with thicknesses varying from 0.9 mm to 1.4 mm and exposed to a radiant heat flux of 20 kW m^{-2}. The heat flux was reduced from a previous, related investigation [121] due to the rapid onset of thermal degradation observed at 35 kW m^{-2}.

Section 8.3.2.4: CAPA Experiments and Thermal Transport Parameter Determination

CAPA tests were conducted at several radiant exposures following the testing procedure described in Section 4.2.5.1. The composites were machined into square samples with 80 mm sides for experimental testing. The samples were stored in a desiccator for a minimum of 48 hours prior to testing to minimize the effects of moisture content on the experimental data. The high emissivity paint applied to the back surface of the samples was found to degrade at temperatures in excess of 650 K [146] and temperature profiles in this chapter have been reported up to this value. The edges of the sample were thermally insulated with a 5 mm wide piece of Kaowool PM insulation. During experimental testing, the glossy surface was coated with the high emissivity paint and the matte surface was exposed to radiation from the cone heater.

Three experiments were performed on each composite composition at heat fluxes of 30, 50, and 70 kW m^{-2} to evaluate the repeatability of the resulting measurements. UP resin samples were also tested in triplicate at 30 and 50 kW m^{-2}. At 30 kW m^{-2}, the top surface of the UP resin samples was coated with the high emissivity paint to eliminate the surface emissivity as an unknown variable in subsequent analysis. The UP resin samples tested at 50 kW m^{-2} had an unaltered top surface. All of the tests on the pure UP resin samples were conducted on the aluminum mesh wrapped in aluminum foil. This was done because preliminary tests indicated that oxidation of the resin samples by ambient air introduced through the openings in the aluminum mesh significantly affect the test results.

The thermal transport model that was constructed for inverse analyses on the composite was constructed according to the parameters and boundary conditions defined in Section 4.2.5.1. It was observed in all gasification tests on composite samples that the thickness of the sample did not change over the duration of the test. As a result, the density of all solid products of degradation were defined proportional to the corresponding stoichiometric coefficient such that the thickness of the sample in the model did not change while sample mass was converted to pyrolyzate gas.

The temperature profile for the back surface was utilized as a target for inverse analyses to characterize the thermal conductivity of the UP resin and fiberglass reinforcement. Experiments were performed on samples of only UP resin to evaluate the thermal conductivity of the UP resin before determining the thermal conductivity of the composites and, by extension, the glass reinforcement. The heat flux of 30 kW m^{-2} was selected for analysis because, as the lowest thermal exposure, it provided the most stable boundary conditions which promoted a higher degree of accuracy to the user-specified

boundary conditions in the model. The thermal conductivities of the initial and intermediate species were specified using temperature-dependent expressions and were determined through the inverse analysis procedure described in Section 4.2.5.1.

The UP resin was tested and its thermal conductivity was evaluated independently from the fiberglass reinforcement. Thus, the complete set of material properties that describe the pyrolysis of the UP resin was validated prior to the introduction of fiberglass to the system. The specific heat capacity and radiative properties of the inert E-glass were specified from well-defined literature values and the thermal conductivity was determined by conducting an inverse analysis on the data collected from gasification tests on the full composite. The validation procedure was repeated for the composite samples. The model was assessed for the ability to predict the pyrolysis behavior of the composite at composition ratios of 41 and 54 wt% resin without making alterations to the characterized material properties and only adjusting the composition ratio.

Section 8.4: Results

Section 8.4.1: Data Analysis for Property Determination

Section 8.4.1.1 Kinetics and Energetics of Thermal Degradation Determination

The observed heating rate data was represented in the ThermaKin model by fitting a curve of the form of Equation 4.7 to the experimental data. The agreement between the experimental results and the time-dependent expression is shown in Figure 2.

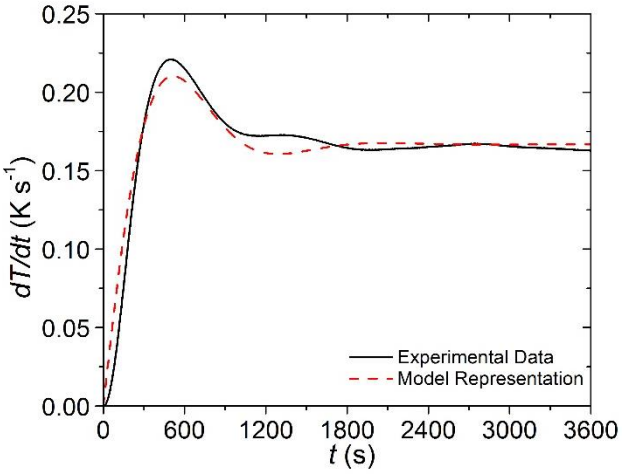

Figure 8.2 Agreement between experimental heating rate from STA and time-dependent expression of the form shown in Equation 4.7 where b1 = 0.167 K s−1, b2 = 0.0023 s−1, b3 = 0.0045 s−1, b4 = 0.434.

The agreement between the results from the parameterized model simulation and the experimental results for the normalized mass and *MLR* as a function of material temperature are shown in Figure 3. The first thermal degradation reaction was observed over a temperature range from 390-530K. The second process corresponded to the largest mass loss and was observed over a temperature range from 530-700K. The third reaction was identified over a temperature range from 630-760 K. The mass of the remaining char was measured at the end of the heating program and it was determined that 7% of the initial mass remained.

The contribution from each individual reaction to the overall *MLR* curve are shown in Figure b. The model prediction represented both experimental measurements well. The first two reactions were clearly necessary to accurately describe the *MLR* profile. The third reaction was deemed necessary to accurately describe the growth, decay, and magnitude of the peak of the main mass loss peak that occurred in the temperature range between 530 K and 760 K. The parameters that were defined to describe the effective degradation reaction mechanism are given in Table 8..

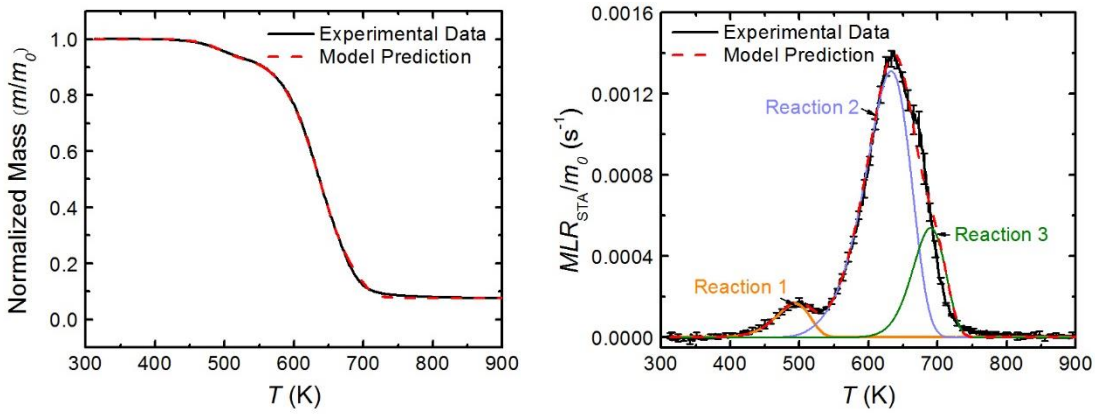

(a) **(b)**

Figure 8.3. Agreement between the experimental results from TGA and the parameterized model for (a) the normalized mass (b) and normalized *MLR* as a function of material temperature.

Table 8.1. Effective degradation reaction mechanism for UP resin.

Reaction	Equation	A (s^{-1})	E (J mol^{-1})
1	Virgin Resin → 0.935 Intermediate 1+ 0.065 Gas	8.3 x 10^5	7.7 x 10^4
2	Intermediate 1 → 0.292 Intermediate 2 + 0.708 Gas	5.0 x 10^5	9.7 x 10^4
3	Intermediate 2 → 0.282 Char + 0.718 Gas	6.2 x 10^8	1.5 x 10^5

The specific heat capacity was evaluated directly from experimental measurements for the temperature range prior to the onset of degradation (i.e., where no mass loss occurred). A second-order temperature-dependent polynomial was used to capture the initial rise in the specific heat capacity. At approximately 340 K, the specific heat capacity of the virgin resin transitioned to a linear temperature-dependent expression. The intermediate species could not be isolated to be tested independently, which required the material property to be assumed based on the behavior relative to the independently measured species.

The heat capacity of the first intermediate species was assumed to follow the same linear temperature dependency as the virgin resin. This linear expression was validated by the accurate representation of the heat flow rate curve during the transition between the first and second reaction, following the addition of the heat of reaction. The apparent

specific heat capacity of the second intermediate was specified as a constant value calculated as the average between the expression for the heat capacity of the first intermediate, evaluated at the onset of the second reaction (approximately 510 K), and the independently evaluated heat capacity of the char. A single value based on the reactant and product species was determined to be appropriate for the second intermediate because the second and third reactions occurred simultaneously, over a 100 K temperature range, and during this transition there was no local minimum to consider as a reference point to evaluate the accuracy of the assumed heat capacity of the second intermediate.

The specific heat capacity of the E-glass was defined using a linear temperature-dependent expression based on literature values [154]. The expressions and values for the specific heat capacity of the initial and decomposition products are given in Table 8.2. The uncertainty of the specific heat capacities of the initial and intermediate species were assumed to be ± 10% based on the scatter in the experimental measurements.

Table 8.2. Specific heat capacity of constituent species.

Component	***c* (J kg^{-1}K^{-1})**
Virgin Resin ($T \leq 340$ K)	$-108136 + 647.5\,T - 0.995\,T^2$
Virgin Resin ($T > 340$ K)	$843.5 + 2.28 \times T$
Intermediate 1	$843.5 + 2.28 \times T$
Intermediate 2	1760
Char	1480
Fiberglass	$440 + 1.24\,T$

The char was assumed to be nonreactive in a non-oxidizing atmosphere and the specific heat capacity was defined as the average apparent heat capacity over a temperature range from 500-700 K, as shown in Figure .4. This temperature range represented the most stable period over the profile, which was calculated from experimental measurements, with reproducible results.

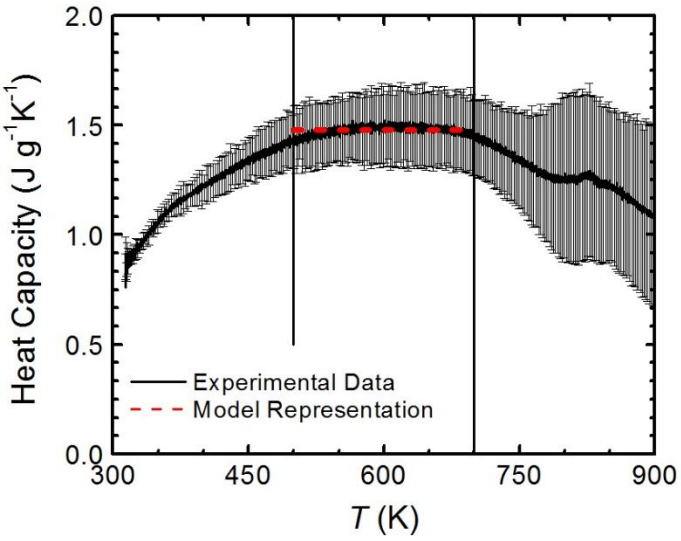

Figure 8.4. Apparent heat capacity from DSC of the char as a function of temperature.

The baseline was developed for the sensible enthalpy and expressed as the heat flow rate to the sample as a function of sample temperature. The temperature boundaries identified to calculate the heat of decomposition for each reaction (i.e., the area between the experimentally measured apparent heat capacity and the sensible enthalpy) are shown in Figure . It should be noted that the limits of integration corresponded to the temperature range over which all reactions occurred. There were no definite boundaries for integration to determine the heat evolved in each reaction because the sequential reactions occurred instantaneously during the transitions.

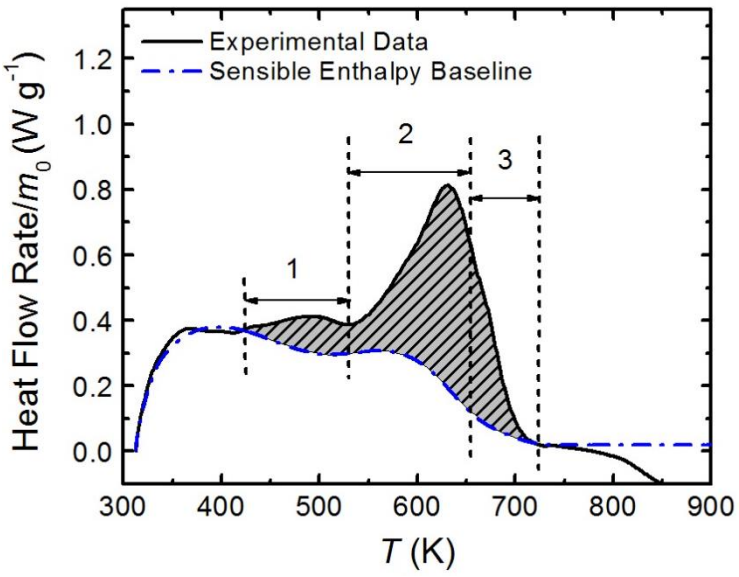

Figure 8.5. Integration of the heat flow rate to the sample between the apparent heat capacity from DSC and the sensible enthalpy baseline to determine the heats of decomposition.

The evaluated heats of decomposition are given in Table 8.. The agreement between the heat flow rate curve from the parameterized model results and the experimental measurements is shown in Figure . The error bars represent two standard deviations of the mean. The total heat flow to the sample (i.e., heat of gasification) was calculated as 990 ± 40 J g^{-1}, where the convention adopted in this work associates a positive heat with an endothermic process. The agreement between the predicted and experimental curves was a result of the fitting process, which used both the heat flow rate curve and the integral of the heat flow rate curve as targets for inverse analyses when determining the heats of reaction.

Table 8.3. Heat of decomposition for each reaction in the effective degradation mechanism. Endothermic quantities (absorb energy during reaction) are presented as positive values

Reaction	Equation	h (J kg^{-1})
1	Virgin Resin → 0.935 Intermediate 1 + 0.065 Gas	3.7×10^4
2	Intermediate 1 → 0.292 Intermediate 2 + 0.708 Gas	3.4×10^5
3	Intermediate 2 → 0.282 Char + 0.718 Gas	1.8×10^5

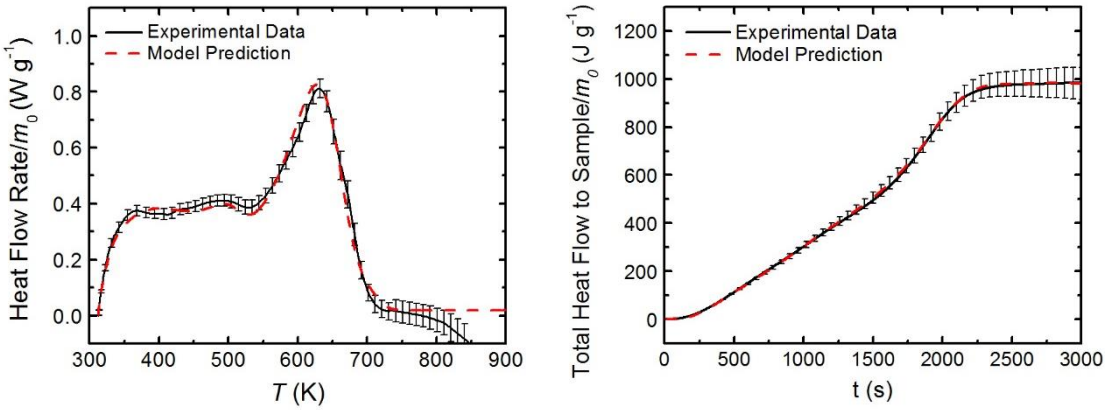

(a) **(b)**

Figure 8.6. Agreement between the model simulation and experimental measurement from DSC for (a) the heat flow rate to the sample (b) and total heat flow to the sample.

Section 8.4.1.2: Heat of Combustion Determination

The general form of Equation 4.7 was used to fit the observed heating rate measured during MCC tests and the agreement between the experimental measurement and the modeled heating rate curve are shown in Figure . There was significantly more scatter in the data for the observed heating rate from MCC tests compared to the STA. The heating rate expression was defined as the boundary condition in the ThermaKin program to model the mass loss process in the MCC in the analysis to determine heats of complete combustion of the pyrolyzate species produced during thermal degradation.

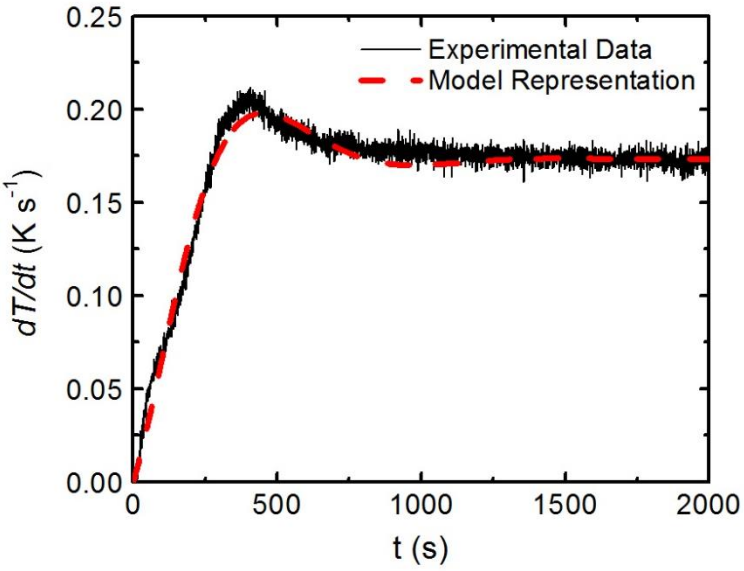

Figure 8.7. Agreement between experimental heating rate from MCC and time-dependent expression of the form shown in Equation 4.7 where b_1 = 0.173 K s^{-1}, b_2 = 0.0039 s^{-1}, b_3 = 0.0060 s^{-1}, b_4 = 0.163.

The values for the heat of combustion for each species are given in Table 8., with negative heats indicating exothermic processes. The final reaction was observed to have a negligible contribution to the overall heat release, corresponding to a heat of combustion with a magnitude of zero. The agreement between the experimental data and model prediction is shown in Figure .

Table 8.4. Effective heat of complete combustion for each volatile species evolved during degradation. Exothermic processes (release energy during reaction) are presented as negative values.

Component	h_c (J kg^{-1})
Reaction $1_{volatiles}$	-8.0 x 10^6
Reaction $2_{volatiles}$	-3.2 x 10^7
Reaction $3_{volatiles}$	0

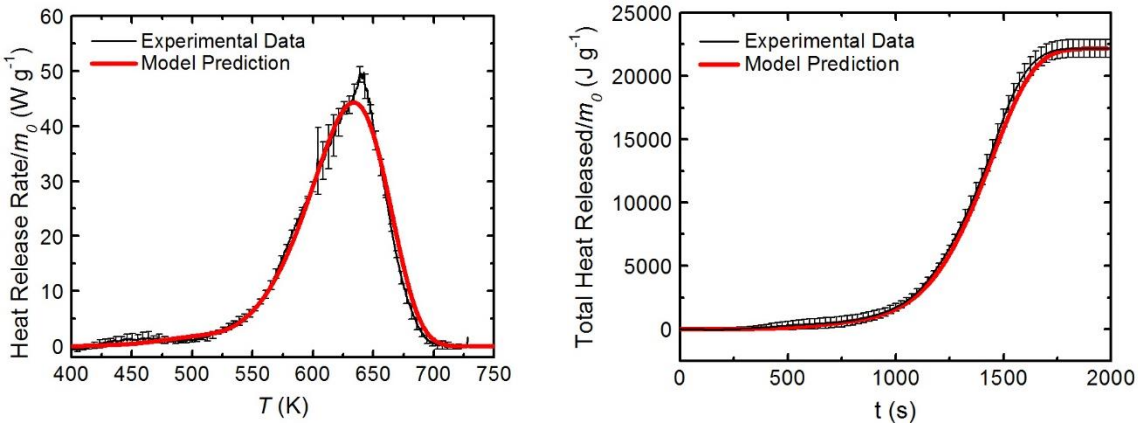

(a) **(b)**

Figure 8.8. Agreement between the model-predicted curves and experimental results from MCC for (a) the heat release rate and (b) the integral of the heat release rate.

Section 8.4.1.3: Optical Properties Determination

The broadband infrared absorption coefficient was calculated directly using Equation 4.11. The average radiative absorption coefficient for the UP resin was calculated as 1.5 $m^2\,kg^{-1}$ with a variance of 1.4%. This value was specified for the undegraded UP resin. The final char was specified to be effectively non-transparent based on observations of the residual mass in gasification tests. This was done by defining the absorption coefficient as 100 $m^2\,kg^{-1}$. The absorption coefficient of the intermediate species were specified based on their assumed behavior relative to the other species. Table 8. gives the absorption coefficient defined for each component.

Table 8.5. Absorption coefficient and emissivity of constituents and evolved species.

Component	κ ($m^2\,kg^{-1}$)	ϵ
Virgin Resin	1.5	0.95
Intermediate 1	1.5	0.95
Intermediate 2	100	0.86
Char	100	0.86
Fiberglass	100	0.85

The emissivity of the constituents and product species were specified from literature. The emissivity of the UP resin and intermediate species were assumed to be 0.95

based on the work of Linteris et al., which showed that most polymers have an emissivity greater than 0.9 [102]. The emissivity of the char was assumed to be equal to that of graphite, 0.86 [106], due to the high carbon content of the char. The absorption coefficient of the char was specified as 100 $m^2 kg^{-1}$ to ensure absorption of the incident radiation at the top surface of the sample. The absorption coefficient and emissivity of the first intermediate were assumed to be similar to the virgin resin and the properties for the second intermediate were assumed to be similar to the char. The emissivity for the fiberglass was taken from literature as 0.85 [155]. The absorption coefficient for the glass phase was assumed to be sufficiently high such that all radiant energy that was incident to the glass was absorbed at the surface. This assumption resulted in a definition of the absorption coefficient as 100 $m^2 kg^{-1}$.

Section 8.4.1.4: Thermal Conductivity Determination

It was observed in all gasification tests on composite samples that the thickness of the sample did not change over the duration of the test. As a result, the density of all solid products of degradation were defined proportional to the corresponding stoichiometric coefficient such that the thickness of the sample in the model did not change while sample mass was converted to pyrolyzate gas.

Inverse analyses were performed in 100-second time increments to reduce the number of unknown parameters influencing the system for each analyses. By limiting the time interval, the thermal conductivity was analyzed for partially-isolated resin components beginning with the virgin resin, followed by the first intermediate, and continuing until all species were characterized. It was determined that a linear temperature-dependent expression for the thermal conductivity adequately described the back

temperature curves of the most ideal composite samples, 48 wt% resin, at the most stable heat flux, 30 kW m^{-2}. The thermal conductivity of the char was characterized as a third-order polynomial based on the radiation diffusion approximation [125].

The behavior of intermediate species was assumed to be related to the behavior of the virgin and char species to limit the independent variables required to define the model. The thermal conductivity of the first intermediate was assumed to follow the same linear temperature dependency as the virgin resin. The thermal conductivity of the second intermediate was defined using a combination of terms from the expressions for the virgin and char components. All expressions for the thermal conductivities are given in Table 8.. The experimental results at 30 kW m^{-2} agreed well with the model curve developed through manual iteration, as shown in Figure . The error bars in the figure were calculated as two standard deviations of the mean.

Table 8.6. Thermal conductivity of UP resin and decomposition species.

Component	***k* (W m^{-1} K^{-1})**
Virgin Resin	$0.03 + 3.5 \times 10^{-4}T$
Intermediate 1	$0.03 + 3.5 \times 10^{-4}T$
Intermediate 2	$0.23 + 3.5 \times 10^{-4}T + 8 \times 10^{-10}T^3$
Char	$0.18 + 8 \times 10^{-10}T^3$

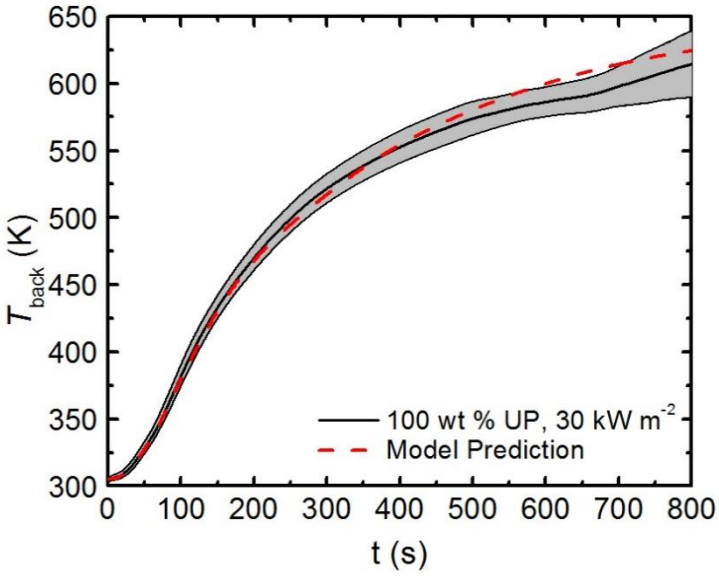

Figure 8.9. Agreement between the experimental measurement from CAPA testing and model-predicted profiles for back-surface temperature at an external heat flux of 30 kW m^{-2}.

The characterized properties were evaluated for the ability to predict the temperature profiles for UP resin at an external heat flux of 50 kW m^{-2}, as shown in Figure . The UP resin samples tested at 50 kW m^{-2} did not have a coating with a well-defined emissivity on the surface facing the heater. The parameterized model was able to reproduce the experimental data well, which supported the values for the absorption coefficient and the high emissivity of the UP resin and decomposition species that were defined in this chapter.

The complete set of material properties were independently validated by evaluating the ability of the model to reproduce experimental *MLR* data at 30 and 50 kW m^{-2}, shown in Figure . The error bars were calculated as two standard deviations of the mean. It should be noted that for all of the profiles shown, the only experimental data targeted during property determination is that shown in Figure a. The model accurately predicts the overall shape and magnitude of the experimental curves well. The error between the experimental results and model prediction are provided in Table 8..

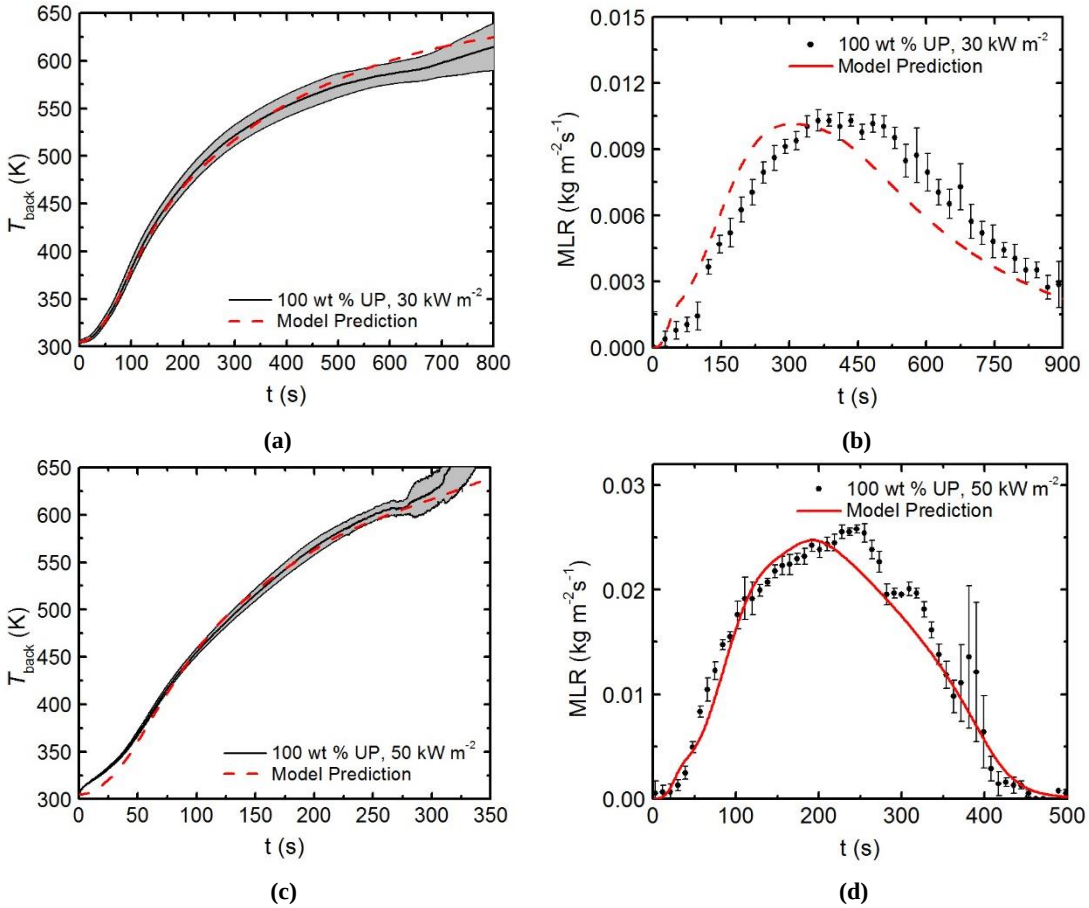

Figure 8.10. Agreement between the experimental measurement from CAPA testing and model-predicted profiles for back-surface temperature and *MLR* for UP resin samples at external heat fluxes of (a) and (b) 30 kW m^{-2} and (c) and (d) 50 kW m^{-2}.

The thermal conductivity of the E-glass was determined through an inverse analysis of the back temperature data collected on a composite with a sample configuration of 48 wt% resin at 30 kW m^{-2} in which the thermal conductivity of the E-glass was the only undefined parameter. These composite samples were selected because they were observed to have minimal imperfections that may have resulted in non-ideal material behavior. The thermal conductivity of the E-glass was described using the linear temperature-dependent expression given in Equation 8.2.

$$k_{\text{glass}} = 0.48 - 5.5 \times 10^{-4}\text{T} \tag{8.2}$$

At temperatures greater than 782K, the expression for the thermal conductivity of the glass decreased to 0.05 W $m^{-1}K^{-1}$, which likely represents a lower limit for the thermal conductivity of a solid. A piece-wise function was introduced to the model that allowed the thermal conductivity to follow Equation 8.2 at temperatures below 781.8 K and transition to a constant value of 0.05 W m^{-1} K^{-1} above this critical temperature. Agreement between the experimental profile targeted during inverse analysis and the model-predicted profile is shown in Figure .

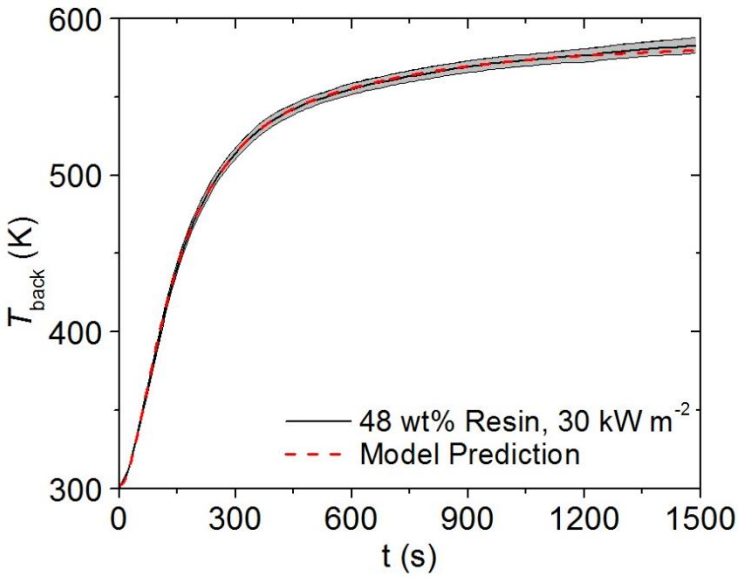

Figure 8.11. Agreement between the back-surface temperature profile from experimental measurement during CAPA testing at 30 kW m^{-2} and the model-predicted curve developed through inverse analysis to characterize the thermal conductivity of the E-glass reinforcement.

Section 8.4.2: Model Predictions for 48 wt% resin Sample Configuration

The fully parameterized model was evaluated for the ability to predict back surface temperature profiles measured in CAPA tests on the sample with a composition of 48 wt% resin at heat fluxes of 50 and 70 kW m^{-2}, as shown in Figure . The model was able to reproduce the temperature profiles accurately for the majority of experiments over the range of tested heat fluxes. The model slightly over-predicted the experimental

measurements for the 48 wt% resin samples at 50 and 70 kW m^{-2} as the surface temperature exceeded 550 K. These over-predictions were probably a result of the onset of thermal degradation of the highly emissive paint on the back of the sample, which would cause the measured temperatures to appear lower than the actual surface temperatures.

The predictive capability of the fully parameterized model of the sample with a composition of 48 wt% resin was validated by comparing the model-predicted *MLR*s with the experimental *MLR* curves collected during gasification tests at external heat fluxes of 30, 50, and 70 kW m^{-2}, as shown in Figure . It should be noted that for all of the profiles, the only data targeted during property determination is plotted in Figure a. The model slightly over-predicted the peak *MLR* at 30 and 50 kW m^{-2} and slightly under-predicted the decay phase at 50 and 70 kW m^{-2}. Overall, the independently characterized constituents were able to accurately predict the experimental *MLR* profiles.

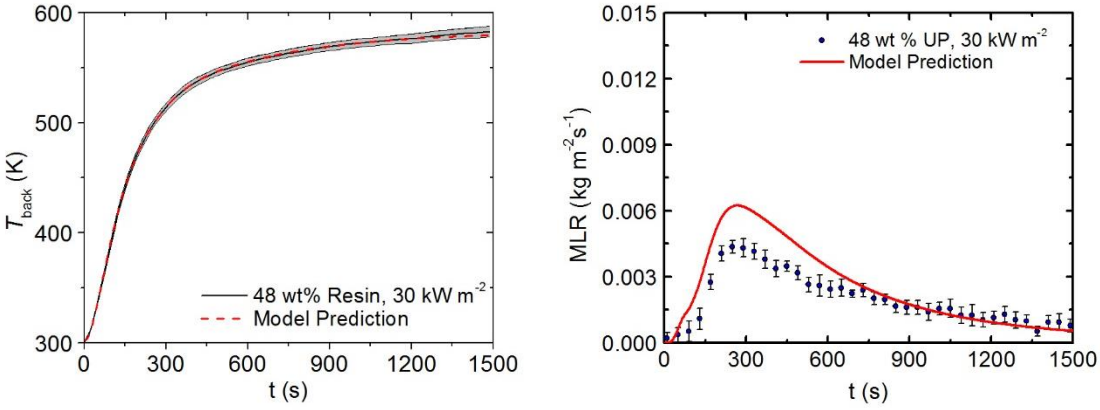

(a) **(b)**

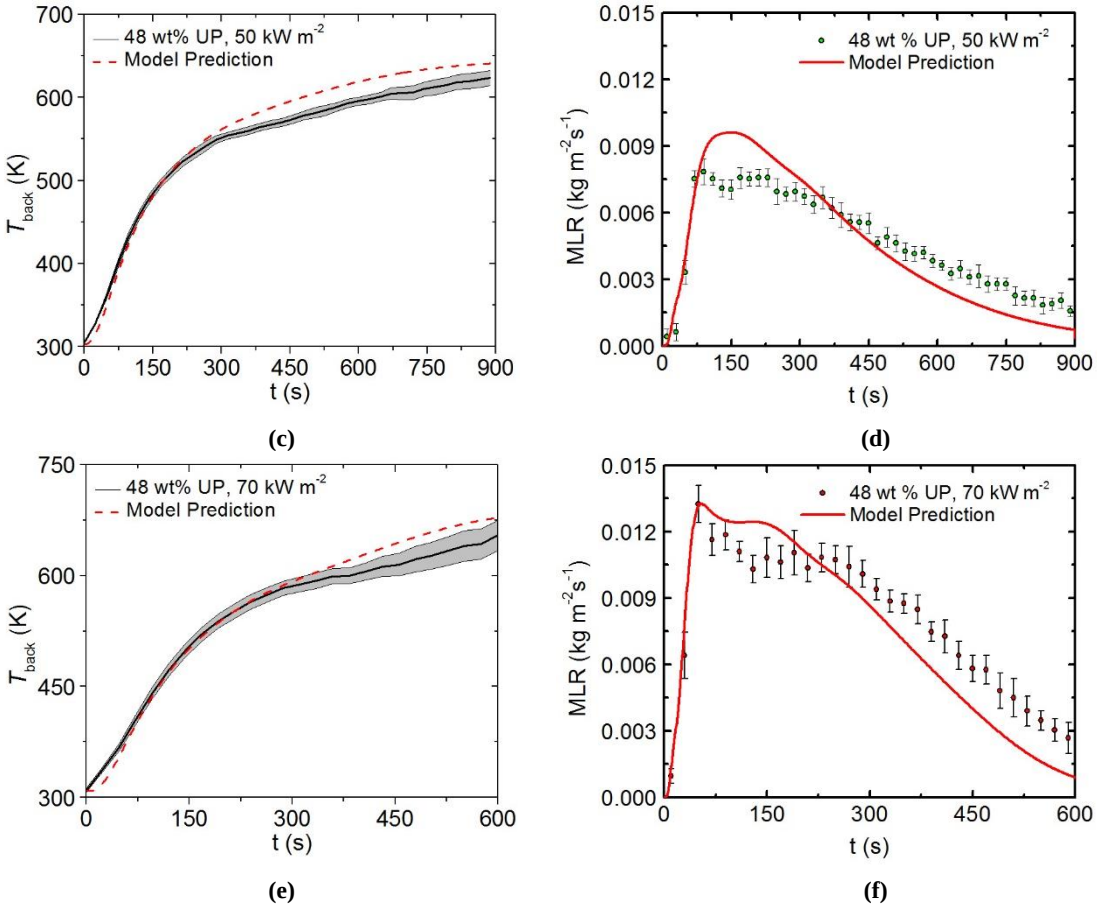

Figure 8.12. Agreement between the experimental measurement from CAPA testing and model-predicted profiles for back-surface temperature for 48 wt% resin composite samples at external heat fluxes of (a) and (b) 30 kW m^{-2}, (c) and (d) 50 kW m^{-2}, and (e) and (f) 70 kW m^{-2}.

Section 8.4.3: Model Predictions at Extrapolated Composition Sample Configurations

The model that was parameterized at a composition of 48 wt% resin was used to generate *MLR* and back temperature predictions at the other tested compositions. The only variations to the model input were the ratio of the initial constituents and the thickness of the sample measured prior to experimental testing. Experimental results of gasification testing at external heat fluxes of 30, 50, and 70 kW m^{-2} on composite samples of 41 wt % were compared with the model-predicted profiles for the back-surface temperature and the *MLR*, as shown in Figure .

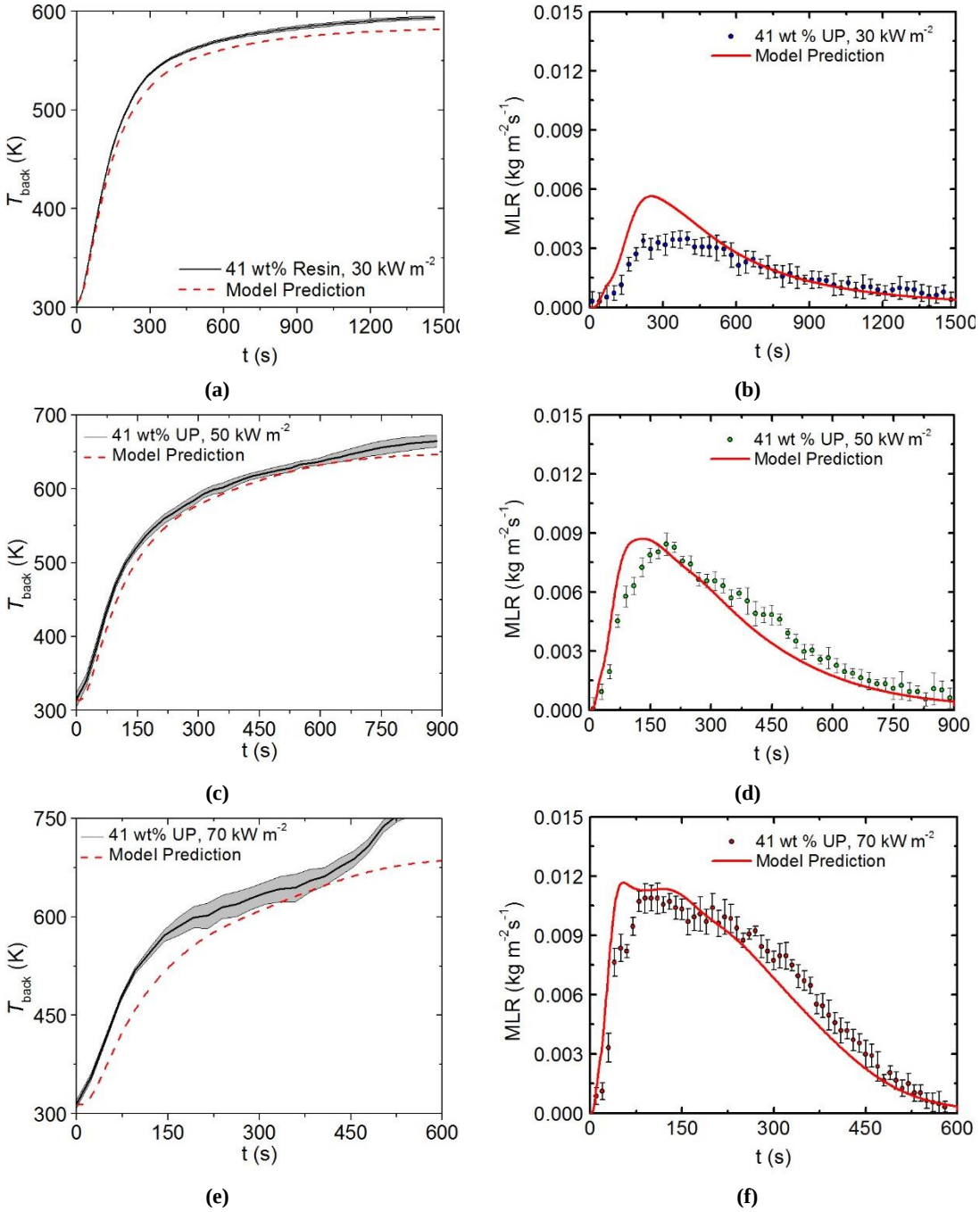

Figure 8.13. Agreement between the experimental measurement from CAPA testing and model-predicted profiles for back-surface temperature for 41 wt% resin composite samples at external heat fluxes of (a) and (b) 30 kW m^{-2}, (c) and (d) 50 kW m^{-2}, and (e) and (f) 70 kW m^{-2}.

There was a minor systematic under-prediction of the experimental temperature histories for 41 wt% resin samples. The model accurately predicted the shape of the *MLR* curve for 41 wt% resin at all of the external heat fluxes tested. However, the peak *MLR*

was over-predicted at 30 kW m^{-2}. The experimental and predicted profiles agreed well for the 41 wt% resin samples at 50 and 70 kW m^{-2}.

Predictions of the pyrolysis behavior of the composite with a composition of 54 wt% resin were generated, but it was found that the deviations between the model and experimental data were relatively large. The model over-predicted the surface temperature measurement at 54 wt% resin at 50 and 70 kW m^{-2} for temperatures above 500 K. The simulated *MLR* profile was able to correctly predict the shape of the experimental curve for 54 wt% resin at 30 kW m^{-2}, although the peak *MLR* was over-predicted. The model profile successfully simulated the initial rise in the *MLR* for the 54 wt% resin samples at 50 and 70 kW m^{-2}. The shape of the predicted profiles agreed with the experimental curve at these heat fluxes, but the peak was over-predicted and the decay was under-predicted.

The deviations between the model prediction and the experimental measurement were attributed to non-uniform distribution of the resin within the samples. A localized concentration of excess resin was observed along the bottom surface of the sample; however, the model was constructed with the assumption that the sample consisted of a homogeneous mixture of the constituents. This difference between the model simulation and the physical composite samples likely caused the model to over-predict the experimental curves and the representation of the sample with a composition of 54 wt% resin was modified for a new model of that sample. A thin layer of UP resin with a composition ratio of 50 wt% resin and the measured thickness of the layer was included at the back-surface of the sample and the composition of the rest of the composite sample was adjusted to yield the original total composition. The back-surface temperature profiles and *MLR* profiles from the adjusted definition of the 54 wt% resin samples are shown in Figure

8.14. The adjusted sample description improved the ability of the model to predict both the back-surface temperature profiles and *MLR* profiles for all of the external heat fluxes. This modification yielded significant improvement in the predictions at all tested heat fluxes.

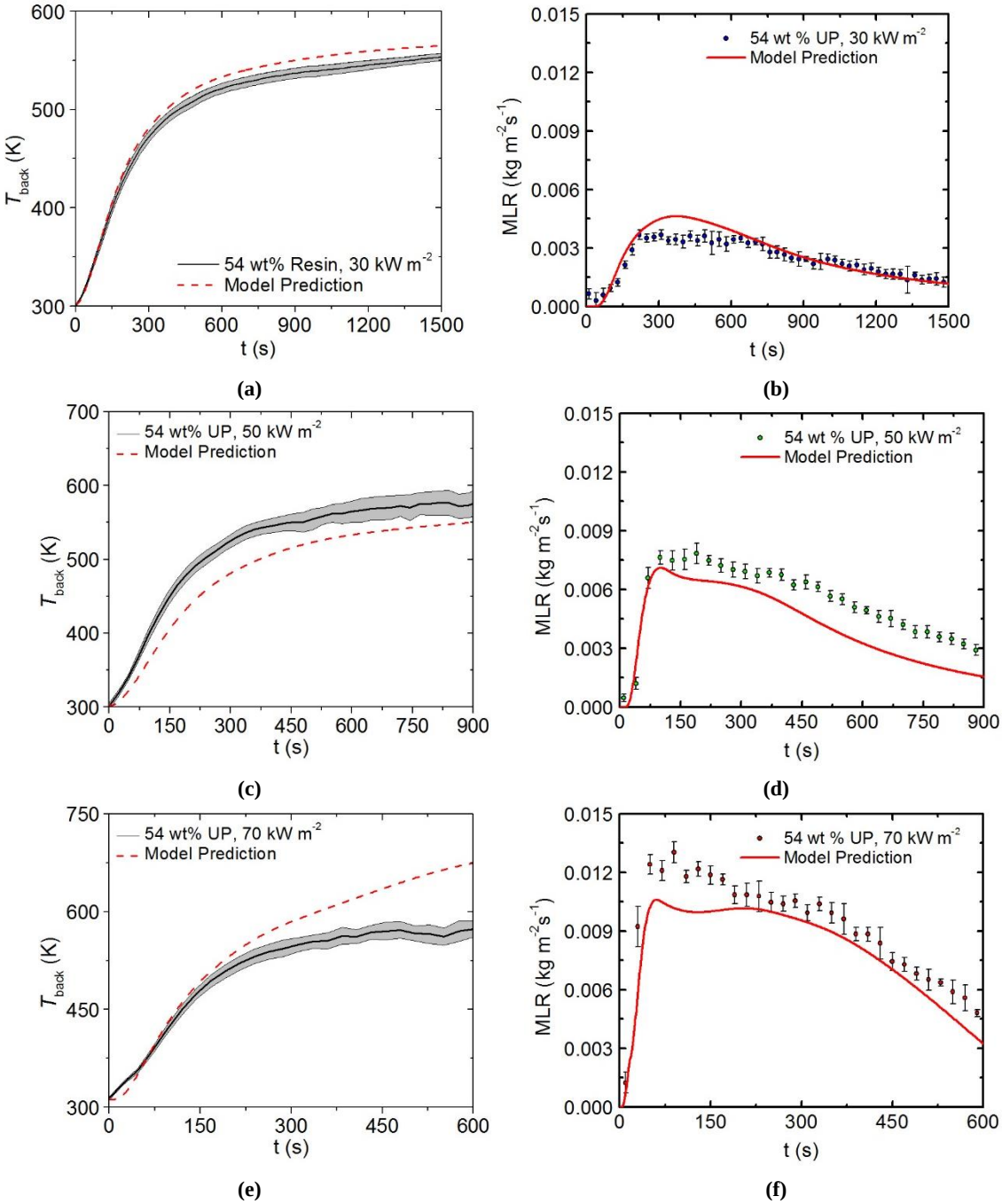

Figure 8.14. Agreement between the experimental measurement from CAPA testing, the initial model-predicted profiles, and the modified model predicted profiles for back-surface temperature for 54 wt% resin composite samples at external heat fluxes of (a) and (b) 30 kW m^{-2}, (c) and (d) 50 kW m^{-2}, and (e) and (f) 70 kW m^{-2}.

The mean instantaneous error between the *MLR* from experimental data and the model simulation was calculated for each configuration and the results are given in Table 8.. The largest deviation for each sample was observed to be at 30 kW m^{-2}, where the model over-predicted the peak *MLR*. The corresponding temperature profiles reproduce the experimental measurement well.

Table 8.7. Mean instantaneous error between the *MLR* from experimental data from CAPA testing and model simulations.

Composition	Error [%]		
	30 kW m^{-2}	**50 kW m^{-2}**	**70 kW m^{-2}**
41 wt% resin	29.1	14.5	11.8
48 wt% resin	28.6	18.2	15.1
54 wt% resin	11.8	15.9	11.7

The amended description of the 54 wt% resin composite sample resulted in a significant reduction in the mean instantaneous error for all of the external heat fluxes and only the final representative errors are included in Table 8.7. The reduced error supported the claim that the localized concentration of UP resin on the back surface of the sample contributed to nonhomogeneous behavior of the constituents for the composite with the highest resin content.

Section 8.5: Conclusions

A complete set of material properties for the pyrolysis of E-glass-reinforced UP resin composites was characterized through the application of a methodology that systematically isolated physical processes during experimental testing for material property determination. To the knowledge of the authors, this is the first successful application of a pyrolysis model to parameterize a composite material with validation provided for multiple compositions based on a single set of material properties.

The constituents were parameterized individually within the model. The material properties were defined based on direct and indirect analyses of experimental data, assumptions regarding the behavior of intermediate species based on the proximate species, and well-defined values from literature sources. Milligram-scale testing was conducted on UP resin using STA and MCC to develop a semi-global effective degradation mechanism and define the energetics associated with thermal decomposition and gas-phase combustion.

Radiation driven gasification testing was conducted using a modified truncated cone-calorimeter equipped with the CAPA. The back-surface temperature was targeted during inverse analyses to characterize the thermal conductivity of UP resin using 100 wt% resin samples. The E-glass was characterized from experimental testing of composite samples after the complete set of material properties for the UP resin was independently validated against the mass loss rate data.

Pyrolysis of the composite was described using one set of material properties for the constituents and validated based on the ability to accurately describe the pyrolysis of samples with varying composition ratios over a range of external heat fluxes. The results for the high resin content samples were improved by including a thin film of UP resin at the back surface of the sample, which was an observed feature of these samples due to the localized concentration of excess resin in the system during sample fabrication. The model produced through this work is capable of predicting mass loss rates although the heats of combustion determined here may be incorporated in to the model to describe the heat release rate resulting from the combustion of the volatile species produced during pyrolysis.

Chapter 9: Concluding Remarks

This dissertation presented a generalized systematic methodology to characterize layered composites for comprehensive pyrolysis models and subsequently validate the models against data outside of the calibration conditions. A flow chart that summarizes this methodology is provided as Figure 9.1.

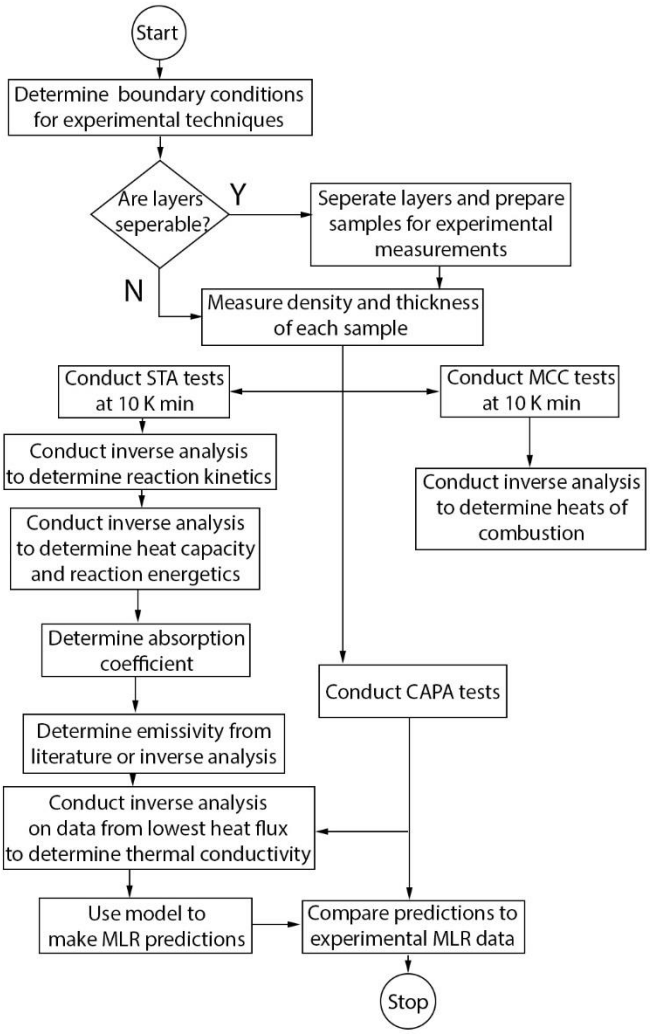

Figure 9.1. Flow Chart that Summarizes the Methodology Presented in this Dissertation.

It was shown that this methodology presents a significant improvement on the status quo in terms of the accuracy of predictions, efficiency of determination of parameters, complexity of materials in the defined scope, and the ability to extrapolate predictions to various compositions and heating scenarios. It was also shown that during

the development of the methodology, an improved understanding of the pyrolysis process for composites was achieved.

An improvement in the efficiency with which the composites were characterized included simultaneously conducting thermogravimetry and differential scanning calorimetry, which reduced the number of experiments required to determine the kinetics and energetics of the degradation process by half. A method for extracting the kinetic and energetic parameters from the experimental data was explained and it was shown that parameters determined through this method were able to predict the mass loss rate at different heating rates without the use of computationally expensive optimization algorithms. In fact, a direct comparison to predictions made in a previous study that determined the kinetic parameters from data collected at multiple heating rates demonstrated the superior fitness of the kinetics determined through this methodology.

An additional improvement in the efficiency was revealed with simultaneous measurement of back surface temperatures and mass loss rates for validation in bench-scale gasification tests. Simultaneous measurement of sample temperature data and mass loss rate data eliminated half of the bench-scale tests required to fully parameterize and validate the pyrolysis model. The back surface temperature data were analyzed through an inverse analysis procedure to determine the thermal transport parameters for each layer of the composite material.

The methodology was demonstrated on four composite materials that are commonly encountered in industrial and commercial applications. The pyrolysis model for each material studied here enabled further investigation into the pyrolysis process of that composite. It was shown that there is no need to represent the geometry of the complicated

fluted layers of corrugated cardboard because homogeneous layers with the same effective density yielded predictions that agreed with validation data. It was shown in the investigation of low-pile carpet that interfacial effects in layered composites may significantly affect the heat transfer process during pyrolysis. The study on fiberglass reinforced polyester demonstrated the ability of a model produced through this methodology to extrapolate not only to the various heating scenarios, but also to various compositions of the composite which has significant implications for the design of composites to meet fire protection and mechanical performance metrics. During the development of the pyrolysis model for the carbon fiber aerospace composite, it was shown that oxidation does not significantly affect the pyrolysis process for the unreacted or residual components of the composite at temperatures corresponding to heat fluxes of 40 and 60 kW m^{-2}. The fully parameterized model allowed the investigation of in-plane heat transfer for the laminate composite and the resulting thermal conductivity value appeared to agree with values reported in the literature.

The models generated through the methodology described here and demonstrated in Chapters 5-8 were capable of simulating experimental bench-scale one-dimensional gasification test results for these complicated composites relatively well. The average mean instantaneous relative error between the experimental *MLR* and the model prediction for all of the materials characterized here for the external conditions used for calibration was 19.4%. with a maximum of 28.8% and a minimum of 13.0%. The models were also shown to reproduce experimental data at a heat flux 20 kW m^{-2} higher than the calibration condition with a mean instantaneous relative error of 20.3% and 17.2% for the highest

external heat flux condition. These mean instantaneous error values are only slightly higher than the expected uncertainty due to scatter in the experimental *MLR* data (5-20%).

Several topics have been identified as targets for future work related to this dissertation. By automating aspects of this process, some of the time-consuming manual iteration may be removed to further improve efficiency without reducing the role of engineering judgement in final acceptance of the model parameters. This would involve creating an algorithm with defined acceptance criteria to conduct many of the coarse adjustments and retaining manual iteration to make fine adjustments to parameters. Though the current version of the gasification device used in this investigation provided well-defined boundary conditions and flexibility in the possible sample materials, these aspects can be improved for the next generation of a gasification device. The next generation gasification device should have less thermal mass to prevent heating of the device from affecting experimental results and should be able to accommodate materials of arbitrary thickness while maintaining a rigorous definition of the boundary conditions throughout the tests. Additional validation tests must be designed to assess the validity of the models developed through this methodology at larger scales and when additional physical phenomena are introduced. Potentially the most important extension of this work is the formation and population of a publicly accessible database filled with pyrolysis model parameters for common building materials. Such a database could decrease possible inefficiencies in this industry caused by redundant studies between independent labs and would create a set of properties accepted by consensus that would ultimately decrease the uncertainty in the results of models for the built environment.

Bibliography

[1] Tewarson A, Pion RF. Flammability of plastics—I. Burning intensity. Combust Flame 1976;26:85–103. doi:10.1016/0010-2180(76)90059-6.

[2] Quintiere JG. A theoretical basis for flammability properties. Fire Mater 2006;30:175–214. doi:10.1002/fam.905.

[3] Babrauskas V, Twilley WH, Janssens M, Yusa S. A cone calorimeter for controlled-atmosphere studies. Fire Mater 1992;16:37–43. doi:10.1002/fam.810160106.

[4] Semmes MR, Liu X, McKinnon MB, Stoliarov SI, Witkowski A. A Model for Oxidative Pyrolysis of Corrugated Cardboard. In: van Hees P, Jansson R, Nilsson D, editors. Proc. 11th Int. Symp. Int. Assoc. Fire Saf. Sci., Canterbury, NZ: Interscience; 2014.

[5] Lattimer BY, Ouellette J, Trelles J. Thermal Response of Composite Materials to Elevated Temperatures. Fire Technol 2011;47:823–50. doi:10.1007/s10694-009-0121-9.

[6] Webster R, Lazaro M, Alvear D, Capote J, Trouve A. Limitations in Current Parameter Estimation Techniques for Pyrolysis Modelling. Proc. Sixth Int. Semin. Fire Explos. Hazards, University of Leeds, UK: 2010, p. 1008–19.

[7] Lautenberger C, Fernandez-Pello C. Generalized pyrolysis model for combustible solids. Fire Saf J 2009;44:819–39. doi:10.1016/j.firesaf.2009.03.011.

[8] McGrattan K, Hostikka S, McDermott R, Floyd J, Weinschenk C, Overholt K. Fire Dynamics Dimulator Technical Reference Guide Volume 3: Validation. Gaithersburg, MD: 2015. doi:http://dx.doi.org/10.6028/NIST.SP.1018-3.

[9] Tsoi M, Zhuge J, Chen R-H, Gou J. Modeling and experimental studies of thermal

degradation of glass fiber reinforced polymer composites. Fire Mater 2014;38:247–63. doi:10.1002/fam.2178.

[10] Marquis DM, Pavageau M, Guillaume E. Multi-scale simulations of fire growth on a sandwich composite structure. J Fire Sci 2012;31:3–34. doi:10.1177/0734904112453010.

[11] Moghtaderi B. The state-of-the-art in pyrolysis modelling of lignocellulosic solid fuels. Fire Mater 2006;30:1–34. doi:10.1002/fam.891.

[12] Bamford C, Crank J, Malan D. The combustion of wood: part I. Proc. Camb. Philol. Soc., Cambridge: 1945, p. 162–82.

[13] Kanury A. Combustion characteristics of biomass fuels. Combust Sci Technol 1994;97:469–91.

[14] Tewarson A, Abu-Isa IA, Cummings DR, LaDue DE. Characterization of the Ignition Behavior of Polymers Commonly Used in the Automotive industry. Proc. 6th Int. Symp. Int. Assoc. Fire Saf. Sci., n.d., p. 991–1002.

[15] Quintiere JG. A Semi-Quantitative model for the Burning Rate of Solid Materials. Gaithersburg, MD: 1992.

[16] Spearpoint M., Quintiere J. Predicting the burning of wood using an integral model. Combust Flame 2000;123:308–25. doi:10.1016/S0010-2180(00)00162-0.

[17] Kung H-C. A mathematical model of wood pyrolysis. Combust Flame 1972;18:185–95. doi:10.1016/S0010-2180(72)80134-2.

[18] Chan W-CR, Kelbon M, Krieger BB. Modelling and experimental verification of physical and chemical processes during pyrolysis of a large biomass particle. Fuel 1985;64:1505–13. doi:10.1016/0016-2361(85)90364-3.

[19] Di Blasi C. Heat, Momentum and Mass Transport through a Shrinking Biomass Particle Exposed to Thermal Radiation. Chem Eng Sci 1996;51:1121–32.

[20] Yuen R, Casey R, De Vahl Davis G, Leonardi E, Yeoh GH, Chandrasekaran V, et al. A Three-dimensioanl Mathematical Model for the Pyrolysis of Wet Wood. Proc. Fifth Int. Symp. Fire Saf. Sci., 1996, p. 189–200.

[21] Lautenberger C. A Generalized Pyrolysis Model for Combustible Solids. ProQuest, 2007.

[22] Stoliarov SI, Lyon RE. Thermo-Kinetic Model of Burning. Atlantic City, NJ: 2008. doi:10.3801/IAFSS.FSS.9-1141.

[23] Stoliarov SI, Leventon IT, Lyon RE. Two-dimensional model of burning for pyrolyzable solids. Fire Mater 2014;38:391–408. doi:10.1002/fam.2187.

[24] Stoliarov SI, Crowley S, Lyon RE, Linteris GT. Prediction of the burning rates of non-charring polymers☆. Combust Flame 2009;156:1068–83. doi:10.1016/j.combustflame.2008.11.010.

[25] Stoliarov SI, Crowley S, Walters RN, Lyon RE. Prediction of the burning rates of charring polymers. Combust Flame 2010;157:2024–34. doi:10.1016/j.combustflame.2010.03.011.

[26] McGrattan K, Hostikka S, McDermott R, Floyd J, Weinschenk C, Overholt K. Sixth Edition Fire Dynamics Simulator Technical Reference Guide Volume 1 : Mathematical Model. vol. 1. Gaithersburg, MD: 2015. doi:http://dx.doi.org/10.6028/NIST.SP.1018-1.

[27] Lautenberger C, Rein G, Fernandez-Pello C. The application of a genetic algorithm to estimate material properties for fire modeling from bench-scale fire test data. Fire

Saf J 2006;41:204–14. doi:10.1016/j.firesaf.2005.12.004.

[28] Matala A, Lautenberger C, Hostikka S. Generalized direct method for pyrolysis kinetic parameter estimation and comparison to existing methods. J Fire Sci 2012;30:339–56. doi:10.1177/0734904112439840.

[29] Bruns M. Inferring and Propagating Kinetic Parameter Uncertainty for Condensed Phase Burning Models. Fire Technol 2015:1–28. doi:10.1007/s10694-015-0457-2.

[30] Kulshreshtha AK, Vasile C. Handbook of Polymer Blends and Composites, Volumes 1-4. Smithers Rapra Technology; 2002.

[31] A.P. Mouritz, A.G. Gibson. Fire Properties of Polymer Composite Materials. 1st ed. Springer Netherlands; 2006. doi:10.1007/978-1-4020-5356-6.

[32] Hegde RR, Dahiya A, Kamath MG. Carbon Fibers 2014. http://www.engr.utk.edu/mse/Textiles/CARBON FIBERS.htm.

[33] Gutierrez E, Bono F. Review of industrial manufacturing capacity for fibre-reinforced polymers as prospective structural components in Shipping Containers. Ispra, Italy: 2013. doi:10.2788/77853.

[34] Shop OSD. Structure Fires by Occupancy 2007-2011- Annual Averages. Quincy, MA: 2013.

[35] Chaos M, Khan MM, Dorofeev SB. Pyrolysis of corrugated cardboard in inert and oxidative environments. Proc Combust Inst 2013;34:2583–90. doi:10.1016/j.proci.2012.06.031.

[36] Johansson L-S, Campbell J., Koljonen K, Stenius P. Evaluation of surface lignin on cellulose fibers with XPS. Appl Surf Sci 1999;144-145:92–5. doi:10.1016/S0169-4332(98)00920-9.

[37] Gollner MJ, Overholt K, Williams FA, Rangwala AS, Perricone J. Warehouse commodity classification from fundamental principles. Part I: Commodity & burning rates. Fire Saf J 2011;46:305–16. doi:10.1016/j.firesaf.2011.03.002.

[38] Gollner MJ, Williams FA, Rangwala AS. Upward flame spread over corrugated cardboard. Combust Flame 2011;158:1404–12. doi:10.1016/j.combustflame.2010.12.005.

[39] Overholt KJ, Gollner MJ, Perricone J, Rangwala AS, Williams FA. Warehouse commodity classification from fundamental principles. Part II: Flame heights and flame spread. Fire Saf J 2011;46:317–29. doi:10.1016/j.firesaf.2011.05.002.

[40] David C, Salvador S, Dirion JL, Quintard M. Determination of a reaction scheme for cardboard thermal degradation using thermal gravimetric analysis. J Anal Appl Pyrolysis 2003;67:307–23. doi:10.1016/S0165-2370(02)00070-0.

[41] Gupta AK, M-uacute P, ller. Pyrolysis of Paper and Cardboard in Inert and Oxidative Environments. J Propuls Power 1999;15:187–94. doi:10.2514/2.5441.

[42] Chaz M. Profiles in Garbage: Corrugated Boxes. waste360 2012. http://waste360.com/research-and-statistics/profiles-garbage-corrugated-boxes (accessed May 11, 2015).

[43] Herlihy J. Statistical Report 2013. Floor Cover Wkly 2014;63. doi:10.1080/0034408180130314.

[44] ASTM International. Standard Test Method for Ignition Characteristics of Finished Textile Floor Covering 2011. doi:10.1520/D2859-06R11.2.

[45] ASTM International. Standard Test Method for Critical Radiant Flux of Floor-Covering Systems Using a Radiant Heat Energy Source 2014. doi:10.1520/D3675-

11.2.

[46] Looyeh MRE, Bettess P. A finite element model for the fire-performance of GRP panels including variable thermal properties. Finite Elem Anal Des 1998;30:313–24. doi:10.1016/S0168-874X(98)00036-5.

[47] Galgano A, Di Blasi C, Branca C, Milella E. Thermal response to fire of a fibre-reinforced sandwich panel: Model formulation, selection of intrinsic properties and experimental validation. Polym Degrad Stab 2009;94:1267–80. doi:10.1016/j.polymdegradstab.2009.04.007.

[48] Kandola B, Ebdon J, Chowdhury K. Flame Retardance and Physical Properties of Novel Cured Blends of Unsaturated Polyester and Furan Resins. Polymers (Basel) 2015;7:298–315. doi:10.3390/polym7020298.

[49] Gann RG, Averill JD, Butler KM, Jones WW, Mulholland GW, Neviaser JL, et al. Phase I Final Report International Study of the Sublethal Effects of Fire Smoke on Survivability and Health (SEFS). 2001.

[50] Lautenberger C, Kim E, Dembsey N, Fernandez-Pello C. The Role of Decomposition Kinetics in Pyrolysis modeling - Application to a Fire Retardant Polyester Composite. Fire Saf. Sci. - Proceedsings Ninth Int. Symp., 2008, p. 1201–12. doi:DOI:10.3801/IAFSS.FSS.9-1201.

[51] Kim E, Lautenberger C, Dembsey N. Property Estimation for Pyrolysis Modeling Applied to polyester FRP Composites with Different Glass Content. Fire Mater., San Francisco, Ca: Interscience; 2009.

[52] Marquis DM, Pavageau M, Guillaume E, Chivas-Joly C. Modelling decomposition and fire behaviour of small samples of a glass-fibre-reinforced polyester/balsa-cored

sandwich material. Fire Mater 2013;37:413–39. doi:10.1002/fam.2136.

[53] Zinchenko VI, Nesmelov V V, Gol'din VD. Prediction of thermal degradation of thermoprotective materials on the basis of their composition and properties of components. Combust Explos Shock Waves 2005;41:57–63. doi:10.1007/s10573-005-0006-2.

[54] Hubbard JA, Brown AL, Dodd AB, Gomez-vasquez S, Ramirez CJ. Carbon fiber composite characterization in adverse thermal environments 2011.

[55] Boeing. Boeing: 787 Dreamliner 2015. http://www.boeing.com/commercial/787/#/design-highlights/visionary-design/composites/advanced-composite-use/ (accessed January 2, 2016).

[56] Mouritz AP. Fire Safety of Advanced Composites for Aircraft B2004/0046 2006:36.

[57] Lyon RE. Fire-Resistant Materials: Research Overview. Atlantic City, NJ: 1997.

[58] Quintiere JG, Walters RN, Crowley S. Flammability Properties of Aircraft Carbon-Fiber Structural Composite. Tech Rep 2007;7:8–72.

[59] McGurn MT, DesJardin PE, Dodd AB. Numerical simulation of expansion and charring of carbon-epoxy laminates in fire environments. Int J Heat Mass Transf 2012;55:272–81. doi:10.1016/j.ijheatmasstransfer.2011.09.013.

[60] ASTM Standard E906, 2014, "Standard Test Method for Heat and Visible Smoke Release Rates for Materials and Products Using a Thermopile Method. 2014. doi:10.1520/E0906-14.

[61] Chaos M, Khan MM, Krishnamoorthy N, Chatterjee P, Wang Y, Dorofeev SB. Experiments and Modeling ofSingle- and Triple-wall Corrugated Cardboard: Effective Material Properties and Fire Behavior. Fire Mater., San Francisco, Ca:

Interscience Communications; 2011, p. 625–36.

[62] Stoliarov SI, Safronava N, Lyon RE. The effect of variation in polymer properties on the rate of burning. Fire Mater 2009;33:257–71. doi:10.1002/fam.1003.

[63] Linteris GT. Numerical simulations of polymer pyrolysis rate: Effect of property variations . Fire Mater 2011;35:463–80. doi:10.1002/fam.1066.

[64] Linteris GT, Lyon RE, Stoliarov SI. Prediction of the gasification rate of thermoplastic polymers in fire-like environments. Fire Saf J 2013;60:14–24. doi:10.1016/j.firesaf.2013.03.018.

[65] Bal N, Rein G. Relevant model complexity for non-charring polymer pyrolysis. Fire Saf J 2013;61:36–44. doi:10.1016/j.firesaf.2013.08.015.

[66] Chaos M. Application of sensitivity analyses to condensed-phase pyrolysis modeling. Fire Saf J 2013;61:254–64. doi:10.1016/j.firesaf.2013.09.016.

[67] Kim E, Dembsey N, Shivkumar S. Evaluating effects of applying different kinetic models to pyrolysis modeling of fiberglass-reinforced polymer composites. Fire Mater 2015;39:153–73. doi:10.1002/fam.2239.

[68] Lyon RE, Safronava N, Stoliarov SI. The Role of Thermal Decomposition Kinetics in the Burning of Polymers. Interflam, Nottingham, UK: Interscience Communications; 2010.

[69] E2550-11 A. Standard Test Method for Thermal Stability by Thermogravimetry 2011. doi:10.1520/E2550-11.

[70] Astm E1641-13. Standard Test Method for Decomposition Kinetics by Thermogravimetry Using the Ozawa/Flynn/Wall Method 2013:1–7. doi:10.1520/E1641.

[71] Brown ME. Introduction to Thermal Analysis: Techniques and Applications. 2nd ed. New York: Springer Netherlands; 2001. doi:10.1007/0-306-48404-8.

[72] Snegirev AY. Generalized approach to model pyrolysis of flammable materials. Thermochim Acta 2014;590:242–50. doi:10.1016/j.tca.2014.07.009.

[73] ASTM International. Standrad Test Method for Kinetic Parameters for Thermally Unstable Materials by Differential Scanning Calorimetry Using the Kissinger Method 2012. doi:10.1520/E2890-12E01.

[74] Maciejewski M. Computational aspects of kinetic analysis . Part B : The ICTAC Kinetics Project Ð the decomposition kinetics of calcium carbonate revisited , or some tips on survival in the kinetic mine ® eld $. Thermochim Acta 2000;355:145–54. doi:10.1016/S0040-6031(00)00444-5.

[75] Zsakó J. The Kinetic Compensation Effect. J Therm Anal Calorim 1976;9:101–8. doi:10.1007/bf01909271.

[76] Barrie PJ. The mathematical origins of the kinetic compensation effect: 1. the effect of random experimental errors. Phys Chem Chem Phys 2012;14:318–26. doi:10.1039/C1CP22666E.

[77] Brown ME, Maciejewski M, Vyazovkin S, Nomen R, Sempere J, Burnham A, et al. Computational aspects of kinetic analysis. Thermochim Acta 2000;355:125–43. doi:10.1016/S0040-6031(00)00443-3.

[78] Vyazovkin S, Sbirrazzuoli N. Isoconversional kinetic analysis of thermally stimulated processes in polymers. Macromol Rapid Commun 2006;27:1515–32. doi:10.1002/marc.200600404.

[79] Friedman HL. New methods for evaluating kinetic parameters from thermal analysis

data. J Polym Sci Part B Polym Lett 1969;7:41–6. doi:10.1002/pol.1969.110070109.

[80] Flynn JH, Wall LA. A quick, direct method for the determination of activation energy from thermogravimetric data. J Polym Sci Part B Polym Lett 1966;4:323–8. doi:10.1002/pol.1966.110040504.

[81] Ozawa T. Methods for Kinetic Analysis of Thermoanalytical Data. Bull Japan Inst Met 1985;24:797–804. doi:10.2320/materia1962.24.797.

[82] Chaos M, Khan MM, Krishnamoorthy N, De Ris JL, Dorofeev SB. Evaluation of optimization schemes and determination of solid fuel properties for CFD fire models using bench-scale pyrolysis tests. Proc Combust Inst 2011;33:2599–606. doi:10.1016/j.proci.2010.07.018.

[83] Matala A. Methods and applications of pyrolysis modelling for polymeric materials. 2013.

[84] Di Blasi C. Comparison of semi-global mechanisms for primary pyrolysis of lignocellulosic fuels. J Anal Appl Pyrolysis 1998;47:43–64. doi:10.1016/S0165-2370(98)00079-5.

[85] Varhegyi G, Jakab E, Antal MJ. Is the Broido-Shafizadeh Model for Cellulose Pyrolysis True? Energy & Fuels 1994;8:1345–52. doi:10.1021/ef00048a025.

[86] Lyon RE, Walters RN, Stoliarov SI. Thermal analysis of flammability. J Therm Anal Calorim 2007;89:441–8. doi:10.1007/s10973-006-8257-z.

[87] International A. Standard Test Method for Determining Specific Heat Capacity by Differential Scanning Calorimetry 2011. doi:10.1520/E1269-11.

[88] Hohne GWH, Hemminger WF, Flammersheim H-J. Differential Scanning Calorimetry. Berlin: Springer Berlin; 2003. doi:10.1007/978-3-662-06710-9.

[89] Li J, Stoliarov SI. Measurement of kinetics and thermodynamics of the thermal degradation for non-charring polymers. Combust Flame 2013;160:1287–97. doi:10.1016/j.combustflame.2013.02.012.

[90] Stoliarov SI, Walters RN. Determination of the heats of gasification of polymers using differential scanning calorimetry. Polym Degrad Stab 2008;93:422–7. doi:10.1016/j.polymdegradstab.2007.11.022.

[91] Li J, Stoliarov SI. Measurement of kinetics and thermodynamics of the thermal degradation for charring polymers. Polym Degrad Stab 2014;106:2–15. doi:10.1016/j.polymdegradstab.2013.09.022.

[92] Staggs JEJ. The heat of gasification of polymers. Fire Saf J 2004;39:711–20. doi:10.1016/j.firesaf.2004.07.001.

[93] ASTM International. Standard Test Method for Determining Flammability Characteristics of Plastics and Other Solid Materials Using Microscale Combustion 2013. doi:10.1520/D7309-11.Copyright.

[94] ASTM International. Standard Test Method for Heat of Combustion of Hydrocarbon Fuels by Bomb Calorimeter (High Precision Method) 1988. doi:10.1520/D2382-88.

[95] Walters RN, Hackett SM, Lyon RE. Heats of combustion of high temperature polymers. Fire Mater 2000;24:245–52. doi:10.1002/1099-1018(200009/10)24:5<245::AID-FAM744>3.0.CO;2-7.

[96] Babrauskas V. From Bunser Burner to Heat Release Rate Calorimeter. In: Babrauskas V, Grayson SJ, editors. Heat Release Fires, New York: E & FN Spon; 1992.

[97] Babrauskas V. Performance of the Ohio State University rate of heat release

apparatus using polymethylmethacrylate and gaseous fuels. Fire Saf J 1982;5:9–20. doi:10.1016/0379-7112(82)90003-0.

[98] ASTM International. Standard Test Method for Heat and Visible Smoke Release Rates for Materials and Products Using an Oxygen Consumption Calorimeter 1 2015:1–20. doi:10.1520/E1354-13.2.

[99] ASTM International. ASTM E2058-13a Standard Test Methods for Measurement of Material Flammability Using a Fire Propagation Apparatus (FPA) 2013;i:1–30. doi:10.1520/E2058-13A.2.

[100] International A. Standard Test Method for Determination of Fire and Thermal Parameters of Materials, Products, and Systems Using and Intermediate Scale Calorimeter (ICAL) 2014. doi:10.1520/E1623-14.

[101] Brewster MQ. Thermal Radiative Transfer and Properties. New York: John Wiley & Sons, Inc.; 1992.

[102] Linteris G, Zammarano M, Wilthan B, Hanssen L. Absorption and reflection of infrared radiation by polymers in fire-like environments. Fire Mater 2012;36:537–53. doi:10.1002/fam.1113.

[103] Tsilingiris PT. Comparative evaluation of the infrared transmission of polymer films. Energy Convers Manag 2003;44:2839–56. doi:10.1016/S0196-8904(03)00066-9.

[104] Försth M, Roos A. Absorptivity and its dependence on heat source temperature and degree of thermal breakdown. Fire Mater 2011;35:285–301. doi:10.1002/fam.1053.

[105] Performance M, Spectrophotom- NI, Mass A, Solar Z, Tables I, Materials S, et al. Standard Test Method for Solar Absorptance , Reflectance , and Transmittance of

Materials Using Integrating Spheres 1 1996;03:1–9. doi:10.1520/E0903-12.2.

[106] Matsumoto T, Ono a. Specific heat capacity and emissivity measurements of ribbon-shaped graphite using pulse current heating. Int J Thermophys 1995;16-16:267–75. doi:10.1007/BF01438977.

[107] Jiang F, de Ris JL, Khan MM. Absorption of thermal energy in PMMA by in-depth radiation. Fire Saf J 2009;44:106–12. doi:10.1016/j.firesaf.2008.04.004.

[108] Bal N, Raynard J, Rein G, Torero JL, Försth M, Boulet P, et al. Experimental study of radiative heat transfer in a translucent fuel sample exposed to different spectral sources. Int J Heat Mass Transf 2013;61:742–8. doi:10.1016/j.ijheatmasstransfer.2013.02.017.

[109] Tsilingiris PT. Comparative evaluation of the infrared transmission of polymer films. Energy Convers Manag 2003;44:2839–56. doi:10.1016/S0196-8904(03)00066-9.

[110] Method ST. ASTM C177-13 Standard Test Method for Steady-State Heat Flux Measurements and Thermal Transmission Properties by Means of the Guarded-Hot-Plate 2014:1–23. doi:10.1520/C0177-13.2.

[111] Conshohocken W. Standard Test Method for Steady-State Thermal Transmission Properties by Means of the Heat Flow Meter Apparatus 1 2003:1–15. doi:10.1520/C0518-10.2.

[112] Standard A. E1461. Standard test method for thermal diffusivity by the flash method. ASTM, West Conshohocken, PA 2001;i:1–11. doi:10.1520/E1461-13.2.

[113] Harada T, Hata T, Ishihara S. Thermal constants of wood during the heating process measured with the laser flash method. J Wood Sci 1998;44:425–31.

doi:10.1007/BF00833405.

[114] ISO. ISO 22007-2, Plastics -- Determination og thermal conductivity and thermal diffusivity -- Part 2: Transient plane heat source (hot disc) method 2015.

[115] Suleiman BM, Larfeldt J, Leckner B, Gustavsson M. Thermal conductivity and diffusivity of wood. Wood Sci Technol 1999;33:465–73. doi:10.1007/s002260050130.

[116] Bentz DP. Combination of Transient Plane Source and Slug Calorimter Measurements to Estimate the Thermal Properties of Fire Resistive Materials. J Test Eval 2007;35.

[117] Myllymaki J, Baroudi D. Boundary Temperature Measurements, 1803, p. 349–57.

[118] Bentz DP. Measurement and Microstructure-Based Modeling of the Thermal Conductivity of Fire Resistive Materials. Proc. 28th Int. Therm. Conduct. Conf., New Brunswick, Canada: 2005.

[119] Childs PRN. Practical Temperature Measurement. Elsevier; 2001. doi:10.1016/B978-075065080-9/50009-5.

[120] J.P. Holman. Heat Transfer. 7 ed. New York: McGraw-Hill; 1990.

[121] Li J, Gong J, Stoliarov SI. Gasification experiments for pyrolysis model parameterization and validation. Int J Heat Mass Transf 2014;77:738–44. doi:10.1016/j.ijheatmasstransfer.2014.06.003.

[122] Chaos M, Khan MM, Krishnamoorthy N, De Ris JL, Dorofeev SB. Bench-scale flammability experiments: Determination of material properties using pyrolysis models for use in CFD simulations. INTERFLAM, 2010.

[123] Staggs JEJ, Whiteley RH. Modelling the combustion of solid-phase fuels in cone

calorimeter experiments. Fire Mater 1999;23:63–9. doi:10.1002/(SICI)1099-1018(199903/04)23:2<63::AID-FAM671>3.0.CO;2-3.

[124] Carvel R, Steinhaus T, Rein G, Torero JLL. Determination of the flammability properties of polymeric materials: A novel method. Polym Degrad Stab 2011;96:314–9. doi:10.1016/j.polymdegradstab.2010.08.010.

[125] Siegel R, Howell J. Thermal Radiation Heat Transfer. New York: Taylor & Howell; 2002.

[126] W.J. Parker. Calculations of the Heat Release Rate by Oxygen Consumption for Various Applications. Washington, D.C.: 1982.

[127] Huggett C. Estimation of rate of heat release by means of oxygen consumption measurements. Fire Mater 1980;4:61–5. doi:10.1002/fam.810040202.

[128] Boulet P, Parent G, Acem Z, Collin a., Försth M, Bal N, et al. Radiation emission from a heating coil or a halogen lamp on a semitransparent sample. Int J Therm Sci 2014;77:223–32. doi:10.1016/j.ijthermalsci.2013.11.006.

[129] Austin PJ, Buch RR, Kashiwagi T. Gasification of silicone fluids under external thermal radiation. Part I. Gasification rate and global heat of gasification. Fire Mater 1998;22:221–37. doi:10.1002/(SICI)1099-1018(199811/12)22:6<221::AID-FAM658>3.0.CO;2-D.

[130] Marquis DM, Guillaume E, Camillo A. Effects of oxygen availabilityon the combustion behavior of materials in a controlled atmosphere cone calorimeter. Proc. 11th Int. Symp. Int. Assoc. Fire Saf. Sci., University of Canterbury, New Zealand: 2014.

[131] Lattimer BY, Ouellette J, Trelles J. Measuring properties for material decomposition

modeling. Fire Mater 2011;35. doi:10.1002/fam.1031.

[132] Salvador S, Quintard M, David C. Combustion of a substitution fuel made of cardboard and polyethylene: influence of the mix characteristics—modeling. Fire Mater 2008;32:417–44. doi:10.1002/fam.978.

[133] Li J, Gong J, Stoliarov SI. Development of pyrolysis models for charring polymers. Polym Degrad Stab 2015;115:138–52. doi:10.1016/j.polymdegradstab.2015.03.003.

[134] McKinnon MB, Stoliarov SI, Witkowski A. Development of a pyrolysis model for corrugated cardboard. Combust Flame 2013;160:2595–607. doi:10.1016/j.combustflame.2013.06.001.

[135] ASTM International. Standard Test Method for Heat and Visible Smoke Release Rates for Materials and Products Using an Oxygen Consumption Calorimeter 2015. doi:10.1520/E1354-15A.

[136] Zhang J, Delichatsios MA. Determination of the convective heat transfer coefficient in three-dimensional inverse heat conduction problems. Fire Saf J 2009;44:681–90. doi:10.1016/j.firesaf.2009.01.004.

[137] Ceramics T. Organic RCF Vacuum Formed Products 2013. http://www.morganthermalceramics.com/sites/default/files/datasheets/mgam_5-14-700_kaowoolbands_9.pdf (accessed January 8, 2016).

[138] NIST Chemistry Webbook n.d. http://webbook.nist.gov/.

[139] LYON R, QUINTIERE J. Criteria for piloted ignition of combustible solids. Combust Flame 2007;151:551–9. doi:10.1016/j.combustflame.2007.07.020.

[140] Chaos M, Khan MM, Dorofeev SB. Inert and Oxidative pyrolysis of a

lignocellulosic material: Corrugated Cardboard. 7th US Natl. Tech. Meet. Combust. Inst., Atlanta, GA: 2011.

[141] Shaw Contract Group. EcoWorx Tile Specification 2009. http://www.shawcontractgroup.com/Content/LiteraturePDFs/Backings_pdf/ecoworx_spec.pdf (accessed January 1, 2015).

[142] Stoliarov SI, Li J. Parameterization and Validation of Pyrolysis Models for Polymeric Materials. Fire Technol 2015. doi:10.1007/s10694-015-0490-1.

[143] Tian T, Cole KD. Anisotropic thermal conductivity measurement of carbon-fiber/epoxy composite materials. Int J Heat Mass Transf 2012;55:6530–7. doi:10.1016/j.ijheatmasstransfer.2012.06.059.

[144] Dowding KJ, Beck J V., Blackwell BF. Estimation of directional-dependent thermal properties in a carbon-carbon composite. Int J Heat Mass Transf 1996;39:3157–64. doi:10.1016/0017-9310(95)00401-7.

[145] Butland ATD, Maddison RJ. The specific heat of graphite: An evaluation of measurements. J Nucl Mater 1973;49:45–56. doi:10.1016/0022-3115(73)90060-3.

[146] McKinnon M, Stoliarov S. Pyrolysis Model Development for a Multilayer Floor Covering. Materials (Basel) 2015;8:6117–53. doi:10.3390/ma8095295.

[147] Buchanan AC, Britt PF. Investigations of restricted mass transport effects on hydrocarbon pyrolysis mechanisms through silica immobilization. J Anal Appl Pyrolysis 2000;54:127–51. doi:10.1016/S0165-2370(99)00078-9.

[148] Matsubara H, Ohtani H. Evaluation of molecular weight of original epoxy acrylates in UV-cured resins by pyrolysis-gas chromatography in the presence of organic alkali. J Anal Appl Pyrolysis 2006;75:226–35. doi:10.1016/j.jaap.2005.06.005.

[149] Balabanovich AI. GC/MS Identification of Pyrolysis Products from Fire-retardant Brominated Epoxy Resin. J Fire Sci 2005;23:227–45. doi:10.1177/0734904105047006.

[150] Galipo RC, Egan WJ, Aust JF, Myrick ML, Morgan SL. Pyrolysis gas chromatography/mass spectrometry investigation of a thermally cured polymer. J Anal Appl Pyrolysis 1998;45:23–40. doi:10.1016/S0165-2370(98)00059-X.

[151] Hariharan R, Test FL, Florio J, Henderson JB. Internal Pressure and Temperature Distribution in DecomposingPolymer Composites. In: Hetsroni G, editor. Proc. Ninth Int. Heat Transf. Conf., Jerusalem: 1990, p. 335–40.

[152] John W. Connell. An Overview of Thermoplastic Structural Composites for Aerospace Applications. High Perform. Plast. 2005 Int. Conf., Vienna, Austria: iSmithers Rapra Publishing; 2005, p. 178.

[153] Mouritz a. P, Gibson a. G. Fire Properties of Polymer Composite Materials. 2006.

[154] MatWeb L. E-Glass Fiber, Generic. MatWeb Mater Prop Data 2015. http://matweb.com/search/DataSheet.aspx?MatGUID=d9c18047c49147a2a7c0b0bb1743e812&ckck=1 (accessed December 15, 2015).

[155] Bräuer G. Large area glass coating. Surf Coatings Technol 1999;112:358–65. doi:10.1016/S0257-8972(98)00737-3.